## Unveiling the Perovskite Single Crystals for

## Photonics Applications via Facile Molecular

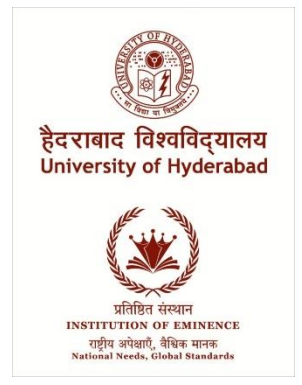
## Engineering

### A Thesis Submitted for the Degree of Doctor of Philosophy

in the Faculty of Science

by

### SARVANI JOWHAR KHANAM



School of Chemistry University of Hyderabad -500053, India

**July - 2023** 

## **Dedicated To**

My Family

## **DECLARATION**

I, *Sarvani Jowhar Khanam*, hereby declare that the matter embodied in the thesis entitled "Unveiling the Perovskite Single Crystals for Photonics Applications via Facile Molecular Engineering" is the result of an investigation carried out by me in the School of Chemistry, University of Hyderabad, Hyderabad, India under supervision of *Dr. Murali Banavoth*.

The except where due acknowledgement has been made, the work is that of the author alone; the work has not been submitted previously, in whole or in part, to qualify for any other academic award; the content of the dissertation is the result of work which has been carried out since the official commencement date of the approved research program; any paid or unpaid editorial work carried out by a third party is acknowledged, and ethics procedures and guidelines have been followed.

School of Chemistry, University of Hyderabad, Hyderabad-500046, Telangana, India.

Phone: +91 40 23134828,

Email: murali.banavoth@uohyd.ac.in, URL: <a href="http://chemistry.uohyd.ac.in/mb/">http://chemistry.uohyd.ac.in/mb/</a>

Dr. Murali Banavoth Associate Professor

### **CERTIFICATE**

This is to certify that the thesis entitled "Unveiling the Perovskite Single Crystals for Photonics Applications via Facile Molecular Engineering", submitted by Mrs. Sarvani Jowhar Khanam bearing the registration number 18CHPH27 in partial fulfilment of the requirements for the award of Doctor of Philosophy (Ph.D.) in the School of Chemistry, University of Hyderabad, India under my supervision and guidance. This thesis is free from plagiarism and has not been submitted previously in part or full to this or another University/Institution for any degree or diploma. Further, the student has the following publications before submission of the thesis for adjudication and has produced evidence for the same in the form of reprints.

Parts of the thesis have been published in the following publications:

- (1) Khanam, S. J.; Banerjee, D.; Soma, VR.; Murali, B. Stability enhancement and pronounced three-photon absorption in SrCl<sub>2</sub>-doped FAPbBr<sub>3</sub> nanocrystals. J. Mater. Chem. C. 2023, 11, 3275–3283.
- (2) Khanam, S. J.; Parikh, N.; Satapathi, S.; Kalam, A.; Murali, B.; Pankaj, Y. Role of Heterocyclic Organic Compounds on the Optoelectronic Properties of Halide Perovskite Single Crystals. ACS Appl. Energy Mater. 2022, 5, 14732–14738.

- (3) Khanam, S. J.; Srinivasa, R. K.; Wei, L.; Murali, B. The Aromatic Additives Boost the Mixed Halide Perovskite Single Crystal's Terahertz Properties. *J. Phys. Chem. Lett.* 2023, 14, 5624–5632
- (4) Khanam, S. J.; Srinivasa, R. K.; Premalatha, A.; Ketavath, R.; Wufeng, F.; Wei, L.; Murali, B. "Additive Engineering in CH<sub>3</sub>NH<sub>3</sub>PbBr<sub>3</sub> Single Crystals for Terahertz Devices and Tunable High Order Harmonics" *J. Mater. Chem. C.* 2023, 2, 1-16
- (5) Khanam, S. J.; Srinivasa, R. K.; Wei, L.; Ketavath, R.; Murali, B. Additive Engineered MAPbBr<sub>3-X</sub>Cl<sub>x</sub> Single Crystals; and Higher-Order Harmonics Study. (*Manuscript Under submission*).

#### **Patents**

1."Additive Assisted Perovskite Single Crystal Growth Method for Optoelectronics Applications", Murali Banavoth, Sarvani Jowhar Khanam, (complete patent, Ref. No. 202141052653).

The student has made presentations at the following conferences:

### **Scientific Presentations**

#### **Oral Presentations:**

- (1) 'Oral presentation' at the International Conference on Nanoscience and Nanotechnology (ICNN-2022), organized by Mindanao State University, Lliagan Institute of Technology, at Naawan and Caraga State University with e-Asia Joint Program and NACENTECH, at Oazis Hotel, Butuan city, via Zoom.
- (2) 'Oral presentation' at "CHEMfest-2022" was organized by the University of Hyderabad, Hyderabad.
- (3) 'Oral presentation' at the 29th edition of the national conference "Condensed Matter Days 2021" (CMDAYS-21) was organized by the Department of Physics, Central University of Jharkhand, Ranchi, India.

(4) 'Oral presentation' at "Hands-on experience on the measurement of EIS under the light" was conducted by the PDEU, Gandhinagar, Gujarat, India.

#### **Poster Presentations:**

- (1) Poster presentation at CHEMFEST-2023 at SOC, UoH, Hyderabad.
- (2) Poster presnetation at CARE-2023, HRI, Prayagraj, UP.
- (3) 'Poster presentation' at the international conference "International Conference on Frontier Areas of Science and Technology" (ICFAST-2022) at the University of Hyderabad, Hyderabad.
- (4) Poster presentation at CHEMFEST-2022 at SOC, UoH, Hyderabad.

#### **Participating in Workshops:**

- (1) ACS on Campus\_Half-Day event at UoH, Hyderabad.
- (2) Participated in the "International Conference on Advanced Nanomaterials and Applications ICANA 2022", held on 16th-18th November 2022. organized by the School of Advanced Sciences, VIT-AP University, India and Indiana University-Purdue University Indianapolis (IUPUI), USA.
- (3) Attended 'Machine Learning (ML) course for Halide Perovskites by Laboratory of Advanced Synthesis & Characterization' by Dr Pankaj Yadav –Assistant Professor, Department of Solar Energy, Pandit Deendayal Energy University, Gandhinagar, Gujarat, India.
- (4) Attended 3 Days workshop on "Fabrication and Characterisation of Flexible Electronic Devices" conducted by Prof Ankur Solanki at PDEU, Gandhinagar, Gujarat.
- (5) Visited DRDO Jodhpur, Rajasthan, as a project assistant, on an official project visit to test the research samples of perovskite crystals and films in the project: Contract for Acquisition of Research Services (CARS) sponsored by Defence Laboratory-Jodhpur, Defence Research & Development Organization, Government of India, Ministry of Defence, titled "Preliminary investigations of inorganic and hybrid perovskite single crystals for their structural and functional properties w.r.t. gamma radiation".

- (6) Visited PDEU, Gandhinagar, Gujarat, with samples to measure EIS under the light for ten days.
- (7) Attended a one-day student conference on "Optics and Photonics 2021" (SCOP-2021) organized by Physical Research Laboratory, Ahmedabad, Gujarat.
- (8) Attended four days E-Workshop on "Advanced Spectroscopy for Emerging Materials" organized online by CSIR-National Physical Laboratory, New Delhi.
- (9) Attended one day conference on "Perovskite Solar Cell" Conducted by Translational Perovskite Research Council.
- (10) Attended a three-day international webinar on "Nanostructured Semiconducting Materials for Energy Applications" (NSME-2020) Organized by the Department of Applied Chemistry, Defence Institute of Advanced Technology, Girinagar, Maharashtra, Pune-411025.
- (11) Attended a five days training programme on "Machine learning in Material Science" conducted by the PDEU, Gandhinagar, Gujarat, India.
- (12) Attended 29 hrs training programme on the Complete Data Science Bootcamp.
- (13) Attended one day conference on "Ultrafast dynamics in Halide perovskite Materials and Devices" organized by the Perovskite society of India.

Further, the student has passed the following courses towards the fulfilment of the coursework requirement for a Ph.D.

S.No	Course No.	Title of the Course	No Of Credits	Grade
1.	CY801	Research Proposal	4	Pass
2.	CY805	Instrumental	4	Pass
		Methods-A		
3.	CY806	Instrumental	4	Pass
		Methods-B		

Dr. Murali Banavoth

MURALI RANAVOTH (PhD)
Mests actions Professor
SCHOOL OF CHEMISTRY (SOC)
University of Nydersited (HCU)
Pad. GR. Star Path. Cestiburit, Had
Ed., India- State Professor (HCU)
Ed., India- State Professor (HCU)
Color Color Path. Professor (HCU)
Color

Dean

School of Chemistry

Dean
SCHOOL OF CHEMISTRY
University of Hyderabad
Hyderabad-500 046.

# Acknowledgements

Since I started my Ph.D. journey with some scepticism, I honestly never imagined I would find myself in this situation. However, my relationships with some extraordinary people and bright minds stretch my capacities and make this journey easy. This has kept me energised over the past six years. It is impossible for me to communicate digitally how much I owe these people for what I am today.

First, I would like to thank my supervisor *Dr. Murali Banavoth* for his exceptional guidance, motivation, and support in carrying out this research work. I consider myself blessed to get a chance to pursue my doctoral studies with him. I am grateful for his guidance, encouragement, cooperation, and input and for allowing me to work in the laboratory. I have really enjoyed working with him over the past six years. I am pleased to thank the former and present Dean, School of Chemistry (SoC), UoH, for the academic support.

I sincerely thank my doctoral committee members, *Prof. Ramu Shridhar* and *Dr. Srinivasa Rao Yaragorla*, for their invaluable suggestions and encouragement throughout my research work. I would like to thank our collaborator *Prof. Soma Venugopal Rao*, School of Physics (SoP), UoH (Acrhem), for his helpful suggestions and comments; for allowing me to avail the NLO studies.

It is a pleasure to acknowledge the financial support from the *University of Hyderabad* that made the work for this dissertation possible. I owe an outstanding debt of gratitude to all my teachers, from my school to the university, for their wonderful teaching and education throughout my academics. In this context, continuous help from the non-teaching staff of SoC, especially from Mr. Venkat, Mr. Abraham, Ms. Geetha, Ms. Radhika, and Ms. Rani (school office) for various official works, Dr. M. Durga Prasad, Mr. Rajesh for TEM imaging, Mr.

Durgesh Kumar Singh and Mr. Mahindar for NMR measurements, Mahesh for XRD, Mr. Sunil and Mr. Vinay Kumar for the FESEM and PXRD measurements, respectively have been absolute helpful to facilitate my research work. It is simply hard to describe how much I am thankful to the "MB group" members. I want to thank my seniors, Mr. Ravi Ketavath, Mr. Santhosh Rompivalasa, Mr. Ranadeep Raj Sumukam and Mr. Ramu Naidu, for their continuous help during the initial days of my Ph.D. journey. I am really grateful to Hema, Narasimha, Shashi Kant, Gunjan, Athira, Ayesha and many others in HCU, with whom I had some wonderful memories throughout my Ph.D. life. I would also like to sincerely thank all my close friends Yasmeen, Mumtaz, Fatima and other school friends for their help and encouragement in various stages of my life.

I would like to express my deepest gratitude to my parents, my beloved mother, Sabeera Begum, and my father, Sarvani Wahab Khanam. I would not have reached this stage of my life. I am greatly indebted from the bottom of my heart to my mother and father for their spiritual guidance and for staying as philosophers in my life. Mother-in-law Mumtaz Begum and Sister-in-law Ms. Haseen Taj deserve special mention for their inseparable support and prayers. Any word would be less to justify their sacrifice, and I don't want to let them down with 'thank you' either. I would like to thank all my elder, younger sisters, elder brothers, sisters-in-law and bother-in-laws for their support and prayers.

I would also like to extend my heartfelt appreciation to my husband, Mohammad Ali Jinnah Khan, for his continuous support and encouragement throughout my research work. I am truly grateful for his unwavering support as my spouse and for blessing me with the most wonderful gifts of love and joy: Zoya Iffath, Sana Rifath, and Owais Masood Khan, my beloved daughters and son.

May-2023

Sarvani Jowhar khanam

# **Outline of the Contents**

## **Table of Contents**

Outline of the Contents	xxxiii
CHAPTER-1 Introduction	1
Chapter-1 Introduction	2
1.1 Introduction to Perovskite single crystals (PSCs)	2
1.2. PSCs Photodeters	3
1.2.1. Types of PD	5
1.2.3. Working principle of PD	6
1.3. Promising Properties of PSCs	8
1.3.1 Large Absorption Coefficient	8
1.3.2 Tunable Bandgap	9
1.3.3. Long Diffusion Length and Large Mobility-Lifetime Product	12
1.3.4. Large Resistivity	14
1.4. Recent Advancements in PD	15
1.5. General Description of Nonlinear Optics	17
1.5.1 Materials for Nonlinear	17
1.5.2. Higher-Order Harmonics Generation (HHG)	20

CHAPTER-2 Materials, Methods & Characterizations	30
2. Materials & Methods	31
2.1. Synthetic Methods	31
2.1.1. Synthesis of MAPbBr <sub>3</sub> Crystals Growth with additives:	33
2.1.2. Synthesis of Cl-doped MAPbBr <sub>3</sub> SCs	35
2.1.3. Synthesis of FAPbBr <sub>3</sub> PNCs	36
2.2. Device architecture:	38
2.2.1. Thermal Evaporator	40
2.3. Characterization	41
2.3.1. Structural Characterization	41
2.3.2. Optical Characterization	43
2.3.3. Thermal Properties	47
2.3.4. Electron Microscopes	49
2.3.5. Electrical measurement:	53
2.4. Experimental details of Terahertz time-domain spectroscopy (THz-TDS)	54
2.5. HHG experimental setup:	55
2.6. Introduction to the Z-scan Technique	56
CHAPTER-3 Additive Engineering in CH <sub>3</sub> NH <sub>3</sub> PbBr <sub>3</sub> Single Crystals for Terahertz De	
Tunable High Order Harmonics	61
3.1. Introduction	63

3.2. Results and Discussion
3.2.1. Morphology and Structural Properties Properties
3.2.2 Optical properties72
3.2.3. THz spectroscopy76
3.3. Application of PSCs toward the generation of higher-order harmonics generation81
3.3.1. Harmonics intensity to describe the stability of PSCs
3.3.2. Harmonics Cut-off:84
3.3.3. Spectral shift of harmonics85
3.3. Conclusions90
CHAPTER-4 Role of Heterocyclic Organic Compound on the optoelectronic properties of Halide
Perovskite Single Crystal111
4.1. Introduction 112
4.2. Results and Discussion
4.3. Conclusion
CHAPTER-5a Additive Engineered MAPbBr <sub>3-X</sub> Cl <sub>x</sub> Single Crystals; and Higher-Order Harmonics Study
5.1.1 Introduction
5.1.2. Results and Discussion
5.1.2.1. Morphology and Structural Properties
5.1.2.2. Thermogravimetric/Differential Scanning Calorimetric Analysis

5.1.2.3. Higher-order harmonics generation from their laser-induced plasm	a plumes141
5.1.3. Conclusions	146
CHAPTER-5b The Aromatic Additives Boost the Mixed Halide Perovskite S	ingle Crystal's
Terahertz Properties	160
5.2.1 Introduction	161
5.2.2. Results and Discussion	163
5.2.2.1. Morphology and Structural Properties	163
5.2.2.2 Optical properties	168
5.2.2.3. THz spectroscopy	171
5.2.3. Conclusions	174
CHAPTER-6 Stability Enhancement and Pronounced Three-photon Absorption	-
FAPbBr <sub>3</sub> Nano Crystals	190
6.1. Introduction	191
6.2. Materials and methods	194
6.3. Experimental Details	195
6.4. Results and Discussion	195
6.4.1. Morphology and structural properties	195
6.4.2. Optical properties	198
6.4.3. Applications of SrCl <sub>2</sub> doped FAPbBr <sub>3</sub> PNCs towards NLO	199
6.5. Conclusions	204
CHAPTER-7 Challenges and Future Directions	213

7.1. Challenges and Future Directions	214
7.2. Performance enhancement	214
7.3. Operational stability	214
7.4. Environment-friendly perovskite materials	215
7.5. Nanosystem with multifunction	215
7.6. Future Outlook	216
Appendix I	220
1. Materials and Methods:	220
1.1. Synthesis of MAPbBr <sub>3</sub> Crystals Growth with additives:	220
Appendix II	236
Appendix III	239
Appendix IV	244
Annendiy V	249

## List of Fig.s

Fig. 1.1 Perovskite materials unit cell structure
Fig. 1.2 Energy diagram of the [PbX6] units wherein atomic levels, representing bandgap of perovskite materials.
Fig. 1.3 varied applications ranging from smoke detectors, thermoelectric power generators,
atomic-structural analysis, medical diagnostic treatment, food preservation, industrial
structural analysis, metal-rolling, radiocarbon dating etc
Fig. 1.4 Working principle of Perovskite PDs device
Fig. 1.5 Promising Properties of PSCs
Fig. 1.6 Change in bandgap with changing composition in ABX <sub>3</sub> 11
Fig. 1.7 Energy diagram representing 1PA, 2PA and HHG in perovskite materials21
Fig. 2. 1 Synthetic strategy for growing perovskite single-crystal a) Antisolvent Vapour-Assisted Crystallization (AVC) B) Top-Seeded Solution Growth (TSSG) C) Melt Crystallization Growth Method d) Inverse Temperature Crystallization (ITC)32
Crystamzation Glowth Method dy inverse Temperature Crystamzation (11C).
Fig. 2. 2 MAPbBr <sub>3</sub> SC grown using the ITC method on ITO
Fig. 2. 3(a) Polyhedral representation of the unit cell of SrCl <sub>2</sub> doped FAPbBr <sub>3</sub> and (b) schematic
illustration of PNCs with OA. Moreover, (c) & (d) depicts photographs of pristine and SrCl <sub>2</sub> -
doped FAPbBr3 NCs in ambient and UV light, respectively. (e) Steps involved in colloidal
solution preparation
Fig. 2. 4 Device architecture

Fig. 2. 5 Photo images of thermal evaporator for gold deposition at SoC, UoH40
Fig. 2. 6 UV used for bandgap investigations at SoC, UoH
Fig. 2. 7 UV used for bandgap investigations at SoC, UoH
Fig. 2. 8 Thermogravimetric analyzer used for thermal properties at SoC, UoH48
Fig. 2. 9 Differential scanning calorimetry (DSC) used for change in material behaviour with temperature at SoC, UoH
Fig. 2. 10 a) Electron Specimen Interactions. b) Schematic illusion of SEM51
Fig. 2. 11 TEM used for investigations of nanoparticle morphology at SoC, UoH52
Fig. 2. 12 Experimental layouts for (a) terahertz time-domain spectroscopy and (b) high-order harmonics from laser-induced plasma plumes of single perovskite crystals
Fig. 2. 13 Femtosecond Z-scan experimental schematic
Fig. 3. 1(a-e) Structure of additives used and photographs of the PSCs with labels on the bottom. (f) A possible model for additive coordination with unit cell while crystal growth process in solution, (g) ITC method used for crystal growth
Fig. 3. 2(a-d) XPS data of C 1s, N 1s, Pb 4f, and Br 3d core-level spectra with molecular level defect and chemical states behaviour in MAPbBr <sub>3</sub> SCs with changing additives (labels are
mentioned at the right side, follows the same order (a-d)). (e) XPS survey spectra69
Fig. 3. 3(a) XRD pattern of a typical MAPbBr <sub>3</sub> SC grown by additive-based ITC technique.  (b-f) TEM images of pristine and modified PSCs

Fig. 3. 5 Current-voltage traces and trap density. Characteristic I-V trace (Green markers)
showing different regimes (at 300 K). A linear ohmic regime is followed by the trap-filled
regime, marked by a steep increase in current. (c-d) The electronic band structure model in
pristine and modified PSCs represents decreasing surface defects by adding additives
schematically
Fig. 3. 6(a-c) THz electric field (temporal profile) and (d-f) measured transmittance (T) @0°,
T@45° and reflectance (R) @45°, respectively. The legend is shown in (b) applicable to all
panels; Black: solid line, Red:solid line, Green: double line, Blue: thick-thin line, Wine: thin-
thick line, and Magenta: triple lines are corresponding to reference pulse, for SCs MA, MA-
CB, MA-PEA, MA-PXA and MA-API
Fig. 3. 7(a) The measured FWHM and central frequency of reference THz pulse, transmitted
and reflected THz pulses from SCs. (b) The measured real refractive index $(n_s)$ , imaginary
refractive index $(k_s)$ and $(c)$ left Y-axis; absorption coefficients $(\alpha)$ of single crystals at
transmittance (T) @ 0°. (c) right Y-axis: theoretical IR absorption spectra of cubic MAPbBr <sub>3</sub>
SC (data is adapted from the Ref [72])
Fig. 3. 8 2D colour map of harmonics spectra for different (a, c) driving pulses intensities ( $I_{DP}$ )
for ps LIPs, at ps heating pulse intensities ( $I_{ps,HP}$ ) = 1.77 × 10 <sup>10</sup> W/cm <sup>2</sup> ) and ns LIPs ( $I_{ns,HP}$ = 7
$\times$ 10 <sup>10</sup> W/cm <sup>2</sup> ), respectively, (b) at fs driving pulse intensities ( $I_{DP}$ ) = 6.0 $\times$ 10 <sup>14</sup> W/cm <sup>2</sup> w.r.to
ps heating pulse intensities ( $I_{ps,HP}$ ). (d) the delay dependence between ns HP and fs DP81
Fig. 3. 9 The maximum harmonic signal obtained (from data shown in Fig. 8 (a-d)) for (a) at
fixed ps heating pulse intensity $(I_{ps,HP}) = 1.77 \times 10^{10} \text{ W/cm}^2$ for changes in driving pulses
intensity ( $I_{DP}$ ), (b) at fixed $I_{DP} = 6.0 \times 10^{14} \text{ W/cm}^2$ , variation in $I_{ps,HP}$ . In case of ns LIPs (at $I_{ns,HP}$ )
$_{\rm HP} = 7 \times 10^{10} \ {\rm W/cm^2})$ (c) w.r.to $I_{\rm DP}$ , (d) the delay dependence between ns HP and fs DP,
respectively. (e) harmonic cut-off in case of ps LIPs with changes in $I_{DP}$ . (f) the cut-off of time
duration until the harmonic's emission (left Y-axis), and the delay cut-off (right Y-axis) for
studied single crystals

Fig. 3. 10 HHG spectra 9H to 15H for (a) ns LIPs (b) ps LIPs at driving pulses intensity $6 \times 10^{14}$ W/cm <sup>2</sup> . For MA-API (c) plasma plumes obtained from ns HP, and (d) plasma plumes
obtained from ps HP. (e) The normalized PL spectra at pump wavelength 800 nm88
Fig. 4. 1 (a) Differentia scanning calorimetry and (b) Thermogravimetric analysis of control and modified crystals
Fig. 4. 2 (a) Semi log plot of I-V characteristics of modified and control SCs in the dark, I-V
characteristics as a function of light intensity for (b) Control and (c) modified crystals (d) I-V
characteristics at 575 Wm <sup>-2</sup> in forward and reverse scan direction for both the crystals. Scan
rate 100 mV/s
Fig. 4. 3(a) Photo-responsivity and (b) Detectivity for control and modified crystals at 88 Wm <sup>-</sup>
<sup>2</sup> in white light
Fig. 4. 4 Temporal response of (a) Control and (b) modified crystals at different illumination
intensities (c) Enlarged view of rise and fall regions for both the crystals121
Fig. 4. 5(a) High-frequency and (b) low-frequency resistance as a function of light intensity
Fig. 4. 6 Capacitance-frequency plot as a function of light intensity for (a) control and (b)
modified crystals, Capacitance-frequency plot as a function of temperature for (c) control and
(d) modified crystals
Fig. 5. 1. 1 a) Average lifetime of MHPSCs with changing additives. b) schematic
representation of decreasing surface defects by adding additives to electronic band structure
model in modified MHPSCs with comparison to pristine

Fig. 5. 1. 2 a) Change in phase transition temperature (insert) second heating in Differential
scanning calorimetry and b) TGA of pristine and modified MHPSCs. c) Plot of $\ln{(1-x)}$ vs
Time and d) Plot of $ln[-ln(1-x)]$ vs 1000/T of organic moiety decomposition in MHPSCs.
Fig. 5. 1. 3 Harmonic spectra (in pixels) for different a) ps heating pulse intensities at $I_{fs}$ =
$6.0 \times 10^{14} \text{ W/cm}^2$ , b) driving pulses intensities for ps LIPs (at $I_{ps} = 0.9 \times 10^{10} \text{ W/cm}^2$ ), and c) ns
LIPs ( $I_{ns} = 7 \times 10^{10} \text{ W/cm}^2$ ), respectively. d) The delay dependence between ns HP and fs DPs.
The spectrum's colour bar is similar in the top right corner
Fig. 5. 1. 4 The maximum harmonic signal for different a) ps heating pulse intensities at
$I_{\rm fs}$ =6.0× 10 <sup>14</sup> W/cm <sup>2</sup> , b) driving pulses intensities for ps LIPs (at $I_{\rm ps}$ =0.9× 10 <sup>10</sup> W/cm <sup>2</sup> ), and c)
ns LIPs ( $I_{\rm ns}$ =7 $\times$ 10 <sup>10</sup> W/cm <sup>2</sup> ), respectively. d) The delay dependence between ns HP and fs
DPs. The shift of 9H for all SCs in case of e) ns LIPs and f) ps LIPs145
Fig. 5. 1. 5 The harmonic spectra of a) MH and b) MH-API concerning time. The harmonic
spectra were recorded as movies and plotted as vertical stack images. Right panels of a) and b)
represent some portion marked with pink and green lines, respectively
Fig. 5. 2. 1 Shematics of surface degradation of MHSCs (a) in presence of atmosphere moisture.
Left Each column from (b-d), (e-g) and (h-j) represents the MABr, PEA, and PXA, chemical
structure photographs and SEM images, respectively
Fig. 5. 2. 2(a-e) XPS data of Cl 2p, Br 3d, Pb 4f, C 1s, and N1s core-level spectra with molecular
level defect and chemical states behaviour in MHSCs with changing additives. (f) Change in
XPS survey of each SCs with different additive and (g) atomic % values164
Fig. 5. 2. 3 The XRD pattern of the modified and pristine SCs, (a, b) Splitting and shifting of
powder and single crystal (SC) p- XRD, (100) peaks shows the transition from single-phase
MHSCs to double-phase segregation with different additives. (c, d) Change in FWHM $\dots$ 165

Fig. 5. 2. 4 From (a-c), (d-f) and (g-i) represnts TEM images, HRTEM images with lattice fringes and SAED of each MH, MH-PEA and MH-PXA SCs, respectivley
Fig. 5. 2. 5(a) UV-visible spectra, enlorged view in insert. (b) The energy vs F(R(hv)) <sup>2</sup> plot. The MH, MH-PEA and MH-PXA SCs are photoexcited with 800 nm, the corresponding (c) PL spectra (d) PL intensity vs input laser power and (e) FT-IR spectra, vibrational modes with respect to additives in the modified MHSCs.
Fig. 5. 2. 6 The THz electric field of THz pulse. Transmission from MH, MH-PEA, MH-PXA SCs at (a) 0°, (b) 45° and (c) reflection at 45° with repective to delay (ps). Transmittance MH, MH-PEA, MH-PXA SCs (d) at 0°, (e) transmittance/reflectance at 45°, (f) absorption coefficients, and (g) real conductivity at 0° and 45°, measured with repective to frequency (THz)
Fig. 6. 1 Distinct count of NLO coefficients for each bandgap broken down by morphology.  Colour shows details about NLO characteristics. SC–Single crystal, F–Film, NC–Nanocrystal,  NS-Nanostructure
Fig. 6. 2 TEM micrographs and calculated particle sizes for each sample at right to it for (a-d) powder and (e-h) solutions respectively
Fig. 6. 3 (a) p-XRD diffraction pattern. (b, c) FT-IR spectra. (d) p-XRD peak at 15 degrees showing the lower angle shift (e) UV-visible absorption spectra and (f) PL spectra of FAPbBr3 NCs (FB-1) along with doped samples as labelled from FB-2 to FB-4
Fig. 6. 4 Open aperture NLO data of (a) FB-1, (b) FB-2, (c) FB-3, (d) FB-4, respectively, under the excitation of 1 kHz, 70 fs, 800 nm fs pulses. Experimental data have been presented in 3-d (blue) spheres and theoretically fitted 3PA Z-scan data is represented by the solid red lines (top). The solid green line (bottom) in (a) represents the two-photon absorption fitting curve. Closed aperture Z-scan data can be observed in olive-colored spheres in (e) FB-1, (f) FB-2, (g)

Appendix I Fig. 1. Experimental layout for (a) terahertz time-domain spectroscopy and (b)
high-order harmonics from laser-induced plasma plumes of single perovskite crystals 222
Appendix I Fig. 2. (a) Atomic Ratio of MAPbBr <sub>3</sub> perovskite single crystal with changing
additives. (b) Lattice strain values of each reported crystal were calculated from the W-H plot
using the XRD data223
Appendix I Fig. 3. (a-e) Confocal and (f-j) scanning electron microscopy (SEM) images of
MA crystals grown using the additives corresponding to CB, PEA, PXA, and API samples,
respectively
Appendix I Fig. 4. SEM images taken after keeping PSCs in ambient conditions for three and
(f-j) seven days, respectively224
Appendix I Fig. 5. (a)-(e) Surface degradation of SCs in the outer atmosphere at a constant
temperature at different time intervals was studied using UV spectroscopy
Appendix I Fig. 6. (a)-(b) Comparative Study of MHPSCs Thermogravimetric Analysis
(TGA), and thermodynamic properties of phase one (P1- Organic part decomposition) for all
the crystals
Appendix I Fig. 7. (a)-(e) Current-voltage traces with insert showing SCs deposited with Au.
The linear fitting is denoted with the green markers showing different regimes (at 300 K). 226
Appendix I Fig. 8. After the conversion of the THz electric field to FFT spectra, the obtained
(a) THz amplitude, (b) phase, (c) frequency spectra in dB, (d) Lorents fits of data points from
THz amplitude shown in (a), for transmittance (T) @ 0°, (upper row), T@ 45° (middle row),
reflection @ 45° from reference and perovskite single crystals, respectively. The legend is
shown in (b, middle panel), applicable to all panels; Black: solid line, red: solid line, green:
double line, blue: thick-thin line, wine: thin-thick line, and magenta: triple lines corresponding
to reference pulse, for Singles crystals MA, MA-CB, MA-PEA, MA-PXA and MA-API. The
Y-axis labels are shown on top of each column after the Fig. labels (a),(b),(c) and (d),228

Appendix I Fig. 9. (a)-(e)The vertical representation of harmonic spectra of SCs. The spectra were recorded for time duration. The plasma plumes are produced by nanoseconds heating pulses at a fixed position on the surface of SCs
Appendix II Fig. 1. Optical images of (a) control and (b) modified SC (c) Powder X-ray diffraction (PXRD) pattern SC of both the
<b>Appendix II Fig. 2.</b> (a) Current-Voltage characteristics of both the crystals at 575 Wm <sup>-2</sup> illumination (b) Photocurrents of both the crystals as a function of illumination intensity236
Appendix II Fig. 3. SEM images of (a) Control and (b) modified SCs. Scale bar 20μm237
Appendix II Fig. 4. Nyquist spectra as a function of illumination for (a) Control and (b) Modified crystals recorded in the frequency range of 1 MHz to 1Hz237
Appendix II Fig. 5 HRMS data of modified crystal High-resolution mass spectrometry (HRMS) data. Molecular ion peak [M+H <sup>+</sup> ] at 174.0611 related to API (3-Aminopiperidine dihydrochloride)
Appendix III Fig. 1. (a) PL spectra recorded with 488 nm laser and (b) EDX data representing elemental weight % correspond to MH, MH-CB, MH-PEA, MH-PXA, and MH-API, respectively
Appendix III Fig. 2 (a-e). Comparative study of MHPSCs thermodynamic properties of phase one (P1) and two (P2) transformations
<b>Appendix IV Fig 2.</b> The EDX weight % values of the modified and pristine MHSCs244

Appendix IV Fig 3. The p-XRD pattern of the modified and pristine MHSCs, (a-c) single crystal (SC) and (d-f) powder samples
<b>Appendix IV Fig 4.</b> (a-c) The calculated microstrain parameters from powder XRD data of each MH, MH-PEA, and MH-PXA SCs
<b>Appendix IV Fig 5.</b> FT-IR spectra, changing vibrational modes with respect to additives in the modified MHSCs from 1000 to 600 cm <sup>-1</sup>
<b>Appendix IV Fig 6.</b> The THz electric field of THz amplitude, phase and frequency spectra in dB (a-c) for reference pulse, (d-f) for single crystals transmission at 0°, (g-i) transmission at 45°, and (j-l) reflection at 45°, respectively. The legends used for all the subgraphs in this Fig. are the same (Solid Wine: Reference THz pulse, Simple Black: MH, Double Red: MH-CB, Thick-Thin Blue: MH-PEA, Thin-Thick Magenta: MH-PXA, Triple Olive: MH-API)248
<b>Appendix V Fig. 1.</b> (a-c) Elemental mapping of Cl (top panel) and Sr (bottom panel) ions for doped sample from left to right and accordingly labels at the top of each image. 249
<b>Appendix V Fig. 2.</b> The calculated microstrain parameters from powder XRD data of each sample; labels are at the top of each sample image, respectively
<b>Appendix V Fig. 3.</b> (a-d) HR-TEM images and SAED pattern (below) patterns for each sample are illustrated from left to right, and labels are at the top of each sample image
Appendix V Fig. 4. Distribution box plot represents the four samples repeated experimental values of (a) bandgap and (b) PL
<b>Appendix V Fig. 6.</b> (a) OA data for toluene (solvent) (b) CA data for toluene. Red lines in both OA and CA data represent the fitted curves, while the open hexagons represent the experimental data.

## **List of Tables**

Table 3.1. The active groups and H bonds are possible in the additives.    6	8
<b>Table 3.2.</b> Comparative study of PSCs fitted parameters for the TRPL decay profiles, $V_{TFL}$ and	
$\eta_{\text{traps}}$	3
Table 5.1 Comparative study of MHPSCs thermodynamic properties of phase on transformations.         14	
Appendix I Table 1. Literature review	0
Appendix I Table 2. Crystal data and structure refinement for MA and modified PSCs22	5
Appendix I Table 3 Crystal data and structure refinement for MA and modified PSCs22	6
Appendix I Table 4 First and second ionization potentials for chemical elements present i	in
single crystals23	0
Appendix III Table 1 Literature Review 23	9
Appendix III Table 2 Comparative study of MHPSCs TRPL decay profiles. 24	0
Appendix IV Table 1 The following table represents the elemental ratios extracted from the	ıe
EDX data.	4

 Table 1.1 Electronic properties of semiconductor material as reported in the literature.......11

## **Symbols and Abbreviations**

Å Angstrom

 $\Delta$  Heat

 $\Delta T$  Change in Temperature

 $\Omega \hspace{1cm} Ohm$ 

η Solar energy-to-electricity conversion efficiency

μ Dipole moment

 $\lambda \hspace{1cm} Wavelength$ 

hv Photon

σ Electrical Conductivity

 $\sigma^2$  Two-photon absorption coefficients

2PA Two-photon absorption

ρ Resistivity

 $\mu_h$  Hole-drift mobility

τ Lifetime

3D Three-Dimensional

A Electron Acceptor

AE Attachment Energy

aq. Aqueous solution

a.u. Arbitrary unit

AM Air Mass (1.5G)

Au Gold

n-BuLi n-ButylLithium

BE Binding Energy

CB Conduction Band

cm Centimeter

CT Charge Transfer

c-TiO<sub>2</sub> Compact Titanium Oxide

CV Cyclic Voltammetry

CBZ Carbazole

DSC Differential scanning calorimetry

DCM Dichloromethane

DMF N, N-Dimethylformamide

DMSO Dimethyl sulfoxide

DSSC Dye-sensitized solar cell

e.g. For example

eq. Equivalent

Ea Activation Energy

Eg/E<sub>0-0</sub> Electronic/Optical bandgap

E<sub>HOMO</sub> Ground-state oxidation potential

E<sub>LUMO</sub> Excited-state redox potential

E<sub>onset</sub> Onset oxidation potential

E.S Excited State

et al. And others

ETL Electron Transporting Layer

ETM Electron Transporting Material

ESRP Excited State Reduction Potentail

eV Electronvolt

FA Formamidinium

FB Forward bias

Fc Ferrocene

FF Fill Factor

FE-SEM Field effect Scanning Electron Microscope

FK209 Tris(2-(1H-pyrazol-1-yl)- tertbutylpyridine)

cobalt (III) tri[bis (trifluoromethane) sulfonimide]

FF Fill Factor

FTO Fluorine-doped Tin Oxide

FTIR Fourier Transform Infrared Spectroscopy

g Gram

GSOP Ground State Oxidation Potential

h Hour

hv Photon of Energy

HOMO Highest Occupied Molecular Orbital

Hz Hertz

ICT Intramolecular Charge Transfer

Ip Ionization potential

ITO Tin-doped Iindium Oxide

J-V Photocurrent-voltage

J<sub>max</sub> Maximum photocurrent

KHz KiloHertz

M Molar

m-TiO<sub>2</sub> Mesoporous titanium dioxide

MA Methylammonium

mA Milliampere

MALDI Matrix-Assisted Laser Desorption/Ionization

MeO- Methoxy

MS Mass Spectrometry

MO Molecular Orbital

mol% Molar Percentage

mW Milliwatt

NBS N-Bromosuccinimide

Nd Charge carrier density

nm Nanometre

NMR Nuclear Magnetic Resonance

NREL National Renewable Energy Laboratory

NLO Non-linear optics

NPs Nano particles

NCs Nanocrystals

 $\eta_2$ Refractive index

O.D Optical Densities

OFET Organic Field-Effect Transistor

Os Oscillator strength

OLED Organic light emitting diode

o-/m-/p- ortho/meta/Para position

PCBM [6,6]-Phenyl-C61-butyric acid methyl ester

PC71BM [6,6]-Phenyl-C71-butyric acid methyl ester

PCE Power Conversion Efficiency

PEDOT:PSS Poly(3,4-ethylenedioxythiophene) polystyrene sulfonate

Pin Power of the incident light

P<sub>max</sub> Maximum power

PL Photoluminescence

ppm Parts per million

Pr Propyl

PSCs Perovskite Solar Cells

PTAA Poly[bis(4-phenyl)(2,4,6- trimethylphenyl)amine]

POZ Phenoxazine

PV Photovoltaic

R<sub>ct</sub> Charge transfer resistance

R<sub>s</sub> Series resistance

RT Room Temperature

R<sub>sh</sub> Shunt resistance

s Seconds

SC Short-circuit

SCE Standard Calomel Electrode

SCL Space-Charge Limited Current

SEM Scanning Electron Microscope

SHG Second harmonic generations

SOMO Single occupied molecular orbital

t- Tertiary

tBP 4-t-butylpyridine

TBP Tertiary butyl pyridine

TCSPC Time-Correlated Single Photon Counting

TGA Thermogravimetric analysis

TEM Transmission electron microscope

TAS Transient Absorption Spectroscopy

TPA Triphenyl amine

PL Photoluminescence

TWTerawatt UV Ultraviolet V Volt  $V_{\text{max}}$ Maximum voltage VBValence band Vis Visible Versus (against) vs.  $\chi^{(3)}$ Third order non-linear susceptibility  $\mathbf{Z}'$ Real part impedance  $\mathbf{Z}^{\prime\prime}$ Imaginary part impedance

## Outline of the Contents

## **Table of Contents**

DECLARATION Error! Bookmark not defined.
CERTIFICATE Error! Bookmark not defined.
Parts of the thesis have been published in the following publications: Error!
Bookmark not defined.
Scientific Presentations Error! Bookmark not defined.
Further, the student has passed the following courses towards fulfillment of the
coursework requirement for Ph.DError! Bookmark not defined.
Acknowledgements Error! Bookmark not defined.
Outline of the Contents xxxiii
List of Fig.s Error! Bookmark not defined.
List of Tables Error! Bookmark not defined.
Symbols and Abbreviations Error! Bookmark not defined.

# **CHAPTER-1**

# Introduction

## **Chapter-1 Introduction**

## 1.1 Introduction to Perovskite single crystals (PSCs)

Due to the intriguing optoelectronic properties of organic-inorganic hybrid perovskites (OIHPs) are considered frontline candidates, such as large stopping power, long diffusion length, high resistivity, high mobility-life time product and low trap states. However, unstable surfaces prone to degradation significantly affect the device performances and circumscribe commercialization. Additive engineering has become the most effective strategy to improve the quality of 3D perovskite single crystal (PSC). Herein the additive engineering resulting in high-quality transparent PSCs by employing various aliphatic, aromatic, and chiral ammonium salts are demonstrated for the photodetection, terahertz (THz) device applications besides its effect on the higher-order harmonics generation (HHG). Remarkably the engineered crystal surfaces showed more stability than pristine ones, thereby enhancing the transmission/reflection of THz pulses.

Interestingly, a blue shift in the harmonics (both nano second-ns and pico second-ps Laser induced plasmas-LIPs) has been observed. The current thesis is anticipated to open new sources of additive-based SCs used entirely for THz devices and tunable high-order harmonic generation avenues. Exploring the inanimate materials via the additive inclusion in perovskite SCs opens new avenues to achieve the blue-shifted UV spectra for diverse applications in attosecond physics and nonlinear spectroscopy, including tunable THz devices because of easy tunability of THz absorption property, *i.e.*, their phonon modes in an OIHPSCs.

## 1.2. PSCs Photodeters

This material possesses an ABX<sub>3</sub> structure,  $A^+$  (cations) located in the voids of these interlinked octahedra indirectly affect these materials' bandgap.  $M^{2+}$  and  $X^-$  combined to form MX<sub>6</sub>( octahedral unit) as illustrated in **Fig. 1.1**, the bandgap of these materials formed by combining the metal (M) and halide (X) s, p orbitals. Changing the concentration of  $X^-$  and  $M^{2+}$  can directly influence the bandgap where as  $A^+$  indirectly affect bandgap (**Fig. 1.2**).

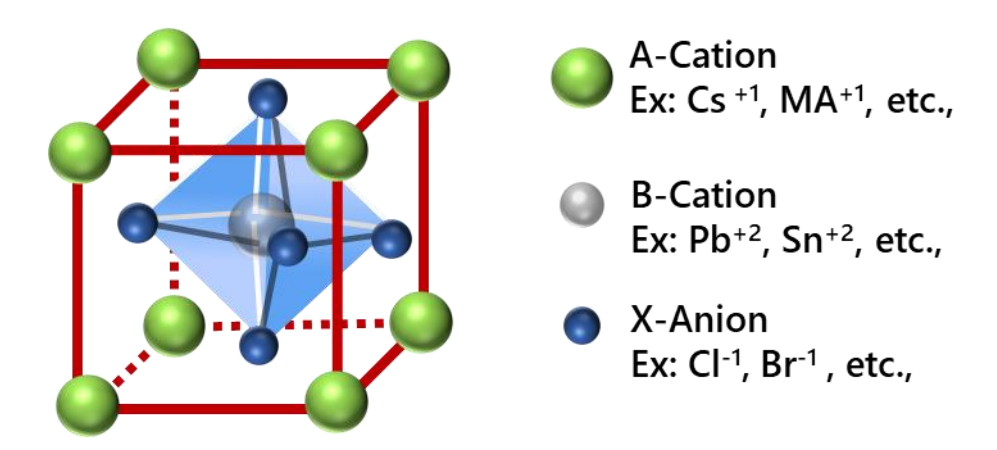


Fig. 1.1 Perovskite materials unit cell structure.

Generally, the material selection and thickness of the detector material will be tuned according to the targeted application to achieve these properties. They depended upon the energy of incident radiations. We can design for various devices ranging from smoke detectors, thermoelectric power generators, atomic-structural analysis, medical diagnostic treatment, food preservation, industrial structural analysis, metal-rolling, radiocarbon dating, etc. (**Fig. 1.3**). With an ongoing trend in perovskites towards high energetic radiation Detection, organic-inorganic hybrid perovskites are emerging as an alternative to conventional detectors owing to their low cost, relatively easy manufacturing process, and flexibility. Ever since the pioneering

work of Kojima *et al.* on metal halide perovskites for sensitized solar cells, a significant scientific allure has been drawn by these materials for energy harvesting and optoelectronic applications, which owes to their superior light-absorbing ability and more extended charge

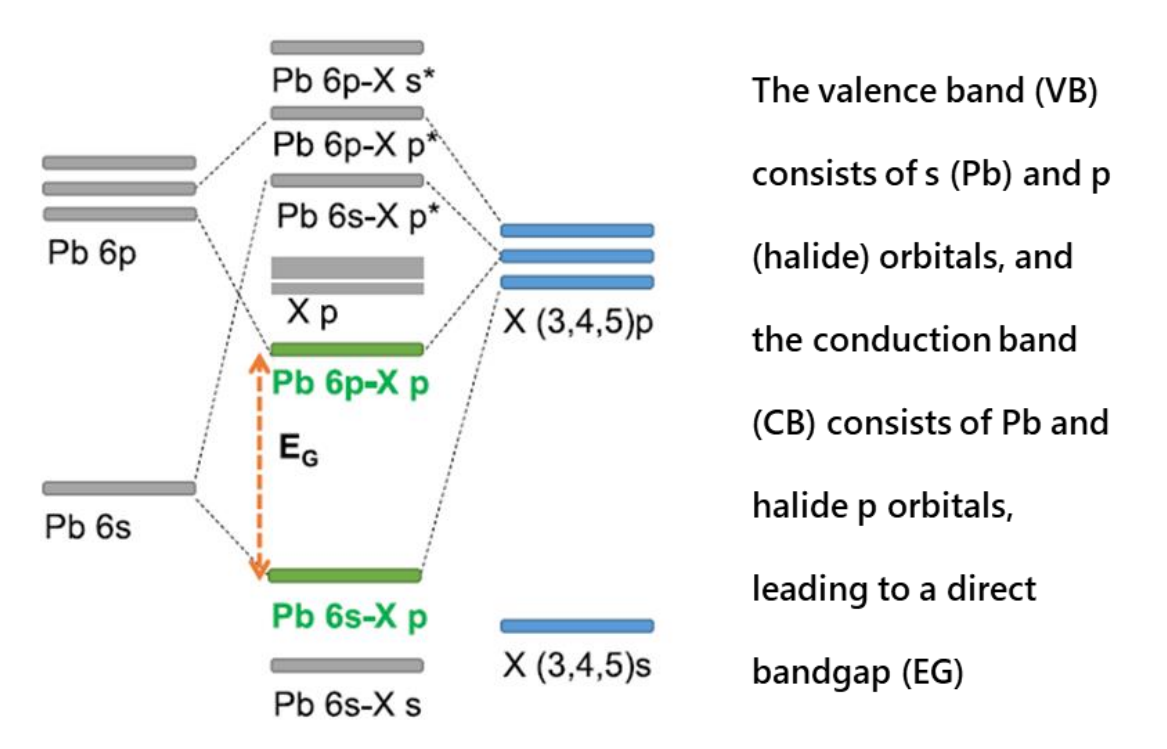


Fig. 1.2 Energy diagram of the [PbX6]<sup>-</sup> units wherein atomic levels, representing bandgap of perovskite materials.

carrier lifetime.<sup>1</sup> For the last decade, perovskites have been explored as a semiconductor detector material to detect a broad range of radiations (ranging from UV rays to high-energy gamma rays). High-energy radiation detectors are topics of continuous interest as they find a wide range of applications from medical diagnostics, non-destructive testing of materials at airports and industries, structural characterizations/crystallography, and even space technology. Several literature reports have been available, mainly focusing on crystallization methods of PSCs and their actual results compared to commercially available NaI:Tl, Si, and CZT detectors. Unfortunately, getting very high energetic radiation detection with long-term

stabilization has been recognized as a fundamental challenge for commercializing these emerging devices.

## **1.2.1. Types of PD**

Mainly two detection modes are available for high-energy radiation detection, optical-based scintillators and electronic-based semiconductors. Scintillation detectors have a higher energy harvesting capacity. However, they suffer from the intrinsic non-proportionality of the light yield, making it challenging to accurately measure energies at ambient temperature. Whereas in a semiconductor detector, the output pulse height is proportional to the charge

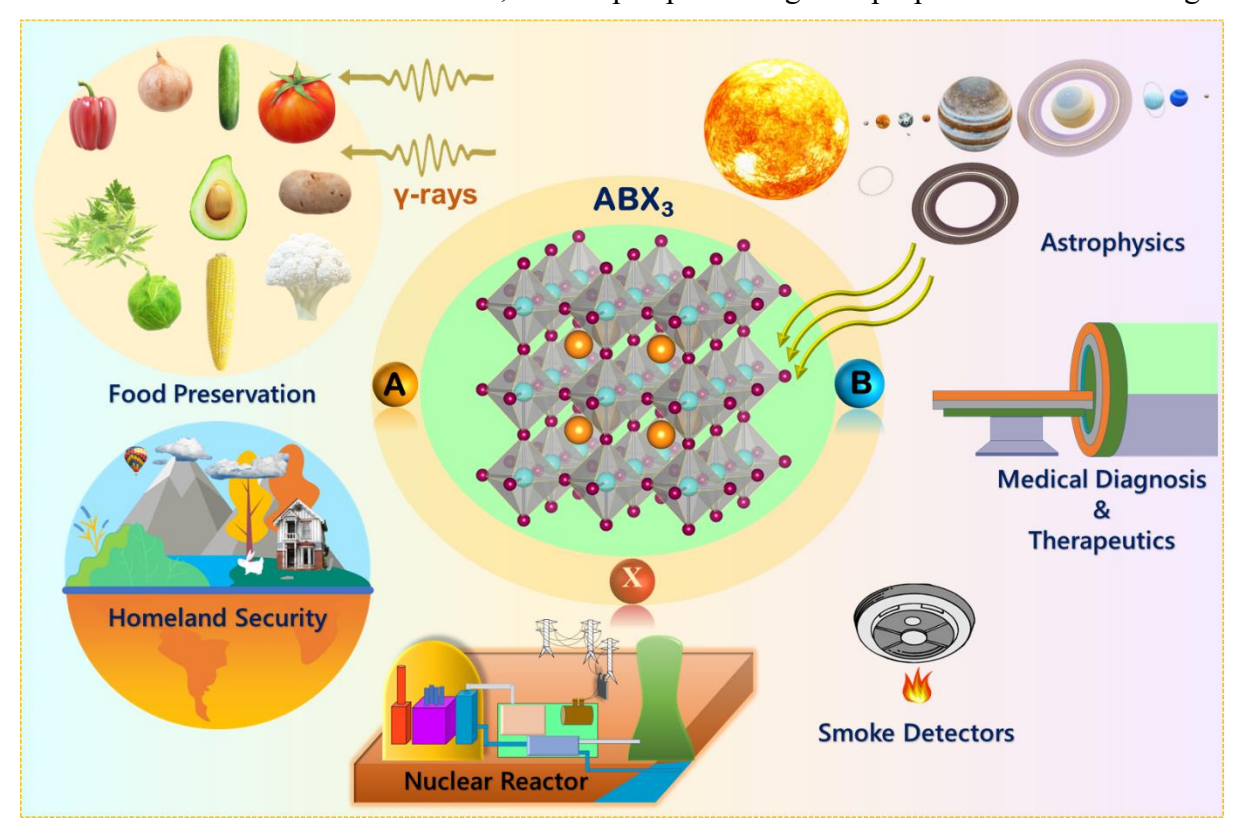


Fig. 1.3 varied applications ranging from smoke detectors, thermoelectric power generators, atomic-structural analysis, medical diagnostic treatment, food preservation, industrial structural analysis, metal-rolling, radiocarbon dating etc.

induced over a specific time interval resulting in superior accuracy in energy resolution. The semiconductor materials generate charge carriers (electron/hole) from incident photons, directly converting this energy into measurable electrical current under an applied electric field. These are usually called direct converters/detectors. The indirect detectors, like the scintillators, generally undergo a secondary process of generating photons, which are subsequently detected by a photo-multiplier tube and then converted to electrical signals.

## 1.2.3. Working principle of PD

A photodetector is a device that harnesses light irradiation and transduces it into a usable electrical signal through the photoelectric effect (**Fg. 1.4**).<sup>2</sup> The detection rate depends on a detector's signal resolution and recombination efficiency. Furthermore, detector systems

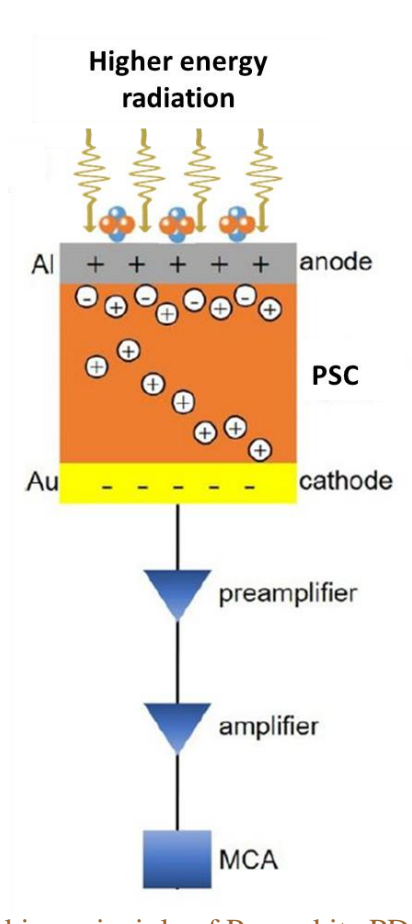


Fig. 1.4 Working principle of Perovskite PDs device.

need to have reasonable sizes for practical purposes PDs can be mainly divided into four types of device architectures depending on the device structure and operation mechanism, including vertical photodiodes, vertical photoconductors, lateral photoconductors, and phototransistors. Usually, in Photoconductors, one type of charge carrier can circulate several times through an external circuit before charge recombination, resulting in a large photocurrent, high responsivity, and high gain. Photodiodes are devices that convert light into electric current. In photodiodes, electron-hole pairs generated by light can be easily separated by electron and hole transfer layers and then transferred to the opposing electrodes. Photodiodes exhibit high detectivity of light, low noise, and a response time shorter than the electron-hole combination time. Phototransistors are extremely sensitive to light due to the high gain provided by the transistor. Some basic requirements must be met for a high-energy radiation detector to detect the presence of radiation.<sup>2</sup> First, detector material must efficiently absorb radiations that pass through it. Second, a spectral response from the device must enable the identification and characterization of radioactive sources. Detectors that satisfy the criteria mentioned above can produce high signal-to-noise ratios while interacting with radiation, which enables the detection of radioactive sources.

The impact of these promising properties has been explained incoming section. Detectors that satisfy the above criteria can produce high signal-to-noise ratios, enabling radioactive sources detection. The detection rate depends on signal resolution and recombination efficiency in a sensor. Furthermore, the characteristics of detectors and the performance of a PD are characterized by detectivity. 1) Responsivity (R) indicates how efficiently a PD can produce an electric signal from incident light.

## 1.3. Promising Properties of PSCs

In order to design PD with a high energy-resolved spectrum, greater photon-electron conversion efficiency is desperately needed. Subsequently, fast detection speed and low dark current are desirable for PD. Recent studies showed that perovskite materials have good potential for high energy resolution; innovative designing of perovskite material may lead to large stopping power, long diffusion length, high resistivity, high mobility-life time product, reduction of trap states, and long-term stability.

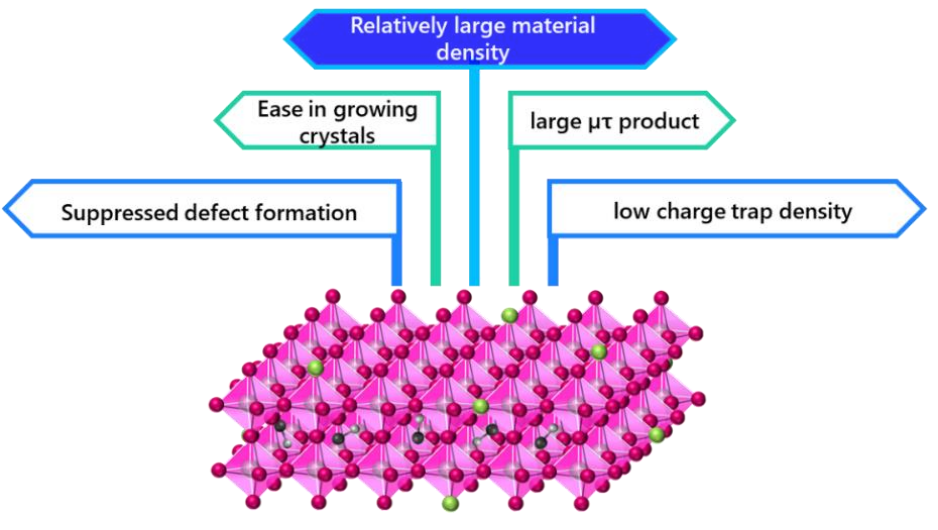


Fig. 1.5 Promising Properties of PSCs

#### 1.3.1 Large Absorption Coefficient

High-energy electromagnetic radiation penetration power is very high. The stopping power of the semiconductor material used in  $\gamma$ -ray detection must be high for complete absorption of gamma rays within the material's depth, resulting in the maximum electron-hole pair generation. The stopping power of any material is directly proportional to its average atomic number. The constituent elements of lead halide perovskite material are generally large atomic number elements like Pb, Sn, Cs, Br, I, Cl, CH<sub>3</sub>NH<sub>3</sub> etc. Thus the average atomic

number of lead halide perovskite is greater than that of silicon and comparable to CZT, as listed in **Table 1.1.** The incorporation of higher atomic number elements in perovskite may lead to higher stopping power; the large atomic number of lead halide perovskite material endows a large attenuation coefficient, compared to silicon and germanium, as evidenced from **Fig. 1.5**, and thus makes perovskite a promising candidate for HEIR detection.

## 1.3.2 Tunable Bandgap

The electronic properties, which are responsible for the high energy resolution of the HEIR Sensor, are dictated by the semiconductor's bandgap. Thermally generated or alternately intrinsic charge carriers do not contribute towards electric signals. A high signal-to-noise ratio (SNR) is crucial for high performance. As intrinsic charge carriers increase, SNR decreases, so the semiconductor bandgap should be as large as possible to lower the population of intrinsic charge carriers in the bulk of the semiconductor. The energy resolution will be high if less energy is required for electron-hole pair generation. In this context, the semiconductor bandgaps should be low for a maximum number of electron-hole pair generations. Thus, the optimization of a bandgap is needed for high energy resolution and high signal-to-noise ratio. Generally, a band gap greater than 1.4eV for room temperature operation is necessary.<sup>3</sup> Recent studies showed that the bandgap, in the range of 1.6 - 3.0 eV, works well to reduce the spectral noise caused by thermally generated charge carriers. The leading and commercialized detector material is the Cd<sub>0.9</sub>Zn<sub>0.1</sub>Te (CZT) which has a bandgap energy of 1.65 eV.<sup>4</sup> Silicon and germanium have a low bandgap, around 0.66 eV and 1.12 eV, so cooling is required to suppress the generation of intrinsic charge carriers when Si and Ge are used as HEIR detector material.<sup>5,6</sup> Interestingly, lead halide perovskite material can tune the band gap by doping or altering the

composition of its constituent element. According to recent studies, the band gaps of MAPbX<sub>3</sub> perovskites are 1.5, 2.2, and 3.1 eV, where X is I<sup>-</sup>, Br<sup>-</sup>, and Cl<sup>-</sup> respectively. <sup>7</sup> In methylammonium lead iodide (CH<sub>3</sub>NH<sub>3</sub>PbI<sub>3</sub>), when methyl ammonium (CH<sub>3</sub>NH<sub>3</sub><sup>+</sup>) is replaced by CH(NH<sub>2</sub>)<sub>2</sub><sup>+</sup>, the bandgap is reduced by 0.07 <sup>8</sup> and when Pb<sup>2+</sup> is partially or completely replaced by Sn<sup>2+</sup>, band gaps reduced from 1.55 eV to the range, 1.17-1.30 eV.<sup>9</sup> When the Iodide ion is completely replaced by Br<sup>-</sup> in MAPbI<sub>3</sub>, the bandgap increases from 1.55 to 2.3 eV.<sup>10</sup> Noh *et al.*, proposed an empirical equation to determine the bandgap when iodine (I) is replaced partially or completely by bromine (Br) in MAPbI<sub>3</sub>, which is as follows: <sup>11</sup>

$$Eg(x) = 1.57 + 0.39X + 0.33X^{2}$$
 (1.1)

Fortunately, PSCs bandgap can be adjusted according to need by carefully doping other halogens or suitable elements (**Fig. 1.6**).

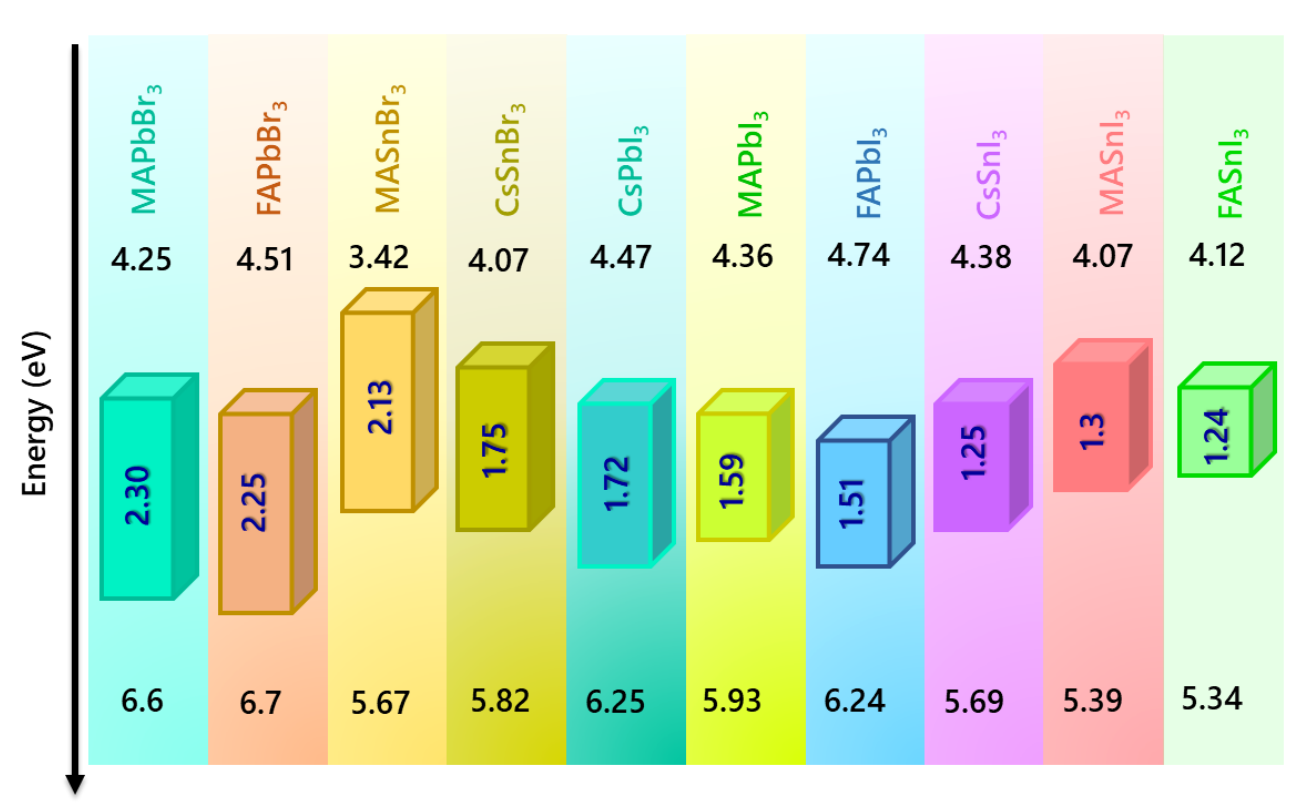


Fig. 1.6 Change in bandgap with changing composition in ABX<sub>3</sub>.

**Table 1.1** Electronic properties of semiconductor material as reported in the literature

Materials	Avg. atomic number	Bandgap	Resistivity	$(\mu\tau)_e$	Ref
	number	(eV)	$(\Omega \text{ cm})$	$(cm^2/V)$	
CdZnTe (CZT)	49.3	1.57	109-1010	7.5×10 <sup>-3</sup>	12
CdTe (CT)	50.2	1.44	1×10 <sup>9</sup>	1-2×10 <sup>-2</sup>	13
TiBr	58	2.68	1×10 <sup>10</sup>	3×10 <sup>-3</sup>	14
$HgI_2$	62	2.15	1×10 <sup>13</sup>	3×10 <sup>-4</sup>	15

CdZnSe	38	2.00	2×10 <sup>10</sup>	1×10 <sup>-4</sup>	16
CdTeSe	44.7	1.47	5×10 <sup>9</sup>	4×10 <sup>-3</sup>	17
Si*	14	1.06-1.12	$10^{4}$	>1	6
Ge*	32	0.66	50	>3	5
MAPbI <sub>3</sub> SC	48.9	1.54	108-109	1×10 <sup>-2</sup>	18
MAPbBr <sub>3</sub> :Cl SC	-	2.3	3.6×10 <sup>9</sup>	1.2×10 <sup>-2</sup>	19
FAPbI <sub>3</sub> SC		1.43	10 <sup>6</sup> -10 <sup>9</sup>	1.8×10 <sup>-2</sup>	20
FACsPb(BrI) <sub>3</sub> SC	-	1.52	108-109	1.2×10 <sup>-1</sup>	21
CsPbBr <sub>3</sub> SC	65.9	2.3	3×10 <sup>11</sup>	1.34×10 <sup>-3</sup>	22

<sup>\*</sup>Only operable at cryogenic temperature; SC denotes single crystal.

## 1.3.3. Long Diffusion Length and Large Mobility-Lifetime Product

When  $\gamma$  ray interacts with the semiconductor material, charge carriers, i.e., electron-hole pairs, are generated within the bulk of the material. After generation, these charge carriers are collected towards the corresponding electrodes under bias and thus producing signal current. The energy resolution of the signal, a critical parameter of the  $\gamma$ -ray sensor for its performance, directly correlates with the collection of charge carriers at electrodes. Collecting the charge carried at electrodes for high energy resolution of signal in  $\gamma$ -ray spectroscopy is highly desirable.

When detector material interacts with high-energy  $\gamma$ - rays, electrons jump from the top of the valence band to the bottom of the conduction band, creating holes in the valance band and electrons in the conduction band. There is a higher probability of band-to-band recombination (radiative), and trap or defect-assisted recombination (non-radiative) of these  $\gamma$ -ray generated charge carriers, resulting in the loss of these charge carriers. Charge carriers generation and charge carrier recombination compete with each other, and the recombination of electron-hole pairs must be suppressed for maximum

collection of charge carriers at electrodes. Radiative and non-radiative, both types of recombination may be suppressed by improving the quality of the material or reducing the defects and trap states in the bulk of the material. In other words, the diffusion length, the length travelled by electrons or holes before it recombines again with each other or at any trap centre, must be greater than the thickness of the semiconductor layer so that charge carriers can reach the electrode and contribute towards the signal current. The mobility-lifetime product ( $\mu\tau$ ), an important figure of merit directly related to diffusion length, predicts charge carriers' collection efficiency (CCE) at electrodes. The CCE depends on  $\mu\tau$  as,<sup>23</sup>

$$CCE(z)*d = E(\mu\tau)_e \left[1 - e^{-(d-z)/(\mu\tau)}_e\right] + E(\mu\tau)_h \left[1 - e^{-(d-z)/(\mu\tau)}_h\right]$$
(1.2)

The mobility-lifetime product ( $\mu\tau$ ) value of electron is generally determined by classical Hetch equation: <sup>23</sup>

$$H/H_O = (\mu \tau)_e * (V/d^2) * (1 - \exp\{-d^2 V/(\mu \tau)_e\})$$
(1.3)

Where  $H/H_0$  is measured as relative pulse height, V is the applied bias voltage, and d is the thickness of the detector material. The above equation holds good for large pixels, but in the case of a small pixel, the  $\mu\tau$  the modified Hetch equation can accurately determine value.<sup>23</sup>

The detection efficiency of the Sensor increases with the thickness of the semiconducting material, so the value of  $\mu\tau$  must be sufficient for an entire collection of charge carriers at electrodes before recombination within the thick layer of semiconducting material. Table 1.1 compares the  $\mu\tau$  value of different semiconductors, which has been used so far as PD. In recent years lead halide perovskite has seen intensive investigation, and its excellent optoelectronic property makes it a promising candidate for  $\gamma$ -ray detection. Stompous *et al.*, reported the  $\mu\tau$  value of  $1.3\times10^{-3}$  for CsPbBr<sub>3</sub> single crystal.<sup>4</sup> The mobility-lifetime product

(μτ) of MAPbI<sub>3</sub> and MAPbBr<sub>3</sub> single crystals are comparable to that of CZT single crystal, as shown in Table 1.1 Wei *et al.*, reported the μτ value of 1.2×10<sup>-2</sup> cm<sup>2</sup> V<sup>-1</sup> for MAPbBr<sub>3</sub> single crystal, corresponding to a long diffusion length of 175 micrometres.<sup>24</sup> In 2017, Nazarenko *et al.*, developed Cesium formamidium lead halide single crystal via solution growth method and μτ value of 0.12 was reported, which is larger than that of commercially available CZT.<sup>21</sup>

## 1.3.4. Large Resistivity

The resistivity of semiconductor material is an important figure of merit in selecting the material for  $\gamma$ -ray detection. When the electric field is applied between the electrodes, leakage current develops because of thermally charged carriers or intrinsic charge carriers. Which is the source of the noise? The resulting noise produced from the leakage current of the detector deteriorates the high signal-to-noise ratio, so the large resistivity of semiconductor material is highly desirable to suppress the leakage current when electrodes are biased. CZT, the leading material in the  $\gamma$ -ray sensor, has a resistivity of order 10, corresponding to 1% energy resolution. Lead iodide perovskite material has a comparatively lower resistivity of order  $10^7$ . However, replacing iodide ions with bromide or chloride ions can reduce intrinsic charge carriers due to an enlarged bandgap. When chloride ion Cl<sup>-</sup> incorporated in lead bromide perovskite MAPbBr<sub>3</sub>, reduced noise and leakage current was observed, resulting in impressive spectra with 6.5% energy resolution at 662 keV. By doping in lead halide perovskite material, the resistivity of perovskite material can be increased up to  $10^{10}$ , sufficient for  $\gamma$ -ray detection.

## 1.4. Recent Advancements in PD

Gamma rays are high-energy EM waves (> 100 keV) generated by nuclear explosions and radioactive decay. Unlike alpha or beta radiations, gamma radiations consist of photons (without mass or charge) of energy emitted from unstable nuclei, making them travel farther than other ionizing radiations. They cannot be captured and reflected by mirrors as their wavelength is short enough to pass through the atoms of an interacting material. These highly penetrative radiations interact with a matter by either photoelectric effect Compton scattering or pair production. These collisions create charged particles that the sensors can detect.

X-rays and  $\gamma$ -rays are ionizing radiations of high energy and short wavelengths demanding some common pool of properties for detector materials viz. high effective atomic number (large linear attenuation coefficient), large detecting volume, significant photoconductivity response, good  $\mu\tau$  value, low charge trap density, and large energy gap (Eg) of 1.6–3.0 eV range (low dark current). But fundamentally, the photon flux generated by X-rays and gamma-rays are different. The detector for  $\gamma$ -rays acts as a single photon detector as the detector material individually detects and collects the incident rays due to limited photon flux of  $\gamma$ -rays. But in X-rays, the detector works in a dynamic equilibrium due to higher flux of X-rays. Semiconductor based detectors for detection of  $\gamma$ -rays are relatively more efficient as compared to scintillator-based detectors as they offer better signal to noise ratio which allow the detection of radioactive sources from a large distance. From more than one decade, many attempts have been made in the development of room temperature semiconductor detector (RTSD) materials which are expected to be easy to use and more robust. Most commonly used CdTe and CdZnTe detectors offer bandgap of 1.4 and 1.57 eV respectively which makes them

easy to operate at room temperature conditions. Three important parameters should be considered in the development of RTSD material viz. resistivity (>10<sup>8</sup>  $\Omega$  cm), electron-hole pair creation energy and  $\mu\tau$  value (> 10<sup>-5</sup> cm<sup>2</sup>/V s). Large resistivity values lead to low dark current and noise in a radiation detector material.<sup>26</sup> In recent years, halide lead perovskites have emerged as a promising material for  $\gamma$ -ray detection due to their large stopping power, outstanding charge transport properties leading to a high mobility-lifetime product, tunable bandgap and low-cost solution-processed method of material preparation at low temperature.<sup>19</sup> Due to having a unique combination of the above properties, lead halide perovskite materials have yielded high energy resolution  $\gamma$ -ray spectra and, thus, have shown the capacity of being future semiconductor material for  $\gamma$ -ray detection.

As discussed, Huang *et al.* introduced the idea of introducing a large organic molecule at the A site of ABX3 lattice in MAPbI3 single crystals and fabricated the DMAMAPbI3 (DMA: dimethylammonium) and GAMAPbI3 (GA: guanidinium) crystals showing high resistivity and charge carrier mobility compared to MAPbI3 single crystals.<sup>27</sup> Later, Peng *et al.* used a similar strategy and alloyed MAPbI3 single crystals with ethyl ammonium (EA) cations to form  $EA_{0.17}MA_{0.83}PbI_3$  crystals with good thermal stability and enhanced the charge carrier lifetime compared to MAPbI3 single crystals.<sup>28</sup> Rybin *et al.* fabricated Cr/MAPbBr<sub>2.85</sub>Cl<sub>0.15</sub>/Cr device with varying chlorine content in perovskite to evaluate their role in gamma-ray detection.<sup>29</sup> This incorporation of Cl in MAPbBr<sub>3-x</sub>Cl<sub>x</sub> suppresses the bromine ion migration. Despite reduced effective carrier masses, a significant increase in  $\gamma$ -ray detection ability for MAPbBr<sub>3-x</sub>Cl<sub>x</sub> compared to pristine MAPbBr<sub>3</sub> single crystals.<sup>28</sup> Recently, Liu *et al.* reported improved dark resistivity of  $1 \times 10^9 \Omega$  m at low reverse bias using Cl(6%) doped CH3NH3PbBr<sub>3</sub> single crystals, using high work function contacts to block out the dark noise, thus allowing for

efficient pulse collection.<sup>30</sup> Yang *et al.* studied the operation stability of the hybrid perovskite  $Cs_{0.05}FA_{0.81}MA_{0.14}PbI_{2.55}Br_{0.45}$  under hard  $\gamma$ -rays.<sup>31</sup>

The excellent optoelectronic properties of perovskite single crystals were exhibited to aid in the development of detectors for sensing various high energy radiations viz. X-rays, α-rays and β-rays. These applications require a common pool of properties; good stopping power, high resistivity, wider bandgap and good μτ value. These selection parameters ensure effective radiation absorption and efficient photo-carrier collection in thick detector materials. In the last decade, the development of perovskite-based X-ray detectors evolved parallel to the γ-ray detectors with the pioneer efforts of Stoumpos *et al.* <sup>4</sup> In a very recent and exciting attempt by Nafradi *et al.* MAPbI<sub>3</sub> single crystal was demonstrated to be a multifunctional radiation protection component exhibiting triple function: a detector, a power generator and a radiation shield. <sup>32</sup> They studied the gamma voltaic response of MAPbI<sub>3</sub>, MAPbBr<sub>3</sub> and MAPbCl<sub>3</sub> single crystals in the vicinity of the core of a nuclear reactor. Among these, MAPbI<sub>3</sub> depicts good energy harvesting ability, radiation shielding, and radiation stability and proposes their possible application in nuclear batteries. <sup>32</sup>

# 1.5. General Description of Nonlinear Optics

#### 1.5.1 Materials for Nonlinear

In the past few decades, scientists have been fascinated by the optical nonlinearity of numerous interesting optical materials for their momentous applicability.<sup>33,34</sup> The diverse applicability of novel entities in the nonlinear domain establishes them as potential candidates in significant photonic applications such as optical switching, optical limiting, optical

communications, biomedical imaging etc. In recent years significant reports and reviews in PNCs have emerged as remarkable optical materials in NLO and electronic responses interacting with an ultrafast laser pulse, giant 2/multi-photon absorption (PA). 35-39 Generally, over a broad range of excitation wavelengths, PCNs have shown 3/4 PA. 40 Some of the research groups have established their candidature as strong saturable absorbers. 41 Rhodamine B (Rh B), an organic laser dye, was recently doped in layered hybrid halide perovskite (LHHP) bis(4methoxybenzylammonium) tetra-chlorido cadmate (4MBA2CdCl4) using simple and costeffective slow solvent evaporation technique. The NLO properties of this perovskite have been studied using the Z-scan method with a 785 nm CW laser, where the RSA with a low optical limiting threshold of 0.8 MW/cm<sup>2</sup> was reported by Ranjhani et al.<sup>42</sup> Zhang et al.<sup>43</sup> also reported the NLA coefficient of Cs<sub>4</sub>Cu<sub>x</sub>Ag<sub>2-2x</sub>Sb<sub>2</sub>Cl<sub>12</sub> double PNCs using 800 nm, 250 nJ, 500 Hz fs laser to be ~10<sup>-8</sup> cm/W. The NLO properties of Cs<sub>2</sub>AgBiBr<sub>6</sub> double PNCs, exhibiting TPA cross sections of ~1906 GM and TPA coefficient of ~10<sup>-11</sup> cm/W, were investigated.<sup>44</sup> Our group has extensively conducted broadband ultrafast laser-interaction triggered spectroscopic studies engaging novel systems such as nano entities, PNCs, organic, inorganic compounds etc. 45-50 unveiling their exotic photonic responses in the NLO domain. The present work, FAPbBr<sub>3</sub> is chosen as a prototype to investigate its interactions with Sr<sup>2+</sup>, Cl<sup>-</sup> ions and its advancement toward NLO studies.

Femtosecond (fs) Z-scan studies have been performed using the Z-scan technique initiated by Sheik-Bahae and co-researchers. <sup>46</sup> We aimed to divulge the electronic nonlinearity of these novel perovskite entities using fs excitation. A schematic NLO experimental setup has been presented in Chapter 2. These novel doped NCs exhibited reverse saturable absorption (it could be one of the 2/3/multi-PA) in the open aperture experimental configuration. In the case

of closed aperture mode, the same nonlinear systems displayed a positive intensity-dependent refractive index  $(n_2)$  with a valley-peak nature. In-depth theoretical fitting and analysis led to the thorough estimations of specific fundamental NLO parameters such as multi-PA cross-sections  $(\sigma)$  and NLO susceptibility  $[\chi^{(3)}]$ . The mathematical relations corresponding to the transmittance of the output beam beyond its interaction with the sample can be expressed using the equations (1, 2). The multi-PA-induced open aperture transmittance beam can be expressed as

$$T_{OA(nPA)} = \frac{1}{[1 + (n-1)\alpha_n L(I_0/(1 + \left(\frac{z}{z_0}\right)^2))^{n-1}]^{\frac{1}{n-1}}}$$
 ......(1.4)

The transmittance of the beam in closed aperture mode can be mathematically depicted

$$T_{CA} = \left(1 \pm \left(\frac{4\left(\frac{z}{z_0}\right)\Delta\phi}{\left[9 + \left(\frac{z}{z_0}\right)^2\right]\left[1 + \left(\frac{z}{z_0}\right)^2\right]}\right)\right) \qquad \dots \dots (1.5)$$

where  $z_0$  is the Rayleigh range,  $\Delta$  is the NLO phase-shift, and z is the position of the sample. The equations (1, 2) were primarily used to fit the experimental data. The extracted NLO parameters were retrieved from the theoretical fits, and the remaining fundamental NLO parameters were subsequently estimated. Our previous reports have detailed elaborations on the Z-scan calculations using fs pulses.<sup>46,47</sup>

as

## 1.5.2. Higher-Order Harmonics Generation (HHG)

High harmonic generation (HHG) is a non-linear process in which an intense laser pulse illuminates a sample. Under such conditions, the sample will emit the high harmonics of the generation beam. In the 2<sup>nd</sup> HHG frequency of emitted beam is twice the fundamental frequency due to the coherent nature (Fig 1.7). HHG is a prerequisite of attosecond physics. Currently, gases are frequently used as HHG medium sources. 51-53 The study on HHG experiments utilizing gases is somewhat limited because there are just a few different types of elements in gas states in nature. Hence, several researchers focused on demonstrating HHG from various solid and liquid elements.<sup>54,55</sup> The laser intensity utilized in the experiment is constrained because of the solid's damage threshold. The photon energy resulting from this method is not particularly high. Strong mid-infrared laser pulses recently demonstrated HHG from thin films from MAPbX<sub>3</sub> (X = I, Br, Cl). <sup>54,55</sup> The near IR wavelength 800 nm is the current work-driving pulse, which possesses stronger energy than the mid-infrared pulses. Therefore, there might be a chance of strong ablation leading to damage to the bulk PSCs. Suppose we choose the DP laser energy below the damage threshold of PSCs due to the illumination of strong photoluminescence; the DP, along with harmonics (if generated), will not transmit from almost ~1 mm thick SCs. Therefore, in the present experiment, we pay attention to the method of LIPs [produced by 800 nm (200 ps) and 1064 nm (5ns) wavelengths] to generate harmonics from five bulk PSCs for the first time. Additionally, substantial resonance enhancement can be used to increase harmonic conversion efficiency by utilizing the HHG from LIPs of various metals. 56,57 The impact of additives (CB, PEA, PXA, and API) on MA SCs were analyzed by measuring HHG spectra in terms of harmonics intensity, cut-off, and spectral shift. Initially, we

describe the stability of crystals, then harmonic-cut-off and spectral shift in the following subsections.

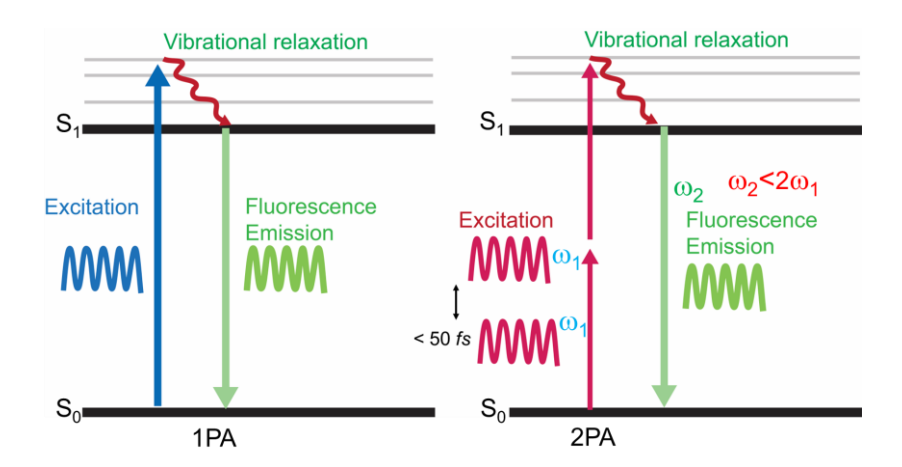


Fig. 1.7 Energy diagram representing 1PA, 2PA and HHG in perovskite materials.

The presence of plasma components (atoms, ions, nanoparticles, clusters) could be identified by the ICCD spectrometer. Meanwhile, It is well aware that HHG is a three-step model<sup>58</sup> [(i) ionization by the intense laser field, (ii) acceleration in the laser field, and (iii) recombination with the parent ion lead to the generation of high energy photons. The emission of high-order harmonics (high energy photons corresponding to driving laser field) is widely subject to plasma components of PSCs. The emitted harmonics are the superposition of the individual contribution of each plasma component. The plasma components' ionization potential (Ip) could influence the harmonics' intensity and cut-off. These parameters are significantly more affected in ps LIPs than in ns LIPs.

## **References**

(1) Kojima, A.; Teshima, K.; Shirai, Y.; Miyasaka, T. Organometal Halide Perovskites as Visible-Light Sensitizers for Photovoltaic Cells. *Journal of the American Chemical Society***2009**, *131*, 6050–6051.

- (2) Zhuang, R.; Wang, X.; Ma, W.; Wu, Y.; Chen, X.; Tang, L.; Zhu, H.; Liu, J.; Wu, L.; Zhou, W.; Liu, X.; Yang, Y. M. Highly Sensitive X-Ray Detector Made of Layered Perovskite-like (NH<sub>4</sub>)<sub>3</sub>Bi<sub>2</sub>I<sub>9</sub> Single Crystal with Anisotropic Response. *Nature Photonics*2019, 13, 602–608.
- (3) Owens, A.; Peacock, A. Compound Semiconductor Radiation Detectors. *Nuclear Instruments and Methods in Physics Research Section A: Accelerators, Spectrometers, Detectors and Associated Equipment***2004**, *531*, 18–37.
- (4) Stoumpos, C. C.; Malliakas, C. D.; Peters, J. A.; Liu, Z.; Sebastian, M.; Im, J.; Chasapis, T. C.; Wibowo, A. C.; Chung, D. Y.; Freeman, A. J.; Wessels, B. W.; Kanatzidis, M. G. Crystal Growth of the Perovskite Semiconductor CsPbBr<sub>3</sub>: A New Material for High-Energy Radiation Detection. *Crystal Growth & Design*2013, 13, 2722–2727.
- (5) Loferski, J. J.; Rappaport, P. Radiation Damage in Ge and Si Detected by Carrier Lifetime Changes: Damage Thresholds. *Physical Review* 1958, 111, 432–439.
- (6) Häcker, R.; Hangleiter, A. Intrinsic Upper Limits of the Carrier Lifetime in Silicon. *Journal of Applied Physics***1994**, *75*, 7570–7572.
- (7) Caputo, M.; Cefarin, N.; Radivo, A.; Demitri, N.; Gigli, L.; Plaisier, J. R.; Panighel, M.; Di Santo, G.; Moretti, S.; Giglia, A.; Polentarutti, M.; De Angelis, F.; Mosconi, E.; Umari, P.; Tormen, M.; Goldoni, A. Electronic Structure of MAPbI3 and MAPbCl3: Importance of

- Band Alignment. Scientific Reports 2019, 9, 15159.
- (8) Stoumpos, C. C.; Malliakas, C. D.; Kanatzidis, M. G. Semiconducting Tin and Lead Iodide Perovskites with Organic Cations: Phase Transitions, High Mobilities, and Near-Infrared Photoluminescent Properties. *Inorganic Chemistry* 2013, 52, 9019–9038.
- (9) Hao, F.; Stoumpos, C. C.; Cao, D. H.; Chang, R. P. H.; Kanatzidis, M. G. Lead-Free Solid-State Organic–Inorganic Halide Perovskite Solar Cells. *Nature Photonics***2014**, *8*, 489–494.
- (10) Ryu, S.; Noh, J. H.; Jeon, N. J.; Chan Kim, Y.; Yang, W. S.; Seo, J.; Seok, S. Il. Voltage Output of Efficient Perovskite Solar Cells with High Open-Circuit Voltage and Fill Factor. *Energy Environ. Sci.* 2014, 7, 2614–2618.
- (11) Noh, J. H.; Im, S. H.; Heo, J. H.; Mandal, T. N.; Seok, S. Il. Chemical Management for Colorful, Efficient, and Stable Inorganic–Organic Hybrid Nanostructured Solar Cells. *Nano Letters***2013**, *13*, 1764–1769.
- (12) Szeles, C.; Cameron, S. E.; Soldner, S. A.; Ndap, J.; Reed, M. D. Development of the High-Pressure Electro-Dynamic Gradient Crystal-Growth Technology for Semi-Insulating CdZnTe Growth for Radiation Detector Applications. *Journal of Electronic Materials* 2004, 33, 742–751.
- (13) Amman, M.; Lee, J. S.; Luke, P. N.; Chen, H.; Awadalla, S. A.; Redden, R.; Bindley, G. Evaluation of THM-Grown CdZnTe Material for Large-Volume Gamma-Ray Detector Applications. *IEEE Transactions on Nuclear Science* 2009, 56, 795–799.
- (14) Kim, H.; Cirignano, L.; Churilov, A.; Ciampi, G.; Higgins, W.; Olschner, F.; Shah, K. Developing Larger TlBr Detectors—Detector Performance. *IEEE Transactions on Nuclear Science* 2009, 56, 819–823.
- (15) Johns, P. M.; Nino, J. C. Room Temperature Semiconductor Detectors for Nuclear

- Security. Journal of Applied Physics 2019, 126, 040902.
- (16) Kishore, V., Saraswat, V. K., Saxena, N. S. & Sharma, T. P. Structural and Electrical Measurements of CdZnSe Composite. *Indian Academy of Sciences***2005**, *28*, 431–436.
- (17) Roy, U. N.; Bolotnikov, A. E.; Camarda, G. S.; Cui, Y.; Hossain, A.; Lee, K.; Marshall,
   M.; Yang, G.; James, R. B. Growth of CdTexSe1-x from a Te-Rich Solution for
   Applications in Radiation Detection. *Journal of Crystal Growth* 2014, 386, 43-46.
- (18) He, Y.; Ke, W.; Alexander, G. C. B.; McCall, K. M.; Chica, D. G.; Liu, Z.; Hadar, I.; Stoumpos, C. C.; Wessels, B. W.; Kanatzidis, M. G. Resolving the Energy of γ-Ray Photons with MAPbI<sub>3</sub> Single Crystals. ACS Photonics 2018, 5, 4132–4138.
- (19) Wei, H.; Desantis, D.; Wei, W.; Deng, Y.; Guo, D.; Savenije, T. J.; Cao, L.; Huang, J. Dopant Compensation in Alloyed CH<sub>3</sub>NH<sub>3</sub>PbBr<sub>3-x</sub>Cl<sub>x</sub> Perovskite Single Crystals for Gamma-Ray Spectroscopy. *Nature Materials***2017**, *16*, 826–833.
- (20) Yakunin, S.; Dirin, D. N.; Shynkarenko, Y.; Morad, V.; Cherniukh, I.; Nazarenko, O.; Kreil, D.; Nauser, T.; Kovalenko, M. V. Detection of Gamma Photons Using Solution-Grown Single Crystals of Hybrid Lead Halide Perovskites. *Nature Photonics* 2016, 10, 585–589.
- (21) Nazarenko, O.; Yakunin, S.; Morad, V.; Cherniukh, I.; Kovalenko, M. V. Single Crystals of Caesium Formamidinium Lead Halide Perovskites: Solution Growth and Gamma Dosimetry. *NPG Asia Materials***2017**, *9*, e373–e373.
- (22) He, Y.; Matei, L.; Jung, H. J.; McCall, K. M.; Chen, M.; Stoumpos, C. C.; Liu, Z.; Peters, J. A.; Chung, D. Y.; Wessels, B. W.; Wasielewski, M. R.; Dravid, V. P.; Burger, A.; Kanatzidis, M. G. High Spectral Resolution of Gamma-Rays at Room Temperature by Perovskite CsPbBr<sub>3</sub> Single Crystals. *Nature Communications* **2018**, *9*, 1609.

(23) Lachish, U. Electron Lifetime Determination in Semiconductor Gamma Detector Arrays, **2000**, 1–6.

- (24) Wei, H.; Fang, Y.; Mulligan, P.; Chuirazzi, W.; Fang, H.; Wang, C.; Ecker, B. R.; Gao, Y.; Loi, M. A.; Cao, L. Sensitive X-Ray Detectors Made of Methylammonium Lead Tribromide Perovskite Single Crystals. **2016**, *10*, 333–340.
- (25) Zhang, F.; Herman, C.; He, Z.; De Geronimo, G.; Vernon, E.; Fried, J. Characterization of the H3D ASIC Readout System and 6.0 Cm 3 3-D Position Sensitive CdZnTe Detectors. *IEEE Transactions on Nuclear Science***2012**, *59*, 236–242.
- (26) Gao, L.; Yan, Q. Recent Advances in Lead Halide Perovskites for Radiation Detectors. Solar RRL2020, 4, 2.
- (27) Huang, Y.; Qiao, L.; Jiang, Y.; He, T.; Long, R.; Yang, F.; Wang, L.; Lei, X.; Yuan, M.; Chen, J. A-site Cation Engineering for Highly Efficient MAPbI 3 Single-Crystal X-ray Detector. *Angewandte Chemie International Edition***2019**, *58*, 17834–17842.
- (28) Peng, W.; Miao, X.; Adinolfi, V.; Alarousu, E.; El Tall, O.; Emwas, A. H.; Zhao, C.; Walters, G.; Liu, J.; Ouellette, O.; Pan, J.; Murali, B.; Sargent, E. H.; Mohammed, O. F.; Bakr, O. M. Engineering of CH3NH3PbI3Perovskite Crystals by Alloying Large Organic Cations for Enhanced Thermal Stability and Transport Properties. *Angewandte Chemie International Edition* 2016, 55, 10686–10690.
- (29) Rybin, N.; Ghosh, D.; Tisdale, J.; Shrestha, S.; Yoho, M.; Vo, D.; Even, J.; Katan, C.; Nie, W.; Neukirch, A. J.; Tretiak, S. Effects of Chlorine Mixing on Optoelectronics, Ion Migration, and Gamma-Ray Detection in Bromide Perovskites. *Chemistry of Materials* 2020, 32, 1854–1863.
- (30) Liu, Y.; Xu, Z.; Yang, Z.; Zhang, Y.; Cui, J.; He, Y.; Ye, H.; Zhao, K.; Sun, H.; Lu, R.;

Liu, M.; Kanatzidis, M. G.; Liu, S. (Frank). Inch-Size 0D-Structured Lead-Free Perovskite Single Crystals for Highly Sensitive Stable X-Ray Imaging. *Matter***2020**, *3*, 180–196.

- (31) Yang, S.; Xu, Z.; Xue, S.; Kandlakunta, P.; Cao, L.; Huang, J. Organohalide Lead Perovskites: More Stable than Glass under Gamma-Ray Radiation. *Advanced Materials* **2019**, *31*, 1–7.
- (32) Náfrádi, G.; Horváth, E.; Kollár, M.; Horváth, A.; Andričević, P.; Sienkiewicz, A.; Forró, L.; Náfrádi, B. Radiation Detection and Energy Conversion in Nuclear Reactor Environments by Hybrid Photovoltaic Perovskites. *Energy Conversion and Management* 2020, 205,1-8.
- (33) Ketavath, R.; Katturi, N. K.; Ghugal, S. G.; Kolli, H. K.; Swetha, T.; Soma, V. R.; Murali, B. Deciphering the Ultrafast Nonlinear Optical Properties and Dynamics of Pristine and Ni-Doped CsPbBr<sub>3</sub> Colloidal Two-Dimensional Nanocrystals. *Journal of Physical Chemistry Letters* 2019, 10, 5577–5584.
- (34) Konda, S. R.; Soma, V. R.; Ganeev, R. A.; Banavoth, M.; Ketavath, R.; Li, W. Third-Order Optical Nonlinearities and High-Order Harmonics Generation in Ni-Doped CsPbBr3 Nanocrystals Using Single- and Two-Color Chirped Pulses. *Journal of Materials Science***2022**, *57*, 3468–3485.
- (35) Shen, W.; Chen, J.; Wu, J.; Li, X.; Zeng, H. Nonlinear Optics in Lead Halide Perovskites: Mechanisms and Applications. *ACS Photonics***2021**, *8* (1), 113–124.
- (36) Wang, G.; Mei, S.; Liao, J.; Wang, W.; Tang, Y.; Zhang, Q.; Tang, Z.; Wu, B.; Xing, G. Advances of Nonlinear Photonics in Low-Dimensional Halide Perovskites. *Small***2021**, *17* (43), 1–21.
- (37) Chen, W.; Zhang, F.; Wang, C.; Jia, M.; Zhao, X.; Liu, Z.; Ge, Y.; Zhang, Y.; Zhang, H. Nonlinear Photonics Using Low-Dimensional Metal-Halide Perovskites: Recent Advances and Future Challenges. *Advanced Materials*. **2021**, *33* (11), 1–46.

(38) Shen, W.; Chen, J.; Wu, J.; Li, X.; Zeng, H. Nonlinear Optics in Lead Halide Perovskites: Mechanisms and Applications. *ACS Photonics***2021**, *8* (1), 113–124.

- (39) Li, M.; Wang, C.; Wang, L.; Zhang, H. Colloidal Semiconductor Nanocrystals: Synthesis, Optical Nonlinearity, and Related Device Applications *Journal of Physical Chemistry C*2021, 9 (21), 6686–6721.
- (40) Krishnakanth, K. N.; Seth, S.; Samanta, A.; Rao, S. V. Broadband Femtosecond Nonlinear Optical Properties of CsPbBr\_3 Perovskite Nanocrystals *Optics Letters* **2018**, *43*, 603.
- (41) Krishnakanth, K. N.; Seth, S.; Samanta, A.; Venugopal Rao, S. Broadband Ultrafast Nonlinear Optical Studies Revealing Exciting Multi-Photon Absorption Coefficients in Phase Pure Zero-Dimensional Cs<sub>4</sub> PbBr<sub>6</sub> Perovskite Films. *Nanoscale* **2019**, *11*, 945–954.
- (42) Ranjani, E.A.; Sangeetha, K.; Sabari Girisun, T. C. Effect of Dye on Luminescent and Nonlinear Optical Properties of Bis(4-Methoxybenzylammonium) Tetra-Chlorido Cadmate (4MBA<sub>2</sub>CdCl<sub>4</sub>) Perovskite *Optics Letters* **2022**, *125*, 112096.
- (43) Zhang, Y.; Sui, N.; Kang, Z.; Meng, X.; Yuan, L.; Li, X.; Zhang, H. Z.; Zhang, J.; Wang, Y. Scanning the Optoelectronic Properties of Cs<sub>4</sub>Cu<sub>x</sub>Ag<sub>2-2x</sub>Sb<sub>2</sub>Cl<sub>12</sub> Double Perovskite Nanocrystals: The Role of Cu<sup>2+</sup> Content. *Journal of Physical Chemistry C*2022, 10 (14), 5526–5533.
- (44) Zhang, Y.; Wang, Q.; Sui, N.; Kang, Z.; Li, X.; Zhang, H. Z.; Zhang, J.; Wang, Y. Temperature-Dependent and Nonlinear Optical Response of Double Perovskite Cs<sub>2</sub>AgBiBr<sub>6</sub> Nanocrystals. *Applied Physics Letters* **2021**, *119* (16), 161904.
- (45) Sheik-Bahae, M.; Said, A. A.; Wei, T. H.; Hagan, D. J.; Van Stryland, E. W. Sensitive Measurement of Optical Nonlinearities Using a Single Beam IEEE Journal of Quantum Electronics **1990**, *26*, 760–769.
- (46) Banerjee, D.; Moram, S. S. B.; Byram, C.; Rathod, J.; Jena, T.; Podagatlapalli, G. K.; Soma, V. R. Plasmon-Enhanced Ultrafast and Tunable Thermo-Optic Nonlinear Optical Properties

of Femtosecond Laser Ablated TiO2 and Silver-Doped TiO2 Nanoparticles Applications of surface science **2021**, *569* (July), 151070.

- (47) Kumar, S.; Acharyya, J. N.; Banerjee, D.; Soma, V. R.; Vijaya Prakash, G.; Sankar, M. Strong Two-Photon Absorption and Ultrafast Dynamics of: Meso -Functionalized "Push-Pull" Trans -A2BC Porphyrins. *Dalton Transactions*. **2021**, *50* (18), 6256–6272.
- (48) Biswas, C.; Palivela, S. G.; Giribabu, L.; Soma, V. R.; Raavi, S. S. K. Femtosecond Excited-State Dynamics and Ultrafast Nonlinear Optical Investigations of Ethynylthiophene Functionalized Porphyrin. *Advanced optical materials*. **2022**, *127* (September 2021), 112232.
- (49) Srivishnu, K. S.; Banerjee, D.; Ramnagar, R. A.; Rathod, J.; Giribabu, L.; Soma, V. R. Optical, Electrochemical, Third-Order Nonlinear Optical Investigations of 3,4,5-Trimethoxy Phenyl Substituted Non-Aqueous Phthalocyanines. *Front. Chem.***2021**, *9*, 1–14.
- (50) Rathi, P.; Ekta; Kumar, S.; Banerjee, D.; Soma, V. R.; Sankar, M. Unsymmetrical β-Functionalized "push-Pull" Porphyrins: Synthesis and Photophysical, Electrochemical and Nonlinear Optical Properties. *Dalton Transactions*. **2020**, *49*, 3198–3208.
- (51) Takahashi, E. J.; Nabekawa, Y.; Midorikawa, K. Low-Divergence Coherent Soft x-Ray Source at 13 Nm by High-Order Harmonics. *Applied Physics Letters* **2004**, *84*, 4–6.
- (52) Takahashi, E.; Nabekawa, Y.; Otsuka, T.; Obara, M.; Midorikawa, K. Generation of Highly Coherent Submicrojoule Soft x Rays by High-Order Harmonics. *Physical Review A Atomic, Molecular, and Optical Physics***2002**, *66*, 021802.
- (53) Constant, E.; Garzella, D.; Breger, P.; Mével, E.; Dorrer, C.; Le Blanc, C.; Salin, F.; Agostini, P. Optimizing High Harmonic Generation in Absorbing Gases: Model and Experiment. *Physical Review Letters* **1999**, *82*, 1668–1671.
- (54) Hirori, H.; Xia, P.; Shinohara, Y.; Otobe, T.; Sanari, Y.; Tahara, H.; Ishii, N.; Itatani, J.; Ishikawa, K. L.; Aharen, T.; Ozaki, M.; Wakamiya, A.; Kanemitsu, Y. High-Order

Harmonic Generation from Hybrid Organic–Inorganic Perovskite Thin Films. *APL Materials***2019**, *7*, 041107.

- (55) Nakagawa, K.; Hirori, H.; Sanari, Y.; Sekiguchi, F.; Sato, R.; Saruyama, M. Interference Effects in High-Order Harmonics from Colloidal Perovskite Nanocrystals Excited by an Elliptically Polarized Laser. *Physical Review Materials* **2021**, *5*, 016001.
- (56) Strelkov, V. Role of Autoionizing State in Resonant High-Order Harmonic Generation and Attosecond Pulse Production. *Physical Review Letters***2010**, *104*, 26–29.
- (57) Rosenthal, N.; Marcus, G. Discriminating between the Role of Phase Matching and That of the Single-Atom Response in Resonance Plasma-Plume High-Order Harmonic Generation. *Physical Review Letters* **2015**, *133901*, 1–4.
- (58) Lewenstein, M.; Balcou, P.; Ivanov, M. Y.; L'Huillier, A.; Corkum, P. B. Theory of High-Harmonic Generation by Low-Frequency Laser Fields. *Physical Review A* **1994**, *49*, 2117–2132.

# **CHAPTER-2**

# Materials, Methods

# & Characterizations

## 2. Materials & Methods

The materials, methodologies, characterization techniques, and concepts employed for this Ph.D. thesis are briefly summarised in this chapter. This chapter gives detailed information about the materials and standard techniques used for synthesis, and device fabrication, to study the non-linear optical properties (NLO) and characterization at various phases of research activity. The methods used to purify desired materials and solvents are described in this chapter. Furthermore, a brief explanation of the materials and device characterization techniques employed for PSCs is provided in the context of the results in this thesis.

## 2.1. Synthetic Methods

For a few years, many affords have been devoted to growing single crystals because of having low trape density, more carrier mobility, and readily available reagents with low cost<sup>1</sup>. Many synthetic methods are available; however, the ways that showcase the promising properties with low-cost material and don't require any critical environment are mentioned here. We can control crystal orientation and morphology in optoelectronic devices by adopting the appropriate synthetic method. Finally, these active materials' promising outlooks were highlighted.<sup>1</sup> Most of the existing lead halide perovskite crystals are synthesized by solution methods like top-seeded solution growth (TSSG), solution temperature-lowering (STL) method, antisolvent vapour-assisted crystallization (AVC) and Inverse Temperature Crystallisation (ITC) method (Fig. 2.1).<sup>2,3</sup> Dong *et al.* reported high-quality MAPbI<sub>3</sub> single crystals with a temperature gradient. They observed lower trap density (3.6×10<sup>10</sup> cm<sup>-3</sup>), more significant carrier mobility (as measured by the Hall effect method), longer carrier life and diffusion length under solar light intensity could exceed 175 µm.<sup>4</sup> Furthermore, it was presumed that the carrier

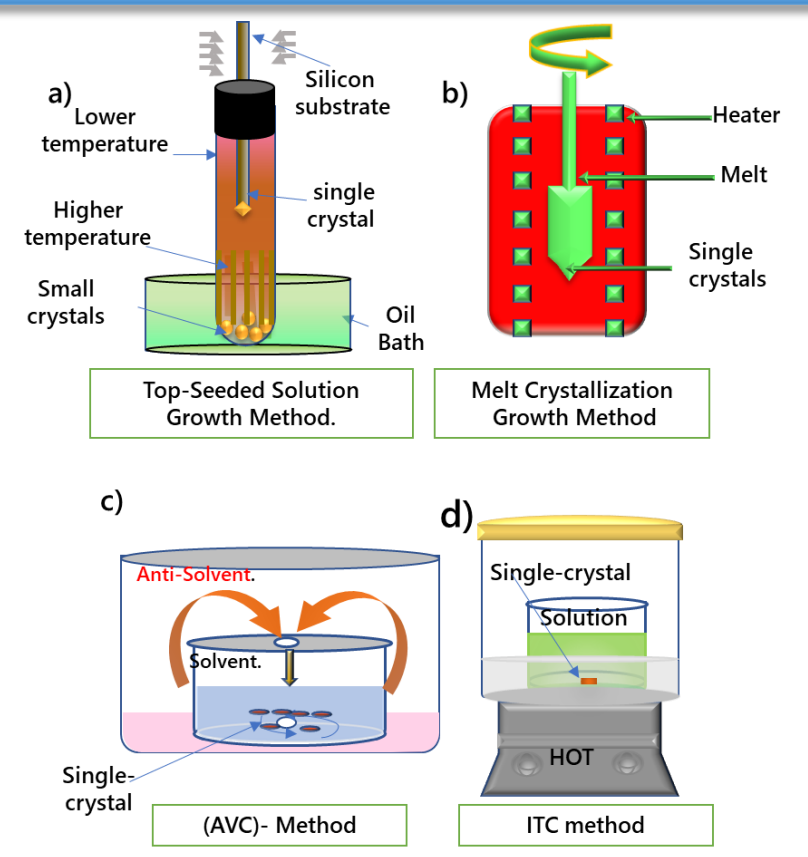


Fig. 2. 1 Synthetic strategy for growing perovskite single-crystal a) Antisolvent Vapour-Assisted Crystallization (AVC) B) Top-Seeded Solution Growth (TSSG) C) Melt Crystallization Growth Method d) Inverse Temperature Crystallization (ITC).

diffusion distance could exceed 3mm under 0.003 mW cm<sup>-2</sup> weak light intensity. In 2016, Lian *et al.* demonstrated that centimetre-sized MAPbI3 single crystals with a low trap density of  $10^8$  cm<sup>-3</sup>) were grown using the solution temperature-lowering (STL) method.<sup>5</sup> In recent studies, crystal growth technique to grow MAPbX<sub>3</sub> single crystals using the inverse temperature crystallisation (ITC) method. Although commercially inorganic single crystals cadmium zinc telluride (CZT), cadmium telluride (CT), germanium (Ge), and silicon (Si) have been widely used in  $\gamma$ -ray detectors, these materials are difficult to deposit uniformly on the film substrate to read out the detection signal. The MAPbBr<sub>3</sub> single crystal is grown directly on a silicon

substrate. Huang and coworkers reported they modified with small organic molecules by chemical bonding so that the detection signal could read out now. Cesium formamidium lead single halide crystal via solution growth method and  $\mu\tau$  value of 0.12 reported by Nazarenko et al. developed, larger than commercially available CZT.

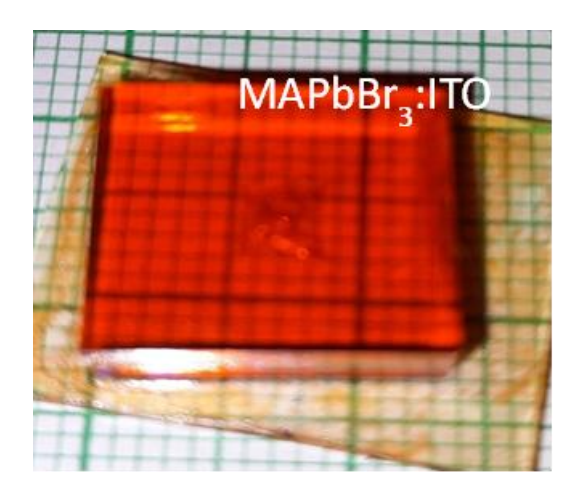


Fig. 2. 2 MAPbBr<sub>3</sub> SC grown using the ITC method on ITO.

### 2.1.1. Synthesis of MAPbBr<sub>3</sub> Crystals Growth with additives:

We used additives to grow methylammonium lead bromide (MAPbBr<sub>3</sub>) [hereafter abbreviated as MA] crystals to investigate the impact of different ammonium salts as an additive on optoelectronic and structural properties. Ammonium salts used are aliphatic, aromatic, and chiral additives to see the effect on HHG studies. Aliphatic like Choline bromide (CB), aromatic additives like Phenylethylamine hydrochloride (PEA), P-Xylylenediamine (PXA), and chiral additives like (R)3-Aminopiperidine dihydrochloride (API).<sup>6</sup>

#### 2.1.1.1. Chemicals:

Lead bromide (≥98%), methylammonium bromide (99.9% trace metals basis), dimethylformamide (DMF) (HPLC, 99.8%), and dimethyl sulfoxide (DMSO) (anhydrous, ≥99.9%), were purchased from Sigma-Aldrich. Phenylethylamine hydrochloride (PEA), (R)3-aminopiperidine dihydrochloride (API), P-xylylene diamine (PXA), and choline bromide (CB) were purchased from TCI and used as received.

#### 2.1.1.2 **Synthesis**:

Optimal volume ratios of the solvents are prepared by dissolving the MABr, PbBr<sub>2</sub>, with 1:1 equivalents labelled as precursor solution (MA crystal without additive for comparison) by following the previous literature in the glove box. We have optimized the percentage of additives (A) from 0.1 to 0.2 equivalents in precursor solution for MA-A crystal growth. For example, we grow MA-API crystal by adding an optimal percentage of API to precursor solution. The precursor solution was then kept for stirring for eight hours and filtered through a polytetrafluoroethylene (PTFE) filer with 0.45 µm pore size. Initially, tiny perovskite crystals with an average length of 1.5 mm, were obtained, which were used as seed crystals for growing larger crystals. Further, a larger crystal was achieved by carefully transferring seed crystals to the freshly prepared 1M precursors solution. We observed a possible shape control of the crystal by the geometry of crystals using the additive. Finally, add the dichloromethane (DCM) to the crystals after removing the precursor solution using the syringe; a white residue will appear on the surface of the crystals need to add; the DMF for clean the excess unreacted material from the surface. Repeat the same procedure until the solution becomes colourless when adding DCM. Finally, perovskite SCs were dried in a vacuum oven and stored in the

desiccator. The thickness of the SCs are measured using the digital vernier callipers, and MA, MA-CB, MA-PEA, MA-PXA and MA-API have a thickness of 1.02, 1.18, 1.12, 1.10, 1.03 mm, respectively.

For modified crystal growth, we have taken one molar solution containing 1:1:0.2 equivalents of PbBr<sub>2</sub> and MABr and API (3-Aminopiperidine dihydrochloride) in DMF, The precursor solution was kept for stirring for 12 hours and was filtered using 0.45 µm pore size polytetrafluoroethylene (PTFE) syringe filter. Five millilitres of the filtrate were placed in a vial, and the vial was kept in an oil bath undisturbed at 80 °C. All procedures were carried out under an N<sub>2</sub> atmosphere. Once the SCs were formed, they were collected and dried in a vacuum oven.

## 2.1.2. Synthesis of Cl-doped MAPbBr<sub>3</sub> SCs

#### 2.1.2.1. Chemicals

Lead(II) bromide (PbBr<sub>2</sub>) (≥98%), lead(II) chloride (PbCl<sub>2</sub>) (≥98%), methylammonium bromide (MABr) (99.9% trace metals basis), dimethylformamide (DMF) (anhydrous, 99.8%), and dimethylsulfoxide (DMSO) (anhydrous, ≥99.9%), were purchased from Sigma-Aldrich. Phenylethylamine Hydrochloride (PEA), and P-Xylylenediamine (PXA), were purchased from TCI and used as received.

#### 2.1.2.1. **Synthesis**

MHSCs has grown using the inverse crystallization method (ITC). A precursor solution has been prepared by taking a stoichiometric ratio of PbBr<sub>2</sub> (330.30 mg), PbCl<sub>2</sub> (34.11 mg) and MABr (111.97 mg) to 1ml of DMF.**P4** The precursor solution was then stirred for eight

hours after adding the additives (for modified MHSCs growth) and then filtered through a PTFE filer with a 0.45 µm pore size. Initially, tiny perovskite crystals, with an average length of 2 mm, were obtained, which were used as seed crystals for growing larger crystals. Further, larger SCs can be achieved by carefully removing and placing them in a new 1M solution. The modified MHSCs have been grown by taking less than 50 µl of 1M additives solution in the precursor solution. We observed a possible shape control of the crystal by the geometry of crystals using the different additives. Finally, add the dichloromethane (DCM) to crystals afterwards, using the syringe to remove the precursor solution, and clean the excess unreacted material from the surface using the DMF. Repeat the same procedure until the solution becomes colourless when adding DCM<sup>7</sup>. One can set only a few crystals by balancing the composition of additives and temperature conditions. Observed the crystals' nucleation temperature changes to a more significant value from 80 °C to 89 °C, indicating different interactions of ammonium slats with the crystalloids towards controlling the nucleation process.<sup>8</sup>

### 2.1.3. Synthesis of FAPbBr<sub>3</sub> PNCs

#### 2.1.3.1. Chemicals

Formamidinium bromide (FABr) (99.9% trace metals basis) was purchased from Dyesol. Dimethylformamide (DMF) (anhydrous, 99.8%), toluene (anhydrous, ≥99.9%), acetonitrile (ACN), chloroform, dimethyl sulfoxide (DMSO) (anhydrous, ≥99.9%), oleic acid (OA) and oleylamine (OAm) were purchased from Sigma-Aldrich. Lead(II) bromide (PbBr) (≥98%) and SrCl₂ were purchased from TCI and used as received.

#### 2.1.3.2. *Synthesis*

FAPbBr<sub>3</sub> NCs were doped using the strontium chloride (SrCl<sub>2</sub>) at 2%, 4% and 6% concentrations to investigate the SrCl<sub>2</sub>-doped FAPbBr<sub>3</sub> NCs in the NLO studies and labelled as FB-2, FB-2 and FB-4, respectively. The steps involved in synthesizing PNCs are illustrated in Fig. 2c. The FAPbBr<sub>3</sub> PNCs synthesis was carried out under the glovebox using the room-temperature synthetic (RTS) method. In a typical procedure, FABr (0.1 mm) and PbBr<sub>2</sub> (0.1 mm) were dissolved in 1 ml of DMF and stirred for 4 h. The solution was filtered via a 0.45 μm pore polytetrafluoroethylene (PTFE). Subsequently, 40 and 120 μL of OAm and OA were added to the filtered solution. Thereafter, 100 μL were taken from this solution and injected into anti-solvent chloroform to obtain PNCs, followed by purification using 1.5 ml of ACN/toluene solution in (1:1), centrifugation at 3500 rpm for 10 min, and finally, stored in

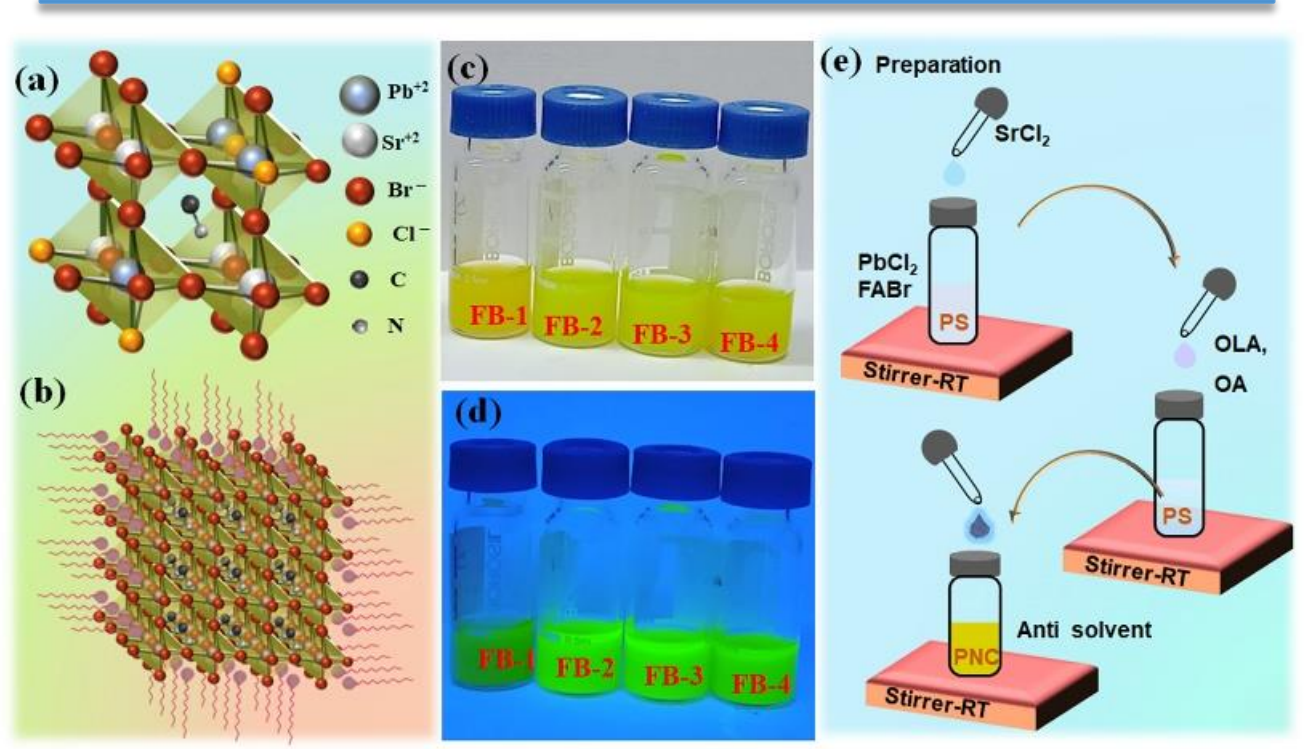


Fig. 2. 3(a) Polyhedral representation of the unit cell of SrCl<sub>2</sub> doped FAPbBr<sub>3</sub> and (b) schematic illustration of PNCs with OA. Moreover, (c) & (d) depicts photographs of pristine and SrCl<sub>2</sub>-doped FAPbBr<sub>3</sub> NCs in ambient and UV light, respectively. (e) Steps involved in colloidal solution preparation.

toluene with an FB-1 label (pristine solution). The preparation of doped FAPbBr<sub>3</sub> PNCs (FB-2 to FB-4), followed the same procedure mentioned above.

## 2.2. Device architecture:

For the fabrication of thin films, one-step\two-step solution and vapour-phase deposition methods have been developed. Usually, Perovskite nanocrystals deposit from precursor solutions<sup>1</sup> QDs/0D and 2D perovskite-based photodetectors effectively act as ultrasensitive to broadband (UV to near IR) and ultraviolet to the visible region. At the same time, 1D perovskite materials applications in photodetectors are hindered due to the low-quality

(Q) factor and extremely long response time. Carbon nanotubes (CNTs) and gold wires improve the sensitivity of perovskite-based materials due to high conductivity and slight surface roughness. Therefore, this advancement has attracted many studies regarding the combination of 1D materials and 3D bulk perovskite materials. More importantly, bulk single crystals and the largescale halide perovskite thin films have recently made tremendous success in  $\gamma$ -ray radiation detection due to their compelling characteristics. They can also be deposited conveniently from the solution by the facile available manufacturing technique. In 2018 Wu *et al.* reported lead-free Cs<sub>4</sub>EuX<sub>6</sub> (X=Br<sup>-</sup>, I<sup>-</sup>) 0D perovskite single crystals as self-activated scintillators.<sup>3</sup>

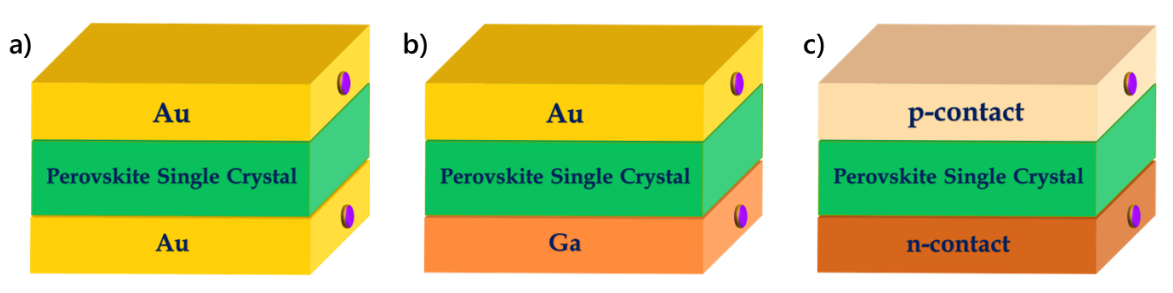


Fig. 2. 4 Device architecture

Perovskite-based photodetectors with different architectures, including photodiodes, photoconductors, and phototransistors. Usually, the photodiodes adopt a vertical-type architecture to reduce dark currents. Device configuration plays a crucial role in evolving the overall performance of perovskite in radiation detection. Here, we demonstrate two approaches: (i) p-i-n architecture with Au\TPD \PSC \fullerene\BCP\Ag and (ii) another approach using an n-i-p architecture with Ga\perovskite\Au or even a simple architecture with Au\PSC\Au. MAPbBr<sub>3-x</sub>Cl<sub>x</sub> crystals have comparable high resistivity reported with both p-i-n or p-i-p device configurations.<sup>8</sup>

# 2.2.1. Thermal Evaporator

Thermal evaporation is used to deposit the metal (Au, Ag, Al, Cu et.,) on the substrate by the physical vapour deposition method. The metal is placed in the crucible and heated by passing a high current until all the material is vaporized via sublimation or boiling. Some of the vapour particles reach the substrates and condense. The thickness of the film was measured using quartz crystal placed next to the substrate.



Fig. 2. 5 Photo images of thermal evaporator for gold deposition at SoC, UoH.

# 2.3. Characterization

#### 2.3.1. Structural Characterization

#### 2.3.1.1. X-ray Photoelectron Spectroscopy (XPS):

Surface elementals mapping of crystals has been done using Thermo Fisher Scientific Pvt. Ltd, X-ray Photoelectron Spectroscopy.

#### 2.3.1.2. Single crystal XRD:

The X-ray crystal data of the MA and Modified MA PSCs were collected on an Xtlab Synergy Rigaku oxford diffraction with HyPix- 3000 detectors, equipped with graphite monochromated Mo Kalpha radiation (= 0.71073 A) at 293K. The 2T range for data collection was from 5.082 to 50. The data interpretation was processed with CrysAlisPro, Xtlab Synergy Rigaku oxford diffraction, version 171.39.exe and an absorption correction based on the multi-scan method.

#### 2.3.1.3. Powder XRD spectra:

The structural studies have been analyzed by a PANalytical xpert3 powder diffractometer with Cu K $\alpha$  radiation and the step size of 0.016711 $^{\circ}$  with 73.025 times per step in ambient conditions.

The microcrystalline strain was calculated using Williamson-Hall (W-H) plots (Equation 1) from powder XRD data.

$$\beta_{hkl}cos\theta = \frac{\kappa\lambda}{D} + 4\varepsilon \sin\theta \tag{1}$$

Where D= crystalline size, K= shape factor (0.9), and  $\lambda=$  wavelength of Cuk $\alpha$  radiation, instrumental broadening ( $\beta_{hkl}$ ). The strain  $\epsilon$  was estimated from the slope of Equation 1.<sup>6,9</sup>

# Peak shift maybe attributed

- 1. changes in stoichiometric composition by doping.
- 2. Instrumentations (Doppler effect during counts)
- 3. Microstructure parameters (crystallize size and lattice strain"
- 4. Thermal annealing

# 2.3.2. Optical Characterization

#### 2.3.2.1. Uv-Vis Spectroscopy

It is very useful to understand the electron transition of the synthesized organic molecules from the ground state (GS) to the excited state (ES), it works depending on the electron transition method. It gives the absorption spectrum of wavelength vs absorption. We predict the band gap and type of transition by using the onset value from this spectrum. The electrons are transition occurs from bonding or non-bonding orbitals to antibonding orbitals when we excite the synthesized molecules between 200 nm and 750 nm. These energy orderings are as follows:  $\sigma$ –  $\sigma^* > n$ – $\sigma^* > n$ – $\pi^*$ . By using the Beer–Lambert law, we estimate the absorption and bandgap values.<sup>6</sup>



Fig. 2. 6 UV used for bandgap investigations at SoC, UoH.

$$A = log \frac{I_0}{I} = \varepsilon cl....(2.6)$$

Where A = absorbance (no units),

 $I_0$  = incident light intensity

I= transmitted light intensity

 $\varepsilon = \text{molar extinction coefficient}$ 

C = the concentration of the absorbing analyte

1 = path distance through the sample or cell in cm.

We determine PSCs absorption and band gap value by using JASCO (V-750) UV-visible spectrometer. For Uv absorption measurement, we make samples in various solvents with different concentrations, and all are given in respective chapters.

#### 2.3.2.2. Confocal Raman Images:

Confocal Raman Images were taken with a Confocal Raman Microscope (Model: Witec-Alpha300)

#### 2.3.2.3. Emission Spectroscopy

It is a complementary measurement to UV-Vis spectroscopy, demonstrating the electrons' transition from the ES to GS and emitting radiative and non-radiative energy based on the molecules. We determine the emission spectra from the photoluminescence spectroscopy (PL) as a function of wavelength (nm). The excited state molecules come to the ground state by emitting the photon with lower energy than the initial absorbed photon energy, leading to the emission spectrum. By using this technique, we determine the bandgap by the intersection of the absorption and emission spectra of the organic molecules from the following equation.



Fig. 2. 7 UV used for bandgap investigations at SoC, UoH.

$$E_{0-0} = \frac{1240}{\lambda_{onset}}.....(2.7)$$

Where,

 $\lambda_{int}$  = onset value at the intersection of UV-Vis & PL spectra.

 $E_{0-0}$  = Zero-Zero<sup>th</sup> level band gap.

We have used Jasco Fu-8500 Spectro fluorometer instruments for recording the PL of the synthesized molecules in various solvents with different concentrations are given in Chapters 3, 4, and 5.

Photoluminescence (PL) spectra recorded with a Confocal Raman Microscope (Model: Witec-Alpha300) using 405 and 488 nm laser and for 800 nm wavelength Ti: Sapphire (Spectra-Physics) laser pulses of 35 fs and 1 kHz repetition rate were used.

#### 2.3.2.4. Time-resolved photoluminescence TRPL

TRPL is a tool for quickly examining electronic deactivation processes that cause the emission of photons is called time-resolved fluorescence. It is also known as time-correlated single photon counting (TCSPC). Lifetime Measurements Photoluminescence (PL) decays and PL lifetime has been recorded on a time-resolved Micro-Time 200 confocal fluorescence lifetime imaging microscopy (FLIM) setup (Pico Quant) equipped with an inverted microscope (Olympus IX 71) using laser 370. A molecule typically has a lifespan of a few picoseconds to a few nanoseconds in its lowest excited singlet form. These measurements were performed at room temperature on a powder-deposited cover slip under atmospheric conditions. Samples were excited at 405 nm ps laser with a stable repetition rate of 20 MHz (FWHM: 176 ps). We explain the TRPL in upcoming Chapters.

#### 2.3.2.5. FTIR Spectroscopy

Fourier Transform Infrared Spectroscopy (FTIR) is mainly used to determine the functional group in synthesized molecules using the infrared absorption/emission spectrum.<sup>4</sup> These instruments give vibrational modes based on the various functional groups. It was recorded on a Nicolet iS5 ATR-FTIR (Thermo Scientific, India) spectrometer in the range of 4000-1100 cm<sup>-1</sup> with a nominal resolution of 4 cm<sup>-1</sup> using 32 scans by using material in powder or liquid form and analyzed by Origin software.

# 2.3.3. Thermal Properties

#### 2.3.3.1. Thermogravimetric Analyzer (TGA)

TGA is a powerful technique to evaluate the thermal degradation or stability of the compounds used in various applications like PSCs, OSCs, DSSCs and OLEDs device fabrication. Using this technique, we find the thermal stability of composite materials for varied applications.

By considering the degradation of materials as 1<sup>st</sup> order reaction, the Kinetics thermodynamic parameters of the reaction can be calculated using the equations below. A detailed description with more explanation is given in Chapter 5.<sup>6</sup>

$$\frac{dx}{dt} = k(1 - x) \tag{2}$$

where 
$$x = \frac{wi - wt}{wi - wf}$$
 (3)

wi is the initial weight, wt is the weight of the sample at a particular time t and wf is the final weight. A straight line of plotted graph (Fig. 5.2c) using Equations 2 and 3 for the

selected phase confirms the first-order reactions. Kinetics parameters were determined using a modified form of the Coats and Redfern model as described in **Equation 4**.

$$\ln[-\ln(1-x)] = \ln\frac{ART^2}{\beta E_a} - \frac{E_a}{RT}$$
(4)

Where A is the pre-exponential factor,  $\beta$  is a heating rate (10 °C/min), R is the general gas constant (8.3143 J mol<sup>-1</sup> K<sup>-1</sup>),  $E_a$  is the activation energy, and T is the temperature (K).



Fig. 2. 8 Thermogravimetric analyzer used for thermal

#### properties at SoC, UoH.

TGA measurements were done using a PerkinElmer, Simultaneous Thermal Analyzer STA 6000 instrument. A small amount of 1 to 1.5 mg of crystal powder in the alumina crucibles is supported by a platinum pan. Samples were measured under nitrogen from room temperature to 665 °C at the ramp rate of 10 °C/ min or 20 10 °C/ min.

#### 2.3.3.2. Differential scanning calorimetry (DSC)

DSC is a thermal analysis apparatus used to determine how the physical properties of a sample change, along with temperature vs time. The glass transition ( $T_g$ ) and phase transition temperature materials can be confirmed using this experiment. We performed this experiment by using  $\sim 2$  mg of a compound in an aluminium sample holder and an empty reference plate. It operated at 10 °C /min or 20 10 °C/min under a nitrogen atmosphere from 30 to 450 °C (**Fig. 2.9**).



Fig. 2. 9 Differential scanning calorimetry (DSC) used for change in

material behaviour with temperature at SoC, UoH.

# 2.3.4. Electron Microscopes

Electron microscopes (EM) have a 50 pm resolution and magnifications of up to about 10,000,000x owing to greater resolving power than a light-powered optical microscope because

electrons have wavelengths about 100,000 times shorter than visible light (photons) and can achieve better than. In contrast, ordinary, non-confocal light microscopes are limited by diffraction to about 200 nm resolution and useful magnifications below 2000x. High energy electrons accelerated onto material result in many interactions (Inelastically and Elastic scattering) with the atoms of the target sample, as shown in **Fig. 2.10.a** Imaging quantitative and semi-quantitative information of the target sample and generating an X-ray source results from the number of elastic and inelastic signals of the materials. Quantitative and semi-quantitative analysis of compounds could be done by the secondary electrons (SE), backscattered electrons (BSE), cathode-luminescence (CL), auger electrons and characteristic X-rays which could be useful in covering the signals which are used for imaging. X- rays are used for as well as element mapping. Elastic scattering may occur if the entered electrons come out without any interactions.

#### 2.3.4.1. Field Emission Scanning Electron Microscope (FESEM)

FE-SEM is a flexible method for evaluating the physical characteristics of materials, such as shape, texture, precipitation, phase transition, and particle size distribution in 3D form. We can also determine the structure of nanoparticles. The micro to the nanoscale range images is acquired by FESEM and viewed through the top and cross-sectional paths with a resolution of less than 10 nm. For the FESEM, we prepare a sample mounting on the metal stub using a sticky carbon disc to increase conductivity. On top of the specimen, we coated conductive material; generally, we use gold (Au) to avoid charge build-up on the sample.

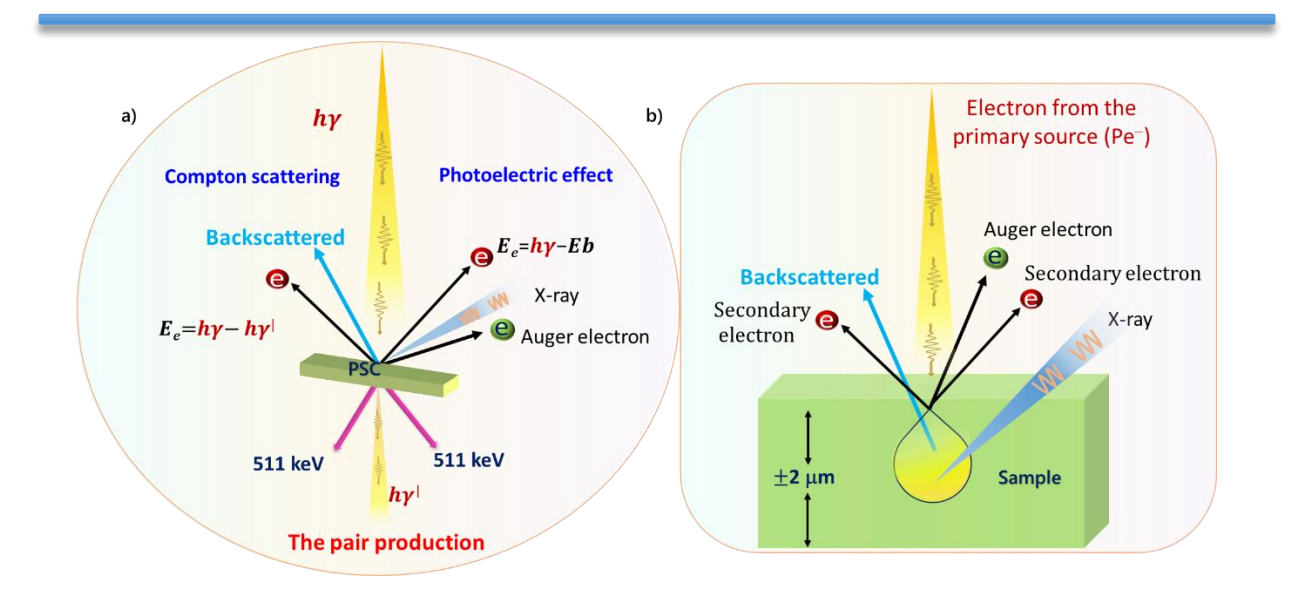


Fig. 2. 10 a) Electron Specimen Interactions. b) Schematic illusion of SEM

In FESEM, the electron guns (thermos ionic gun or field emission gun) are generally used to generate a fine, controlled electron beam that passes through the lenses and strikes the sample's surface at a low vacuum level. The position of the electron beam on the specimen is controlled by scan coils positioned over the objective lens. The electron beam scanned the surface of the sample through the coils. Finally, the signals are generated from the interaction of the specimen, and the electron which generates images is detected by the detector, which contains the composition and surface morphology of the material. Depending on the accelerating voltage and sample density, the high-energy electron beam penetrates a few microns deep into the sample and generates signals in the form of secondary electrons, backscattered electrons, and characteristic X-rays schematic illustration given in Fig. 2.10b.

We are using Carl Zeiss FESEM operating at 3 kV to record the FESEM images of the perovskite single crystals and nanocrystals included in upcoming working Chapters.

# 2.3.4.2. High-Resolution Transition Electron Microscope (HRTEM)

TEM images are recorded using a JEM-F200 kV (**Fig. 2.11**). The sample was prepared by taking the powder on the Cu grid, and TEM image analysis was done using Gatan Digital software.

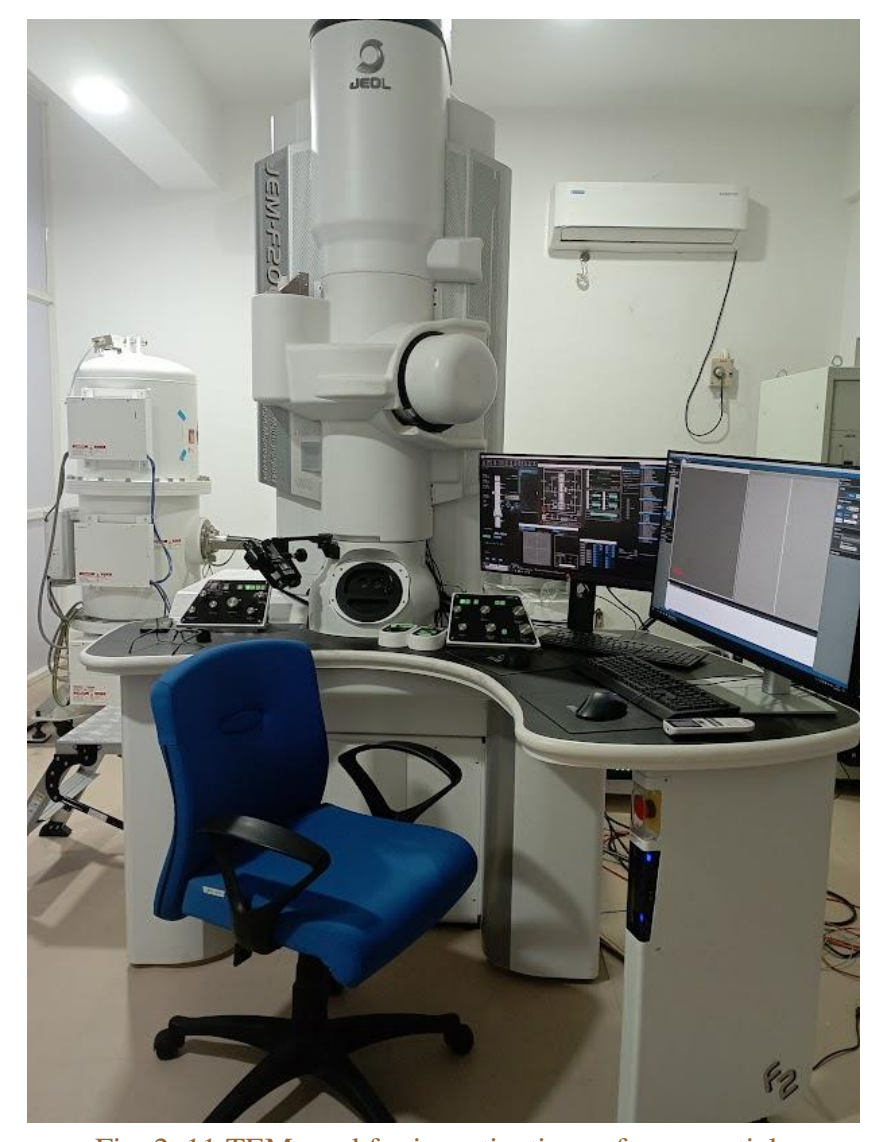


Fig. 2. 11 TEM used for investigations of nanoparticle morphology at SoC, UoH.

#### 2.3.5. Electrical measurement:

#### 2.3.5.1. Space charge limited current (SCLC)

The trap density of the synthesized PSCs has been calculated in dark conditions using Keithly 2400 as a source meter. For this measurement, we fabricate hole only a device as **Au/PSCs/Au** configuration. We analyze it by using the following Equation (2.1).<sup>10</sup> A detailed explanation of SCLC measurement is given in Chapter 3,4.<sup>6,11</sup>

$$J = \frac{9}{8} \frac{\varepsilon \varepsilon_o \mu_h V^2}{L^3} \dots (2.1)$$

Where,

J= Current density

 $\varepsilon$ = permittivity of the material

 $\varepsilon_0$ = Vacuum permittivity

V=Voltage

L= Thickness of the material

 $\mu_h$ = Hole mobility

#### 2.3.5.2. Electrochemical impedance spectroscopy (EIS)

The current-voltage (I-V) measurement and electrochemical impedance spectroscopy (EIS) under temperature and light were carried out using a Biologic Potentiostate SP 300 and Laboratory of Advance Synthesis and Characterization (LASC) probe station. The thin layers of gold (Au) were deposited on the surface of all crystals examined for all the measurements

present in the manuscript. A detailed explanation of EIS measurement with analysis is given in Chapter 4.

# 2.4. Experimental details of Terahertz time-domain spectroscopy (THz-TDS)

We have built the THz-TDS system in the 0.1 to 3.0 THz range. The setup consists of a Ti: Sapphire laser (800 nm, 35 fs, 1 kHz). A beam splitter (90:10) was used to split the output beam into pump (generation arm) and probe (detection arm) sources. We have fixed the pump's laser pulse energy at 1.5 mJ and 3 µJ for probe pulses. The pump and probe pulses were focused by a spherical lens of 150 mm (beam waist ( $\omega_0$ ) =16.5  $\mu$ m ) and 300 mm ( $\omega_0$ = 30.75  $\mu$ m) focal lengths. A 200 µm thick type 1 BBO crystal was used to convert the fundamental 800 nm to second harmonic 400 nm wavelength and placed between the spherical lens and its focus position. The generated THz radiation from air plasma was guided by four gold-coated halfaxis parabolic mirrors (PM) until the THz signal was focused on the ZnTe (110) crystal (EKSMA optics) having a 1 mm thickness. For the SCs THz reflection and transmission measurements, the SCs are positioned at 0° and 45° to the incident THz pulse. The THz pulse reflection from single crystals was collected by PM5 and guided with a gold-coated mirror. In the case of transmission, this mirror was flipped down. THz radiation was detected using an electro-optical sampling technique consisting of ZnTe crystal, quarter waveplate, Wollaston prism, and balanced photodiodes. The residual input laser was blocked by high-resistivity float zone silicon (HRFZ-Si) after the PM1. The output of the balanced diode signal was connected to the lock-in amplifier (Stanford Research Systems, model no. SR830). The pump pulse is

chopped at 500 Hz using a mechanical, optical chopper as a reference to the lock-in amplifier. The LabVIEW program controlled the delay stage's data acquisition and motion control.

# 2.5. HHG experimental setup:

The schematic used for HHG measurements was earlier reported.<sup>6</sup> In brief, we used a Ti: Sapphire laser (800 nm, 35 fs) operated at a 1 kHz pulse repetition rate used as a DP. Used picoseconds (800 nm, 200 ps, 1 kHz) and nanoseconds (1064 nm, 5ns, 10 Hz) HP to create the plasma plumes of SCs. The picoseconds pulses are obtained from an uncompressed portion of

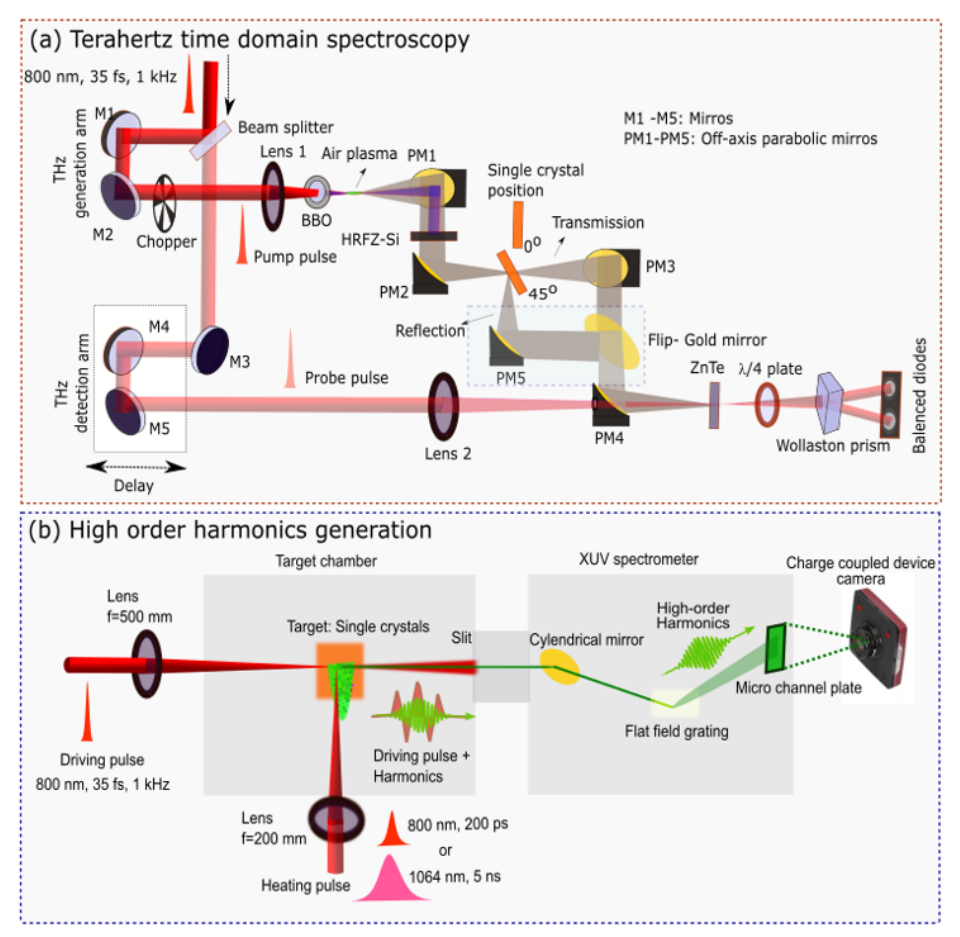


Fig. 2. 12 Experimental layouts for (a) terahertz time-domain spectroscopy and (b) high-order harmonics from laser-induced plasma plumes of single perovskite crystals.

amplified laser pulses of the same Ti: Sapphire laser system. The delay between the fs DP and ps HP was fixed at approximately 80 ns. In contrast, the delay dependence between ns HP and fs DP was varied using the digital delay line and controlled by a delay generator (DG535, Stanford Research Systems). The DPs and HPs are focused using a spherical lens of 500 mm and 200 mm, respectively. In case of ps HPs the HHG studies were carried out at (a) different DP intensities between 1.5 to  $9 \times 10^{14}$  W/cm² at fixed ps HP intensity  $1.17 \times 10^{10}$  W/cm² and (b) ps HP intensities are varied from 0.6 to  $2.25 \times 10^{10}$  W/cm² at fixed DP intensity  $6.0 \times 10^{14}$  W/cm². In the case of ns HP its intensity was fixed at  $7 \times 10^{10}$  W/cm². The synthesized SCs are placed on a glass substrate and kept perpendicular to the HP propagation in the target chamber. The DPs propagated through the plasma plumes approximately 0.2 mm above the target surface. The emitted harmonics from LIPs were directed to the XUV spectrometer chamber, consisting of a gold-coated cylindrical mirror, flat field grating, and a microchannel plate. The harmonic spectra were recorded using a charge-coupled device camera.

# 2.6. Introduction to the Z-scan Technique

NLO experimental setup has been presented **Fig. 2.13**. These novel doped NCs exhibited reverse saturable absorption (it could be one of the 2/3/multi-PA) in the open aperture experimental configuration. In the case of closed aperture mode, the same nonlinear systems displayed a positive intensity-dependent refractive index (n<sub>2</sub>) with a valley-peak nature. Indepth theoretical fitting and analysis led to the thorough estimations of specific fundamental NLO parameters such as multi-PA cross-sections ( $\sigma$ ) and NLO susceptibility [ $\chi$ <sup>(3)</sup>]. The mathematical relations corresponding to the transmittance of the output beam beyond its

interaction with the sample can be expressed using the equations (1, 2). The multi-PA-induced open aperture transmittance beam can be expressed as

$$T_{OA(nPA)} = \frac{1}{[1 + (n-1)\alpha_n L(I_0/(1 + \left(\frac{z}{z_0}\right)^2))^{n-1}]^{\frac{1}{n-1}}}$$
 .....(1)

The transmittance of the beam in closed aperture mode can be mathematically depicted as

$$T_{CA} = \left(1 \pm \left(\frac{4\left(\frac{Z}{Z_0}\right)\Delta\Phi}{\left[9 + \left(\frac{Z}{Z_0}\right)^2\right]\left[1 + \left(\frac{Z}{Z_0}\right)^2\right]}\right)\right) \qquad \dots \dots (2)$$

where  $z_0$  is the Rayleigh range,  $\Delta$  is the NLO phase-shift, and z is the position of the sample. The equations (1, 2) were primarily used to fit the experimental data. The extracted NLO parameters were retrieved from the theoretical fits and the remaining fundamental NLO parameters were subsequently estimated.

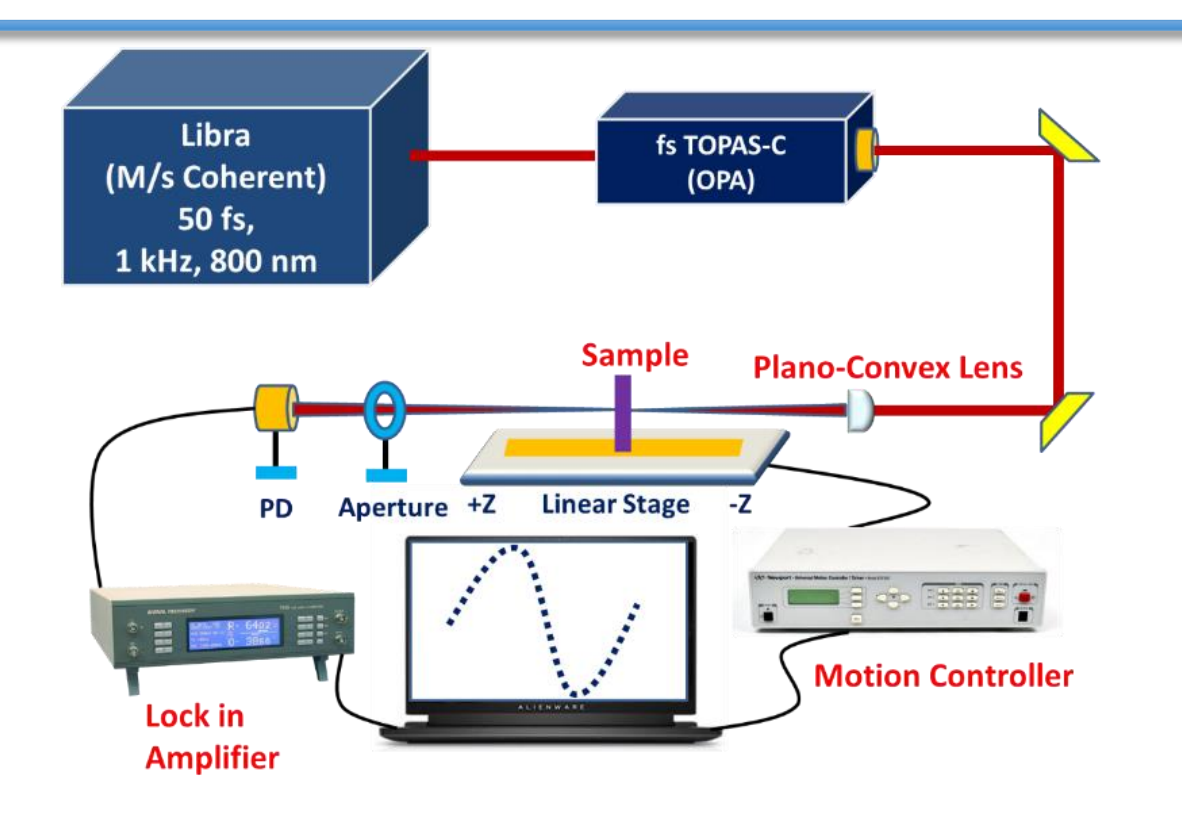


Fig. 2. 13 Femtosecond Z-scan experimental schematic.

## **References:**

(1) Gao, L. & Yan, Q. Recent Advances in Lead Halide Perovskites for Radiation Detectors **2020**, *4*, 1900210.

- (2) Cho, N. *et al.* Pure crystal orientation and anisotropic charge transport in large-area hybrid perovskite films. *Nature Communications* **2016**, **7**, 13407,
- (3) Wu, Y. *et al.* Zero-dimensional Cs<sub>4</sub>EuX<sub>6</sub> (X = Br, I) all-inorganic perovskite single crystals for gamma-ray spectroscopy. *Journal of Materials Chemistry C* **2018**, 6, 6647-6655.
- (4) Dong, Q. Electron-Hole Diffusion Lengths > 175 μ m in Solution-Grown CH 3 NH 3 PbI 3 Single Crystals. Science 2015, 347, 967–970.
- (5) Lian Z.; Yan, Q.; Gao, T.; Ding, J.; Lv, Q.; Ning, C.; Li, Q.; Sun, J.L. Perovskite CH<sub>3</sub>NH<sub>3</sub>PbI<sub>3</sub>(Cl) Single Crystals: Rapid Solution Growth, Unparalleled Crystalline Quality, and Low Trap Density toward 10(8) cm(-3). *Journal of the American Chemical Society* **2016**, *138*, 9409-9412.
- (6) Khanama SJ, Srinivasa Rao Kondab, Azmeera Premalatha, Ravi Ketavath, Wufeng Fu, Wei Lib, and Murali, B. Additive Engineering in CH<sub>3</sub>NH<sub>3</sub>PbBr<sub>3</sub> Single Crystals for Terahertz Devices and Tunable High Order Harmonics" *Journal of Materials Chemistry C* **2023**,1-16.
- (7) Saidaminov, M. I.; Abdelhady, A. L.; Murali, B.; Alarousu, E.; Burlakov, V. M.; Peng, W.; Dursun, I.; Wang, L.; He, Y.; Maculan, G.; Goriely, A.; Wu, T.; Mohammed, O. F.; Bakr, O. M. High-Quality Bulk Hybrid Perovskite Single Crystals within Minutes by Inverse Temperature Crystallization. Nature Communications **2015**, *6*, 7586.

(8) Khanama SJ, Srinivasa Rao Kondab, Wei Li, and Banavoth Muralia, The Aromatic Additives Boost the Mixed Halide Perovskite Single Crystal's Terahertz Properties.

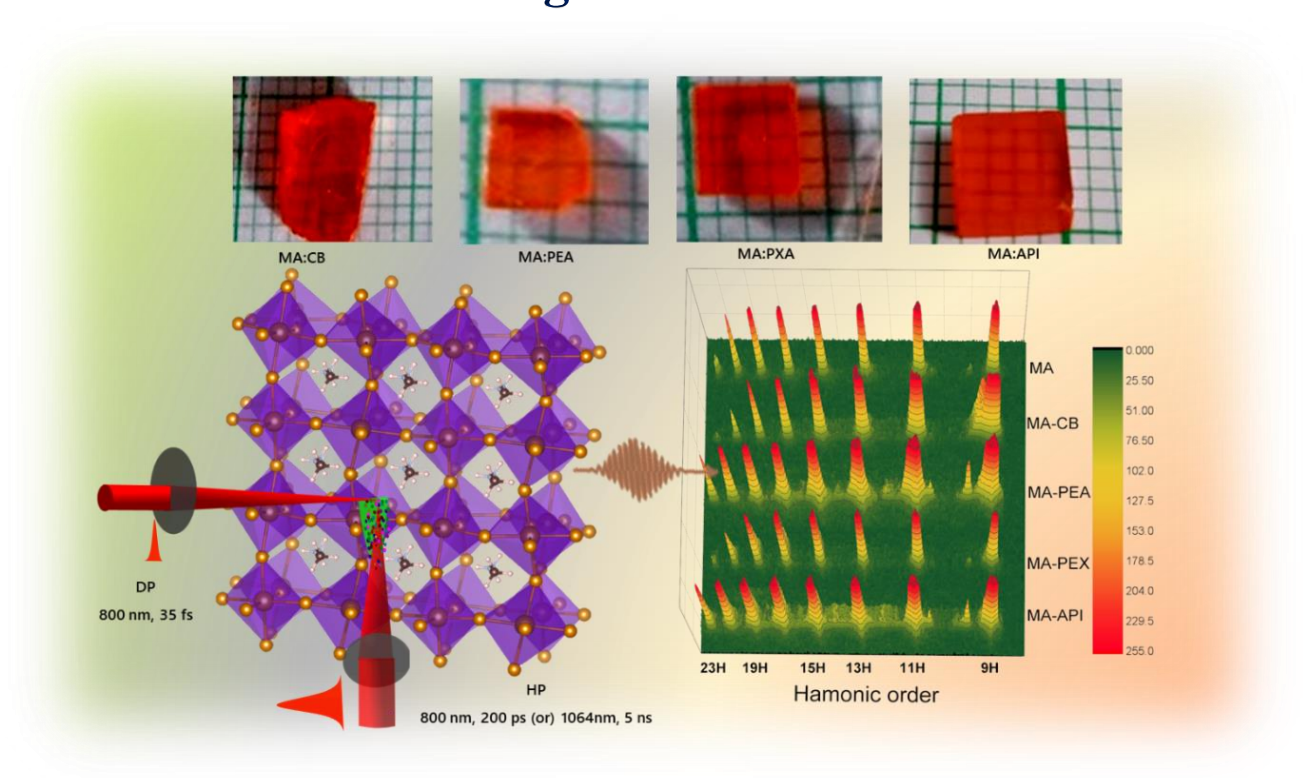
\*Journal of Materials Chemistry 2023.\*

- (9) Khanam SJ, Banerjee D, Soma VR, Murali B (2023) Stability enhancement and pronounced three-photon absorption in SrCl<sub>2</sub>-doped FAPbBr<sub>3</sub> nano crystals. *Journal of Materials Chemistry* **2019**, 11, 3275–3283.
- (10) Wangyang, P. et al. Recent Advances in Halide Perovskite Photodetectors Based on Different Dimensional Materials. *Advanced optical materials* **2018**, 6, 1701302.
- (11) Khanam SJ, Parikh N, Satapathi S, Khanam, Sarvani Jowhar, Parikh, Nishi, Satapathi, Soumitra, Kalam, Abul, Banavoth, Murali, Yadav, Pankaj (2022) Role of Heterocyclic Organic Compounds on the Optoelectronic Properties of Halide Perovskite Single Crystals. *ACS Applied Energy Materials* **2019**, 5,14732–14738.

# **CHAPTER-3** Additive Engineering in

# CH<sub>3</sub>NH<sub>3</sub>PbBr<sub>3</sub> Single Crystals for Terahertz Devices

# and Tunable High Order Harmonics



Sarvani Jowhar Khanam<sup>a</sup>, Srinivasa Rao Konda<sup>b,#</sup>, Azmeera Premalatha <sup>a</sup>, Ravi Ketavath <sup>a</sup>, Wufeng Fu <sup>b</sup>, Wei Li<sup>b,†</sup>, and Banavoth Murali <sup>a,\*</sup>

corresponding authors: \*murali.banavoth@uohyd.ac.in, # ksrao@ciomp.ac.cn,

<sup>&</sup>lt;sup>a</sup> Solar Cells and Photonics Research Laboratory, School of Chemistry, University of Hyderabad, Hyderabad 500046, Telangana, India

<sup>&</sup>lt;sup>b</sup> The GPL Photonics Laboratory, State Key Laboratory of Luminescence and Applications, Changchun Institute of Optics, Fine Mechanics and Physics, Chinese Academy of Sciences, Changchun, 130033, China

†weili1@ciomp.ac.cn

# **ABSTRACT**

Albeit the organic-inorganic hybrid perovskites are considered frontline candidates owing to their intriguing optoelectronic properties, the unstable surfaces prone to degradation significantly affect the device performances and hence circumscribe the commercialization. Additive engineering has become the most effective strategy to improve the quality of 3D perovskite single crystal (PSC). Herein the additive engineering resulting in high-quality transparent methylammonium lead bromide (MAPbBr<sub>3</sub>) PSCs by employing various aliphatic, aromatic, and chiral ammonium salts are demonstrated for the terahertz (THz) device applications besides sources for the higher-order harmonics generation (HHG). Remarkably the engineered crystal surfaces showed resistance to surface degradation compared to pristine ones, thereby enhancing the transmission/reflection of THz pulses. Moreover, a noticeable blue shift in the harmonics (both nano second-ns and pico second-ps Laser induced plasmas-LIPs) has been achieved compared to pristine MAPbBr<sub>3</sub> (MA). The current research is anticipated to open new sources of additive-based SCs used entirely for THz devices and tunable high-order harmonic generation avenues. Exploring the inanimate materials via the additive inclusion in MA SCs opens new avenues to achieve the blue-shifted UV spectra for diverse applications in attosecond physics and nonlinear spectroscopy, including tunable THz devices because of easy tunability of THz absorption property, i.e., their phonon modes in an OIHPSCs.

## 3.1. Introduction

Perovskite materials have acquired much interest in optoelectronics research, e.g., photovoltaics, <sup>1-5</sup> light-emitting diodes (LEDs), <sup>6-10</sup> memristors, <sup>11</sup> laser <sup>12,13</sup> luminescent solar concentrators, 14 and detectors, 3,15-22 owing to their promising optoelectronic properties and practical processability.<sup>23–28</sup> The tuneable bandgap from 1.48–1.62 eV makes the organicinorganic hybrid perovskites (OIHPs) alluring semiconductors suitable for photovoltaic application and > 2.23 eV for Higher Energy Radiation Detection (HERD), respectively. <sup>20,21,29,30</sup> Notably, surface quality is paramount to the efficacies of numerous device applications. The surface quality, crystallinity, and morphology of single crystals mainly depend on the PSC growth techniques,<sup>31</sup> including solvents,<sup>32</sup> the concentration/composition of the precursors, <sup>33,34</sup> annealing temperature, <sup>31,32,34,35</sup> and time duration for crystal growth. <sup>35</sup> So far, various crystallization techniques have been reported, including the inverse temperature method (ITC),<sup>36</sup> temperature lowering method,<sup>37</sup> and anti-solvent vapour assisted method (AVC). 38,39 A comprehensive comparison of PSCs and their application in literature is presented in the Appendix I Table 3.1. Nevertheless, the marginal PSCs performance and stability issues, such as surface degradation<sup>40,41</sup> and hysteresis <sup>42–44</sup> are the pressing challenges for commercialization.

The additive engineering method is one of the versatile approaches to growing more stable, high-quality PSCs, which is explored further in the case of 2D and quasi-2D perovskite materials synthesis. <sup>16,29,45–49</sup> Fu *et al.* studied second harmonic generation circular dichroism (SHG-CD) in one dimensional (1D) [(R/S)-3-aminopiperidine]PbI<sub>4</sub>. <sup>50</sup> On the other hand,

terahertz (THz)-wave absorption properties in a mixed phase of 3D FAPbI<sub>3</sub> with theoretically performed (ab initio) calculations was demonstrated by Maeng et al. 51 Herein, the current work aimed to study the changes in THz and HHG properties by changing the additives in 3D MA SCs grown using the additive engineering method (Appendix I **Table 1**). Therefore, we have taken different ammonium salts as an additive (A) to investigate their role in preventing PSCs degradation. We used the ammonium salts of aliphatic: Choline bromide (CB), aromatic: Phenylethylamine hydrochloride (PEA), P-Xylylenediamine (PXA), and heterocyclic: (R)3-Aminopiperidine dihydrochloride (API) as an additive, and respective crystals labelled as MA:A (A=CB, PEA, PXA, API), images of crystals obtained are presented in Fig. 1(a)-(e). The pragmatic role of the additive's interaction on morphological, optical and surface properties of 3D PSCs is obscured and yet to be explored for THz and high-order harmonic generation (HHG) application. Herein, our work focused on designing the stable 3D MAPbBr<sub>3</sub> (MA) PSCs using the additive engineering method as reported elsewhere in the literature for 2D materials 16,29,45-49 and the structure-property-performance correlations between the pristine (MA) and modified PSCs. Furthermore, as a way towards advanced characterizations, HHG of these PSCs from their laser-induced plasmas(LIPs) using 800 nm and 35 fs as driving pulses (DP) and heating pulses (HP) of 800 nm, 200 ps and 1064 nm, 6 ns. Recently, we have demonstrated the higher-order harmonics from LIPs of Ni-doped CsPbBr<sub>3</sub> 2D nanocrystals having average size distribution of 20 nm using different DP and LIPs created by the same HP and explained how the Ni-dopants play a crucial role in enhancing harmonics and cut-off. 52,53 Generally, the blueshift of harmonics could be achieved for a particular DP with negative chirps. 53-56

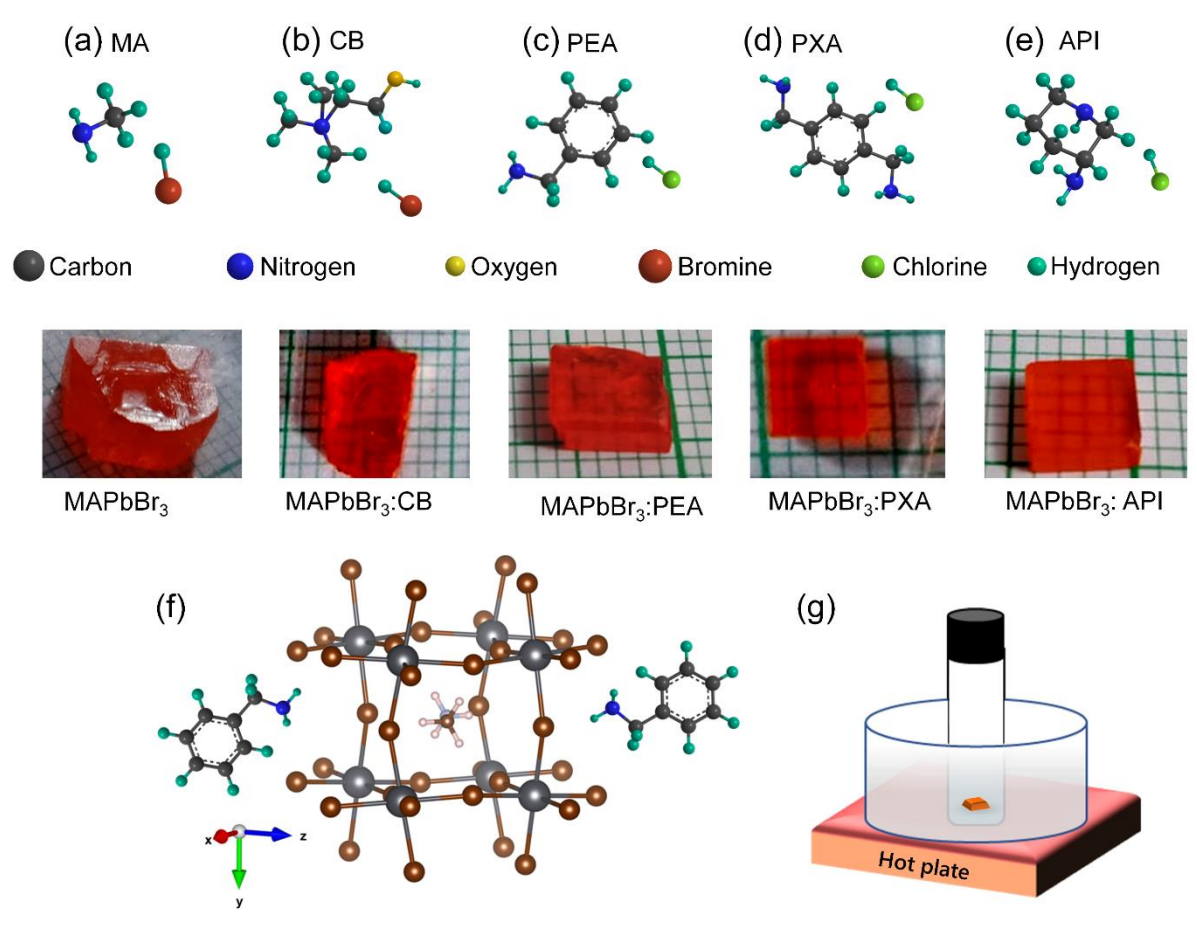


Fig. 3. 1(a-e) Structure of additives used and photographs of the PSCs with labels on the bottom. (f) A possible model for additive coordination with unit cell while crystal growth process in solution, (g) ITC method used for crystal growth.

Interestingly, in the current scenario, the blueshift of harmonics is obtained due to the additive's influence on MA SCs. <sup>57–60</sup> Experimental layout for THz-time-domain spectroscopy (THz-TDS) and HHG generation from LIPs of reported PSCs shown in **Appendix I Fig. 1(a)** and (b). A detailed description of both setups is given in the SI.

## 3.2. Results and Discussion

# 3.2.1. Morphology and Structural Properties Properties

One of the significant challenges associated with the surface sensitivity of these PSCs to high levels of relative humidity (RH ≥ 55%) as the surface transforms and becomes disordered due to hydration, masking its actual properties. Recent reports have revealed from SEM images that exposure to humidity for several days results in surface degradation of thin films.<sup>61</sup> However, for PSCs, it has been found that their surface properties differ from bulk properties, including morphology, absorption coefficients, carrier mobility, photocurrent, carrier dynamics and optical bandgap. Such effects have been marginally exploited in PSCs with changing additives; therefore, the surface recombination losses, which play a decisive role in determining the intrinsic optoelectronic properties, must be fully understood. While MABr is hygroscopic salt, in ambient conditions, it absorbs moisture and converts to MA by leaving the PbBr<sub>2</sub> crystal surface or vacant surface. Typically, PbBr<sub>2</sub> PbBr<sub>2</sub>-rich textures with pinholes and the construction of hydrate phases are formed. The N-based additives interact differently with the facet and have higher stability than their MABr counterparts. Hence, surface degradation of modified and pristine PSC to the environment has been studied using SEM measurements when exposed to ambient air. Confocal and SEM micrographs were recorded on the surface of fresh PSCs (Appendix I Fig. 3(a)-(j)).

Furthermore, to study the change in morphology and pinholes after exposure to ambient conditions for three and seven days, SEM images were collected (Appendix I Fig. 4(a)-(j)). The lower surface roughness has been observed for additive-based PSCs than pristine MA; this

implies that additives act as adequate passivating layers on the crystal surface. The chemical reaction on the surface of the crystal is shown below in Equation. (1)

The attachment energy (AE) model developed by Hartman and Bennema helps predict how additives interact with the surface of the growing facet and SCs shape.<sup>62,63</sup> AE of a facet is the release of energy when layers of atoms are attached to the growing PSC surface; this energy depends on the bonding strength and number of bonds at a given facet. A possible mechanism for the additive engineering method can be explained using a model in **Fig. 1(f)**: where the positively charged ammonium group coordinates with Br<sup>-</sup> ions on the growing facet surface (with electrostatic interactions). Consecutively blocks the incoming CH<sub>3</sub>NH<sub>3</sub><sup>+</sup> (methyl ammonium ion) or Pb<sup>2+</sup> and maintains the same AE all over the growing facet (**Fig. 1(f)**).

Herein, the strength of interaction between the ammonium ion and facet decides the outcome quality of the crystal, which depends on the number of hydrogen bonds and electron density around the ammonium ion. The previous reports concluded that heterocyclic amine could effectively coordinate with a growing facet of the crystal, resulting in lower defects and enhancing crystallinity without altering the unit cell structure. In **Table. 3.1**, we have demonstrated the possible number of active groups with elements and the number of H bonds among all additives. API additive can coordinate more effectively among all additives owing to more electron density groups around the N atom (+I inductive groups are present) and can form 5 H-bonds more effectively with less steric hindrance. The cuboid, transparent modified PSCs with lower roughness were obtained without any polishing to improve the crystal surface

quality (**Fig. 1(a)-(e)**).<sup>68,69</sup> Interestingly, we observed enhanced optical and THz transmission properties, elaborated on in subsequent experimental results.

**Table 3.1.** The active groups and H bonds are possible in the additives.

Additive	Number of active groups (elements)	Possible number of H bonds
СВ	2, (3° N, O)	3
PEA	1, (1° N)	3
PXA	2, (1° N)	6
API	2, (2° N, 1° N)	5

<sup>\*</sup>Primary (1°), secondary (2°) and tertiary (3°) amines.

Furthermore, to study the hydrate phase traces and chemical state behaviour on PSCs surface, XPS studies have been conducted. Interestingly, a single peak has been observed in C 1s and N1s core-level bonding state chemical behaviour of MA-API SCs, indicating no new chemical state (**Fig. 2a,b**). On the other hand, more intense molecular defect peaks were seen in MA-PXA SCs. A striking shift towards higher energy has been observed in modified PSCs Pb 4*f* core-level spectrum, as shown in **Fig. 2c**, attributing to increased binding energy and decreased halide vacancies. <sup>70–72</sup> Additionally, we confirmed the H bond strength difference among the additives depending on the chemical state shift seen for the Br 3*d* core-level spectra compared to the pristine crystal; this might be due to a decrease in the electron cloud around

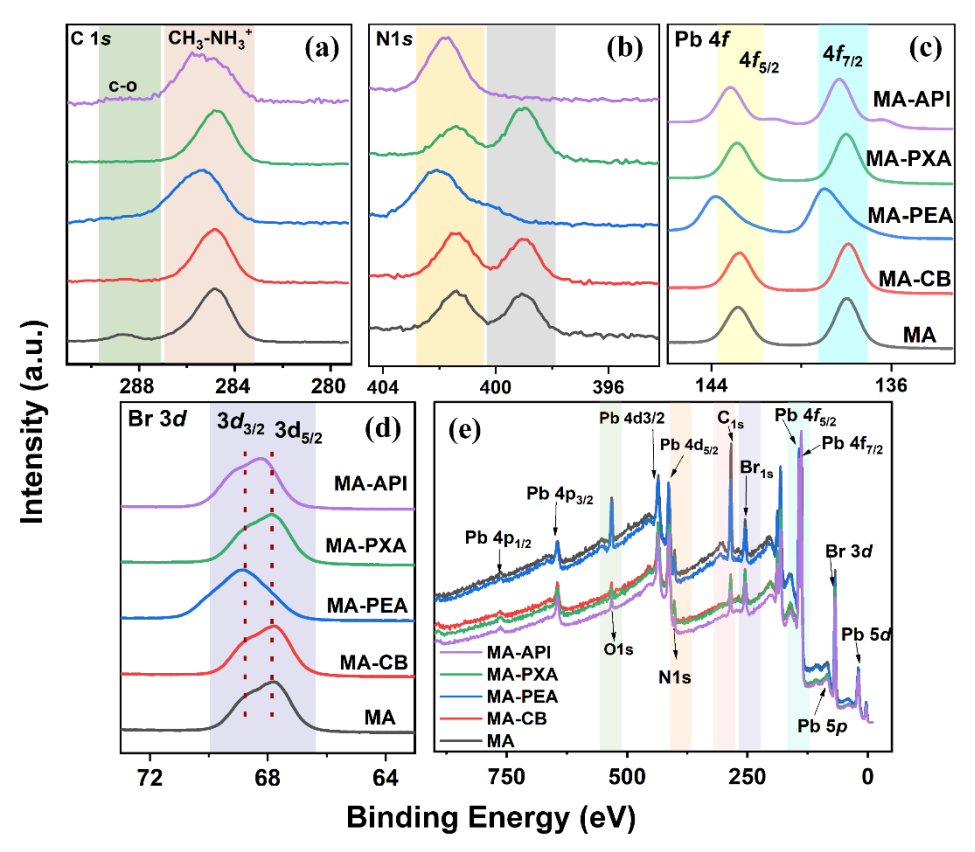


Fig. 3. 2(a-d) XPS data of C 1s, N 1s, Pb 4f, and Br 3d core-level spectra with molecular level defect and chemical states behaviour in MAPbBr<sub>3</sub>

SCs with changing additives (labels are mentioned at the right side, follows the same order (a-d)). (e) XPS survey spectra.

the halide ion. Subsequently, oxygen levels in modified crystals were minimal, indicating the passivating nature of additives and the presence of the hydrate phase on the crystal surface, which shows the main component around 532 eV corresponding to the O–H, as discussed above.<sup>73</sup> It is to be noted that an increase in oxygen concentration is linked with the breakdown of MABr to CH<sub>3</sub>NH<sub>2</sub> and HX, which destroys the perovskite structure by incorporating deeper into PSCs, which is consistent with long-term exposed PSCs SEM images.<sup>73</sup> Detailed XPS analysis of these modified PSCs indicated that the additive engineering method allows the

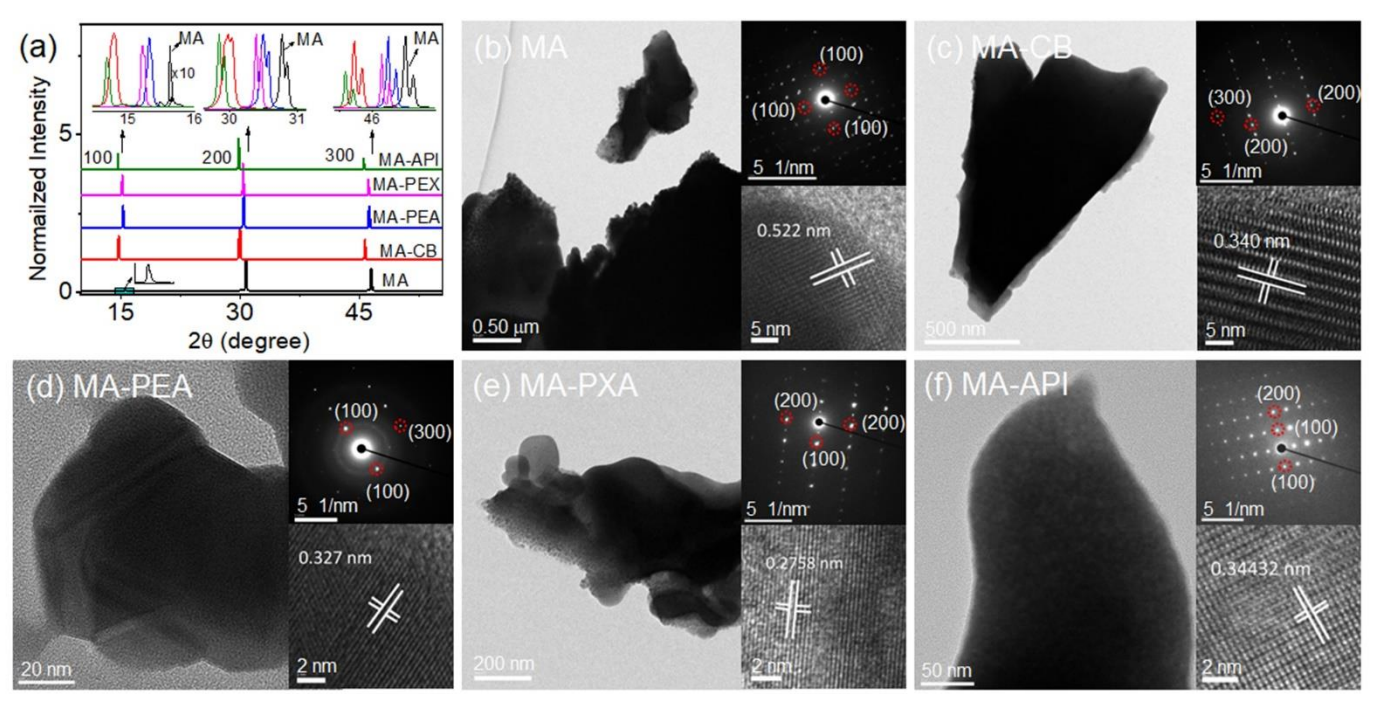


Fig. 3. 3(a) XRD pattern of a typical MAPbBr<sub>3</sub> SC grown by additive-based ITC technique. (b-f) TEM images of pristine and modified PSCs.

formation of fewer molecular defects. Among all the modified PSCs surface, it is evident that; CB, PEA and API effectively passivated the surface and decreased the trap density, which is consistent with SCLC measurement values. We conducted powder XRD to determine whether additives were incorporated deeper into the lattice crystal lattice. Interestingly, no additional peak has been observed relating to additives (**Fig. 3(a)**). Instead, increased peak intensities and a slight shift in the diffraction peaks to lower angles in modified PSCs were observed (from  $15.621^{\circ}$  to  $14.688^{\circ}$  for API-MA crystal) with increased peak intensity. This might be attributed to replacing some Br<sup>-</sup> with Cl<sup>-</sup> ions and non-preferential crystal growth in all directions with higher crystallinity. The peaks at  $2\theta = 15.62^{\circ}$ ,  $30.77^{\circ}$ ,  $46.62^{\circ}$  correspond to the miller indices of (100), (200), and (300) of the MA PSCs, matching with the previously reported data.  $^{38.75-78}$  Notably, the negative strain values in the case of MA-API SCs indicate lower ionic vacancies and compositional uniformity. Further, the single crystal X-ray diffraction (SC-XRD) data

for MA and modified PSCs were collected at 25 °C. Subsequently, data processing and indexing were automated within the CrysAlis Pro software, and these results are in convergence to a cubic cell for MA SCs refined in the cubic space group Pm–3m similar to that reported by Baikie *et al.*<sup>79</sup> However, no change in unit-cell was observed by changing the additives, which may be indicative that additives act as the passivating layer on a surface without disturbing the unit-cell structure (**Appendix I Table. 5**).

Subsequently, higher-resolution transmission electron microscopy (HR-TEM) of PSCs has been performed to study changes in SAED pattern with changing additives (**Fig. 3(b)-(f)**). The HR-TEM image of MA provides the lattice fringes at ~ 0.522 nm, related to the (200) planes of the cubic structure, close to the calculated value from powder XRD using the Bragg diffraction equation. SAED result for pure SCs complies with reported data. 80–82 The TEM images of pristine and modified PSCs have been collected from various spots on the grid (as samples were very sensitive to incoming electrons).

# 3.2.2 Optical properties

Steady-state absorption spectra of crystals were collected from the diffuse reflectance mode (DR). The bandgap (E<sub>g</sub>) of MA, MA-CB, MA-PEA, MA-PXA, and MA-API have been calculated from Tauc plots (**Fig. 4(a)**), (E<sub>g</sub>) values are 2.174, 2.125, 2.133, 2.129, and 2.130 eV, respectively. As discussed for XPS data, a decrease in halide vacancy and incorporation of

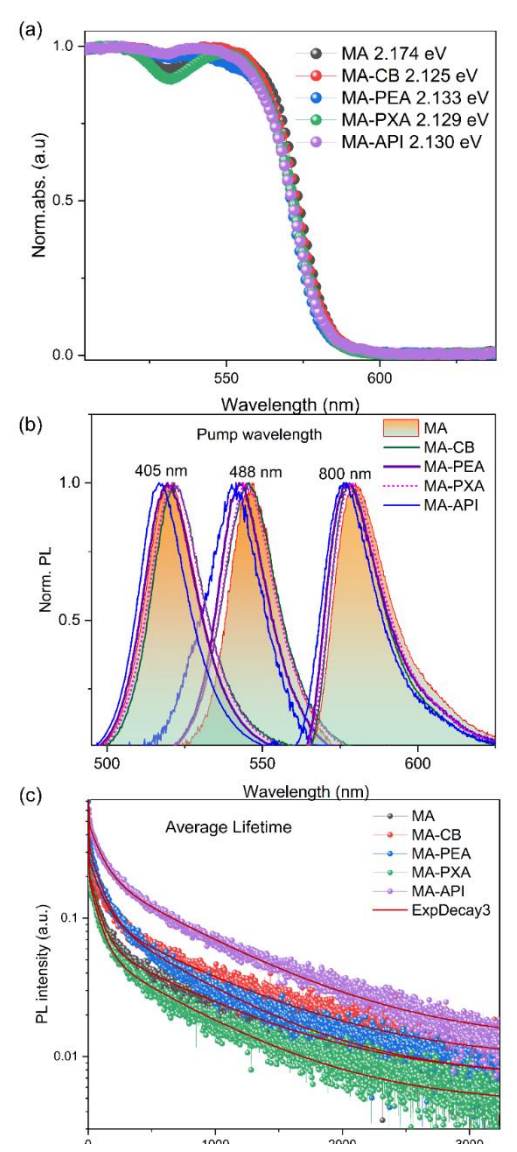


Fig. 3. 4(a) UV-visible spectra, (b) photoluminescence spectra with 1PA and 2PA photoexcitation and (c) average lifetime of MAPbBr<sub>3</sub> SCs with changing additives.

Cl is expected to increase the bandgap of modified crystals. In this work, the bandgap values for MA SCs are similar to the earlier work reported in the literature.<sup>28,32</sup>

The photoluminescence spectra (PL) have been recorded using 405, 488 and 800 lasers; interestingly, the peaks shifted towards a high wavelength (from 520 nm to 579 nm for MA) observed. Single photon absorption (1PA) [at 488 nm and 405 nm] and two-photon absorption (2PA) (at 800 nm) were used to photoexcite the surface and bulk PSCs to record the photoemission spectra. The appropriate reason for a shift in PL peak position with 2PA in comparison to 1PA could be due to the following factors; a) the reabsorption of bulk emission by the thick PSC on route to the detector resulting in the absorption of the high energy region of the emission spectrum, which is minimal. 83,84 b) The band shift from the bulk to the surface. A blue shift in steady-state PL spectra for modified crystals in the case of 1PA indicates fewer ionic vacancies (causing trap states), as discussed in XPS data. The PL values for pristine PSC agree well with reported crystals grown by ITC and AVC methods (Fig. 4(b)). 32,86-88 Modified

**Table 3.2.** Comparative study of PSCs fitted parameters for the TRPL decay profiles,  $V_{TFL}$  and  $\eta_{traps}$ 

PSCs	τ <sub>1</sub>	τ <sub>2</sub>	τ <sub>3</sub>	τ	V <sub>TFL</sub>	$\eta_{traps}$
	(ns)	(ns)	(ns)	(ns)	(V)	(× 10 <sup>10</sup> cm <sup>-3</sup> )
MA	2.48	80.11	857.37	2.48	1.67	5.24
MA-CB	2.47	101.08	864. 96	2.14	1.64	5.16
MA-PEA	2.88	87.58	684.78	2.89	1.61	5.07
MA-PXA	2.41	81.35	765.30	2.41	1.66	5.20

PSCs showed a slight change in optical properties confirmed from steady-state PL. Transient evolution of the electron-hole population after impulsive photoexcitation can be calculated from time-resolved PL (TRPL) measurements (Fig. 4(c)). Subsequently, the decay curves of the excited carrier in the modified PSCs are fitted using a tri-exponential decay model to quantify the carrier dynamics, and the fitted parameters are summarized in **Table. 3.2.** The relatively faster decay components ( $\tau_1$  and  $\tau_2$ ) are attributed to charge carrier trapping defect states, while the slower decay components  $(\tau_2)$  are assigned to bimolecular radiative recombination in the bulk crystals. In proportion to the fast decay component  $(\tau_1)$  observed, a slower trapping time constant (2.88 ns for MA-PEA and 3.79 ns for M-API) compared to that of the pristine PSCs (2.48 ns), which is indicative of a reduced defect density. Furthermore, the  $\tau_3$  value enhanced from 857.37 ns (pristine) to 949.01 ns (MA-API), suggesting that the additives elongate charge carrier lifetimes within the bulk crystal. As a result, the average PL lifetime significantly enhanced from 2.48 ns to 6.25 ns (MA-API) (**Fig. 4(c**)). <sup>89,90</sup> To unveil the difference in electronic properties with additives in-gap deep electronic trap states measured using the current-voltage (I-V) response of the PSCs in the space-charge limited current (SCLC) regime for all PSCs(Appendix I Fig. 5(a)-(e)). The SCLC values obtained for MA and MA- API SCs has shown in Fig. 5(a) and (b). At low voltages, the I-V response was ohmic (i.e., linear), as confirmed by the fit to an  $I \approx V$  (n =1). At intermediate voltages, the current exhibited a rapid nonlinear rise. It signalled the transition onto the trap-filled limit (TFL)—a regime in which the injected carriers filled all the available trap states and were linearly proportional to the density of trap states ( $\eta_{trap}$ ). Correspondingly, we found remarkably low  $\eta_{\text{traps}}$  for modified PSCs (MA-API  $\eta_{\text{traps}} = 4.79 \times 10^{10} \text{ cm}^{-3}$ ) together with the extremely clean absorption and PL profiles points to a nearly defect-free electronic structure. The lower defect

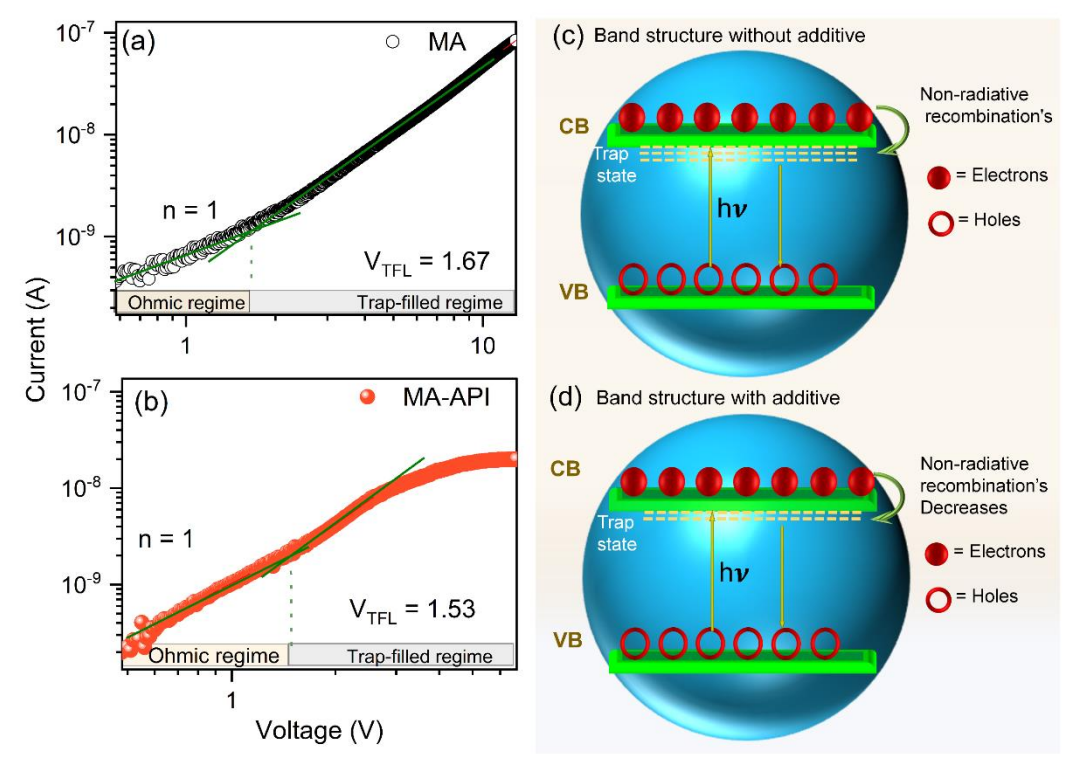


Fig. 3. 5 Current-voltage traces and trap density. Characteristic I-V trace (Green markers) showing different regimes (at 300 K). A linear ohmic regime is followed by the trap-filled regime, marked by a steep increase in current. (c-d) The electronic band structure model in pristine and modified PSCs represents decreasing surface defects by adding additives schematically.

density might be the origin of the reduced charge carrier trapping. The obtained  $V_{TFL}$  for all the samples (**Appendix I Fig. 5(a)-(e)**) with  $\eta_{trap}$  parameters are summarized in **Table. 3.2.** This result suggests a more significant trap-induced recombination rate in the MA, which has a much higher trap density than the MA-API SCs, explained using a model (**Fig. 5(c) and (d)**). <sup>90</sup> A focused explanation of the change in photodetection properties with additives has been explained in our recently published work. <sup>91,92</sup>

#### 3.2.3. THz spectroscopy

THz spectroscopy is well-explored in various scientific research fields. 93-98 The transmission and reflection of the reported PSCs were performed using THz-TDS, one of the well-known methods to ascertain the material response in the far-infrared (IR) to near microwaves region (THz region).

We have measured PSC's transmittance, reflectance, and absorption coefficients (at positioned normal incidence to THz pulses, referred to as T  $(@0^\circ)$ ). From the THz temporal profiles (electric field), one can obtain the real and imaginary refractive indices (n,k) and absorption coefficient using the **Equations**. (3.1-3.4) provided below. The complex FFT transmission data of the sample is compared to that of the reference given by

$$\frac{\psi_S}{\psi_{ref}} = \rho(\omega)e^{-i\phi(\omega)} \tag{3.2}$$

Where  $\psi_S$  and  $\psi_{ref}$  is the complex FFT of the sample (single crystals) and reference THz pulse, and  $\phi(\omega)$  is the phase difference (phase samp- phase ref), and  $\rho(\omega)$  is the ratio of peak amplitudes of single crystal and reference pulses (transmittance). The real part of the refractive index  $(n_S)$  and imaginary part of the refractive index  $(k_S)$  can be written in terms of  $\phi(\omega)$  and  $\rho(\omega)$  as follows  $^{99,100}$ 

$$n_S(\omega) = 1 + \frac{c_o}{\omega d} \phi(\omega) \tag{3.3}$$

$$k_{S}(\omega) = \frac{c_{o}}{\omega d} \ln \left( \frac{4 n_{S}(\omega)}{\rho(\omega)(n_{S}(\omega)+1)^{2}} \right)$$
(3.4)

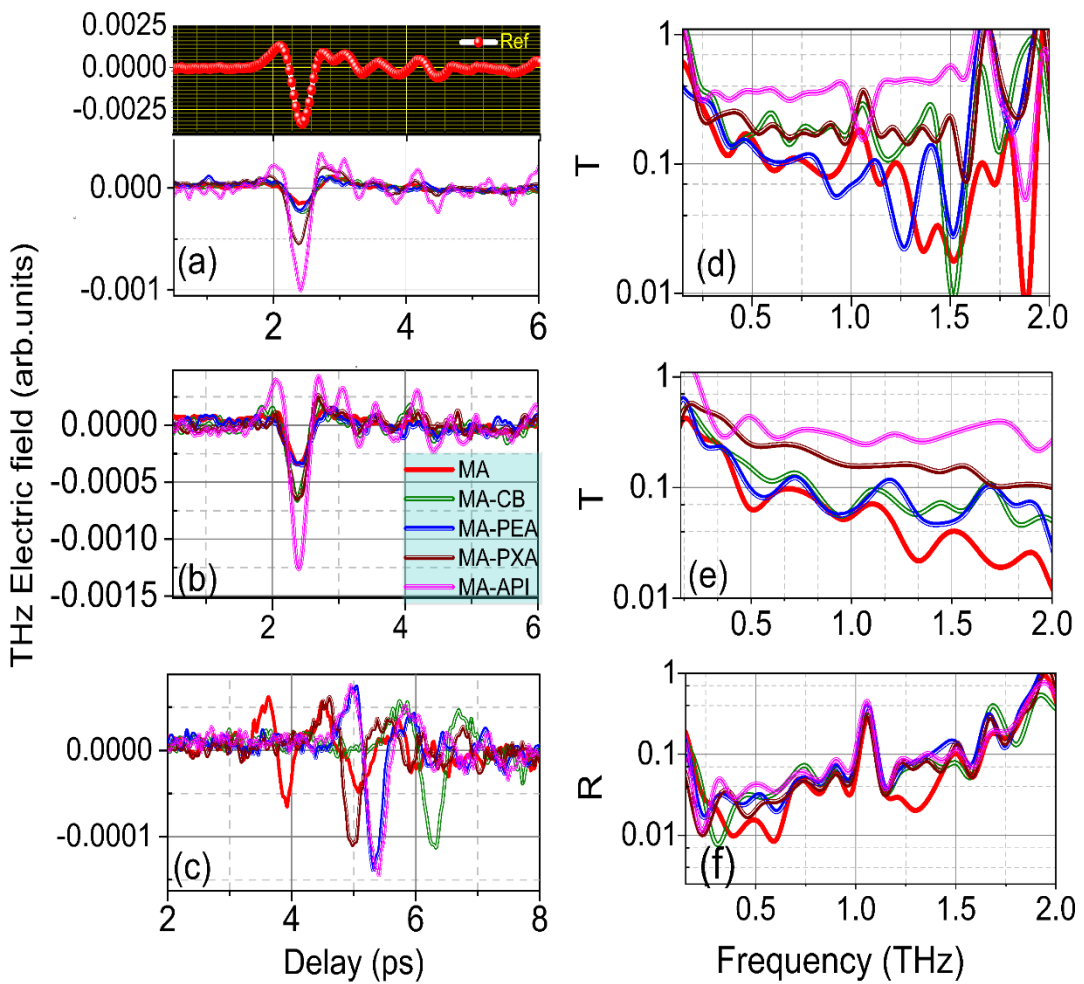


Fig. 3. 6(a-c) THz electric field (temporal profile) and (d-f) measured transmittance (T) @0°, T@45° and reflectance (R) @45°, respectively. The legend is shown in (b) applicable to all panels; Black: solid line, Red:solid line, Green: double line, Blue: thick-thin line, Wine: thin-thick line, and Magenta: triple lines are corresponding to reference pulse, for SCs MA, MA-

Where  $c_0$  is the speed of light and d is the single crystal thickness. From the imaginary part of the refractive index, one can determine the absorption coefficient  $\alpha$  (cm<sup>-1</sup>) as

CB, MA-PEA, MA-PXA.and MA-API.

$$\alpha(\omega) = \frac{2}{d} \ln \frac{4 \, n_{\mathcal{S}}(\omega)}{\rho(\omega) (n_{\mathcal{S}}(\omega) + 1)^2} \tag{3.5}$$

To measure the transmittance/ reflectance,  $n_s$ ,  $k_s$ , and  $\alpha$ ; amplitude and phase of reference pulse and transmitted/reflected THz from PSCs are important parameters. Therefore, we have converted the THz electric field into a frequency domain using Fast Fourier Transform (FFT). In addition to amplitude and phase, we have shown the frequency in dB for three measurements, i.e.,  $T@0^\circ$ ,  $T@45^\circ$  and  $R@45^\circ$  in **Appendix I Fig. 6(a)-(c)**, respectively.

The ratios of amplitudes of reference and samples for three measurements are shown in Fig. 6(d)-(e). Either from amplitudes (Appendix I Fig. 6 (a)) or frequency spectra in dB (Fig. Appendix I Fig. 6(c)), or the transmittance/reflectance (Fig. 4(d)-(e)), the modified PSCs showed enhancement in THz transmission/reflection than the pristine MA. Meanwhile, it is observed that this increment is not only bound to overall THz pulses; the modified SCs show a massive impact on the bandwidth (fullwidth half maximum (FWHM) for transmitted and reflected THz pulse from PSCs) and variations in the central frequencies of THz pulses. In this regard, we have fitted the THz amplitude data shown in **Appendix I Fig. 6 (d)** with Lorents fits to obtain the central frequency and FWHM of THz pulses (Fig.7(a)). Here, it can be identified that the tendency of central frequency and FWHM is increased from MA to MA-API PSCs. The presented results indicate that the transmittance and reflectance are increased for modified SCs and follow the order of MA<MA-CB<MA-PEA<MA-PXA<MA-API. Therefore, it is reasonable to establish that the minimum crystal defects with good surface quality enhanced the optical and structural properties in modified SCs. Further, this can be reflected in measured real and imaginary refractive indices shown in Fig.7(b). It is identified that  $n_s$  values are higher than the ks values ( $k_s$  related to the amount of absorption), which indicates that the samples possess an ordinary refractive index and have a small amount of absorption ( $k_s$  values are non-zero). If the  $k_s$  value is 0, the material is non-absorbing. However,

the studied PSCs. Crystals absorb considerably because the ks values are non-zero (**Fig.7(b**), bottom panel). Subsequently, we have measured absorption coefficient ( $\alpha$ ) using experimental THz-TDS data at T@0° using **Equation.** (5) as shown in **Fig. 7(c, left Y-axis)** and compared the phonon vibrations of reported PSCs <sup>99,100</sup> with theoretical IR absorption spectra of cubic MAPbBr<sub>3</sub>, earlier reported by Maeng *et al.*<sup>72</sup> shown in **Fig. 7(c, right Y-axis)**. The experimentally calculated absorption peak values of MA approximately match theoretically predicted values. <sup>72</sup> However, in the case of modified PSCs, the absorption amount is decreased, with a slight difference in the peak positions.

In organic-inorganic hybrid perovskite, the organic unit possesses molecular vibrations, leading to lattice vibrations due to a weak interaction between the organic and inorganic parts. Maeng *et al.*<sup>72</sup> demonstrated that the molecular defects do not influence the three major phonon modes originating from the transverse vibration (0.8 THz) and longitudinal optical vibrations (1.4 THz) of the Pb–Br–Pb bonds and the optical Br vibration (2.0 THz). However, in the present case, the modified PSCs showed slight variations in the optical and vibrational frequencies due to changes in their interplanar distances. The powder XRD measurements in the present study revealed that interplanar distance is increased slightly for modified SCs. Therefore, this might be a reason for decreasing optical/vibrational absorption in modified SCs compared to MA; the results are shown in Fig. 7(c). Interestingly, the MA-API shows more negligible THz absorption, with peak positions at 0.48, 0.96, and 1.56 THz. At 1.56 THz, the other crystals do not have any peak positions. The THz peak amplitude curve for MA-API (magenta: triple curve) is almost identical to the reference pulse (solid black line), having lower values, as shown in Fig. S6(a). Similarly, the absorption coefficients decreased for SCs grown in CB, PEA, and PXA additives. Overall, the THz measurements indicate that the modified

SCs possess higher transmission and reflection than pristine MA, which offers advantages to utilizing these PSCs for THz devices.

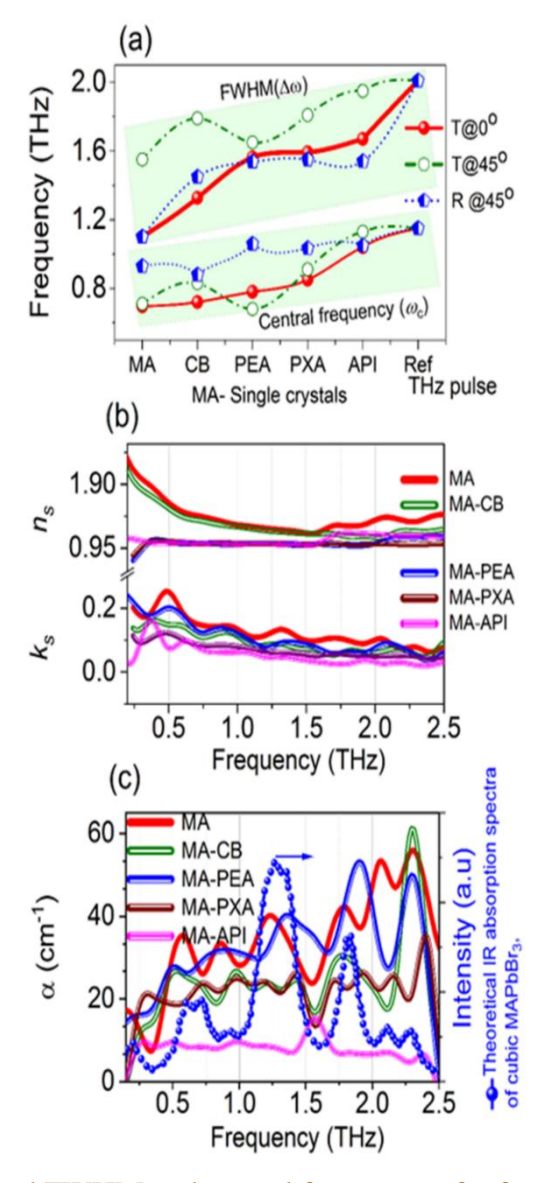


Fig. 3. 7(a) The measured FWHM and central frequency of reference THz pulse, transmitted and reflected THz pulses from SCs. (b) The measured real refractive index ( $n_s$ ), imaginary refractive index ( $k_s$ ) and (c) left Y-axis; absorption coefficients ( $\alpha$ ) of single crystals at transmittance (T) @  $0^{\circ}$ . (c) right Y-axis: theoretical IR absorption spectra of cubic MAPbBr<sub>3</sub> SC (data is adapted from the Ref [72]).

# 3.3. Application of PSCs toward the generation of higher-order

### harmonics generation

Currently, gases are frequently used as HHG medium sources <sup>101–103</sup>. The study on HHG experiments utilizing gases is rather limited because there are just a few different types of

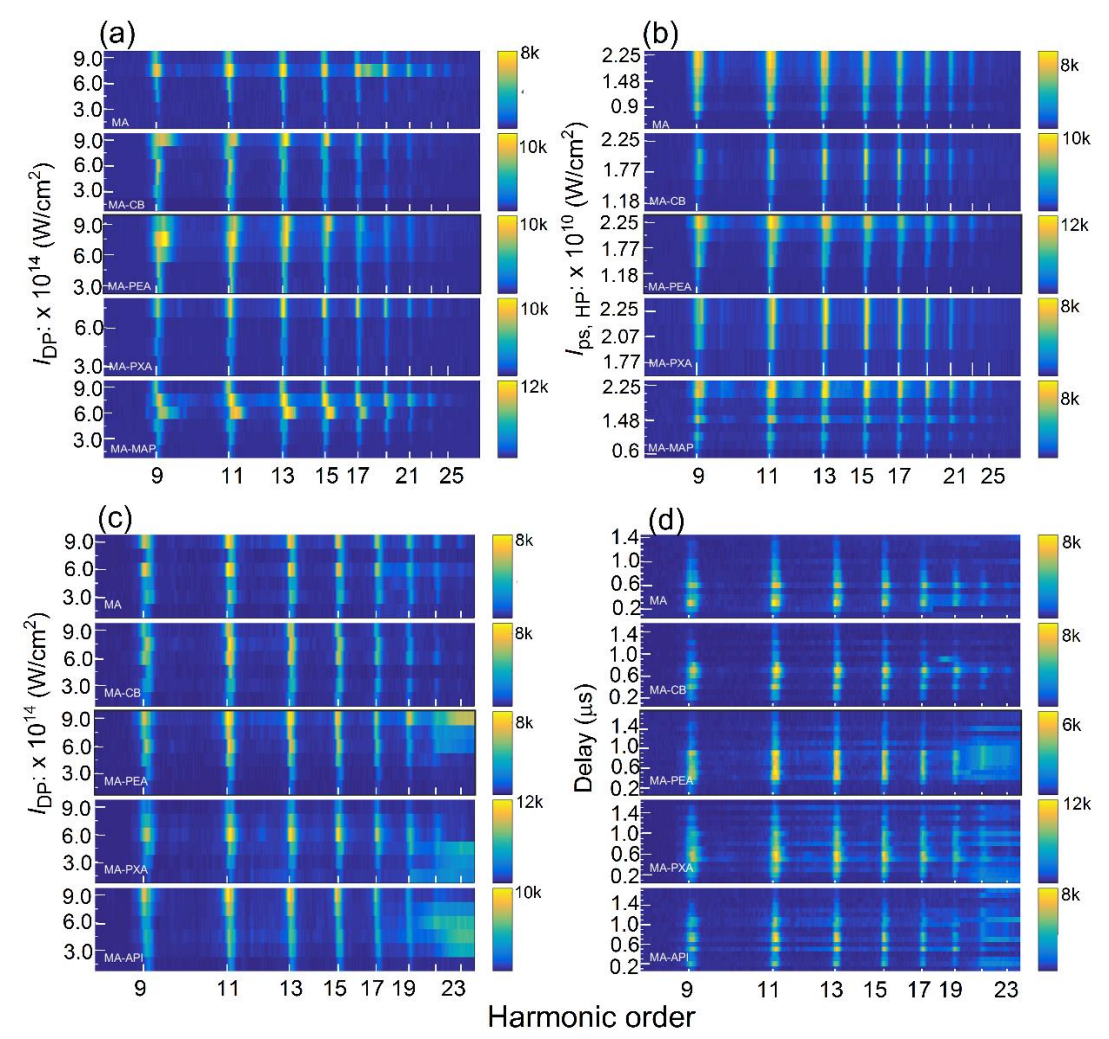


Fig. 3. 8 2D colour map of harmonics spectra for different (a, c) driving pulses

intensities( $I_{DP}$ ) for ps LIPs, at ps heating pulse intensities ( $I_{ps,HP}$ ) = 1.77 × 10<sup>10</sup> W/cm<sup>2</sup>) and ns LIPs ( $I_{ns,HP}$  = 7 × 10<sup>10</sup> W/cm<sup>2</sup>), respectively, (b) at fs driving pulse intensities ( $I_{DP}$ ) = 6.0 × 10<sup>14</sup> W/cm<sup>2</sup> w.r.to ps heating pulse intensities ( $I_{ps,HP}$ ). (d) the delay dependence between ns HP and fs DP.

elements in gas states in nature. Hence, several researchers focused on demonstrating HHG from various solid and liquid elements. 104,105 The laser intensity utilized in the experiment is constrained because of the solid's damage threshold. The photon energy resulting from this method is not particularly high. Recently, strong mid-infrared laser pulses demonstrated HHG from MAPbX3 (X = I, Br, Cl) thin films. 104,105 The near IR wavelength 800 nm is the current work-driving pulse, which possesses stronger energy than the mid-infrared pulses. Therefore, there might be a chance of strong ablation leading to damage to the bulk PSCs. Suppose if we choose the DP laser energy below the damage threshold of PSCs due to the illumination of strong photoluminescence, the DP, along with harmonics (if generated), will not transmit from almost ~1 mm thick SCs. Therefore, in the present experiment, we pay attention to the method of LIPs [produced by 800 nm (200 ps) and 1064 nm (5ns) wavelengths] to generate harmonics from five bulk PSCs for the first time. Additionally, substantial resonance enhancement can be used to increase harmonic conversion efficiency by utilizing the HHG from LIPs of various metals. 106,107 The impact of additives (CB, PEA, PXA, and API) on MA SCs were analyzed by measuring HHG spectra in terms of harmonics intensity, cut-off, and spectral shift. Initially, we describe the stability of crystals, then harmonic-cut-off and spectral shift in the following subsections.

### 3.3.1. Harmonics intensity to describe the stability of PSCs

In the case of ps LIPs, the 2D color map of harmonics spectra of PSCs for different DP intensities between 1.5 to  $9 \times 10^{14}$  W/cm<sup>2</sup> range (at fixed ps HP intensity  $1.77 \times 10^{10}$  W/cm<sup>2</sup>) shown in **Fig. 8(a)**, and with variation in ps HP intensities between 0.6 to  $2.25 \times 10^{10}$  W/cm<sup>2</sup> at fixed  $I_{DP} = 6 \times 10^{14}$  W/cm<sup>2</sup> presented in **Fig. 8(b)**, the corresponding maximum harmonic

signal for studied PSCs are shown in **Fig. 9 (a) and (b)**, respectively. With the increase of DP intensity, the modified SCs show a higher harmonic signal than the pristine MA. The additives PEA, PEX, and API required a minimum of  $3.0 \times 10^{14}$  W/cm<sup>2</sup> to obtain the harmonic spectra, whereas MA and MA-CB show the harmonic spectra even at  $1.5 \times 10^{14}$  W/cm<sup>2</sup>. From **Fig. 8(b)**, or **Fig. 9(b)**, it is observed that for MA SCs and MA-API, the harmonics emission obtained within the range of 0.6 to  $2.25 \times 10^{10}$  W/cm<sup>2</sup> range, whereas for MA-PEA, MA-CB, and MA-PEX, the harmonics emission imitated at 1.05, 1.18 and  $1.77 \times 10^{10}$  W/cm<sup>2</sup>, respectively. This confirms that adding additives to the MA increased the stability of PSCs, which required high intensity of ps pulses to create the plasma plumes. The maximum harmonic signal for additives PEA and API is slightly higher than MA, whereas for CB and PEX, the intensity of the harmonic signal is less than MA.

Likewise, ps LIPs harmonic spectra from SCs (**Fig. 8(a) and (b)**), the harmonic emission from modified crystals at fixed ns HP intensity  $7 \times 10^{10}$  W/cm<sup>2</sup> compared with pristine crystals for different  $I_{DP}$  is shown in **Fig.8(c)**, and the delay dependence harmonics spectra between ns HP and fs DP is denoted in **Fig. 8(d)**. The maximum harmonic signal obtained from these **Fig. 8(c)** and (d) HHG spectra were shown in **Fig. 9(c)** and (d). In the case of ns LIPs, the intensities of harmonics among the PSCs are almost close to each other with respect to the increase in the  $I_{DP}$  (at  $6.0 \times 10^{14}$  W/cm<sup>2</sup> MA-PEX possess high intensity among all). However, the advantages of ns HPs could be useful for measuring delay dependence harmonics spectra. The additive-based PSCs increased the emission of harmonics at longer delays, as shown in **Fig. 9(d)**. The cut-off delays were achieved at 1400, 1500, 1700, 1600, and 1700 ns for MA, MA-CB, MA-PEA, MA-PEX, and MA-API, respectively. Within these delay ranges, MA shows the first and second maxima of harmonics achieved at delays of 300 and 600 ns, respectively. At the same

time, the maxima are moved for modified PSCs. For MA-CB, MA-PEA, MA-PEX, and MA-API, the first maxima presented at 400, 500, 600, and 700 ns, and the second maxima were obtained at 700, 900, 1000 and 1100 ns, respectively. Subsequently, in the case of MA-PEX, an additional maximum is presented at 300 ns; for MA-API, the maxima are located at 200 ns and 500 ns. The periodicity of maximum harmonic signals indicates that the PSCs possess not only single components atoms or ions but the small- to large-sized clusters produced by ns HP and travel at different velocities. Overall, the studies of recording HHG spectra in the case of ps HP intensities variations and ns HP with delay dependence revealed that the modified SCs show higher stability than pristine MA. The stability of SCs also confirmed by ablating them with ns HP at a fixed position on the sample surface and collecting the HHG spectra within the exposure time (Fig. S7). The harmonic spectra shown in (Fig. S7(a)) indicate that pristine MA ablation continuously produced the plasma plumes for 2.66 mins (frame rate 100 ns, saving five frames in 1 s using CCD). However, as shown in Fig. S7(b)-(e), the MA-CB, MA-PEA, MA-PEX, and MA-API have some gaps in presented harmonic spectra and extend the stability of the signal until 3.10, 3.31, 3.19, and 3.46 mins, respectively. The gaps in harmonic spectra for additive-based crystals revealed that plasma formation requires more ablating laser pulses. The cut-off of time duration until the harmonic's emission vs studied SCs (Fig. 9) showed that the time duration is increased from MA to MA-API. This is direct evidence that modified SCs possess longer stability than pristine MA with exposure to ns HP.

#### 3.3.2. Harmonics Cut-off:

The maximum cut-off achieved for ns LIPs is close to 21 to 23H. As shown in **Fig. 9(c)**, the cut-off of MA and MA-CB at  $I_{DP}$ = 1.5 × 10<sup>10</sup> W/cm<sup>2</sup> possess 19 H; this cut-off increased to

23H with an increase in the  $I_{DP}$ . Similarly, MA-PEA, MA-PXA, and MA-API possess almost 21H-23H [due to the appearance of plasma lines for these PSCs, the 23H could not be able to see in the HHG spectra of Fig. 8(c) 3 to 5 panels (top to bottom)]. HHG spectra for ns LIPs are only one order smaller than ps LIPs (25 H). Earlier, we have shown that in the case of Ni-doped CsPbBr<sub>3</sub>, perovskites nanocrystals in the case of ps LIPs produce 27 H and ns LIPs 21 H using 800 nm DP.<sup>52</sup> In the present case for ps LIPs, the cut-off for five PSCs with respect to changes in  $I_{DP}$  is shown in Fig. 9(e). MA possess a minimum cut-off at 15H, and a maximum at 27H, and the modified MA-SCs possess a higher cut-off at a lower  $I_{DP}$ . This indicates that the presence of additive plasma components might lead to an increase in overall density. As a result, a higher cut-off and highly intense harmonics are achieved for modified SCs. The general tendency of the harmonic cut-off, as shown in Fig. 9(e), is increasing with further growth in  $I_{DP}$  because it will well know that energy cut-off is linearly proportional to the input driving pulse intensity (as per the energy cut-off formulae  $E_{cut-off} = I_p + 3.17U_p$ . Where Ip is the ionization potential,  $U_P = 9.33 \times 10^{-14}$  I (W/cm<sup>2</sup>)  $\lambda^2$  ( $\mu$ m)). <sup>108</sup>

### 3.3.3. Spectral shift of harmonics

The intensities of ps HP variation and ns & fs delay dependence studies due not influence the harmonic spectra in terms of their spectral shift. Because we have utilized the same  $I_{DP}$  for these measurements, the variation in  $I_{ps}$  and delay between ns and fs pulses leads to changes in the density of plasma components, which impacts the harmonics' intensity.

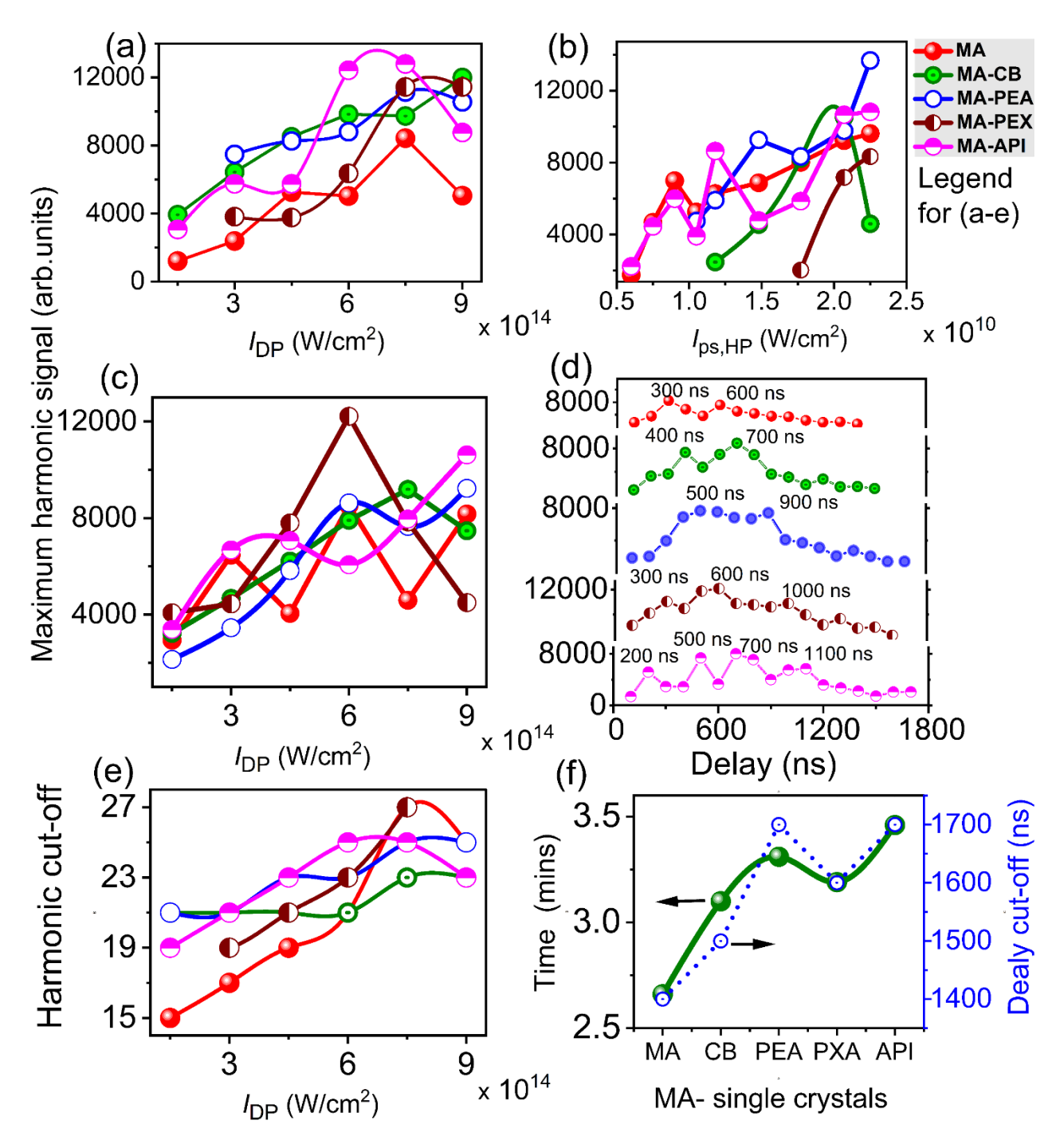


Fig. 3. 9 The maximum harmonic signal obtained (from data shown in Fig. 8 (a-d)) for (a) at fixed ps heating pulse intensity ( $I_{ps,HP}$ ) = 1.77 × 10<sup>10</sup> W/cm<sup>2</sup> for changes in driving pulses intensity ( $I_{DP}$ ), (b) at fixed  $I_{DP}$  = 6.0 × 10<sup>14</sup> W/cm<sup>2</sup>, variation in  $I_{ps,HP}$ . In case of ns LIPs (at  $I_{ns,HP}$  = 7 × 10<sup>10</sup> W/cm<sup>2</sup>) (c) w.r.to  $I_{DP}$ , (d) the delay dependence between ns HP and fs DP, respectively. (e) harmonic cut-off in case of ps LIPs with changes in  $I_{DP}$ . (f) the cut-off of time duration until the harmonic's emission (left Y-axis), and the delay cut-off (right Y-axis) for studied single crystals.

However, the clear small blueshift of harmonics can be visible with respect to variation in  $I_{DP}$ 

variation shown in **Fig. 10(a) and (c)** for ps and ns LIPs. Generally, the blue shift of harmonics could be achieved by changing the chirp of driving laser pulses. The HHG spectra from the same material with variation in the DP intensity may not impose the shift of harmonics. However, in these modified PSCs, probably due to the presence of additive components leads to the variation of bandgap and crystallinity changes, which leads to interaction with the lower spectral components of DP 800 nm. This bluer shift is more prominent in the case of ps LIPs than ns LIPs, as shown in **Fig. 10 (a) and (b)**. **Fig. 10(a) and (b)** shows the 9H (88.88 nm), 11H (72.72 nm) to 13H (61.53 nm), 15H (53.33 nm) HHG spectra for ns LIPs and ps LIPs at driving pulses intensity  $6 \times 10^{14}$  W/cm², respectively. The shift of harmonics towards shorter wavelengths (bluer shift) is more prominent for additive-based SCs. **Fig. 10(c) and (d)**, shows the plasma plumes formed by the ablation of MA-API SCs with ns and ps pulses. A similar pattern has been achieved for all other PSCs. It is observed that with the ablation of ns pulses, only the plasma plumes expanded from the surface of PSCs. In the case of ps pulses, the PSCs themselves illuminate the green emission along with plasma plume expansion. In the case of

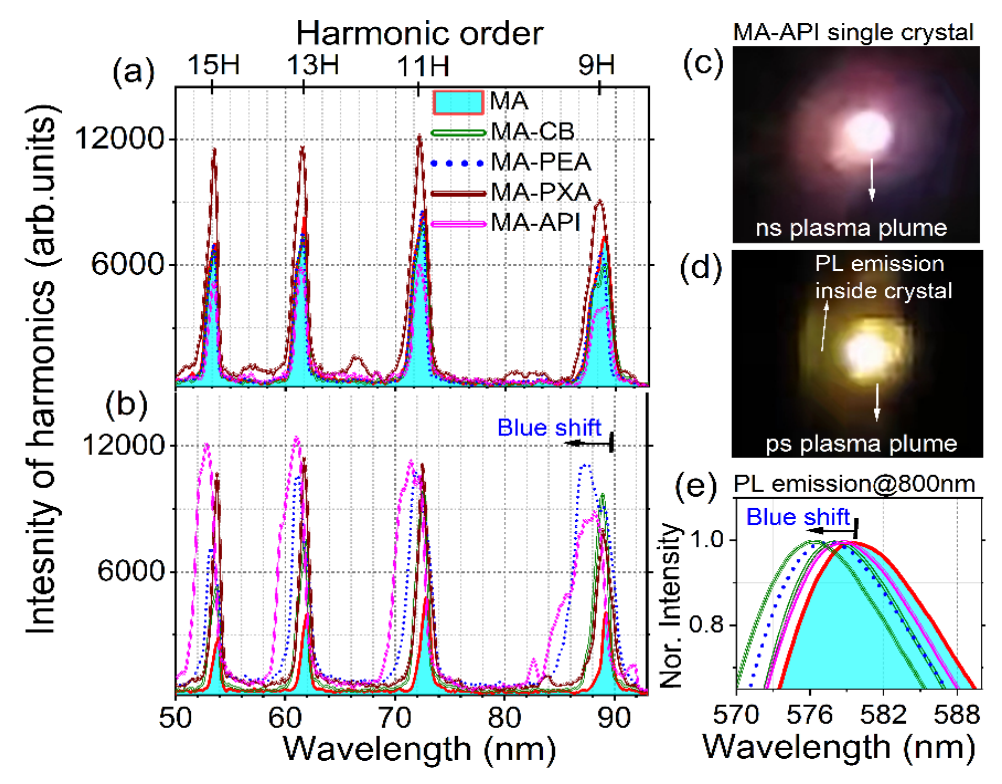


Fig. 3. 10 HHG spectra 9H to 15H for (a) ns LIPs (b) ps LIPs at driving pulses intensity 6× 10<sup>14</sup> W/cm<sup>2</sup>. For MA-API (c) plasma plumes obtained from ns HP, and (d) plasma plumes obtained from ps HP. (e) The normalized PL spectra at pump wavelength 800 nm.

ns pulses, used 1064 nm as an ablating laser pulse, and for ps pulses, the excitation wavelength is 800 nm; due to the nonlinear absorption of 800 nm, there is PL emission. Therefore, it is assumed that the plasma components (atoms, ions, and nanoparticles) of PSCs may interact with the blue spectral components of 800 nm and decrease their harmonics wavelengths. **Fig. 10(e)** depicts the normalized PL spectra of PSCs measured at 800 nm, 35 fs, and 1 kHz pulses with an average power of 100 mW. This blueshift order of PSCs matches the HHG case and the order followed by MA-API>MA-PEA>MA-CB>MA-PXA>MA.

The presence of plasma components (atoms, ions, nanoparticles, clusters) could be identified by the ICCD spectrometer. Meanwhile, It is well aware that HHG is a three-step model<sup>109</sup> [(i) ionization by the intense laser field, (ii) acceleration in the laser field, and (iii) recombination with the parent ion lead to the generation of high energy photons. The emission of high-order harmonics (high energy photons corresponding to driving laser field) is widely subject to plasma components of PSCs. The emitted harmonics are the superposition of the individual contribution of each plasma component. The ionization potential  $(I_p)$  of plasma components could influence the harmonics' intensity and cut-off. The molecular formulae and the first and second ionization potentials of the reported five PSCs are shown in Appendix I Table 3. The MA and modified PSCs have C, H, N, Pb, Br, O, and Cl chemical components. Among them, Pb possesses the lowest first ionization potential, i.e., 7.41 eV, by shortening the chemical elements in ascending order as per their first ionization potential followed by Pb<C<Br<Cl>H<O<N. Interestingly, the Pb, Br and N weight percentage increases, and the C quantity decreases than MA (Fig. S2(a)). MA-CB has additional O, and MA-PEA, MA-PXA, and MA-API have additional Cl quantities compared to pristine MA. Therefore, it is expected that the modified PSC will contain a higher number of chemical components. Due to this, the plasma density (contains atoms and singly charged ions) will be higher in the case of these modified PSCs ablated by ns HP and ps HP. Therefore, the intensity of harmonics, cut-off (ps LIPs), and a spectral higher shift have been observed for modified PSCs than pristine MA PSCs. These parameters are significantly more affected in ps LIPs than in ns LIPs. Experimentally, we cannot directly differentiate or estimate plasma components' contributions. We could not flexibly control the relative concentrations of the ions' distinct charge states, as they are always present in plasma. However, as mentioned above, we might estimate their contributions by assuming the overall HHG yield is proportionate to the plasma density.

#### 3.3. Conclusions

Understanding the surface properties of PSCs, including their crystallinity, surface qualities, and stability, is essential to improve the transmission of these crystals. Here, we directly visualized the surface transformation of pristine PSC using spectroscopy and microscopy techniques. The results based on THz time-domain spectroscopy revealed that additive-engineered SCs are prominent for applications in the THz regime. Out of all the additives used, the transmission/reflection of THz pulse, higher intensity of HHG signal and stability improved in MAPbBr3: API SC in comparison to pristine crystal because of effective passivation of heterocyclic moiety (piperidine) with fewer molecular defects. Interestingly, a bluer shift was observed in the HHG spectra of additive-based MAPbBr3 SCs with DP 800 nm. HHG studies based on ps and ns LIPs found that additives such as CB, PEA, PXA and API increase the stability of SCs and good emitters of HHG. Several pieces of evidence from our experimental results indicate that modified PSC surfaces with fewer defects have enhanced transmittance and structural properties compared to pristine MA. These findings open a new avenue for THz devices and tunable HHG applications using additive-based PSCs.

## **References**

Dong, Q. Electron-Hole Diffusion Lengths > 175 μ m in Solution-Grown CH 3 NH 3
 PbI<sub>3</sub> Single Crystals. Science 2015, 347, 967–970.

- (2) Lin, K.; Xing, J.; Quan, L. N.; de Arquer, F. P. G.; Gong, X.; Lu, J.; Xie, L.; Zhao, W.; Zhang, D.; Yan, C.; Li, W.; Liu, X.; Lu, Y.; Kirman, J.; Sargent, E. H.; Xiong, Q.; Wei, Z. Perovskite Light-Emitting Diodes with External Quantum Efficiency Exceeding 20 per Cent. *Nature* 2018, 562, 245–248.
- (3) Jia, Y.; Kerner, R. A.; Grede, A. J.; Rand, B. P.; Giebink, N. C. Continuous-Wave Lasing in an Organic-Inorganic Lead Halide Perovskite Semiconductor. *Nature Photonics* **2017**, *11*, 784–788.
- (4) Jiang, X.; Fu, X.; Ju, D.; Yang, S.; Chen, Z.; Tao, X. Designing Large Area Single Crystal Perovskite Solar Cells. *ACS Energy Letters* **2020**, *5*, 1797–1803.
- (5) Turedi, B.; Yeddu, V.; Zheng, X.; Kim, D. Y.; Bakr, O. M.; Saidaminov, M. I. Perovskite Single-Crystal Solar Cells: Going Forward. *ACS Energy Letters* **2021**, *6*, 631–642.
- (6) Zhao, M.; Zhang, Q.; Xia, Z. Narrow-Band Emitters in LED Backlights for Liquid-Crystal Displays. *Materials Today* 2020, 40, 246–265.
- (7) Li, Y.; Zhang, X.; Huang, H.; Kershaw, S. V.; Rogach, A. L. Advances in Metal Halide Perovskite Nanocrystals: Synthetic Strategies, Growth Mechanisms, and Optoelectronic

- Applications. Materials Today 2020, 32, 204–221.
- (8) Li, Y.; Allegro, I.; Kaiser, M.; Malla, A. J.; Richards, B. S.; Lemmer, U.; Paetzold, U. W.; Howard, I. A. Exciton versus Free Carrier Emission: Implications for Photoluminescence Efficiency and Amplified Spontaneous Emission Thresholds in Quasi-2D and 3D Perovskites. *Materials Today* 2021, 49, 35–47.
- (9) Adjokatse, S.; Fang, H. H.; Loi, M. A. Broadly Tunable Metal Halide Perovskites for Solid-State Light-Emission Applications. *Materials Today* **2017**, *20*, 413–424.
- (10) Zhang, J.; Wang, L.; Zhang, X.; Xie, G.; Jia, G.; Zhang, J.; Yang, X. Blue Light-Emitting Diodes Based on Halide Perovskites: Recent Advances and Strategies. *Materials Today* **2021**, *51*, 222–246.
- (11) Xing, J.; Zhao, C.; Zou, Y.; Kong, W.; Yu, Z.; Shan, Y.; Dong, Q.; Zhou, D.; Yu, W.; Guo, C. Modulating the Optical and Electrical Properties of MAPbBr3 Single Crystals via Voltage Regulation Engineering and Application in Memristors. *Light: Science & Applications* 2020, 9, 11.
- (12) Xing, G.; Mathews, N.; Lim, S. S.; Yantara, N.; Liu, X.; Sabba, D.; Grätzel, M.; Mhaisalkar, S.; Sum, T. C. Low-Temperature Solution-Processed Wavelength-Tunable Perovskites for Lasing. *Nature Materials* 2014, 13, 476–480.
- (13) Deschler, F.; Price, M.; Pathak, S.; Klintberg, L. E.; Jarausch, D. D.; Higler, R.; Hüttner, S.; Leijtens, T.; Stranks, S. D.; Snaith, H. J.; Atatüre, M.; Phillips, R. T.; Friend, R. H. High Photoluminescence Efficiency and Optically Pumped Lasing in Solution-

Processed Mixed Halide Perovskite Semiconductors. *Journal of Physical Chemistry Letters* **2014**, *5*, 1421–1426.

- (14) Xia, P.; Xu, S.; Wang, C.; Ban, D. Perovskite Luminescent Solar Concentrators for Photovoltaics. *APL Photonics* **2021**, *6*, 120901.
- (15) Bai, F.; Bian, K.; Huang, X.; Wang, Z.; Fan, H. Pressure Induced Nanoparticle Phase Behavior, Property, and Applications. *Chemical Reviews* **2019**, *119*, 7673–7717.
- (16) Feng, Y.; Pan, L.; Wei, H.; Liu, Y.; Ni, Z.; Zhao, J.; Rudd, P. N.; Cao, L. R.; Huang, J. Low Defects Density CsPbBr<sub>3</sub> single Crystals Grown by an Additive Assisted Method for Gamma-Ray Detection. *Journal of Materials Chemistry C* **2020**, *8*, 11360–11368.
- (17) Tang, Y.; Liang, M.; Zhang, M.; Honarfar, A.; Zou, X.; Abdellah, M.; Pullerits, T.; Zheng, K.; Chi, Q. Photodetector Based on Spontaneously Grown Strongly Coupled MAPbBr3/N-RGO Hybrids Showing Enhanced Performance. ACS Applied Materials and Interfaces 2020, 12, 858–867.
- (18) Bao, C.; Chen, Z.; Fang, Y.; Wei, H.; Deng, Y.; Xiao, X.; Li, L.; Huang, J. Low-Noise and Large-Linear-Dynamic-Range Photodetectors Based on Hybrid-Perovskite Thin-Single-Crystals. *Advanced Materials* **2017**, *29*, 1–7.
- (19) Liu, Y.; Zhang, Y.; Yang, Z.; Yang, D.; Ren, X.; Pang, L.; Liu, S. F. Thinness- and Shape-Controlled Growth for Ultrathin Single-Crystalline Perovskite Wafers for Mass Production of Superior Photoelectronic Devices. *Advanced Materials* 2016, 28, 9204–9209.

(20) Lin, Q.; Armin, A.; Burn, P. L.; Meredith, P. Filterless Narrowband Visible Photodetectors. *Nature Photonics* **2015**, *9*, 687–694.

- (21) Yao, F.; Gui, P.; Chen, C.; Li, B.; Li, R.; Tao, C.; Lin, Q.; Fang, G. High-Rubidium-Formamidinium-Ratio Perovskites for High-Performance Photodetection with Enhanced Stability. *ACS Applied Materials and Interfaces* **2019**, *11*, 39875–39881.
- (22) Gui, P.; Chen, Z.; Li, B.; Yao, F.; Zheng, X.; Lin, Q.; Fang, G. High-Performance Photodetectors Based on Single All-Inorganic CsPbBr3 Perovskite Microwire. *ACS Photonics* **2018**, *5*, 2113–2119.
- (23) Huang, Q.; Liu, Y.; Li, F.; Liu, M.; Zhou, Y. Advances in Cesium Lead Iodide Perovskite Solar Cells: Processing Science Matters. *Materials Today* **2021**, *47*, 156–169.
- (24) Zhang, F.; Castaneda, J. F.; Chen, S.; Wu, W.; DiNezza, M. J.; Lassise, M.; Nie, W.; Mohite, A.; Liu, Y.; Liu, S.; Friedman, D.; Liu, H.; Chen, Q.; Zhang, Y. H.; Huang, J.; Zhang, Y. Comparative Studies of Optoelectrical Properties of Prominent PV Materials: Halide Perovskite, CdTe, and GaAs. *Materials Today* 2020, 36, 18–29.
- (25) Bibi, A.; Lee, I.; Nah, Y.; Allam, O.; Kim, H.; Quan, L. N.; Tang, J.; Walsh, A.; Jang, S. S.; Sargent, E. H.; Kim, D. H. Lead-Free Halide Double Perovskites: Toward Stable and Sustainable Optoelectronic Devices. *Materials Today* 2021, 49, 123–144.
- (26) Im, T. H.; Lee, J. H.; Wang, H. S.; Sung, S. H.; Kim, Y. Bin; Rho, Y.; Grigoropoulos,C. P.; Park, J. H.; Lee, K. J. Flashlight-Material Interaction for Wearable and Flexible

- Electronics. *Materials Today* **2021**, *51*, 525–551.
- (27) Sánchez, S.; Vallés-Pelarda, M.; Alberola-Borràs, J. A.; Vidal, R.; Jerónimo-Rendón, J. J.; Saliba, M.; Boix, P. P.; Mora-Seró, I. Flash Infrared Annealing as a Cost-Effective and Low Environmental Impact Processing Method for Planar Perovskite Solar Cells. Materials Today 2019, 31, 39–46.
- (28) Zhang, H.; Nazeeruddin, M. K.; Choy, W. C. H. Perovskite Photovoltaics: The Significant Role of Ligands in Film Formation, Passivation, and Stability. *Advanced materials (Deerfield Beach, Fla.)* **2019**, *31*, e1805702.
- (29) Balis, N.; Zaky, A. A.; Athanasekou, C.; Silva, A. M.; Sakellis, E.; Vasilopoulou, M.; Stergiopoulos, T.; Kontos, A. G.; Falaras, P. Investigating the Role of Reduced Graphene Oxide as a Universal Additive in Planar Perovskite Solar Cells. *Journal of Photochemistry and Photobiology A: Chemistry* **2020**, *386*, 112141.
- (30) Chao, L.; Xia, Y.; Li, B.; Xing, G.; Chen, Y.; Huang, W. Room-Temperature Molten Salt for Facile Fabrication of Efficient and Stable Perovskite Solar Cells in Ambient Air. *Chem* **2019**, *5*, 995–1006.
- (31) Liu, Y.; Zhang, Y.; Yang, Z.; Feng, J.; Xu, Z.; Li, Q.; Hu, M.; Ye, H.; Zhang, X.; Liu, M.; Zhao, K.; Liu, S. Low-Temperature-Gradient Crystallization for Multi-Inch High-Quality Perovskite Single Crystals for Record Performance Photodetectors. *Materials Today* 2019, 67–75.
- (32) Saidaminov, M. I.; Abdelhady, A. L.; Murali, B.; Alarousu, E.; Burlakov, V. M.; Peng,

W.; Dursun, I.; Wang, L.; He, Y.; Maculan, G.; Goriely, A.; Wu, T.; Mohammed, O. F.; Bakr, O. M. High-Quality Bulk Hybrid Perovskite Single Crystals within Minutes by Inverse Temperature Crystallization. *Nature Communications* **2015**, *6*, 7586.

- (33) Schötz, K.; Askar, A. M.; Peng, W.; Seeberger, D.; Gujar, T. P.; Thelakkat, M.; Köhler, A.; Huettner, S.; Bakr, O. M.; Shankar, K.; Panzer, F. Double Peak Emission in Lead Halide Perovskites by Self-Absorption. *Journal of Materials Chemistry C* **2020**, 8, 2289–2300.
- (34) Ng, M.; Halpert, J. E. Single Crystals of Mixed Br/Cl and Sn-Doped Formamidinium Lead Halide Perovskites: Via Inverse Temperature Crystallization. *RSC Advances* **2020**, *10*, 3832–3836.
- (35) Ding, J.; Zhao, Y.; Du, S.; Sun, Y.; Cui, H.; Zhan, X.; Cheng, X.; Jing, L. Controlled Growth of MAPbBr3 Single Crystal: Understanding the Growth Morphologies of Vicinal Hillocks on (100) Facet to Form Perfect Cubes. *Journal of Materials Science* **2017**, *52*, 7907–7916.
- (36) Liu, Y.; Yang, Z.; Cui, D.; Ren, X.; Sun, J.; Liu, X.; Zhang, J.; Wei, Q.; Fan, H.; Yu, F.; Zhang, X.; Zhao, C.; Liu, S. Two-Inch-Sized Perovskite CH<sub>3</sub>NH<sub>3</sub>PbX<sub>3</sub> (X = Cl, Br, I) Crystals: Growth and Characterization. *Advanced Materials* **2015**, *27*, 5176–5183.
- (37) Dang, Y.; Liu, Y.; Sun, Y.; Yuan, D.; Liu, X.; Lu, W.; Liu, G.; Xia, H.; Tao, X. Bulk Crystal Growth of Hybrid Perovskite Material CH<sub>3</sub>NH<sub>3</sub>PbI<sub>3</sub>. *CrystEngComm* **2015**, *17*, 665–670.

(38) Shi, D.; Adinolfi, V.; Comin, R.; Yuan, M.; Alarousu, E.; Buin, A.; Chen, Y.; Hoogland,
S.; Rothenberger, A.; Katsiev, K.; Losovyj, Y.; Zhang, X.; Dowben, P. A.; Mohammed,
O. F.; Sargent, E. H.; Bakr, O. M. Low Trap-State Density and Long Carrier Diffusion in Organolead Trihalide Perovskite Single Crystals. *Science* 2015, 347, 519–522.

- (39) Efrati, A.; Aharon, S.; Wierzbowska, M.; Etgar, L. First Evidence of Macroscale Single Crystal Ion Exchange Found in Lead Halide Perovskites. *EcoMat* **2020**, *2*, e12016.
- (40) Misra, R. K.; Aharon, S.; Li, B.; Mogilyansky, D.; Visoly-Fisher, I.; Etgar, L.; Katz, E.
   A. Temperature- and Component-Dependent Degradation of Perovskite Photovoltaic
   Materials under Concentrated Sunlight. *The Journal of Physical Chemistry Letters* 2015,
   6, 326–330.
- (41) Niu, G.; Guo, X.; Wang, L. Review of Recent Progress in Chemical Stability of Perovskite Solar Cells. *Journal of Materials Chemistry A* **2015**, *3*, 8970–8980.
- (42) van Reenen, S.; Kemerink, M.; Snaith, H. J. Modeling Anomalous Hysteresis in Perovskite Solar Cells. *The Journal of Physical Chemistry Letters* **2015**, *6*, 3808–3814.
- (43) Raga, S. R.; Jung, M. C.; Lee, M. V.; Leyden, M. R.; Kato, Y.; Qi, Y. Influence of Air Annealing on High-Efficiency Planar Structure Perovskite Solar Cells. *Chemistry of Materials* **2015**, *27*, 1597–1603.
- (44) Han, Y.; Meyer, S.; Dkhissi, Y.; Weber, K.; Pringle, J. M.; Bach, U.; Spiccia, L.; Cheng,
   Y. B. Degradation Observations of Encapsulated Planar CH<sub>3</sub>NH<sub>3</sub>PbI<sub>3</sub> Perovskite Solar
   Cells at High Temperatures and Humidity. *Journal of Materials Chemistry A* 2015, 3,

8139-8147.

- (45) Kuang, C.; Hu, Z.; Yuan, Z.; Wen, K.; Qing, J.; Kobera, L.; Abbrent, S.; Brus, J.; Yin, C.; Wang, H.; Xu, W.; Wang, J.; Bai, S.; Gao, F. Critical Role of Additive-Induced Molecular Interaction on the Operational Stability of Perovskite Light-Emitting Diodes. *Joule* 2021, 5, 618–630.
- (46) Ma, Y.; Cheng, Y.; Xu, X.; Li, M.; Zhang, C.; Cheung, S. H.; Zeng, Z.; Shen, D.; Xie, Y.; Chiu, K. L.; Lin, F.; So, S. K.; Lee, C.; Tsang, S. Suppressing Ion Migration across Perovskite Grain Boundaries by Polymer Additives. *Advanced Functional Materials* **2021**, *31*, 2006802.
- (47) Zhang, Z.; Xu, C.; Wang, D.; Zhang, X.; Zhang, J. Electrical Properties of Carbon-Based Fully-Printed Mesoscopic Perovskite Solar Cells with BAI as an Additive. *Journal of Materials Science: Materials in Electronics* **2022**, *33*, 3091–3100.
- (48) Wang, Y.; Liu, X.; Zhang, T.; Wang, X.; Kan, M.; Shi, J.; Zhao, Y. The Role of Dimethylammonium Iodide in CsPbI 3 Perovskite Fabrication: Additive or Dopant? .

  Angewandte Chemie 2019, 131, 16844–16849.
- (49) He, L.; Xiao, Z.; Yang, X.; Wu, Y.; Lian, Y.; Peng, X.; Yang, X. Green and Sky Blue Perovskite Light-Emitting Devices with a Diamine Additive. *Journal of Materials Science* **2020**, *55*, 7691–7701.
- (50) Fu, D.; Xin, J.; He, Y.; Wu, S.; Zhang, X.; Zhang, X. M.; Luo, J. Chirality-Dependent Second-Order Nonlinear Optical Effect in 1D Organic-Inorganic Hybrid Perovskite

Bulk Single Crystal. *Angewandte Chemie - International Edition* **2021**, *60*, 20021–20026.

- (51) Maeng, I.; Lee, S.; Han, E. Q.; Zhang, Y.; Oh, S. J.; Nakamura, M.; Yun, J.-H.; Wang, L.; Kwon, Y.-K.; Jung, M.-C. Unusual Terahertz-Wave Absorptions in δ/α-Mixed-Phase FAPbI<sub>3</sub> Single Crystals: Interfacial Phonon Vibration Modes. NPG Asia Materials 2021, 13, 75.
- (52) Konda, S. R.; Soma, V. R.; Banavoth, M.; Ketavath, R.; Mottamchetty, V.; Lai, Y. H.; Li, W. High Harmonic Generation from Laser-Induced Plasmas of Ni-Doped CsPbBr<sub>3</sub> Nanocrystals: Implications for Extreme Ultraviolet Light Sources. ACS Applied Nano Materials 2021, 4, 8292–8301.
- (53) Konda, S. R.; Soma, V. R.; Ganeev, R. A.; Banavoth, M.; Ketavath, R.; Li, W. Third-Order Optical Nonlinearities and High-Order Harmonics Generation in Ni-Doped CsPbBr3 Nanocrystals Using Single- and Two-Color Chirped Pulses. *Journal of Materials Science* 2022, 57, 3468–3485.
- (54) Hussain, M.; Kaassamani, S.; Auguste, T.; Boutu, W.; Gauthier, D.; Kholodtsova, M.; Gomes, J.-T.; Lavoute, L.; Gaponov, D.; Ducros, N.; Fevrier, S.; Nicolas, R.; Imran, T.; Zeitoun, P.; Williams, G. O.; Fajardo, M.; Merdji, H. Spectral Control of High Order Harmonics through Non-Linear Propagation Effects. *Applied Physics Letters* 2021, 119, 071101.
- (55) Ganeev, R. A.; Singhal, H.; Naik, P. A.; Chakravarty, U.; Arora, V.; Chakera, J. A.; Khan, R. A.; Raghuramaiah, M.; Kumbhare, S. R.; Kushwaha, R. P.; Gupta, P. D.

Optimization of the High-Order Harmonics Generated from Silver Plasma. *Applied Physics B: Lasers and Optics* **2007**, *87*, 243–247.

- (56) Konda, S. R.; Lai, Y. H.; Li, W. Improvement of High-Order Harmonics from Silver Plasma Plumes Induced by Femtoseconds Laser Pulses. *Optics and Laser Technology* 2022, 146, 107602.
- (57) Mikaelsson, S.; Vogelsang, J.; Guo, C.; Sytcevich, I.; Viotti, A. L.; Langer, F.; Cheng, Y. C.; Nandi, S.; Jin, W.; Olofsson, A.; Weissenbilder, R.; Mauritsson, J.; L'Huillier, A.; Gisselbrecht, M.; Arnold, C. L. A High-Repetition Rate Attosecond Light Source for Time-Resolved Coincidence Spectroscopy. *Nanophotonics* 2020, 10, 117–128.
- (58) Hadrich, S.; Krebs, M.; Hoffmann, A.; Klenke, A.; Rothhardt, J.; Limpert, J.; Tu, A. Exploring New Avenues in High Repetition Rate Table-Top Coherent Extreme Ultraviolet Sources. *Light: Science & Applications* **2015**, *4*, e320.
- (59) Li, J. J.; Lu, J.; Chew, A.; Han, S.; Li, J. J.; Wu, Y.; Wang, H.; Ghimire, S.; Chang, Z. Attosecond Science Based on High Harmonic Generation from Gases and Solids. *Nature Communications* **2020**, *11*, 2748.
- (60) Kanda, N.; Imahoko, T.; Yoshida, K.; Tanabashi, A.; Amani Eilanlou, A.; Nabekawa, Y.; Sumiyoshi, T.; Kuwata-Gonokami, M.; Midorikawa, K. Opening a New Route to Multiport Coherent XUV Sources via Intracavity High-Order Harmonic Generation. Light: Science and Applications 2020, 9, 168.
- (61) Murali, B.; Yengel, E.; Yang, C.; Peng, W.; Alarousu, E.; Bakr, O. M.; Mohammed, O.

F. The Surface of Hybrid Perovskite Crystals: A Boon or Bane. *ACS Energy Letters* **2017**, *2*, 846–856.

- (62) Li, J.; Tilbury, C. J.; Kim, S. H.; Doherty, M. F. A Design Aid for Crystal Growth Engineering. *Progress in Materials Science* **2016**, *82*, 1–38.
- (63) Hartman, P. The Attachment Energy as a Habit Controlling Factor. III. Application to Corundum. *Journal of Crystal Growth* **1980**, *49*, 166–170.
- (64) Gao, J.; Zhang, W.; Wu, Z.; Zheng, Y.; Fu, D. Enantiomorphic Perovskite Ferroelectrics with Circularly Polarized Luminescence. *Journal of the American Chemical Society* **2020**, *142*, 6.
- (65) Dang, Y.; Liu, X.; Sun, Y.; Song, J.; Hu, W.; Tao, X. Bulk Chiral Halide Perovskite Single Crystals for Active Circular Dichroism and Circularly Polarized Luminescence.

  The Journal of Physical Chemistry Letters 2020, 11, 1689–1696.
- (66) Zhang, F.; Zhu, K. Additive Engineering for Efficient and Stable Perovskite Solar Cells. *Advanced Energy Materials* **2020**, *10*, 1902579.
- (67) Mangrulkar, M.; Stevenson, K. J. The Progress of Additive Engineering for CH3NH3PbI3 Photo-Active Layer in the Context of Perovskite Solar Cells. *Crystals* **2021**, *11*, 814.
- (68) Sekimoto, T.; Suzuka, M.; Yokoyama, T.; Uchida, R.; Machida, S.; Sekiguchi, T.; Kawano, K. Energy Level Diagram of HC(NH2)2PbI3 Single Crystal Evaluated by Electrical and Optical Analyses. *Physical Chemistry Chemical Physics* **2018**, *20*, 1373–

1380.

- (69) Lv, Q.; Lian, Z.; He, W.; Sun, J. L.; Li, Q.; Yan, Q. A Universal Top-down Approach toward Thickness-Controllable Perovskite Single-Crystalline Thin Films. *Journal of Materials Chemistry C* **2018**, *6*, 4464–4470.
- (70) Abdelhady, A. L.; Saidaminov, M. I.; Murali, B.; Adinolfi, V.; Voznyy, O.; Katsiev, K.;
  Alarousu, E.; Comin, R.; Dursun, I.; Sinatra, L.; Sargent, E. H.; Mohammed, O. F.; Bakr,
  O. M. Heterovalent Dopant Incorporation for Bandgap and Type Engineering of Perovskite Crystals. *Journal of Physical Chemistry Letters* 2016, 7, 295–301.
- (71) Sarmah, S. P.; Burlakov, V. M.; Yengel, E.; Murali, B.; Alarousu, E.; El-Zohry, A. M.; Yang, C.; Alias, M. S.; Zhumekenov, A. A.; Saidaminov, M. I.; Cho, N.; Wehbe, N.; Mitra, S.; Ajia, I.; Dey, S.; Mansour, A. E.; Abdelsamie, M.; Amassian, A.; Roqan, I. S.; Ooi, B. S.; Goriely, A.; Bakr, O. M.; Mohammed, O. F. Double Charged Surface Layers in Lead Halide Perovskite Crystals. *Nano Letters* 2017, *17*, 2021–2027.
- (72) Maeng, I.; Lee, S.; Tanaka, H.; Yun, J.-H.; Wang, S.; Nakamura, M.; Kwon, Y.-K.; Jung, M.-C. Unique Phonon Modes of a CH<sub>3</sub>NH<sub>3</sub>PbBr<sub>3</sub> Hybrid Perovskite Film without the Influence of Defect Structures: An Attempt toward a Novel THz-Based Application. *NPG Asia Materials* **2020**, *12*, 53.
- (73) Rocks, C.; Svrcek, V.; Maguire, P.; Mariotti, D. Understanding Surface Chemistry during MAPbI3 Spray Deposition and Its Effect on Photovoltaic Performance. *Journal of Materials Chemistry C* **2017**, *5*, 902–916.

(74) Rybin, N.; Ghosh, D.; Tisdale, J.; Shrestha, S.; Yoho, M.; Vo, D.; Even, J.; Katan, C.; Nie, W.; Neukirch, A. J.; Tretiak, S. Effects of Chlorine Mixing on Optoelectronics, Ion Migration, and Gamma-Ray Detection in Bromide Perovskites. *Chemistry of Materials* 2020, 32, 1854–1863.

- (75) Shen, H.; Nan, R.; Jian, Z. J; Li, X. Materials Defect Step Controlled Growth of Perovskite MAPbBr<sub>3</sub> Single Crystal. *Journal of Materials Science* **2019**, *54*, 11596–11603.
- (76) Ding, J.; Zhao, Y.; Du, S.; Sun, Y.; Cui, H. Controlled Growth of MAPbBr 3 Single Crystal: Understanding the Growth Morphologies of Vicinal Hillocks on (100) Facet to Form Perfect Cubes. *Journal of Materials Science* **2017**, *52*, 7907–7916.
- (77) Wang, W.; Wang, X.; Zhang, B.; Guo, Y.; Xu, Q. Physica B: Physics of Condensed Matter Ion Migration of MAPbBr 3 Single Crystal Devices with Coplanar and Sandwich Electrode Structures. *Physica B: Physics of Condensed Matter* **2020**, *593*, 412310.
- (78) Liu, Y.; Zhang, Y.; Zhao, K.; Yang, Z.; Feng, J.; Zhang, X. A 1300 Mm 2 Ultrahigh-Performance Digital Imaging Assembly Using High-Quality Perovskite Single Crystals.

  \*Advanced Materials 2018, 30, 1707314.
- (79) Baikie, T.; Barrow, N. S.; Fang, Y.; Keenan, P. J.; Slater, P. R.; Piltz, R. O.; Gutmann, M.; Mhaisalkar, S. G.; White, T. J. A Combined Single Crystal Neutron/X-Ray Diffraction and Solid-State Nuclear Magnetic Resonance Study of the Hybrid Perovskites CH<sub>3</sub>NH<sub>3</sub>PbX<sub>3</sub> (X = I, Br and Cl). *Journal of Materials Chemistry A* **2015**, 3, 9298–9307.

(80) Wang, X.; Li, Y.; Xu, Y.; Pan, Y.; Zhu, C.; Zhu, D.; Wu, Y.; Li, G.; Zhang, Q.; Li, Q.; Zhang, X.; Wu, J.; Chen, J.; Lei, W. Solution-Processed Halide Perovskite Single Crystals with Intrinsic Compositional Gradients for X-Ray Detection. *Chemistry of Materials* 2020, 32, 4973–4983.

- (81) Zou, Y.; Zou, T.; Zhao, C.; Wang, B.; Xing, J.; Yu, Z.; Cheng, J.; Xin, W.; Yang, J.; Yu, W.; Dong, H.; Guo, C. A Highly Sensitive Single Crystal Perovskite–Graphene Hybrid Vertical Photodetector. *Small* 2020, 16, 2000733.
- (82) Saidaminov, M. I.; Adinolfi, V.; Comin, R.; Abdelhady, A. L.; Peng, W.; Dursun, I.; Yuan, M.; Hoogland, S.; Sargent, E. H.; Bakr, O. M. Planar-Integrated Single-Crystalline Perovskite Photodetectors. *Nature Communications* **2015**, *6*, 8724.
- (83) Yamada, Y.; Yamada, T.; Phuong, L. Q.; Maruyama, N.; Nishimura, H.; Wakamiya, A.; Murata, Y.; Kanemitsu, Y. Dynamic Optical Properties of CH<sub>3</sub>NH<sub>3</sub>PbI<sub>3</sub> Single Crystals As Revealed by One- and Two-Photon Excited Photoluminescence Measurements.

  Journal of the American Chemical Society 2015, 137, 10456–10459.
- (84) Wu, B.; Nguyen, H. T.; Ku, Z.; Han, G.; Giovanni, D.; Mathews, N.; Fan, H. J.; Sum,
   T. C. Discerning the Surface and Bulk Recombination Kinetics of Organic–Inorganic
   Halide Perovskite Single Crystals. Advanced Energy Materials 2016, 6, 1600551.
- (85) Adjokatse, S.; Shao, S.; Even, J.; Loi, M. A. Long-Lived Hot-Carrier Light Emission and Large Blue Shift in Formamidinium Tin Triiodide Perovskites. *Nature Communications* **2018**, *9*, 243.

(86) Rubaiya Murshed and Shubhra Bansal. Additive-Assisted Optimization in Morphology and Optoelectronic. *Materials* **2022**, *15*, 899.

- (87) Wu, Y.; Wan, L.; Fu, S.; Zhang, W.; Li, X.; Fang, J. Liquid Metal Acetate Assisted Preparation of High- e Ffi Ciency and Stable Inverted Perovskite Solar. *Journal of Materials Chemistry A* **2019**, *7*, 14136–14144.
- (88) Mei, Y.; Sun, M.; Liu, H.; Li, X.; Wang, S. Polymer Additive Assisted Crystallization of Perovskite Films for High-Performance Solar Cells. *Organic Electronics* **2021**, *96*, 106258.
- (89) Han, T.-H.; Lee, J.-W.; Choi, C.; Tan, S.; Lee, C.; Zhao, Y.; Dai, Z.; De Marco, N.; Lee, S.-J.; Bae, S.-H.; Yuan, Y.; Lee, H. M.; Huang, Y.; Yang, Y. Perovskite-Polymer Composite Cross-Linker Approach for Highly-Stable and Efficient Perovskite Solar Cells. *Nature Communications* **2019**, *10*, 520.
- (90) Shi, D.; Adinolfi, V.; Comin, R.; Yuan, M.; Alarousu, E.; Buin, A.; Chen, Y.; Hoogland,
  S.; Rothenberger, A.; Katsiev, K.; Losovyj, Y.; Zhang, X.; Dowben, P. A.; Mohammed,
  O. F.; Sargent, E. H.; Bakr, O. M. Low Trap-State Density and Long Carrier Diffusion in Organolead Trihalide Perovskite Single Crystals. *Science* 2015, 347, 519–522.
- (91) Parikh, N.; Sevak, P.; Jowhar Khanam, S.; Prochowicz, D.; Akin, S.; Satapathi, S.; Tavakoli, M. M.; Banavoth, M.; Kalam, A.; Yadav, P. Rationalizing the Effect of Polymer-Controlled Growth of Perovskite Single Crystals on Optoelectronic Properties.
  ACS Omega 2022, 7, 36535–36542.

(92) Khanam, S. J.; Parikh, N.; Satapathi, S.; Kalam, A.; Banavoth, M.; Yadav, P. Role of Heterocyclic Organic Compounds on the Optoelectronic Properties of Halide Perovskite Single Crystals. *ACS Applied Energy Materials* **2022**, *5*, 14732–14738.

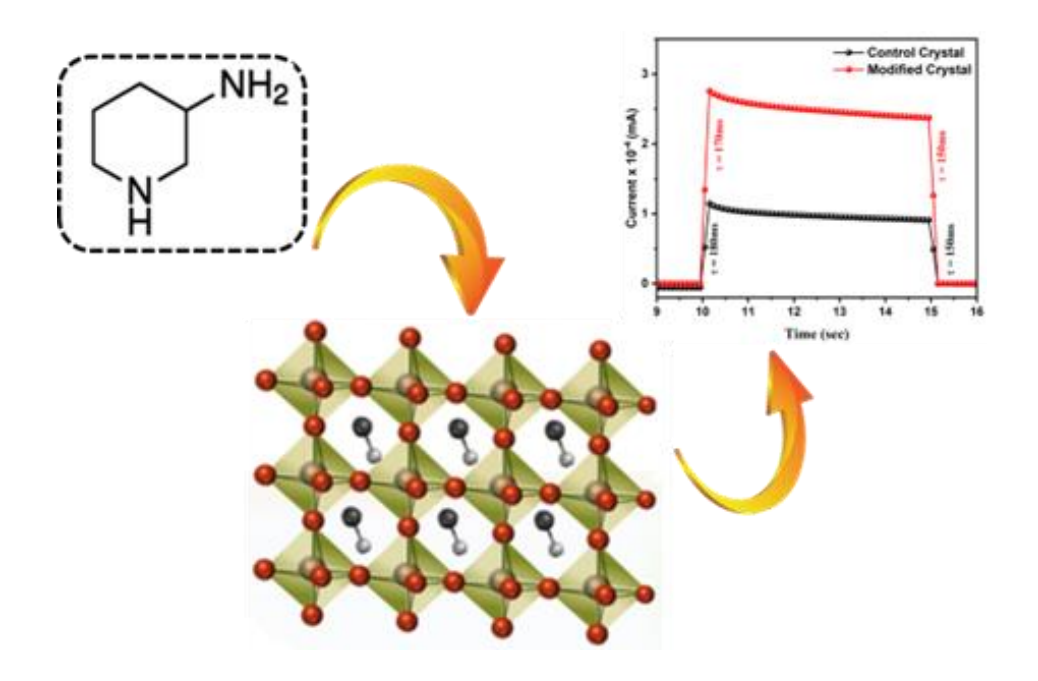
- (93) Bera, A.; Bera, S.; Kalimuddin, S.; Gayen, S.; Kundu, M.; Das, B.; Mondal, M. Review of Recent Progress on THz Spectroscopy of Quantum Materials: Superconductors, Magnetic and Topological Materials. *The European Physical Journal Special Topics* 2021, 230, 4113–4139.
- (94) Heindl, M. B.; Kirkwood, N.; Lauster, T.; Lang, J. A.; Retsch, M.; Mulvaney, P.; Herink,
   G. Ultrafast Imaging of Terahertz Electric Waveforms Using Quantum Dots. *Light: Science and Applications* 2022, 11, 31–33.
- (95) Roussel, E.; Szwaj, C.; Evain, C.; Steffen, B.; Gerth, C.; Jalali, B.; Bielawski, S. Phase Diversity Electro-Optic Sampling: A New Approach to Single-Shot Terahertz Waveform Recording. *Light: Science and Applications* **2022**, *11*, 14.
- (96) Peng, Y.; Shi, C.; Zhu, Y.; Gu, M.; Zhuang, S. Terahertz Spectroscopy in Biomedical Field: A Review on Signal-to-Noise Ratio Improvement. *PhotoniX* **2020**, *1*, 12.
- (97) Chen, Z.; Segev, M. Highlighting Photonics: Looking into the next Decade. *eLight* **2021**, 1, 2.
- (98) Chen, X.; Lindley-Hatcher, H.; Stantchev, R. I.; Wang, J.; Li, K.; Hernandez Serrano, A.; Taylor, Z. D.; Castro-Camus, E.; Pickwell-MacPherson, E. Terahertz (THz) Biophotonics Technology: Instrumentation, Techniques, and Biomedical Applications.

- Chemical Physics Reviews 2022, 3, 011311.
- (99) Duvillaret, L.; Garet, F.; Coutaz, J.-. A Reliable Method for Extraction of Material Parameters in Terahertz Time-Domain Spectroscopy. *IEEE Journal of Selected Topics in Quantum Electronics* **1996**, *2*, 739–746.
- (100) Withayachumnankul, W.; Naftaly, M. Fundamentals of Measurement in Terahertz Time-Domain Spectroscopy. *Journal of Infrared, Millimeter, and Terahertz Waves* **2014**, *35*, 610–637.
- (101) Takahashi, E. J.; Nabekawa, Y.; Midorikawa, K. Low-Divergence Coherent Soft x-Ray Source at 13 Nm by High-Order Harmonics. *Applied Physics Letters* **2004**, *84*, 4–6.
- (102) Takahashi, E.; Nabekawa, Y.; Otsuka, T.; Obara, M.; Midorikawa, K. Generation of Highly Coherent Submicrojoule Soft x Rays by High-Order Harmonics. *Physical Review A Atomic, Molecular, and Optical Physics* **2002**, *66*, 021802.
- (103) Constant, E.; Garzella, D.; Breger, P.; Mével, E.; Dorrer, C.; Le Blanc, C.; Salin, F.; Agostini, P. Optimizing High Harmonic Generation in Absorbing Gases: Model and Experiment. *Physical Review Letters* **1999**, *82*, 1668–1671.
- (104) Hirori, H.; Xia, P.; Shinohara, Y.; Otobe, T.; Sanari, Y.; Tahara, H.; Ishii, N.; Itatani, J.; Ishikawa, K. L.; Aharen, T.; Ozaki, M.; Wakamiya, A.; Kanemitsu, Y. High-Order Harmonic Generation from Hybrid Organic–Inorganic Perovskite Thin Films. APL Materials 2019, 7, 041107.
- (105) Nakagawa, K.; Hirori, H.; Sanari, Y.; Sekiguchi, F.; Sato, R.; Saruyama, M. Interference

Effects in High-Order Harmonics from Colloidal Perovskite Nanocrystals Excited by an Elliptically Polarized Laser. *Physical Review Materials* **2021**, *5*, 016001.

- (106) Strelkov, V. Role of Autoionizing State in Resonant High-Order Harmonic Generation and Attosecond Pulse Production. *Physical Review Letters* **2010**, *104*, 26–29.
- (107) Rosenthal, N.; Marcus, G. Discriminating between the Role of Phase Matching and That of the Single-Atom Response in Resonance Plasma-Plume High-Order Harmonic Generation. *Physical Review Letters* **2015**, *133901*, 1–4.
- (108) Corkum, P. B. Plasma Perspective on Strong Field Multiphoton Ionization. *Physical Review Letters* **1993**, *71* (13), 1994–1997.
- (109) Lewenstein, M.; Balcou, P.; Ivanov, M. Y.; L'Huillier, A.; Corkum, P. B. Theory of High-Harmonic Generation by Low-Frequency Laser Fields. *Physical Review A* **1994**, 49, 2117–2132.

# CHAPTER-4 Role of Heterocyclic Organic Compound on the optoelectronic properties of Halide Perovskite Single Crystal



Sarvani Jowhar Khanam, <sup>a#</sup> Nishi Parikh, <sup>b#</sup> Soumitra Satapathi, <sup>c</sup> Abul Kalam, <sup>d</sup> Murali Banavoth, <sup>a\*</sup> Pankaj Yadav <sup>e</sup>\*

Email:pankajphd11@gmail.com, Pankaj.yadav@sse.pdpu.ac.in, murali.banavoth@uohyd.ac.in

<sup>&</sup>lt;sup>a</sup> Solar Cells and Photonics Research Laboratory, School of Chemistry, University of Hyderabad, Hyderabad 500046, Telangana, India

<sup>&</sup>lt;sup>b</sup> Department of Science, School of Technology, Pandit Deendayal Energy University, Gandhinagar-382 007, Gujarat, India

<sup>&</sup>lt;sup>c</sup> Department of Physics, Indian Institute of Technology Roorkee, Roorkee, Haridwar, Uttarakhand, 247667, India

<sup>&</sup>lt;sup>d</sup> Department of Chemistry, Faculty of Science, King Khalid University, Abha 61413, P.O. Box 9004, Saudi Arabia

<sup>&</sup>lt;sup>e</sup> Department of Solar Energy, School of Technology, Pandit Deendayal Energy University, Gandhinagar-382 007, Gujarat, India

<sup>#</sup> S.J. and N.P. contributed equally to the work.

#### Abstract

Single crystals (SCs) of Metal halide perovskites (MHPs) are known to possess superior properties. However, the surface of the SCs possesses higher defect density which can deteriorate the optoelectronic properties of SCs. Herein, we have engineered the growth of methylammonium lead tribromide (MAPbBr3) SCs using (R)-3-aminopiperidine dihydrochloride (API). The modified crystals also showed improved photoresponse validated by increased photocurrent. The modified crystal showed the highest photosensitivity of 0.47 mA/W and defectivity of 3.7 x 10<sup>11</sup> Jones at 2 V applied bias. On the other hand, the control crystal showed 0.32 mA/W resistivity and detectivity of 1.0 x 10<sup>11</sup> Jones. This shows that the API additive improves the charge collection efficiency and reduces recombination. The charge accumulation and ion migration was further studied using electrochemical impedance spectroscopy and capacitance-frequency measurement. Thus, this study presents a systematic investigation of the electrical response of additive-modified crystals.

Keywords: Halide perovskites, single crystals, additive engineering, recombination, crystal growth

#### 4.1. Introduction

Metal halide perovskites (MHPs), archetypically CH<sub>3</sub>NH<sub>3</sub>PbX<sub>3</sub> (X = I, Br, Cl), have drawn considerable attention due to their outstanding optoelectronic properties.<sup>1,2</sup> Beyond their properties, the feasibility of solution processing makes them promising candidates for

laboratory and industrial applications.<sup>3,4</sup> Owing to these advantageous properties, the power conversion efficiency (PCE) of perovskite solar cells (PSCs) has reached > 25% in a short time span.<sup>5</sup> However, some fundamental questions on stability and the intrinsic properties of material need to be answered.<sup>6–8</sup> Single crystals (SCs) provide an ideal platform to discern these properties.<sup>9</sup> It is well established that the SCs of MHPs possess even superior optoelectronic properties than polycrystalline thin films.<sup>10,11</sup>

However the surface of the SCs possesses dangling bonds, point defects and under-coordinated atoms. 12 This results in relative high defect density on the surface than the bulk region. 13 In view of this, the exact nature of traps and their effect on the optoelectronic properties is under active investigation. 14-16 Many efforts have been devoted to passivating the defects to increase the stability and performance of the halide perovskites SCs. To this end, one approach is to treat the crystals with various lewis acid or base-based ligands post-synthesis 12,17,18 or to control the growth of SCs using additives. 19,20 Duim et al. investigated the mechanism of surface passivation of MAPbBr3 SCs using benzylamine, and it was reported that exposure to benzylamine results in the formation of two-dimensional (2D) (BA)<sub>2</sub>PbBr<sub>4</sub> on the surface of three-dimensional (3D) perovskite by replacing the methylammonium cations. <sup>17</sup> They studied the mechanism of surface passivation and stabilization of 2D perovskite using in-situ imaging. However, the electrical response of the crystals after passivation was not studied. In our previous report, we showed the surface passivation of Methylammonium lead tribromide (MAPbBr<sub>3</sub>) SCs with lead sulphate by in-situ reaction with octyl ammonium sulphate. <sup>12</sup> The hydrophobic layer of lead sulphate suppressed ion migration and improved the electrical properties of the crystal. In the case of additive engineering for SCs, the growth of the crystal is modulated by the addition of various ligands directly in the growth solution. Recently, Liu

et al. reported the use of 3-(decyldimethylammonio)-propane-sulfonate inner salt (DPSI) as an additive to regulate crystal growth. <sup>19</sup> The DPSI ligand bonded with the surface Pb atoms and controlled the crystal growth, which yielded high-quality crystals. There are not many reports on the additive engineering of crystals as compared to the polycrystalline thin films. <sup>21</sup> In this case, the electronic properties of the resulting crystals are equally important with the mechanism of the crystal growth for the targeted application in devices. However, there are a very few reports present on this topic. <sup>22–24</sup>

In this paper, we report the use of (R)-3-aminopiperidine dihydrochloride (API) as an additive in the growth of MAPbBr<sub>3</sub> SC. Our results suggest that API increases the thermal stability of the crystal. It effectively reduces the defect density in the modified crystal, as validated by the lower dark current in these crystals. Additionally, the modified crystal showed improved photoresponse, as evident by the current-voltage (I-V) characteristics. The I<sub>photo</sub> – P<sub>light</sub> data suggests better collection efficiency and reduced recombination after doping. This is consistent with the improved photoresponsivity and detectivity as compared to the control crystals without additives. We further performed Electrochemical Impedance Spectroscopy (EIS) and Capacitance – frequency measurement to validate the charge accumulation and ion migration in crystals. Thus, this study gives a systematic overview of the electrical response of additive-assisted growth of the crystal.

### 4.2. Results and Discussion

We synthesized MAPbBr<sub>3</sub> SC using the previously reported inverse temperature crystallization (ITC) method denoted as control crystal hereafter.<sup>25</sup> We modified the crystal growth by adding (R)-3-aminopiperidine dihydrochloride (API) in an optimized amount (denoted as modified

crystal). The detailed experimental procedure is presented in Supporting Information. **Fig.** S1(a) and S1(b) present the optical image of MAPbBr<sub>3</sub> SCs and additive-based SCs. Powder x-ray diffraction (pXRD) measurement was performed on the crystals to check their crystal structure and phase purity (**Appendix II Fig.** S1c). Interestingly, we observed decreased microcrystalline strain in additive-based crystal in comparison to pristine crystal. The diffraction peaks correspond to the cubic MAPbBr<sub>3</sub> perovskite, and it matches well with the previously reported data.<sup>26</sup> We have confirmed molecular ion peak [M+H<sup>+</sup>] at 174.0611 related to API (3-Aminopiperidine dihydrochloride) from High-resolution mass spectrometry (HRMS) data which is collected by dissolving modified crystal in DMSO solvent representing the presence of API in the modified crystal (**Appendix II Fig.** S5).

To understand the changes in the thermal properties of the modified crystal, we calculated the phase transition temperature of reference and modified SCs using the DSC250 differential scanning calorimetry. The obtained results showed no change in the phase transition temperature with additive, obtained at around 328.28 °C for two samples, and this value is nearly close to the earlier reported (**Fig.** 4.1a).<sup>27,28</sup> We also performed thermogravimetric analysis (TGA) of the crystals. The modified crystal exhibits a two-step decomposition process with weight losses of 22.7% and 73.41% at each step, whereas in the control crystal, two-step decomposition with weight losses of 20.8% and 66% is observed (**Fig.** 4.1b). The thermal decomposition of the modified crystal began and finished at 265.7 and 447.6 °C, respectively. As compared with the control crystal, the thermal stability of the modified crystal is relatively high. The enhanced thermal stability of the modified crystal can be attributed to its increased crystallinity and passivating effect of API on the crystal.

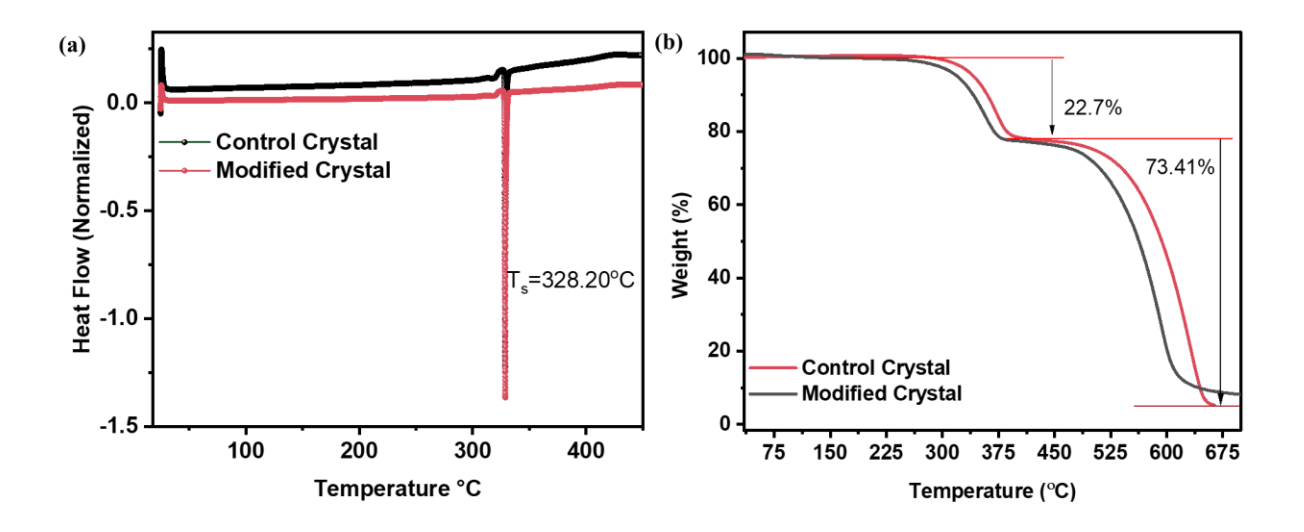


Fig. 4. 1 (a) Differentia scanning calorimetry and (b) Thermogravimetric analysis of control and modified crystals

To investigate the effect of API on the electronic properties of SCs, we first recorded the *I-V* characteristics of the crystals. For this, 100 nm Au electrodes were thermally deposited on the surface of both crystals. The dark current is an important measure for the application of SCs in photodetectors. It is established that dark current originates from material imperfections such as traps.<sup>29</sup> The modified crystal showed a dark current of 7.04 x 10<sup>-6</sup> mA, which is one order of magnitude lower than the control crystal with a dark current of 3.14 x 10<sup>-5</sup> mA at 2 V applied bias (**Fig. 2a**). This lower dark current suggests that modified crystal has lower defect density than the control crystal. The lower defect density can also be due to the passivation of defects induced by API cation.<sup>30</sup> **Fig. 2**(a) compares the dark currents of both the crystals upto 5V applied bias. Furthermore, we recorded the photo-response of both crystals. **Fig. 2**(b) and 2(c) present the illumination power-dependent current-voltage characteristics of control and modified crystals, respectively. As evident from the **Fig.**, the photocurrents increase with the increase in illumination power and bias for both crystals. However, the rising rate of

photocurrent is different for both crystals. In the case of a control crystal, the photocurrent increases exponentially, whereas, in the case of a modified crystal, the current increases dramatically up to 0.5V and then the rise in the rate is slow at a higher bias. Under 575 Wm<sup>-2</sup> illumination, the modified crystal showed a photocurrent of 8.79 x  $10^{-3}$  mA, whereas the control crystal showed a photocurrent of 5.7 x  $10^{-3}$  mA at 2 V applied bias (**Appendix II Fig.** S2a); this can be understood by the fact that photon absorption generated electron-hole pairs in the crystal which drifted to each electrode by the potential difference between electrodes. In the case of a modified electrode, vacancy-assisted carrier recombination is reduced as the trap states are reduced, leading to a higher net current. **Appendix II Fig.** S2(b) compares the photocurrents of both crystals as a function of illumination intensity. According to the light power low,  $I = AP^0$ , where I, A, P and  $\theta$  represent the photocurrent, the constant de-pending on the wavelength, the light power intensity and the exponent determining the response to light intensity, respectively.<sup>31</sup>

The control and modified crystal showed  $\theta$  value of 0.87 and 0.93, respectively. The different value of  $\theta$  suggests different charge collection efficiency of both the crystals. We next studied the effect of doping on hysteresis in the crystals, as perovskites are known to exhibit hysteretic behaviour because of ion migration. Fig. 4.2(d) compares the I-V characteristics measured under forward and reverse scan direction under 575 Wm<sup>-2</sup> illumination. As evident from Fig. 4.2(d), the difference in current under forward and reverse bias ( $\Delta$ I = I<sub>backward</sub> – I<sub>forward</sub>) is marginal, suggesting that both the crystals possess fewer defect densities and therefore suppressed ion migration. Therefore it is difficult to comment on ion migration comparing the hysteresis response observed. To further check the surface of both crystals, we carried out an SEM analysis. As evident from Appendix II Fig. S3, the modified crystal showed a smooth

surface as compared to the control crystal. Peng et al. also reported lower hysteresis in the case of 2D perovskite than 3D perovskite owing to the fact of mobile MA<sup>+</sup> dominant hysteresis.<sup>34</sup>

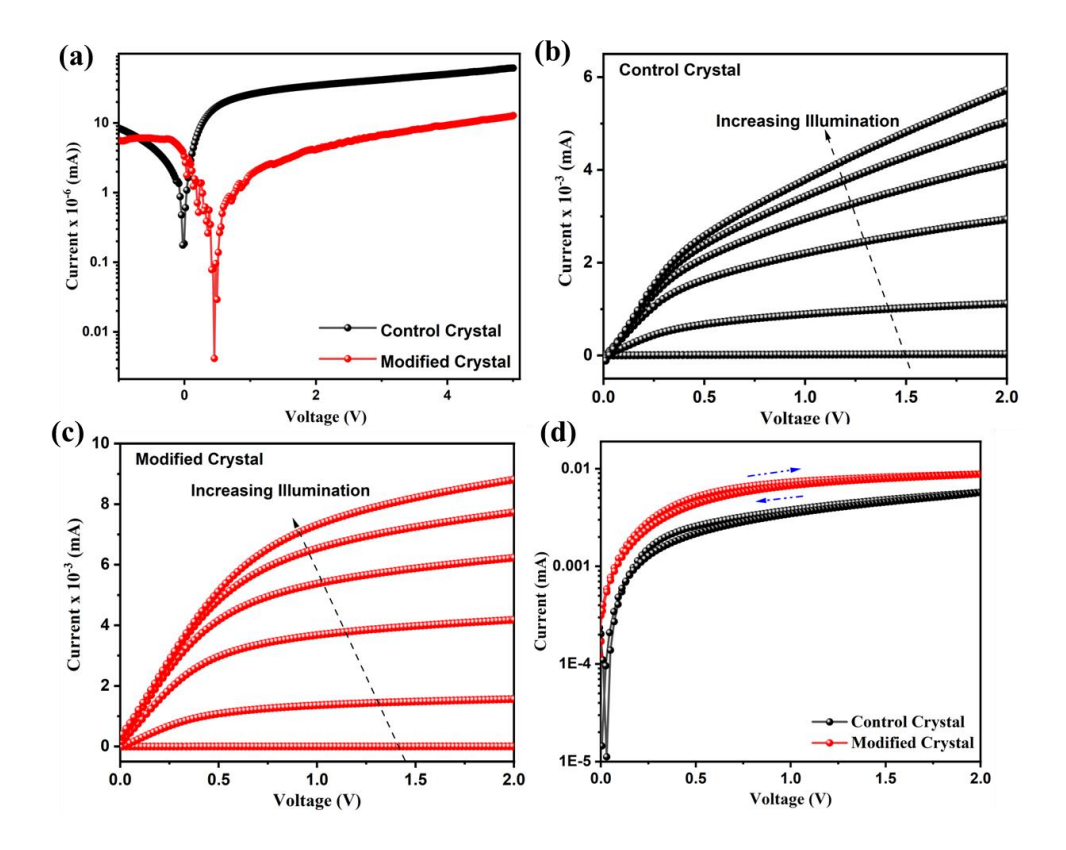


Fig. 4. 2 (a) Semi log plot of I-V characteristics of modified and control SCs in the dark, I-V characteristics as a function of light intensity for (b) Control and (c) modified crystals (d) I-V characteristics at 575 Wm<sup>-2</sup> in forward and reverse scan direction for both the crystals. Scan rate 100 mV/s.

Subsequently, we calculated the responsivity (R) and detectivity (D) of the crystals using the expression  $R = {}^{I_{PC} - I_{dark}}/{}_{P_{irra}.S}$  and  $D = {}^{R}/{}_{(2eI_{dark})^{0.5}}$ , where  $I_{PC}$  and  $I_{dark}$  are photocurrent under illumination and under dark,  $P_{irra}$  is irradiation power density, and S is the effective area of the detector.<sup>35</sup> **Fig.** 4.3 displays the R and D curves for control and modified

crystals. It can be seen from **Figure** that both R & D are remarkably affected by bias. The highest value of R and D obtained for the control crystal is 0.32 mA/W and 1.0 x 10<sup>11</sup> Jones, respectively, at 2V applied bias and 88 Wm<sup>-2</sup> incident illumination intensity. In contrast, the highest value of R and D for modified crystal is 0.47 mA/W and 3.7 x 10<sup>11</sup> Jones, respectively. This improved photoresponsivity is in accordance with the I<sub>photo</sub>-P<sub>light</sub> data discussed above. The higher photoresponsivity suggests lower binding energy in the case of modified crystals, and additionally, the API molecule passivates the defects present in the crystal.<sup>36</sup> Therefore, the photogenerated carriers are collected efficiently at the electrode.

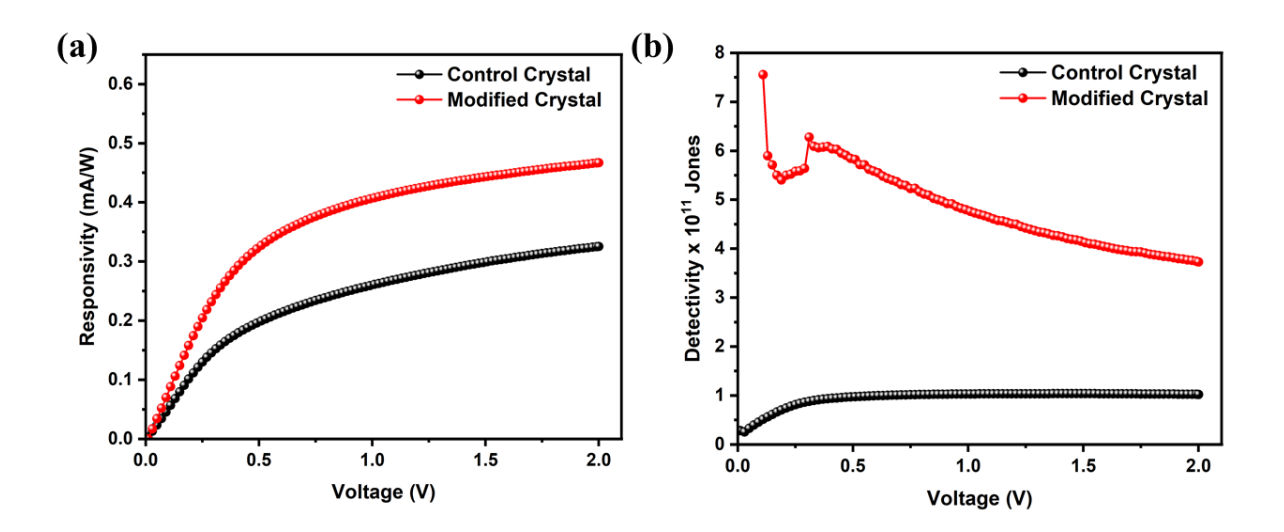


Fig. 4. 3(a) Photo-responsivity and (b) Detectivity for control and modified crystals at 88 Wm<sup>-2</sup> in white light

The response time of both crystals was further investigated by performing time-related current measurements triggered by periodic illumination with different illumination intensities. **Fig. 4.**4(a) and 4(b) depict the crystal's temporal response. The photocurrent increases as soon as the light is turned on and drops to zero when the light is turned off, indicating a quick transfer from optical to electrical signal. However, the photocurrent changing tendency is quite

different. In the control crystal, the photocurrent increases gradually and reaches the maximum when the light is turned on. On the other hand, in the modified crystal, it decreases rapidly after getting the maximum value.

Additionally, the rise time (photocurrent increases from 10% to 90% of the peak value) and fall time (photocurrent decreases from 90% to 10% of the peak value) were extracted from the normalised photoresponse characteristics (**Fig.** 4.4c).<sup>37</sup> The control crystal showed a rise time of 180 ms. This is reduced in the case of modified crystal (170 ms). In principle, the rise and fall time should be related to charge trapping and de-trapping processes, as the other phenomenon is much faster.<sup>38</sup> The faster rise time in the case of a modified crystal can be due to reduced defect sites or ion migration. As for lead halide perovskite materials, the low activation energy of site vacancy enables ion migration and causes anomalous photocurrent hysteresis in various perovskite solar cells. Physically, the ion migration in perovskite will lead to complex electrical phenomena, such as the accumulated charge-induced localized interfacial electric field, which may accelerate or decelerate charge transport or charge rearrangement in response to ionic migration and slow drift and diffusion of ionic defects.<sup>36,39</sup> However, the abovementioned hysteresis suggests little influence of API doping on ion migration. Therefore, we performed EIS and capacitance-frequency measurements to further understand the charge accumulation and recombination in these crystals.

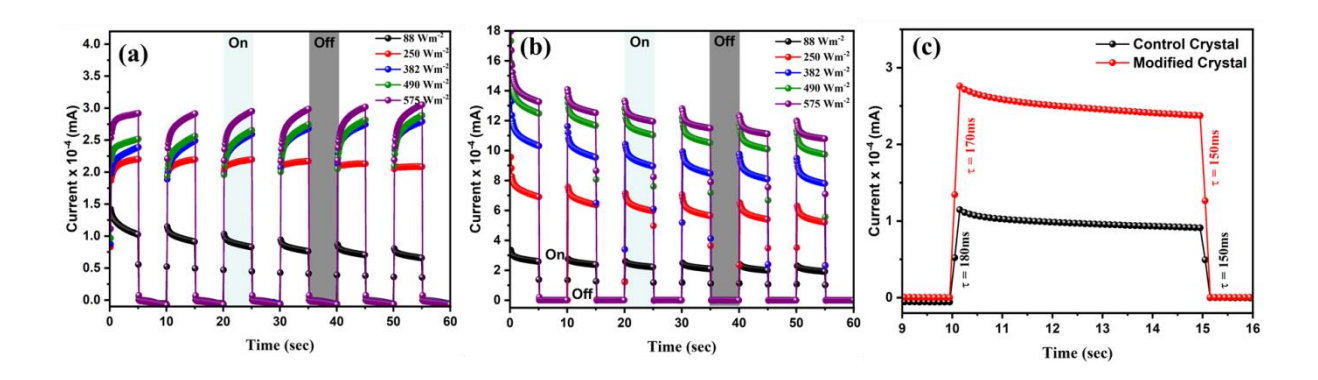


Fig. 4. 4 Temporal response of (a) Control and (b) modified crystals at different illumination intensities (c) Enlarged view of rise and fall regions for both the crystals.

EIS is considered a powerful tool to understand the charge accumulation and recombination dynamics of an electrochemical system. EIS of control and modified SCs are measured as a function of illumination intensity in the frequency range of 1 MHz to 1 Hz (Fig. S4). The Nyquist spectra of both samples exhibit two semicircles with a difference in magnitude in the probed frequency range. The semicircles centred at 10 Hz and 1200 Hz in the case of control crystal and 10 Hz and 25000 Hz in the case of modified crystal at low illumination level (88 Wm<sup>-2</sup>), which shifts to 10 Hz and 22000 Hz at high illumination (575 Wm<sup>-2</sup>) in case of control crystal and 10 Hz and 29000 Hz in case of modified crystal. In both cases, the semi-circle centred at 10Hz is found to be illumination independent. Similar behaviour of low frequency centred frequency or corresponding time response with change in illumination is observed by other authors. It is well established that in perovskite materials, the low-frequency arc corresponding to a time scale of ms or sec is due to ion motions and is found to be mostly due to halides. One can ignore the contribution of incorporated API cation on the low frequency as relaxation time is generally in Sec or hour range. Interestingly the incorporation of API in reference SCs significantly alters the resistive properties. The series resistance of 0.59 and 0.26

 $M\Omega$  is found at an illumination level of 88 Wm<sup>-2</sup> and has been reduced to 68.8 k $\Omega$  and 0.19 M $\Omega$  at 575 Wm<sup>-2</sup>illumination for control and modified SCs. Reduced series resistance is because of the improved surface conductivity and smooth surface of the modified crystals. The smooth surface of the modified crystal is also evident in SEM images, as discussed above. With an increase in illumination level, the series resistance and the arc of low and high frequency for both the crystals change significantly, which signifies the change in surface and bulk conductivity. However, the faster rate of change of resistance and lower order of magnitude of resistance in modified crystals signifies that the incorporation of API significantly improves the conductive properties of crystals. The change in low and high-frequency resistance with illumination for both the crystals is shown in **Fig.** 5(a) and 5(b). Both the high and low-frequency resistance decreases drastically with the increase in illumination intensity in modified crystals as compared to control crystals.

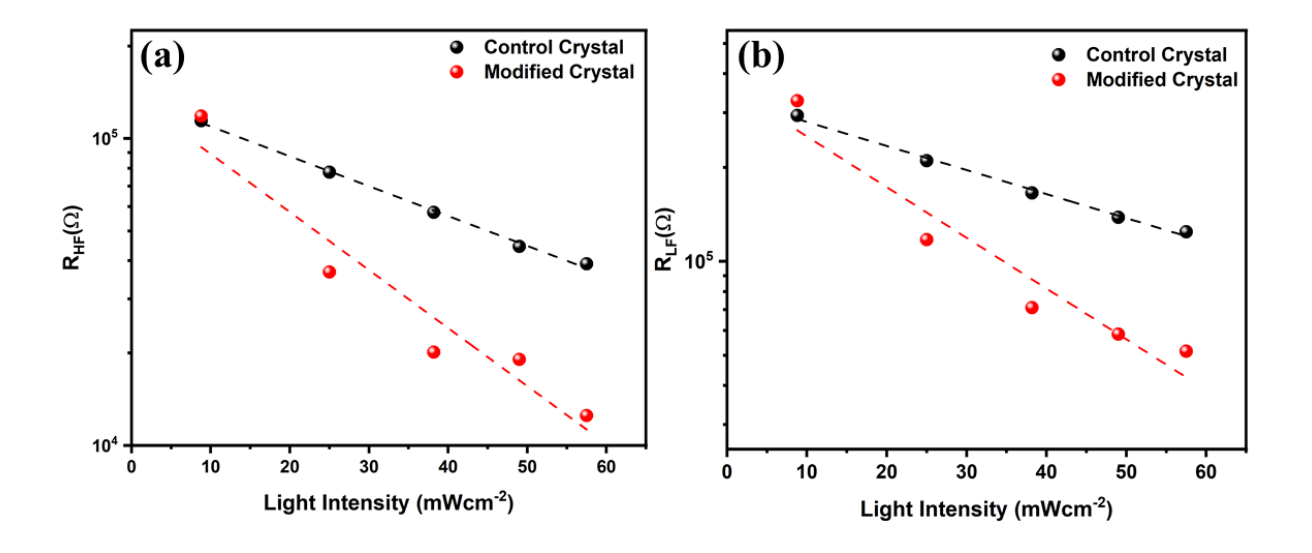


Fig. 4. 5(a) High-frequency and (b) low-frequency resistance as a function of light intensity

Looking at the hysteresis behaviour in **Fig.** 2(d), a comparatively similar behaviour was noted. To further confirm this behaviour capacitance-frequency plot of both the crystals is measured and shown in **Fig.** 6(a) and 6(b) for the control and modified crystal, respectively. A comparative value of capacitance at low frequency further confirms the similar hysteresis behaviour in both crystals. From the analysis of hysteresis in J-V, peak frequency of low arc in Nyquist spectra and capacitance-frequency plot, it is interpreted that both the crystals depict similar behaviour in terms of ions accumulation or ions motion. To further confirm the nature of ions capacitance-frequency plot as a function of temperature is measured and shown in **Fig.** 6(c) and 6(d) for control and modified crystal, respectively. The capacitance plot of the crystals depicts similar values and trends in the probed low-frequency region (<100Hz). From the shown plot, one can expect the comparable ion activation energy to signify that the incorporation of API modulates the structural and conductive properties while ions' behaviour is the same.

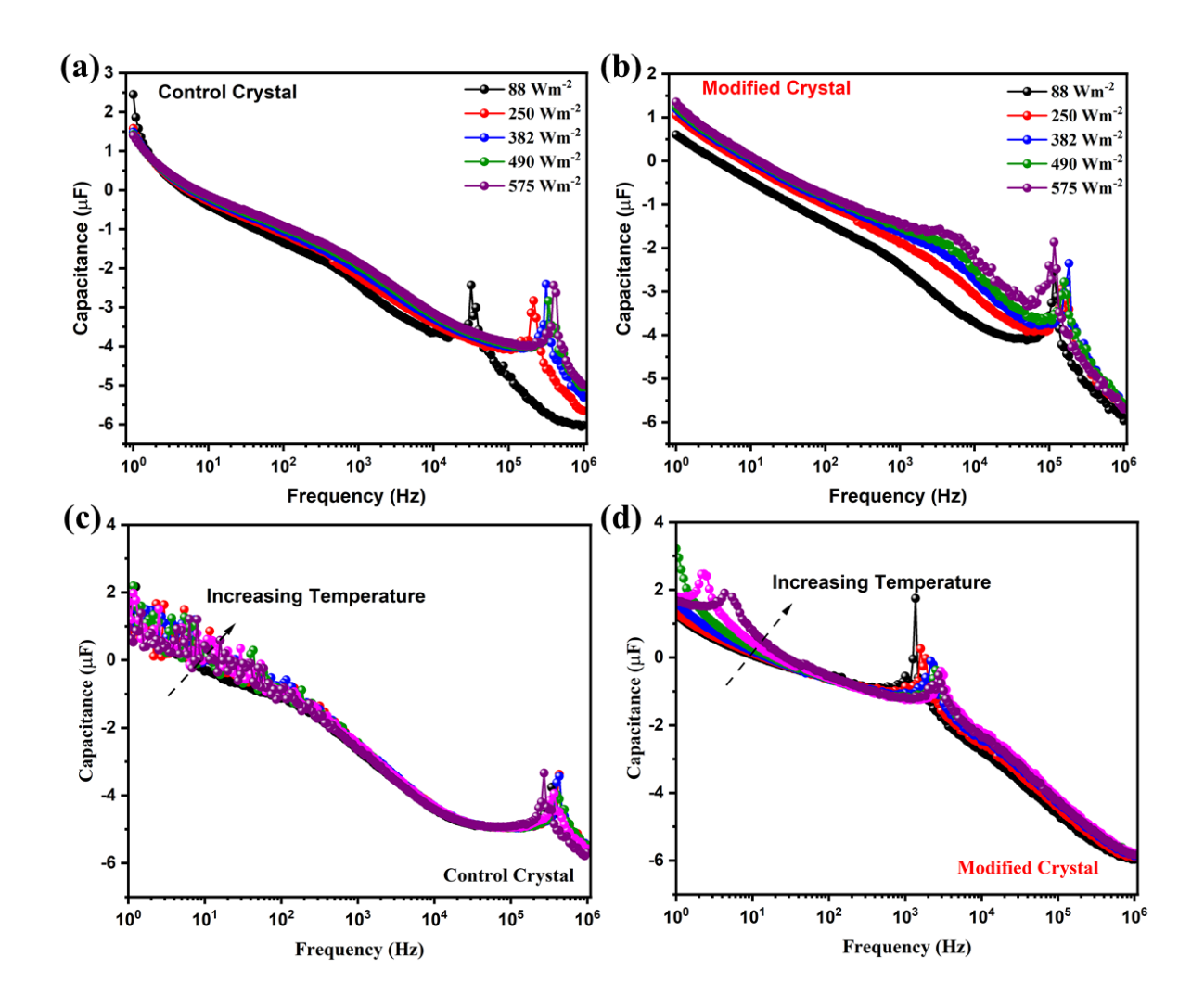


Fig. 4. 6 Capacitance-frequency plot as a function of light intensity for (a) control and (b) modified crystals, Capacitance-frequency plot as a function of temperature for (c) control and (d) modified crystals

## 4.3. Conclusion

In summary, we have modulated the crystal growth of MAPbBr<sub>3</sub> SCs using a heterocyclic additive with two active nitrogen sites. The modified crystal effectively passivates the defects, improves charge collection efficiency and reduces recombination. The lower dark current of

 $7.04 \times 10^{-6}$  mA, compared to the control crystal with a dark current of  $3.14 \times 10^{-5}$  mA, suggests lower trap density in the modified crystal. Furthermore, the modified crystal showed improved photoresponsivity and detectivity, which is in accordance with the result obtained  $I_{photo}$ - $P_{light}$  data. The high and low-frequency resistance as a function of illumination intensity also shows drastically reduced resistance in the case of modified crystals with increasing light intensity. Thus, we have systematically studied the effect of heterocyclic additives on the electrical response of halide perovskite SCs.

### **Supporting Information**

Optical Images of crystals, Plots of XRD, SEM, Current -Voltage, Nyquist spectra of EIS

## **References**

- (1) Yin, W. J.; Shi, T.; Yan, Y. Unique Properties of Halide Perovskites as Possible Origins of the Superior Solar Cell Performance. *Advanced Materials* **2014**, *26*, 4653–4658.
- (2) Frost, J. M.; Butler, K. T.; Brivio, F.; Hendon, C. H.; Van Schilfgaarde, M.; Walsh, A. Atomistic Origins of High-Performance in Hybrid Halide Perovskite Solar Cells. *Nano Letters* **2014**, *14*, 2584–2590.
- (3) Park, N. G. Perovskite Solar Cells: An Emerging Photovoltaic Technology. *Materials Today* **2015**, *18*, 65–72.
- (4) Tress, W. Perovskite Solar Cells on the Way to Their Radiative Efficiency Limit Insights Into a Success Story of High Open-Circuit Voltage and Low Recombination.

  \*Advanced Energy Material 2017, 7, 1602358.
- (5) Best Research-Cell Efficiency Chart | Photovoltaic Research | NREL.
- (6) Lira-Cantú, M. Perovskite Solar Cells: Stability Lies at Interfaces. *Nature Energy* 2017,2, 17115.
- (7) Zhao, X.; Park, N. G. Stability Issues on Perovskite Solar Cells. *Photonics* **2015**, *2*, 1139–1151.
- (8) Urbina, A. The Balance between Efficiency, Stability and Environmental Impacts in

- Perovskite Solar Cells: A Review. Journal of Physics: Energy 2020, 2, 022001.
- (9) Trivedi, S.; Prochowicz, D.; Parikh, N.; Mahapatra, A.; Pandey, M. K.; Kalam, A.; Tavakoli, M. M.; Yadav, P. Recent Progress in Growth of Single-Crystal Perovskites for Photovoltaic Applications. ACS Omega 2021, 6, 1030–1042.
- (10) Parikh, N.; Tavakoli, M. M.; Pandey, M.; Kumar, M.; Prochowicz, D.; Chavan, R. D.; Yadav, P. Two-Dimensional Halide Perovskite Single Crystals: Principles and Promises. *Emergent Materials* **2021**, 1–16.
- (11) Peng, W. Single Crystals of Organolead Halide Perovskites: Growth, Characterization, and Applications. *Thesis* **2017**.
- (12) Mahapatra, A.; Parikh, N.; Kumari, H.; Pandey, M. K.; Kumar, M.; Prochowicz, D.; Kalam, A.; Tavakoli, M. M.; Yadav, P. Reducing Ion Migration in Methylammonium Lead Tri-Bromide Single Crystal via Lead Sulfate Passivation. *Journal of Applied Physics* 2020, 127, 185501.
- (13) Wu, B.; Nguyen, H. T.; Ku, Z.; Han, G.; Giovanni, D.; Mathews, N.; Fan, H. J.; Sum, T.
  C. Discerning the Surface and Bulk Recombination Kinetics of Organic-Inorganic Halide Perovskite Single Crystals. *Advanced Energy Materials* 2016, 6, 1600551.
- (14) Parikh, N.; Pandey, M.; Prochowicz, D.; Kalam, A.; Tavakoli, M. M.; Satapathi, S.; Akin, S.; Yadav, P. Investigation on the Facet-Dependent Anisotropy in Halide Perovskite Single Crystals. *Journal of Photochemistry C* **2022**, *126*, 8906–8912.
- (15) Rakita, Y.; Lubomirsky, I.; Cahen, D. When Defects Become 'Dynamic': Halide

- Perovskites: A New Window on Materials? *Materials Horizons* **2019**, *6*, 1297–1305.
- (16) Shi, D.; Adinolfi, V.; Comin, R.; Yuan, M.; Alarousu, E.; Buin, A.; Chen, Y.; Hoogland,
  S.; Rothenberger, A.; Katsiev, K.; Losovyj, Y.; Zhang, X.; Dowben, P. A.; Mohammed,
  O. F.; Sargent, E. H.; Bakr, O. M. Low Trap-State Density and Long Carrier Diffusion in Organolead Trihalide Perovskite Single Crystals. *Science* (80) 2015, 347, 519–522.
- (17) Duim, H.; Fang, H.-H.; Adjokatse, S.; ten Brink, G. H.; Marques, M. A. L.; Kooi, B. J.; Blake, G. R.; Botti, S.; Loi, M. A. Mechanism of Surface Passivation of Methylammonium Lead Tribromide Single Crystals by Benzylamine. *Applied Physics Reviews* 2019, 6, 031401.
- (18) Chen, L.; Wang, H.; Zhang, W.; Li, F.; Wang, Z.; Wang, X.; Shao, Y.; Shao, J. Surface Passivation of MAPbBr3Perovskite Single Crystals to Suppress Ion Migration and Enhance Photoelectronic Performance. *ACS Applied Materials and Interfaces* **2022**, *14*, 10917–10926.
- (19) Liu, Y.; Zheng, X.; Fang, Y.; Zhou, Y.; Ni, Z.; Xiao, X.; Chen, S.; Huang, J. Ligand Assisted Growth of Perovskite Single Crystals with Low Defect Density. *Nature Communications*. 2021 121 2021, 12, 1–8.
- (20) Daniel J. F.; Hiroaki S.; Ashwin N.; James V. P.; Michelle C.; Joseph P.; Liam C. P.; Michael R. W.; Samuel I. S. Structure and Chemical Stability in Perovskite-Polymer Hybrid Photovoltaic Materials *Journal of Material Chemistry A* 2019, 7, 1687-1699.
- (21) Mahapatra, A.; Prochowicz, D.; Tavakoli, M. M.; Trivedi, S.; Kumar, P.; Yadav, P. A

Review of Aspects of Additive Engineering in Perovskite Solar Cells. *Journal of Material Chemistry A* **2020**, *8*, 27–54.

- (22) Peng, J.; Xia, C. Q.; Xu, Y.; Li, R.; Cui, L.; Clegg, J. K.; Herz, L. M.; Johnston, M. B.; Lin, Q. Crystallization of CsPbBr<sub>3</sub> Single Crystals in Water for X-Ray Detection. *Nature Communications* 2021 121 **2021**, 12, 1–10.
- (23) Feng, Y.; Pan, L.; Wei, H.; Liu, Y.; Ni, Z.; Zhao, J.; Rudd, P. N.; Cao, L. R.; Huang, J. Low Defects Density CsPbBr<sub>3</sub> Single Crystals Grown by an Additive Assisted Method for Gamma-Ray Detection Low Defects Density CsPbBr<sub>3</sub> Single Crystals Grown by an Additive Assisted Method for Gamma-Ray Detection *Journal of Material Chemistry C* **2020**, *8*, 11360-11368.
- (24) Peng, W.; Aranda, C.; Bakr, O. M.; Garcia-Belmonte, G.; Bisquert, J.; Guerrero, A. Quantification of Ionic Diffusion in Lead Halide Perovskite Single Crystals. *ACS Energy Letters* **2018**, *3*, 1477–1481.
- (25) Saidaminov, M. I.; Abdelhady, A. L.; Murali, B.; Alarousu, E.; Burlakov, V. M.; Peng, W.; Dursun, I.; Wang, L.; He, Y.; Maculan, G.; Goriely, A.; Wu, T.; Mohammed, O. F.; Bakr, O. M. High-Quality Bulk Hybrid Perovskite Single Crystals within Minutes by Inverse Temperature Crystallization. *Nature Communications* 2015, 6, 7586.
- (26) Wang, T.; Jin, L.; Hidalgo, J.; Chu, W.; Snaider, J. M.; Deng, S.; Zhu, T.; Lai, B.; Prezhdo, O.; Correa-Baena, J. P.; Huang, L. Protecting Hot Carriers by Tuning Hybrid Perovskite Structures with Alkali Cations. *Science Advances* **2020**, *6*.

(27) Zhang, L.; Liu, Y.; Ye, X.; Han, Q.; Ge, C.; Cui, S.; Guo, Q.; Zheng, X.; Zhai, Z.; Tao, X. Exploring Anisotropy on Oriented Wafers of MAPbBr<sub>3</sub> Crystals Grown by Controlled Antisolvent Diffusion. *Crystal Growth & Design* 2018, 18, 6652–6660.

- (28) Yang, B.; Ming, W.; Du, M.-H.; Keum, J. K.; Puretzky, A. A.; Rouleau, C. M.; Huang, J.; Geohegan, D. B.; Wang, X.; Xiao, K. Real-Time Observation of Order-Disorder Transformation of Organic Cations Induced Phase Transition and Anomalous Photoluminescence in Hybrid Perovskites. *Advanced Materials* 2018, 30, 1705801.
- (29) Duijnstee, C.; Corre, L.; Jan Anton, L.; Duijnstee, E. A.; Le Corre, V. M.; Johnston, M.
   B.; Jan Anton Koster, L.; Lim, J.; Snaith, H. J. Understanding Dark Current-Voltage
   Characteristics in Metal-Halide Perovskite Single Crystals. APS 2021, 15, 14006.
- (30) Mao, L.; Ke, W.; Pedesseau, L.; Wu, Y.; Katan, C.; Even, J.; Wasielewski, M. R.; Stoumpos, C. C.; Kanatzidis, M. G. Hybrid Dion-Jacobson 2D Lead Iodide Perovskites. *Journal of the American Chemical Society* **2018**, *140*, 3775–3783.
- (31) Kim, J. H.; Han, H.; Kim, M. K.; Ahn, J.; Hwang, D. K.; Shin, T. J.; Min, B. K.; Lim, J. A. Solution-Processed near-Infrared Cu(In, Ga)(S, Se)<sub>2</sub> Photodetectors with Enhanced Chalcopyrite Crystallization and Bandgap Grading Structure via Potassium Incorporation. *Scientific reports* 2021, 11, 7820.
- (32) Snaith, H. J.; Abate, A.; Ball, J. M.; Eperon, G. E.; Leijtens, T.; Noel, N. K.; Stranks, S. D.; Wang, J. T. W.; Wojciechowski, K.; Zhang, W. Anomalous Hysteresis in Perovskite Solar Cells. *Journal of Physical Chemistry Letters* 2014, 5, 1511–1515.

(33) Meloni, S.; Moehl, T.; Tress, W.; Franckeviius, M.; Saliba, M.; Lee, Y. H.; Gao, P.; Nazeeruddin, M. K.; Zakeeruddin, S. M.; Rothlisberger, U.; Graetzel, M. Ionic Polarization-Induced Current-Voltage Hysteresis in CH3NH3PbX3 Perovskite Solar Cells. *Nature Communications* **2016**, *7*, 1–9.

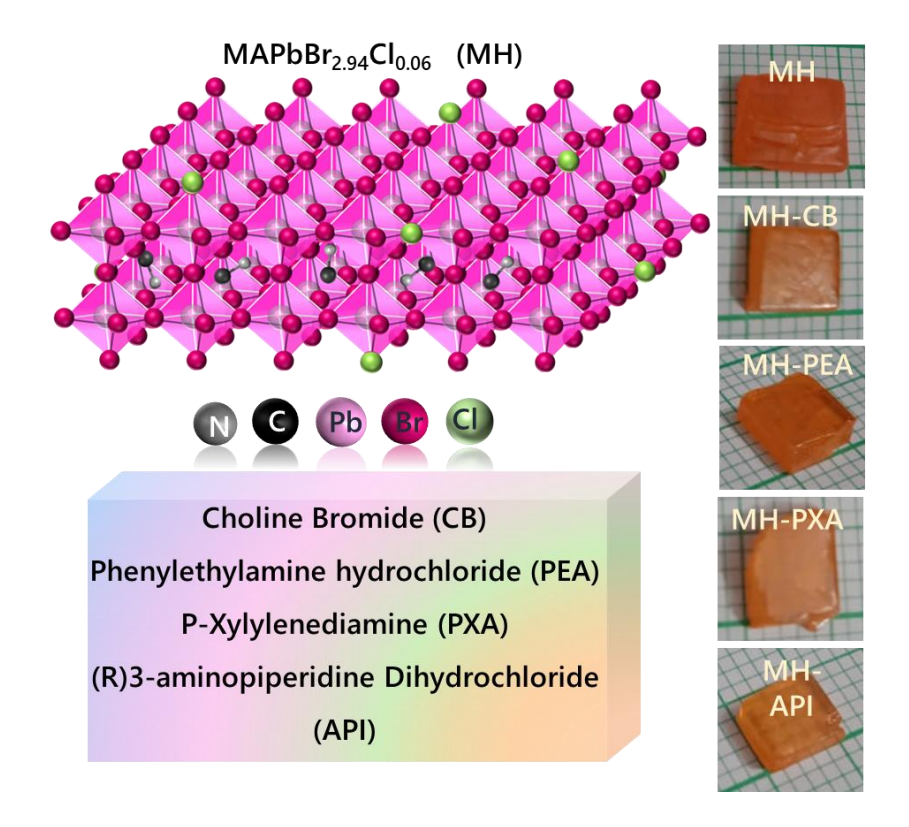
- (34) Peng, W.; Yin, J.; Ho, K. T.; Ouellette, O.; De Bastiani, M.; Murali, B.; El Tall, O.; Shen, C.; Miao, X.; Pan, J.; Alarousu, E.; He, J. H.; Ooi, B. S.; Mohammed, O. F.; Sargent, E.; Bakr, O. M. Ultralow Self-Doping in Two-Dimensional Hybrid Perovskite Single Crystals. *Nano Letters* **2017**, *17*, 4759–4767.
- (35) Ding, J.; Jing, L.; Cheng, X.; Zhao, Y.; Du, S.; Zhan, X.; Cui, H. Design Growth of MAPbI3 Single Crystal with (220) Facets Exposed and Its Superior Optoelectronic Properties. *Journal of Physical Chemistry Letters* 2018, 9, 216–221.
- (36) Wang, K.; Wu, C.; Yang, D.; Jiang, Y.; Priya, S. Quasi-Two-Dimensional Halide Perovskite Single Crystal Photodetector. *ACS Nano* **2018**, *12*, 4919–4929.
- (37) Fang, Y.; Dong, Q.; Shao, Y.; Yuan, Y.; Huang, J. Highly Narrowband Perovskite Single-Crystal Photodetectors Enabled by Surface-Charge Recombination. *Nature Photonics* **2015**, *9*, 679–686.
- (38) Dong, R.; Fang, Y.; Chae, J.; Dai, J.; Xiao, Z.; Dong, Q.; Yuan, Y.; Centrone, A.; Zeng, X. C.; Huang, J. High-Gain and Low-Driving-Voltage Photodetectors Based on Organolead Triiodide Perovskites. *Advanced Materials* 2015, 27, 1912–1918.
- (39) Yuan, Y.; Huang, J. Ion Migration in Organometal Trihalide Perovskite and Its Impact

on Photovoltaic Efficiency and Stability. *Accounts of chemical research* **2016**, *49*, 286–293.

- (40) Contreras-Bernal, L.; Ramos-Terrón, S.; Riquelme, A.; Boix, P. P.; Idígoras, J.; Mora-Seró, I.; Anta, J. A. Impedance Analysis of Perovskite Solar Cells: A Case Study. *Journal of Material Chemistry A* **2019**, *7*, 12191–12200.
- (41) Afroz, M. A.; Aranda, C. A.; Tailor, N. K.; Yukta; Yadav, P.; Tavakoli, M. M.; Saliba, M.; Satapathi, S. Impedance Spectroscopy for Metal Halide Perovskite Single Crystals: Recent Advances, Challenges, and Solutions. ACS Energy Letters 2021, 6, 3275–3286.
- (42) Prochowicz, D.; Trivedi, S.; Parikh, N.; Saliba, M.; Kalam, A.; Mahdi Tavakoli, M.; Yadav, P. In the Quest of Low-Frequency Impedance Spectra of Efficient Perovskite Solar Cells. *Energy Technology* **2021**, *9*, 1–9.

# CHAPTER-5a Additive Engineered MAPbBr<sub>3-X</sub>Cl<sub>x</sub>

# Single Crystals; and Higher-Order Harmonics Study



Sarvani Jowhar Khanam<sup>a</sup>, Srinivasa Rao Konda<sup>b,#</sup>, Ravi Ketavath<sup>a</sup>, Wufeng Fu<sup>b</sup>, Wei Li<sup>b,†</sup> and Banavoth Murali<sup>a,\*</sup>

corresponding authors: \* murali.banavoth@uohyd.ac.in, #ksrao@ciomp.ac.cn,† weili1@ciomp.ac.cn

<sup>&</sup>lt;sup>a</sup>Solar Cells and Photonics Research Laboratory, School of Chemistry, University of Hyderabad, Hyderabad 500046, Telangana, India

<sup>&</sup>lt;sup>b</sup>The GPL Photonics Laboratory, State Key Laboratory of Luminescence and Applications, Changchun Institute of Optics, Fine Mechanics and Physics, Chinese Academy of Sciences, Changchun, 130033, China

# **ABSTRACT**

Mixed-halide perovskite materials (MHSCs) are alluring materials for photonics applications. Tunable bandgap, defect tolerance properties, and easy processability made these materials promising for many applications. However, the commercialization of these materials is severely affected by Phase segregation. Current work focuses on the change in higher harmonics in MAPbBr<sub>3-x</sub>Cl<sub>x</sub> single crystals (MHSC) with changing nitrogen-based additives. These additives act as a passivating layer and improve the nano-level crystallinity. The additive engineering strategy has an impact on morphological and optical properties. Moreover, the x-ray diffraction data revealed no influence on unit cell structure in modified MHSCs. Subsequently, of higher bond strength of 3-aminopiperidine (API), HHG MH: API crystal compared to other modified MHSC.

Keywords: High-order harmonics, Laser, Mixed halides, 3D perovskite single crystals, additives.

### **5.1.1 Introduction**

Organic-inorganic hybrid mixed-halide perovskites are auspicious resources in nearly all fields of science and technology like light-emitting diodes (LEDs), <sup>1–10</sup> leaser, <sup>11,12</sup> luminescent solar concentrators, <sup>13,14</sup> memristors, <sup>15</sup> photovoltaics, <sup>16,17,26,18–25</sup> X-rays, <sup>27</sup> and gamma rays because of its tunable bandgap, and higher optoelectronic properties with a large dielectric constant <sup>28</sup> and low-cost processability. <sup>29</sup> This material possesses an ABX<sub>3</sub> structure in which a bandgap is formed by combining the metal and halide (MX<sub>6</sub>( octahedral unit) *s*, *p* orbitals. Changing the concentration of halides and metals can directly influence bandgap tuning. Cations located in the voids of these interlinked octahedra indirectly affect these materials' bandgap. <sup>30–33</sup>

Crystals are grown either by optimizing the material composition or by optimizing the temperature. Some crystallization methods include the inverse temperature method (ITC),<sup>34</sup> temperature lowering method,<sup>35</sup> top-seeded crystallization method,<sup>36</sup> anti-solvent vapor assistant method (AVC),<sup>37,38</sup> Bridgman growth method,<sup>39</sup> low-temperature gradient crystallization,<sup>40</sup> cavitations triggered asymmetrical crystallization and room temperature liquid diffused separation induced crystallization (LDSC).<sup>41</sup> Although PSCs growth techniques have rapidly improved the surface quality<sup>1,42</sup> and crystals' performance, stability issues like phase segregation,<sup>43–45</sup> rapid material degradation,<sup>46,47</sup> hysteresis,<sup>48,49</sup> and environmental factors, such as moisture and heat<sup>50</sup> are the challenge that hampers the commercialization of these materials.<sup>1,20,22,34,41,42</sup>

Phase segregation has been explained using experiments with a continuous wave (CW) diode laser in the case of microcrystalline thin films. Additionally, forming formamidinium and

cesium lead iodide solid-state alloys stabilized the perovskite structures by tuning the tolerance factor. Cl-doping into perovskite precursor solutions has been widely reported to tune the optoelectronic properties of perovskite materials. Meanwhile, a traditional class of MAPbBr<sub>3-x</sub>Cl<sub>x</sub> (x = 0 to 3) SCs at different concentrations of Cl doping has been investigated by Tyler Mix et al. with increased LED performances in the case of x = 0.06 (2% Cl). However, only a few reports are available in the literature on the additives engineering strategy for 3D MHSC growth and its tunable HHG.

In this work, different additives added to the targeted 2% Cl-doped MHSCs band gap of 2.3 eV were reported elsewhere to study the change in HHG in modified MHPSCs.<sup>52</sup> owing to its outperformed its 2.3 eV counterpart in optoelectronic properties with increased Cl fraction. We have used the additive engineering method to stabilize the MHSCs surface further and improve the transparency by increasing the crystallinity. Injecting different additives into a mixed halide precursor solution has been reported herein to provide an adequate understanding of improving the MHPSCs surface morphology and crystallinity with changing bonding interactions. This formats an ionic interaction with the crystallites in a solution that can modify the nucleation and prevent preferential directional growth and crystal growth dynamics. Herein, successive experiments have been carried out to investigate the structural, morphological and optical properties of pure and additive-engineered SCs (modified SCs). This paper addresses the stability issue of MHPSCs for tunable HHG applications using the N group additives with aliphatic, aromatic and heterocyclic moieties during crystal growth.

### 5.1.2. Results and Discussion

### **5.1.2.1.** Morphology and Structural Properties

N-based aliphatic, aromatic with one or two amine groups and heterocyclic organic molecules as an additive interact differently with the surface and have higher stability than their MABr counterparts. In the present work, we have chosen salts of additives like choline bromide (CB, aliphatic), phenylethylamine hydrochloride (PEA, aromatic), P-xylylenediamine dihydrochloride (PXA, aromatic) and (R)3-aminopiperidine dihydrochloride (API, heterocyclic) to grow the MAPbBr<sub>2.94</sub>Cl<sub>0.06</sub> SC (pristine), which acts as a passive layer on the surface of MHSCs. The PL measurements carried out using a 488 nm laser observed the blue shift as the Cl concentration increased in the modified MHSCs, as shown in **Fig. S1a**. Further, the change in Cl concentrations of SCs confirmed using EDX measurements (**Fig. S1b**).

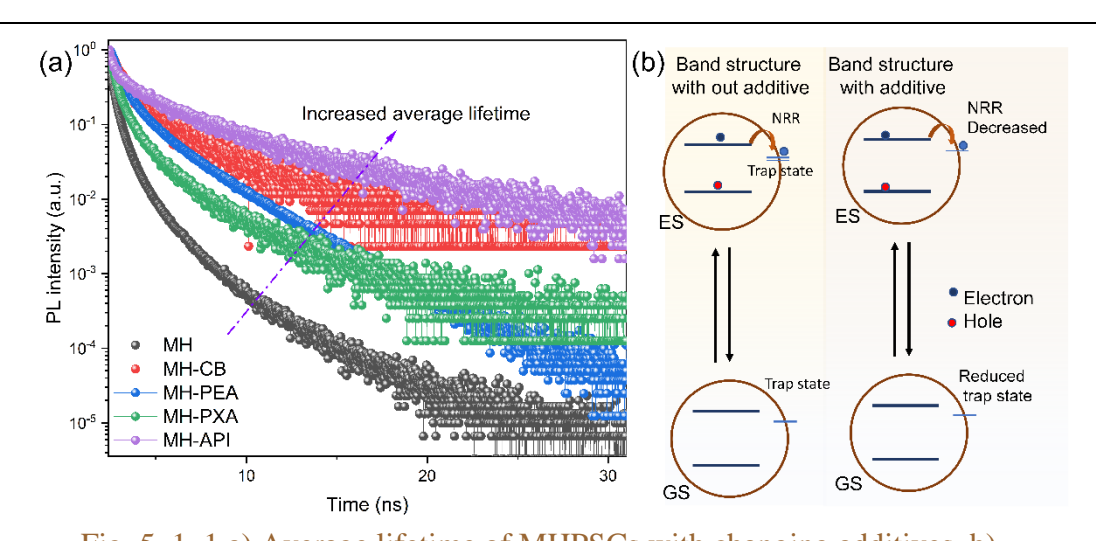


Fig. 5. 1. 1 a) Average lifetime of MHPSCs with changing additives. b) schematic representation of decreasing surface defects by adding additives to electronic band structure model in modified MHPSCs with comparison to

pristine.

Generally, the transient evolution of the electron-hole population after impulsive photoexcitation can be calculated from time-resolved PL (TRPL) measurements. As discussed above, Modified PSCs showed a slight change in optical properties confirmed by steady-state PL. Furthermore, to investigate the changes in average exciton lifetime, TRPL has been recorded. Subsequently, the decay curves of the excited carrier in the modified PSCs are fitted using a tri-exponential decay model to quantify the carrier dynamics, and the fitted parameters are summarized in **Table. 5.1**. The average PL lifetime considerable increase from 0.37 ns (pristine) to 1.51 ns in MH-CB SCs (**Fig. 5.1a**).<sup>53,54</sup>

#### 5.1.2.2. Thermogravimetric/Differential Scanning Calorimetric Analysis

The thermodynamic properties in modified MHPSCs have been anlyzed using Differential scanning calorimetry (DSC) and thermogravimetric analysis (TGA) with a heating rate of 10 °C/min in an N<sub>2</sub> atmosphere. Interestingly, a change in the phase transition temperature (T<sub>s</sub>) in modified MHPSCs was observed, around 328.69 to 329.52 °C in DSC. Subsequently, indicates whether the process is exothermic or endothermic, as shown in **Fig.** 

5.2a. Most PSCs' thermal decomposition follows two steps, first organic moiety and second lead halide decomposition in TGA, as shown in **Equation 1**.<sup>55</sup>

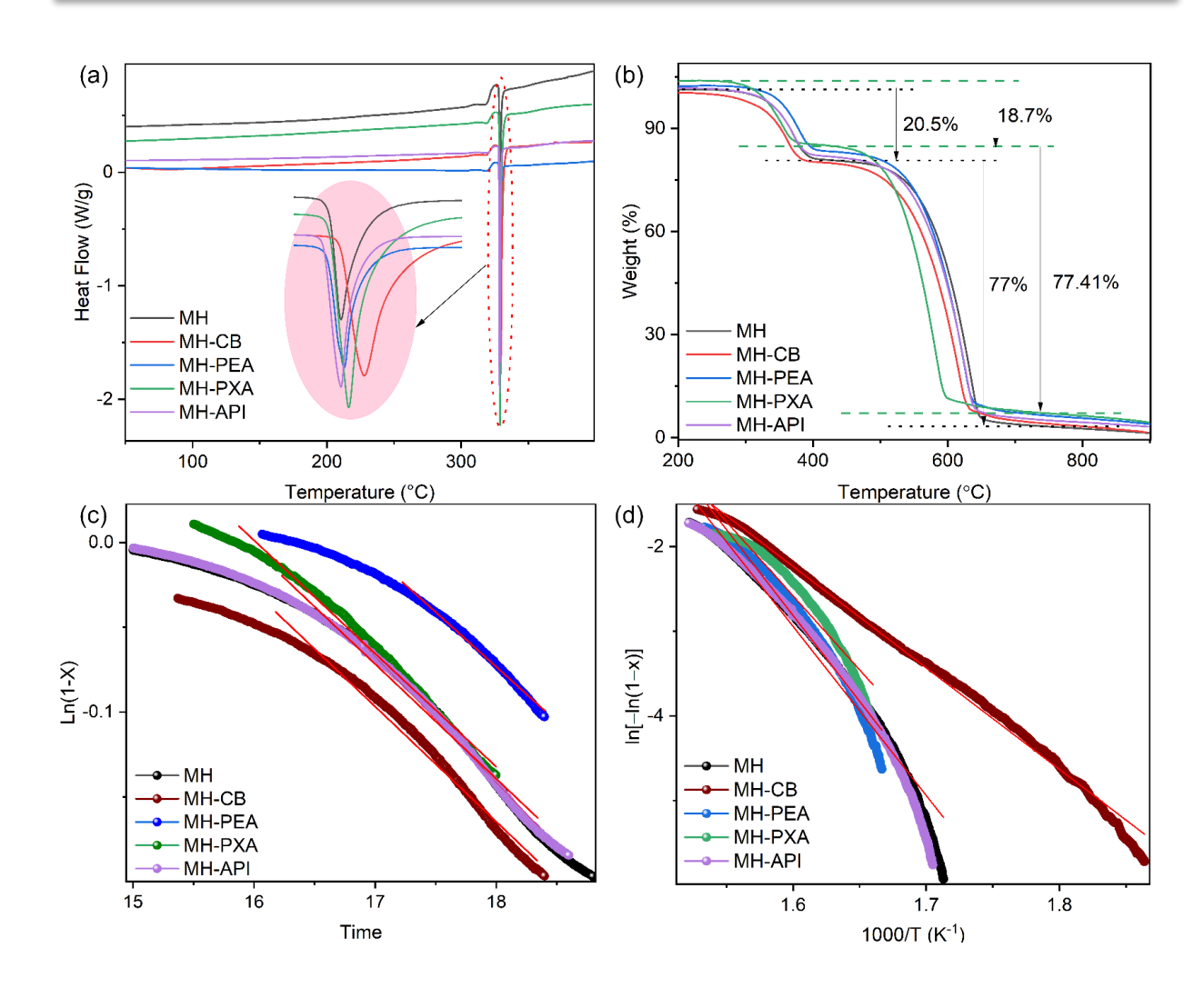


Fig. 5. 1. 2 a) Change in phase transition temperature (insert) second heating in Differential scanning calorimetry and b) TGA of pristine and modified MHPSCs. c) Plot of  $\ln (1-x)$  vs Time and d) Plot of  $\ln [-\ln(1-x)]$  vs 1000/T of organic moiety decomposition in MHPSCs.

TGA of pristine and modified MH-PXA SCs have shown a decomposition with weight losses of 22.7, 73.41%, and 20.8, 66% at each step, respectively (**Fig. 5.2b**). Herein, the organic moiety degradation stat and ends at ~ 300 and 382 °C. Considering phase one transformations as a first-order reaction, the Kinetics and thermodynamic parameters of the reaction were calculated using the equations reported in the literature.<sup>56</sup>

$$\frac{dx}{dt} = k(1 - x) \tag{2}$$

where 
$$x = \frac{wi - wt}{wi - wf}$$
 (3)

wi is the initial weight, wt is the weight of the sample at a particular time t, and wf is the final weight. A straight line of plotted graph (Fig. 5.2c) using Equations 2 and 3 for the selected phase confirms the first-order reactions. Kinetics parameters were determined using a modified form of the Coats and Redfern model as described in Equation 4.

$$\ln[-\ln(1-x)] = \ln\frac{ART^2}{\beta E_a} - \frac{E_a}{RT}$$
(4)

Where A is the pre-exponential factor,  $\beta$  is a heating rate (10 °C/min), R is the general gas constant (8.3143 J mol<sup>-1</sup> K<sup>-1</sup>),  $E_a$  is the activation energy, and T is the temperature (K).

**Table 5.1** Comparative study of MHPSCs thermodynamic properties of phase one transformations.

MHPSCs	Temperature	Ea	ΔHs	ΔS	ΔG
	(T <sub>s</sub> ) °C				
		(kJ mol <sup>-1</sup> )	kJ/g	J/g °C	(kJ mol <sup>-1</sup> )
МН	328.69	177.93	172.43	-32.14	193.70
МН-СВ	329.52	127.98	122.39	-104.99	192.93
MH-PEA	328.70	169.77	164.20	-46.299	195.23
МН-РХА	328.97	183.79	178.34	-20.251	191.62
MH-API	328.69	168.19	162.61	-49.259	195.69

Activation energy ( $E_a$ ) values extracted from the slope of ln[-ln(1-x)] vs 1000/T plot (**Fig.** 5.2d). Furthermore, changes in entropy ( $\Delta S$ ), enthalpy ( $\Delta H$ ) and Gibbs free energy ( $\Delta G$ ) were determined using basic thermodynamic equations. Resulted, values obtained for phase one were tabulated in **Table 5.1** and plotted in Appendix III **Fig.** 2. Herein, positive values of  $\Delta H$  and  $\Delta G$  show that the decomposition of the organic moiety is a non-spontaneous reaction. From overall thermodynamic parameters, it could be concluded that MH-CB SCs have relatively higher thermal stability than the pristine ones. The enhanced thermal stability of the modified crystal can be attributed to its increased interactions of additives with the crystal surface. Moreover, our results are nearly close to previous observations in the literature.  $^{57,58}$ 

# 5.1.2.3. Higher-order harmonics generation from their laser-induced plasma plumes.

Nowadays, several researchers focus towards demonstrating HHG from various solid and liquid elements.<sup>59,60</sup> Recently, high-order nonlinear properties using higher-order harmonics generation (HHG) in laser-induced plasma plumes (LIPs) of Ni-doped CsPbBr<sub>3</sub> 2D colloidal nanocrystals have been researched, and the improvement of harmonics was determined for optimized % of Ni.<sup>61,62</sup> Harmonic spectra of modified crystals were obtained as stacks illustrated in **Fig. 5.3a-d**. In the first step, (a) at DP intensity, *i.e.*,  $6 \times 10^{14}$  W/cm<sup>2</sup>, we measured the harmonic spectra by changing the ps HP intensities. All the samples emitted the harmonics at lower ps HP intensity ( $I_{ps}$ ) of  $0.75 \times 10^{10}$  W/cm<sup>2</sup>. The harmonics intensity and cutoff were significantly improved with a further increase in the  $I_{ps}$  up to  $1.77 \times 10^{10}$  W/cm<sup>2</sup>.

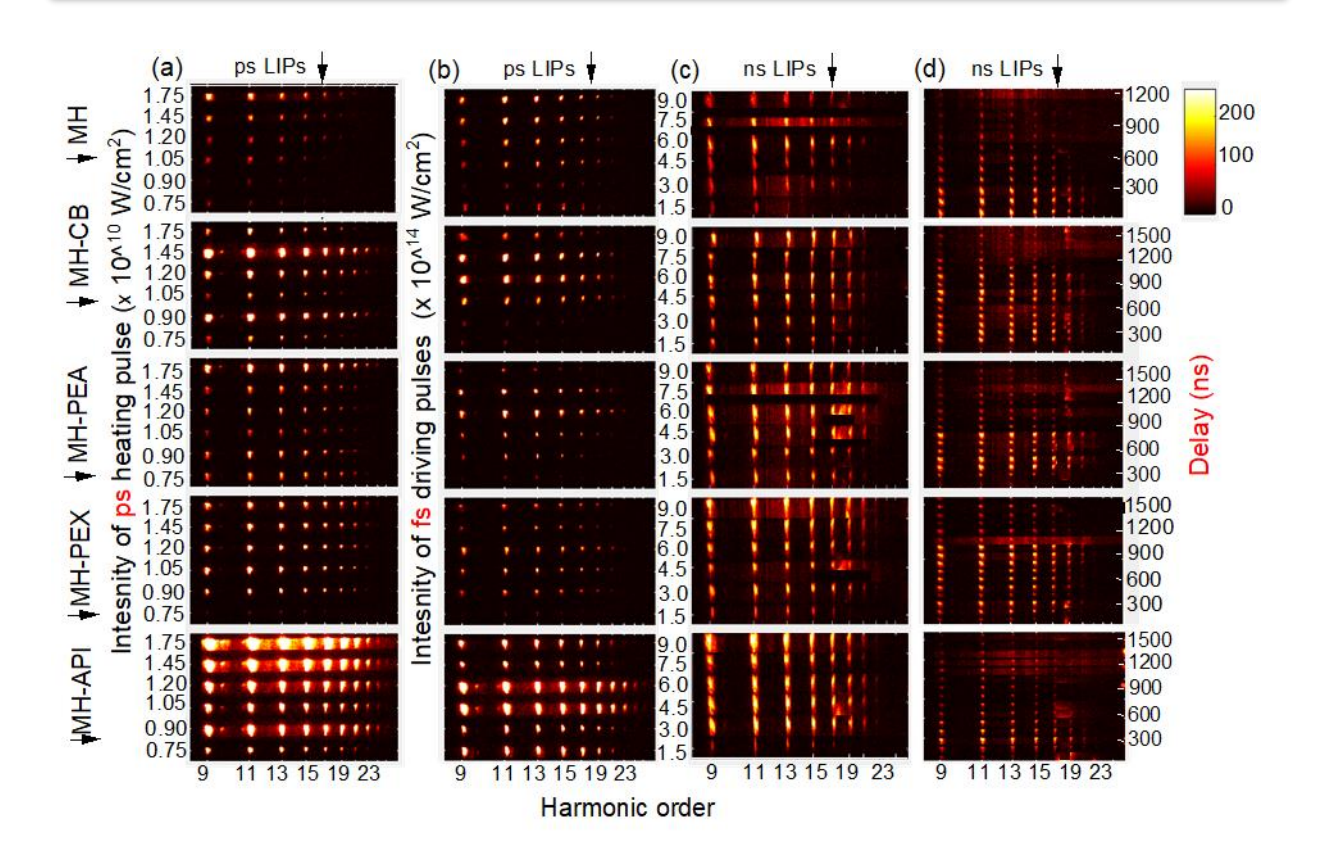


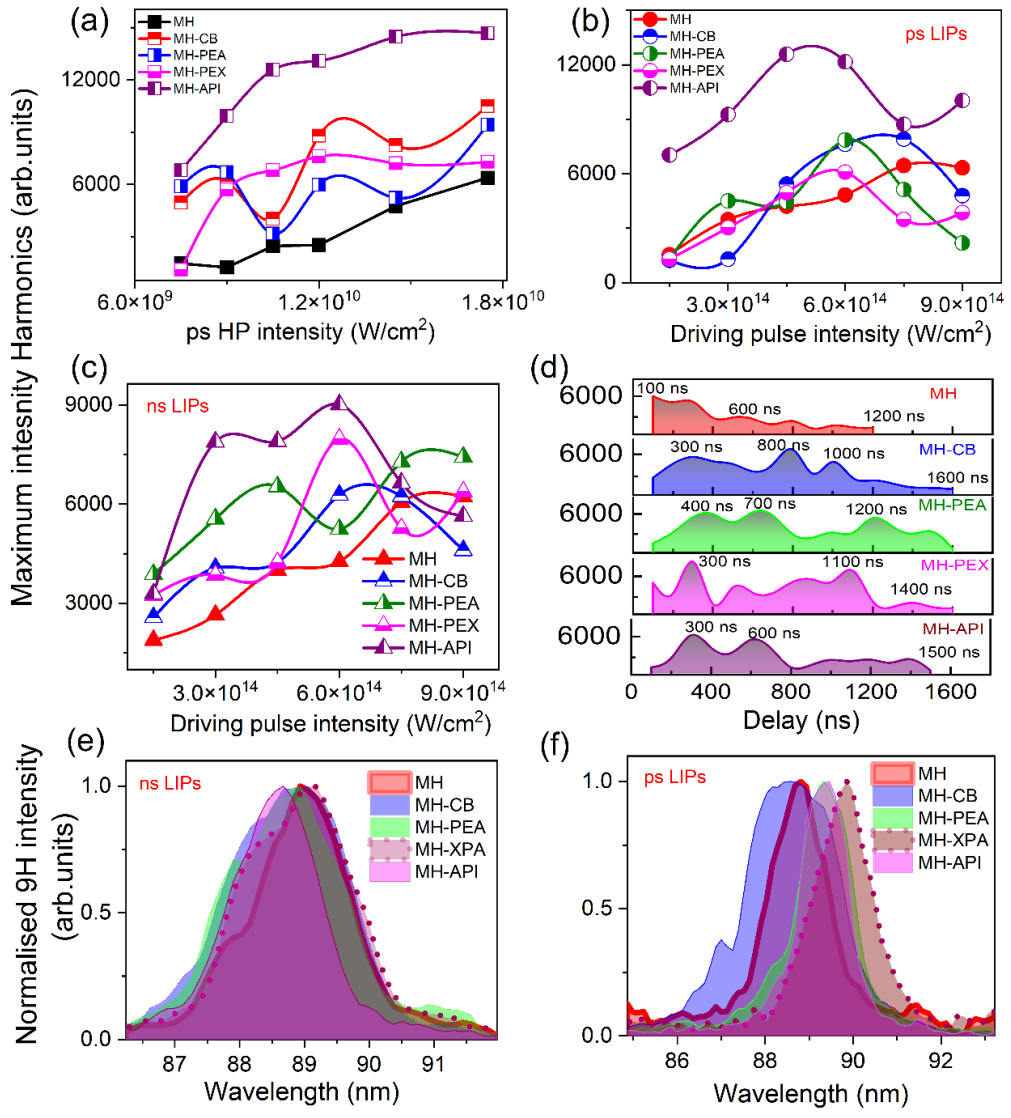
Fig. 5. 1. 3 Harmonic spectra (in pixels) for different a) ps heating pulse intensities at  $I_{fs}$ =  $6.0\times10^{14}$  W/cm<sup>2</sup>, b) driving pulses intensities for ps LIPs (at  $I_{ps}$  =  $0.9\times10^{10}$  W/cm<sup>2</sup>), and c) ns LIPs ( $I_{ns}$  =  $7\times10^{10}$  W/cm<sup>2</sup>), respectively. d) The delay dependence between ns HP and fs DPs. The spectrum's colour bar is similar in the top right corner.

Notably, at low  $I_{ps}$  for MH obtained, the harmonics cut-off up to 13H, whereas for additive-based SCs, the cut-off was extended to 19H. This indicates that plasma plume density was enhanced in the case of additives than MH. In the second and third steps (b, c), we measured the harmonics spectra individually at fixed ps and ns HP intensities, *i.e.*, 0.9 and  $7 \times 10^{10}$  W/cm<sup>2</sup>, and varied the DP intensity ( $I_{fs}$ ) between 1.5 to  $9 \times 10^{10}$  W/cm<sup>2</sup> range. In the case of ps LIPs, the cut-off achieved up to 19H (MH) and 21H (MH-CB, MH-PEA and MH-PEX). In contrast,

it is increased up to 25H for MH-API. However, in the case of ns LIPs, the cut-off is similar for all the crystals, *i.e.*, up to 21H.

In the fourth step (d), we fixed the ns HP intensity  $(I_{ns})$  at  $7 \times 10^{10}$  W/cm<sup>2</sup> and measured the harmonic spectra concerning the delay between ns HP and fs DPs. In the case of ns LIPs, either variation in  $I_{\rm fs}$  or change in the delay, we could not observe much difference in the harmonic cut-off. However, the intensity of harmonics is improved for additive-based crystals at longer delays, as shown in Fig. 3d. The cut-off delays were achieved at 1200 ns for MH, while for MH-CB, MH-PEA, and MH-API is similar to around 1600 ns, whereas for MH-API, it is up to 1500 ns. MA shows the first maxima at 100 ns delay within these delay ranges, continuously decreasing the harmonic intensity and having peaks at every 200 ns, whereas MH-PEX and MH-API have 300 ns. The modified SCs also show a similar trend with MH while all their peaks appear at each 200 ns delay. This indicates the ejection of plasma components such as atoms, ions, and nanoparticles with different masses. The DP is propagating above the target surface at approximately 0.2 mm distance. Meanwhile, it is observed that the harmonics emitted for additive SCs show a shift compared to MH. Fig. 4e,f shows the normalized intensity of 9H in the case of ns and ps LIPs, respectively. The shift in ps LIPs is much higher than the ns LIPs. In the case of ns LIPs, the MH-CB, MH-PEA and MH-API show a bluer shift, whereas MH-PXA shows a redshift in both cases of plasma plumes. The DP we have used is 800 nm, and in the case of ns pulses, we used 1064 nm as an ablating laser pulse, and for ps pulses, the wavelength is the same as DP. Nonlinear absorption of MHPSCs at 800 nm emits PL radiation and ejection of plasma components during laser ablation. At the same time, only plasma plume formation is achieved in the case of ns laser ablation. Therefore, it is assumed that the plasma components (atoms, ions, and nanoparticles) of modified MHPSCs with low/higher bandgaps

might be interacted with the blue/red spectral components of 800 nm and decrease/increase the wavelengths of the harmonics.Moreover, as discussed, the order of PL emission intensity follows the order of MH>MH-PEA>MH-PXA>MH-CB>MH-API; this order is reversed in the case of harmonics intensity, as appears in **Fig. 4a-c**. This confirms that at probing of 800 nm, the MHPSCs lead to higher absorption and principals to PL emission (either by ablation



of ps and ns pulses) and decrease the intensity of the harmonics compared to the modified MHPSCs. The MH-CB and MH-PEA SCs have first maxima around 800 ns and 700 ns, 1200 ns range.

Fig. 5. 1. 4 The maximum harmonic signal for different a) ps heating pulse intensities at  $I_{fs}$ =6.0× 10<sup>14</sup> W/cm<sup>2</sup>, b) driving pulses intensities for ps LIPs (at  $I_{ps}$ =0.9× 10<sup>10</sup> W/cm<sup>2</sup>), and c) ns LIPs ( $I_{ns}$ =7 × 10<sup>10</sup> W/cm<sup>2</sup>), respectively. d) The delay dependence between ns HP and fs DPs. The shift of 9H for all SCs in case of e) ns LIPs and f) ps LIPs.

In addition, we measured the harmonics spectra continuously until the disappearance of harmonic signal from SCs plasma plumes. Fig. 5.5a,b depicts the harmonic spectra of MH and MH-API as a function of time. The plasma plumes are produced by ns heating pulses at a fixed position of the crystal surface, and recorded the harmonic spectra as a movie (.avi file) using CCD. Each frame harmonics spectra plotted as a vertical stack image. It is observed that the MH crystal emits the harmonics until 3.15 mins, and the modified MHPSCs are exceeded this time duration. For example, the MH-API (shown in Fig. 5.5b) emits the harmonic signal for up to 3.35 mins. Approximately a similar time was achieved for MH-CB, MH-PEA and MH-PEX. Therefore, one can assume that the additives increased the stability of crystals. Overall, the measured harmonics spectra, either ps or ns LIPs from these SCs, the additives increased the stability of crystals further, which leads to enhancing the intensity and possessing the shift in the harmonics. Among all reported SCs, MA-API has a higher intensity than others, and in the case of ps LIPs, MH-PXA shows a larger redshift (for 9H,  $\Delta \lambda = +1.05$  nm). The HHG studies with various laser parameters, such as intensities of DP, HP, and delay dependence between DP and HP, revealed that the additives-based SCs enhanced the emission of harmonics in the XUV region more than pristine MHPSCs.

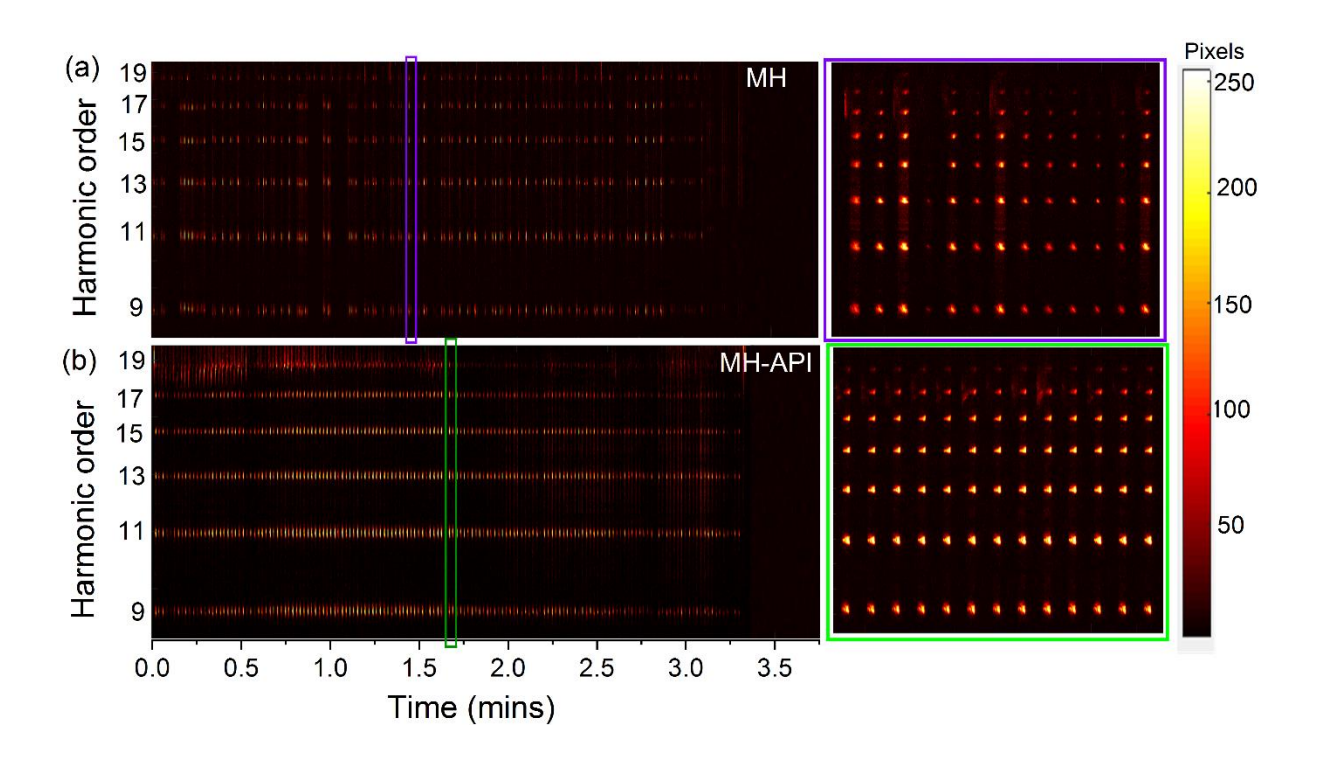


Fig. 5. 1. 5 The harmonic spectra of a) MH and b) MH-API concerning time. The harmonic spectra were recorded as movies and plotted as vertical stack images. Right panels of a) and b) represent some portion marked with pink and green lines, respectively.

### 5.1.3. Conclusions.

In summary, we have successfully demonstrated an additive engineering strategy for mitigating the mixed halide phase segregation effect of 2% Cl-doped MHSCs with the additives. Out of all the additives we have observed, a bluer shift in PL emission for MH-PXA SC when exited with a 2PA source laser indicates more nonradiative recombination. Interestingly, we observed increased crystallinity with mitigated phase separation (concluded from PXRD and XPS studies). The heterocyclic amine (API) coordination with crystallite facets resulted in enhanced harmonics emission and stability. From overall basic characterization and HHG observations, it's estimated that additives' interaction with the

surface plays an essential role in passivation along with Cl incorporated into the perovskite lattice with decreasing halide vacancies rather than being sacrificed as a volatile phase. The lattice constant of the API-MHSCs is more than other additives, suggesting increased Schottky order and transparency in the bulk perovskite. This explanation is consistent with the increased interaction between the formation of MHPSCs, with API additives being more thermodynamically preferred than other additives. The present work will open the doors for tuning the higher-order harmonics' wavelength without changing the driving pulse's chirps, i.e., either positive or negative. Interestingly, in modified MHSCs, enhanced harmonics intensity and stability have been observed. Therefore, we can conveniently use modified MHPSC in plasma HHG with advanced properties in harmonic spectroscopic applications.

## **References**

- (1) He, L.; Xiao, Z.; Yang, X.; Wu, Y.; Lian, Y.; Peng, X.; Yang, X. Green and Sky Blue Perovskite Light-Emitting Devices with a Diamine Additive. *Journal of Materials Science* **2020**, *55*, 7691–7701.
- (2) Kuang, C.; Hu, Z.; Yuan, Z.; Wen, K.; Qing, J.; Kobera, L.; Abbrent, S.; Brus, J.; Yin, C.; Wang, H.; Xu, W.; Wang, J.; Bai, S.; Gao, F. Article Critical Role of Additive-Induced Molecular Interaction on the Operational Stability of Perovskite Light-Emitting Diodes Interaction on the Operational Stability. *Joule* 2021, 5, 618–630.
- (3) Cao, Y.; Wang, N.; Tian, H.; Guo, J.; Wei, Y.; Chen, H.; Miao, Y.; Zou, W.; Pan, K.; He, Y.; Cao, H.; Ke, Y.; Xu, M.; Wang, Y.; Yang, M.; Du, K.; Fu, Z.; Kong, D.; Dai, D.; Jin, Y.; Li, G.; Li, H.; Peng, Q.; Wang, J.; Huang, W. Perovskite Light-Emitting Diodes Based on Spontaneously Formed Submicrometre-Scale Structures. *Nature* 2018, 562, 249–253.
- Lin, K.; Xing, J.; Quan, L. N.; de Arquer, F. P. G.; Gong, X.; Lu, J.; Xie, L.; Zhao, W.;
  Zhang, D.; Yan, C.; Li, W.; Liu, X.; Lu, Y.; Kirman, J.; Sargent, E. H.; Xiong, Q.; Wei,
  Z. Perovskite Light-Emitting Diodes with External Quantum Efficiency Exceeding 20 per Cent. *Nature* 2018, 562, 245–248.
- (5) Xiao, M.; Hao, M.; Liu, M.; Moore, E. G.; Zhang, C.; Luo, B.; Hou, J.; Lipton-Duffin, J.; Wang, L. Surface Ligands Stabilized Lead Halide Perovskite Quantum Dot Photocatalyst for Visible Light-Driven Hydrogen Generation. Advanced Functional

- Materials 2019, 29, 1905683.
- (6) Jin, S.; Li, R.; Huang, H.; Jiang, N.; Lin, J.; Wang, S.; Zheng, Y.; Chen, X.; Chen, D. Compact Ultrabroadband Light-Emitting Diodes Based on Lanthanide-Doped Lead-Free Double Perovskites. *Light: Science & Applications* 2022, 11, 52.
- (7) Zhang, D.; Fu, Y.; Zhan, H.; Zhao, C.; Gao, X.; Qin, C.; Wang, L. Suppressing Thermal Quenching via Defect Passivation for Efficient Quasi-2D Perovskite Light-Emitting Diodes. *Light: Science & Applications* **2022**, *11*, 69.
- (8) Zhang, M.-N.; Wu, X.; Riaud, A.; Wang, X.-L.; Xie, F.; Liu, W.-J.; Mei, Y.; Zhang, D. W.; Ding, S.-J. Spectrum Projection with a Bandgap-Gradient Perovskite Cell for Colour Perception. *Light: Science & Applications* 2020, 9, 162.
- (9) Lee, J.-W.; Park, N.-G. Quasi-Two-Dimensional Perovskite Light Emitting Diodes for Bright Future. *Light: Science & Applications* **2021**, *10*, 86.
- (10) Zhang, L.; Sun, C.; He, T.; Jiang, Y.; Wei, J.; Huang, Y.; Yuan, M. High-Performance Quasi-2D Perovskite Light-Emitting Diodes: From Materials to Devices. *Light: Science & Applications* **2021**, *10*, 61.
- (11) Xing, G.; Mathews, N.; Lim, S. S.; Yantara, N.; Liu, X.; Sabba, D.; Grätzel, M.; Mhaisalkar, S.; Sum, T. C. Low-Temperature Solution-Processed Wavelength-Tunable Perovskites for Lasing. *Nature Materials* 2014, 13, 476–480.
- (12) Deschler, F.; Price, M.; Pathak, S.; Klintberg, L. E.; Jarausch, D. D.; Higler, R.; Hüttner, S.; Leijtens, T.; Stranks, S. D.; Snaith, H. J.; Atatüre, M.; Phillips, R. T.; Friend, R. H.

- High Photoluminescence Efficiency and Optically Pumped Lasing in Solution-Processed Mixed Halide Perovskite Semiconductors. *Journal of Physical Chemistry Letters* **2014**, *5* (8), 1421–1426.
- (13) Xia, P.; Xu, S.; Wang, C.; Ban, D. Perovskite Luminescent Solar Concentrators for Photovoltaics. *APL Photonics* **2021**, *6*, 120901.
- (14) Fang, H. H.; Wang, F.; Adjokatse, S.; Zhao, N.; Even, J.; Loi, M. A. Photoexcitation Dynamics in Solution-Processed Formamidinium Lead Iodide Perovskite Thin Films for Solar Cell Applications. *Light: Science and Applications* **2016**, *5*, e16056-7.
- (15) Xing, J.; Zhao, C.; Zou, Y.; Kong, W.; Yu, Z.; Shan, Y.; Dong, Q.; Zhou, D.; Yu, W.; Guo, C. Modulating the Optical and Electrical Properties of MAPbBr<sub>3</sub> Single Crystals via Voltage Regulation Engineering and Application in Memristors. *Light: Science & Applications* 2020, 9, 11.
- Jacobsson, T. J.; Hultqvist, A.; García-Fernández, A.; Anand, A.; Al-Ashouri, A.; Hagfeldt, A.; Crovetto, A.; Abate, A.; Ricciardulli, A. G.; Vijayan, A.; Kulkarni, A.; Anderson, A. Y.; Darwich, B. P.; Yang, B.; Coles, B. L.; Perini, C. A. R.; Rehermann, C.; Ramirez, D.; Fairen-Jimenez, D.; Di Girolamo, D.; Jia, D.; Avila, E.; Juarez-Perez, E. J.; Baumann, F.; Mathies, F.; González, G. S. A.; Boschloo, G.; Nasti, G.; Paramasivam, G.; Martínez-Denegri, G.; Näsström, H.; Michaels, H.; Köbler, H.; Wu, H.; Benesperi, I.; Dar, M. I.; Bayrak Pehlivan, I.; Gould, I. E.; Vagott, J. N.; Dagar, J.; Kettle, J.; Yang, J.; Li, J.; Smith, J. A.; Pascual, J.; Jerónimo-Rendón, J. J.; Montoya, J. F.; Correa-Baena, J. P.; Qiu, J.; Wang, J.; Sveinbjörnsson, K.; Hirselandt, K.; Dey, K.;

Frohna, K.; Mathies, L.; Castriotta, L. A.; Aldamasy, M. H.; Vasquez-Montoya, M.; Ruiz-Preciado, M. A.; Flatken, M. A.; Khenkin, M. V.; Grischek, M.; Kedia, M.; Saliba, M.; Anaya, M.; Veldhoen, M.; Arora, N.; Shargaieva, O.; Maus, O.; Game, O. S.; Yudilevich, O.; Fassl, P.; Zhou, Q.; Betancur, R.; Munir, R.; Patidar, R.; Stranks, S. D.; Alam, S.; Kar, S.; Unold, T.; Abzieher, T.; Edvinsson, T.; David, T. W.; Paetzold, U. W.; Zia, W.; Fu, W.; Zuo, W.; Schröder, V. R. F.; Tress, W.; Zhang, X.; Chiang, Y. H.; Iqbal, Z.; Xie, Z.; Unger, E. An Open-Access Database and Analysis Tool for Perovskite Solar Cells Based on the FAIR Data Principles. *Nature Energy* **2022**, *7*, 107–115.

- (17) Turren-Cruz, S. H.; Hagfeldt, A.; Saliba, M. Methylammonium-Free, High-Performance, and Stable Perovskite Solar Cells on a Planar Architecture. *Science* **2018**, *362*, 449–453.
- (18) Sadegh, F.; Akin, S.; Moghadam, M.; Keshavarzi, R.; Mirkhani, V.; Ruiz-Preciado, M. A.; Akman, E.; Zhang, H.; Amini, M.; Tangestaninejad, S.; Mohammadpoor-Baltork, I.; Graetzel, M.; Hagfeldt, A.; Tress, W. Copolymer-Templated Nickel Oxide for High-Efficiency Mesoscopic Perovskite Solar Cells in Inverted Architecture. *Advanced Functional Materials* **2021**, *31*, 2102237.
- (19) Correa Baena, J. P.; Steier, L.; Tress, W.; Saliba, M.; Neutzner, S.; Matsui, T.; Giordano, F.; Jacobsson, T. J.; Srimath Kandada, A. R.; Zakeeruddin, S. M.; Petrozza, A.; Abate, A.; Nazeeruddin, M. K.; Grätzel, M.; Hagfeldt, A. Highly Efficient Planar Perovskite Solar Cells through Band Alignment Engineering. *Energy and Environmental Science* 2015, 8, 2928–2934.

- (20) Correa-Baena, J. P.; Saliba, M.; Buonassisi, T.; Grätzel, M.; Abate, A.; Tress, W.; Hagfeldt, A. Promises and Challenges of Perovskite Solar Cells. *Science* **2017**, *358*, 739–744.
- (21) Kim, M.; Jeong, J.; Lu, H.; Lee, T. K.; Eickemeyer, F. T.; Liu, Y.; Choi, I. W.; Choi, S. J.; Jo, Y.; Kim, H. B.; Mo, S. I.; Kim, Y. K.; Lee, H.; An, N. G.; Cho, S.; Tress, W. R.; Zakeeruddin, S. M.; Hagfeldt, A.; Kim, J. Y.; Grätzel, M.; Kim, D. S. Conformal Quantum Dot-SnO<sub>2</sub> Layers as Electron Transporters for Efficient Perovskite Solar Cells. *Science* 2022, 375, 302–306.
- (22) Xiang, W.; Wang, Z.; Kubicki, D. J.; Tress, W.; Luo, J.; Prochowicz, D.; Akin, S.; Emsley, L.; Zhou, J.; Dietler, G.; Grätzel, M.; Hagfeldt, A. Europium-Doped CsPbI<sub>2</sub>Br for Stable and Highly Efficient Inorganic Perovskite Solar Cells. *Joule* **2019**, *3*, 205–214.
- Yang, B.; Suo, J.; Di Giacomo, F.; Olthof, S.; Bogachuk, D.; Kim, Y.; Sun, X.; Wagner, L.; Fu, F.; Zakeeruddin, S. M.; Hinsch, A.; Gratzel, M.; Di Carlo, A.; Hagfeldt, A. Interfacial Passivation Engineering of Perovskite Solar Cells with Fill Factor over 82% and Outstanding Operational Stability on N-i-p Architecture. ACS Energy Letters 2021, 6, 3916–3923.
- (24) Li, X.; Bi, D.; Yi, C.; Décoppet, J. D.; Luo, J.; Zakeeruddin, S. M.; Hagfeldt, A.; Grätzel,
   M. A Vacuum Flash-Assisted Solution Process for High-Efficiency Large-Area
   Perovskite Solar Cells. Science 2016, 353, 58–62.
- (25) Jeong, J.; Kim, M.; Seo, J.; Lu, H.; Ahlawat, P.; Mishra, A.; Yang, Y.; Hope, M. A.;

- Eickemeyer, F. T.; Kim, M.; Yoon, Y. J.; Choi, I. W.; Darwich, B. P.; Choi, S. J.; Jo, Y.; Lee, J. H.; Walker, B.; Zakeeruddin, S. M.; Emsley, L.; Rothlisberger, U.; Hagfeldt, A.; Kim, D. S.; Grätzel, M.; Kim, J. Y. Pseudo-Halide Anion Engineering for α-FAPbI<sub>3</sub> Perovskite Solar Cells. *Nature* **2021**, *592*, 381–385.
- (26) Jeong, J.; Kim, M.; Seo, J.; Lu, H.; Ahlawat Paramvir; Mishra, A.; Yang, Y.; Hope, M. A.; Eickemeyer; T., F.; Kim, M.; Yung Jin Yoon, In Woo Choi, B. P. D.; Choi, S. J.; Jo, Y.; Jun Hee Lee, B. W.; Shaik M. Zakeeruddin, L. E.; Rothlisberger, U.; Hagfeldt, A.; Dong Suk Kim, M. G. & J. Y. K. Pseudo-Halide Anion Engineering for α-FAPbI3 Perovskite Solar Cells. *Nature* 2020, *592*, 16.
- (27) Bai, F.; Bian, K.; Huang, X.; Wang, Z.; Fan, H. Pressure Induced Nanoparticle Phase Behavior, Property, and Applications. *Chemical Reviews* **2019**, *119*, 7673–7717.
- (28) Gui, P.; Chen, Z.; Li, B.; Yao, F.; Zheng, X.; Lin, Q.; Fang, G. High-Performance Photodetectors Based on Single All-Inorganic CsPbBr<sub>3</sub> Perovskite Microwire. *ACS Photonics* **2018**, *5*, 2113–2119.
- (29) Zhang, H.; Nazeeruddin, M. K.; Choy, W. C. H. Perovskite Photovoltaics: The Significant Role of Ligands in Film Formation, Passivation, and Stability. *Advanced materials (Deerfield Beach, Fla.)* **2019**, *31*, e1805702.
- (30) Balis, N.; Zaky, A. A.; Athanasekou, C.; Silva, A. M.; Sakellis, E.; Vasilopoulou, M.; Stergiopoulos, T.; Kontos, A. G.; Falaras, P. Investigating the Role of Reduced Graphene Oxide as a Universal Additive in Planar Perovskite Solar Cells. *Journal of Photochemistry and Photobiology A: Chemistry* **2020**, *386*, 112141.

- (31) Lin, Q.; Armin, A.; Burn, P. L.; Meredith, P. Filterless Narrowband Visible Photodetectors. *Nature Photonics* **2015**, *9*, 687–694.
- (32) Yao, F.; Gui, P.; Chen, C.; Li, B.; Li, R.; Tao, C.; Lin, Q.; Fang, G. High-Rubidium-Formamidinium-Ratio Perovskites for High-Performance Photodetection with Enhanced Stability. *ACS Applied Materials and Interfaces* **2019**, *1*, 39875–39881.
- (33) Chao, L.; Xia, Y.; Li, B.; Xing, G.; Chen, Y.; Huang, W. Room-Temperature Molten Salt for Facile Fabrication of Efficient and Stable Perovskite Solar Cells in Ambient Air. *Chem* **2019**, *5*, 995–1006.
- (34) Liu, Y.; Yang, Z.; Cui, D.; Ren, X.; Sun, J.; Liu, X.; Zhang, J.; Wei, Q.; Fan, H.; Yu, F.; Zhang, X.; Zhao, C.; Liu, S. Two-Inch-Sized Perovskite CH<sub>3</sub>NH<sub>3</sub>PbX<sub>3</sub> (X = Cl, Br, I) Crystals: Growth and Characterization. *Advanced Materials* **2015**, *27*, 5176–5183.
- (35) Dang, Y.; Liu, Y.; Sun, Y.; Yuan, D.; Liu, X.; Lu, W.; Liu, G.; Xia, H.; Tao, X. Bulk Crystal Growth of Hybrid Perovskite Material CH<sub>3</sub>NH<sub>3</sub>PbI<sub>3</sub>. *CrystEngComm* **2015**, *17*, 665–670.
- (36) Dong, Q. DigitalCommons @ University of Nebraska Lincoln Electron-Hole Diffusion Lengths > 175 μ m in Solution-Grown CH<sub>3</sub>NH<sub>3</sub>PbI<sub>3</sub> Single Crystals. Science 2015, 347, 967–970.
- (37) Shi, D.; Adinolfi, V.; Comin, R.; Yuan, M.; Alarousu, E.; Buin, A.; Chen, Y.; Hoogland,
  S.; Rothenberger, A.; Katsiev, K.; Losovyj, Y.; Zhang, X.; Dowben, P. A.; Mohammed,
  O. F.; Sargent, E. H.; Bakr, O. M. Low Trap-State Density and Long Carrier Diffusion

- in Organolead Trihalide Perovskite Single Crystals. Science 2015, 347, 519–522.
- (38) Efrati, A.; Aharon, S.; Wierzbowska, M.; Etgar, L. First Evidence of Macroscale Single Crystal Ion Exchange Found in Lead Halide Perovskites. *EcoMat* **2020**, *2*, e12016.
- (39) Stoumpos, C. C.; Malliakas, C. D.; Peters, J. A.; Liu, Z.; Sebastian, M.; Im, J.; Chasapis, T. C.; Wibowo, A. C.; Chung, D. Y.; Freeman, A. J.; Wessels, B. W.; Kanatzidis, M. G. Crystal Growth of the Perovskite Semiconductor CsPbBr<sub>3</sub>: A New Material for High-Energy Radiation Detection. *Crystal Growth and Design* 2013, 13, 2722–2727.
- (40) Peng, W.; Wang, L.; Murali, B.; Ho, K. T.; Bera, A.; Cho, N.; Kang, C. F.; Burlakov, V. M.; Pan, J.; Sinatra, L.; Ma, C.; Xu, W.; Shi, D.; Alarousu, E.; Goriely, A.; He, J. H.; Mohammed, O. F.; Wu, T.; Bakr, O. M. Solution-Grown Monocrystalline Hybrid Perovskite Films for Hole-Transporter-Free Solar Cells. *Advanced Materials* 2016, 28, 3383–3390.
- (41) Yao, F.; Peng, J.; Li, R.; Li, W.; Gui, P.; Li, B.; Liu, C.; Tao, C.; Lin, Q.; Fang, G. Perovskite Single Crystals. *Nature Communications* **2019**, *31*, 1–9.
- (42) Tang, Y.; Liang, M.; Zhang, M.; Honarfar, A.; Zou, X.; Abdellah, M.; Pullerits, T.; Zheng, K.; Chi, Q. Photodetector Based on Spontaneously Grown Strongly Coupled MAPbBr3/N-RGO Hybrids Showing Enhanced Performance. ACS Applied Materials and Interfaces 2020, 12, 858–867.
- (43) Knight, A. J.; Herz, L. M. Preventing Phase Segregation in Mixed-Halide Perovskites: A Perspective. *Energy and Environmental Science* **2020**, *13*, 2024–2046.

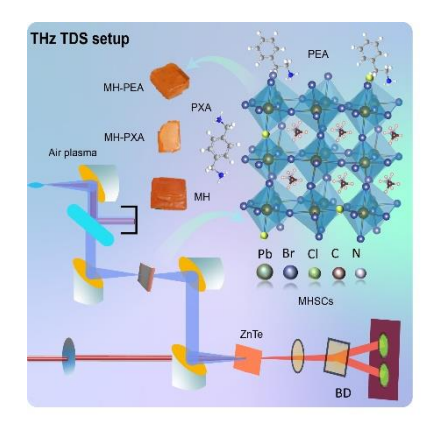
- (44) Levchuk, I.; Osvet, A.; Tang, X.; Brandl, M.; Perea, J. D.; Hoegl, F.; Matt, G. J.; Hock,
   R.; Batentschuk, M.; Brabec, C. J. Brightly Luminescent and Color-Tunable
   Formamidinium Lead Halide Perovskite FAPbX<sub>3</sub> (X = Cl, Br, I) Colloidal Nanocrystals.
   Nano Letters 2017, 17, 2765–2770.
- (45) Chen, L.; Tan, Y. Y.; Chen, Z. X.; Wang, T.; Hu, S.; Nan, Z. A.; Xie, L. Q.; Hui, Y.; Huang, J. X.; Zhan, C.; Wang, S. H.; Zhou, J. Z.; Yan, J. W.; Mao, B. W.; Tian, Z. Q. Toward Long-Term Stability: Single-Crystal Alloys of Cesium-Containing Mixed Cation and Mixed Halide Perovskite. *Journal of the American Chemical Society* 2019, 141, 1665–1671.
- (46) Misra, R. K.; Aharon, S.; Li, B.; Mogilyansky, D.; Visoly-Fisher, I.; Etgar, L.; Katz, E.
   A. Temperature- and Component-Dependent Degradation of Perovskite Photovoltaic
   Materials under Concentrated Sunlight. *The Journal of Physical Chemistry Letters* 2015,
   6, 326–330.
- (47) Niu, G.; Guo, X.; Wang, L. Review of Recent Progress in Chemical Stability of Perovskite Solar Cells. *Journal of Materials Chemistry A* **2015**, *3*, 8970–8980.
- (48) van Reenen, S.; Kemerink, M.; Snaith, H. J. Modeling Anomalous Hysteresis in Perovskite Solar Cells. *The Journal of Physical Chemistry Letters* **2015**, *6*, 3808–3814.
- (49) Raga, S. R.; Jung, M. C.; Lee, M. V.; Leyden, M. R.; Kato, Y.; Qi, Y. Influence of Air Annealing on High-Efficiency Planar Structure Perovskite Solar Cells. *Chemistry of Materials* **2015**, *27*, 1597–1603.

- (50) Han, Y.; Meyer, S.; Dkhissi, Y.; Weber, K.; Pringle, J. M.; Bach, U.; Spiccia, L.; Cheng,
   Y. B. Degradation Observations of Encapsulated Planar CH<sub>3</sub>NH<sub>3</sub>PbI<sub>3</sub> Perovskite Solar
   Cells at High Temperatures and Humidity. *Journal of Materials Chemistry A* 2015, 3,
   8139–8147.
- (51) Feng, Y.; Pan, L.; Wei, H.; Liu, Y.; Ni, Z.; Zhao, J.; Rudd, P. N.; Cao, L. R.; Huang, J. Low Defects Density CsPbBr<sub>3</sub>single Crystals Grown by an Additive Assisted Method for Gamma-Ray Detection. *Journal of Materials Chemistry C* **2020**, *8*, 11360–11368.
- (52) Mix, L. T.; Ghosh, D.; Tisdale, J.; Lee, M.-C.; O'Neal, K. R.; Sirica, N.; Neukirch, A. J.; Nie, W.; Taylor, A. J.; Prasankumar, R. P.; Tretiak, S.; Yarotski, D. A. Hot Carrier Cooling and Recombination Dynamics of Chlorine-Doped Hybrid Perovskite Single Crystals. *The Journal of Physical Chemistry Letters* 2020, 11, 8430–8436.
- (53) Han, T.-H.; Lee, J.-W.; Choi, C.; Tan, S.; Lee, C.; Zhao, Y.; Dai, Z.; De Marco, N.; Lee, S.-J.; Bae, S.-H.; Yuan, Y.; Lee, H. M.; Huang, Y.; Yang, Y. Perovskite-Polymer Composite Cross-Linker Approach for Highly-Stable and Efficient Perovskite Solar Cells. *Nature Communications* **2019**, *10*, 520.
- (54) Shi, D.; Adinolfi, V.; Comin, R.; Yuan, M.; Alarousu, E.; Buin, A.; Chen, Y.; Hoogland,
  S.; Rothenberger, A.; Katsiev, K.; Losovyj, Y.; Zhang, X.; Dowben, P. A.; Mohammed,
  O. F.; Sargent, E. H.; Bakr, O. M. Low Trap-State Density and Long Carrier Diffusion in Organolead Trihalide Perovskite Single Crystals. *Science* 2015, 347, 519–522.
- (55) Juarez-Perez, E. J.; Ono, L. K.; Maeda, M.; Jiang, Y.; Hawash, Z.; Qi, Y. Photodecomposition and Thermal Decomposition in Methylammonium Halide Lead

- Perovskites and Inferred Design Principles to Increase Photovoltaic Device Stability. Journal of Materials Chemistry A 2018, 6, 9604–9612.
- (56) Farrukh, M. A.; Butt, K. M.; Chong, K.; Chang, W. S. Photoluminescence Emission Behavior on the Reduced Band Gap of Fe Doping in CeO<sub>2</sub>-SiO<sub>2</sub> Nanocomposite and Photophysical Properties. *Journal of Saudi Chemical Society* **2019**, *23*, 561–575.
- (57) Zhang, L.; Liu, Y.; Ye, X.; Han, Q.; Ge, C.; Cui, S.; Guo, Q.; Zheng, X.; Zhai, Z.; Tao, X. Exploring Anisotropy on Oriented Wafers of MAPbBr<sub>3</sub> Crystals Grown by Controlled Antisolvent Diffusion. *Crystal Growth and Design* 2018, 18, 6652–6660.
- Yang, B.; Ming, W.; Du, M.-H.; Keum, J. K.; Puretzky, A. A.; Rouleau, C. M.; Huang, J.; Geohegan, D. B.; Wang, X.; Xiao, K.; Perovskites Yang, O. B.; Yang, B.; Keum, J. K.; Puretzky, A. A.; Rouleau, C. M.; Geohegan, D. B.; Xiao, K.; Ming, W.; Du, M.; Wang, X.; Huang, J. CommuniCation Real-Time Observation of Order-Disorder Transformation of Organic Cations Induced Phase Transition and Anomalous Photoluminescence in Hybrid Perovskites. Adv. Mater 2018, 30, 1705801.
- (59) Hirori, H.; Xia, P.; Shinohara, Y.; Otobe, T.; Sanari, Y.; Tahara, H.; Ishii, N.; Itatani, J.; Ishikawa, K. L.; Aharen, T.; Ozaki, M.; Wakamiya, A.; Kanemitsu, Y. High-Order Harmonic Generation from Hybrid Organic–Inorganic Perovskite Thin Films. APL Materials 2019, 7, 041107.
- (60) Nakagawa, K.; Hirori, H.; Sanari, Y.; Sekiguchi, F.; Sato, R.; Saruyama, M. Interference Effects in High-Order Harmonics from Colloidal Perovskite Nanocrystals Excited by an Elliptically Polarized Laser. *Physical Review Materials* **2021**, *5*, 016001.

- (61) Konda, S. R.; Soma, V. R.; Ganeev, R. A.; Banavoth, M.; Ketavath, R.; Li, W. Third-Order Optical Nonlinearities and High-Order Harmonics Generation in Ni-Doped CsPbBr3 Nanocrystals Using Single- and Two-Color Chirped Pulses. *Journal of Materials Science* 2022, 57, 3468–3485.
- (62) Konda, S. R.; Soma, V. R.; Banavoth, M.; Ketavath, R.; Mottamchetty, V.; Lai, Y. H.; Li, W. High Harmonic Generation from Laser-Induced Plasmas of Ni-Doped CsPbBr<sub>3</sub> Nanocrystals: Implications for Extreme Ultraviolet Light Sources. ACS Applied Nano Materials 2021, 4, 8292–8301.

# CHAPTER-5b The Aromatic Additives Boost the Mixed Halide Perovskite Single Crystal's Terahertz Properties



Sarvani Jowhar Khanam<sup>a</sup>, Srinivasa Rao Konda<sup>b,#</sup>, Wei Li <sup>b,†</sup>, and Banavoth Murali<sup>a,\*</sup>

<sup>a</sup>Solar Cells and Photonics Research Laboratory, School of Chemistry, University of Hyderabad, Hyderabad 500046, Telangana, India

<sup>b</sup>The GPL Photonics Laboratory, State Key Laboratory of Applied Optics, Changchun Institute of Optics, Fine Mechanics and Physics, Chinese Academy of Sciences, Changchun, 130033, China

Corresponding authors: \*murali.banavoth@uohyd.ac.in, #ksrao@ciomp.ac.cn, †weili1@ciomp.ac.cn

#### **Abstract**

Perovskite materials are distinguished by their tunable bandgap, heigh attenuation coefficient, easy fabrication, and carrier mobility. mixed-halide perovskite (MHP) materials are promising candidates for photonics applications because to their pronounced optoelectronic properties. However, phase segregation in these materials severely impacts their scalability. Additive engineering (AE) strategy in most perovskite crystal's (PSC) growth has proved more effective. Current work focused towards enhancing the stability of 6.67% Cl-doped methyl ammonium lead(II) bromide single crystals (MHSC) using aromatic nitrogen-based additives. Modified MHSC showed enhanced terahertz (THz) radiation transmission and reflection. Moreover, the evidence from powder x-ray diffraction (p-XRD), x-ray photoelectron spectroscopy (XPS) and THz transmission in modified MHSCs revealed the mitigated phase segregation in modified MHSCs.

## **5.2.1 Introduction**

MHSCs are auspicious resources in nearly all fields of science and technology, such as light-emitting diodes (LEDs), <sup>1-5</sup> laser, <sup>6,7</sup> memristors, <sup>8</sup> photovoltaics, <sup>9-16</sup> photocatalysis <sup>17</sup> and higher energy radiation detectors. <sup>18,19</sup> MHSCs are promising materials for future application owing to their tunable bandgap, higher optoelectronic properties, dielectric constant <sup>20</sup> and low-cost processability. <sup>21</sup> ABX<sub>3</sub> type of unit cell structure is present in these materials in which monovalent 'A' cations are located in the voids between interlinked octahedra, indirectly affecting the bandgap. <sup>22-26</sup> The bandgap is formed by combining the metal and halide (MX<sub>6</sub>, octahedral unit) *s*, *p* orbitals. Changing the concentration of halides/metals can directly affect

the bandgap.<sup>27</sup> The standard crystallization techniques are anti-solvent vapour assistant crystallization (AVC)<sup>28,29</sup> and inverse temperature crystallization (ITC).<sup>30,31</sup>

The potential factors influencing surface quality, crystallinity, and halide segregation

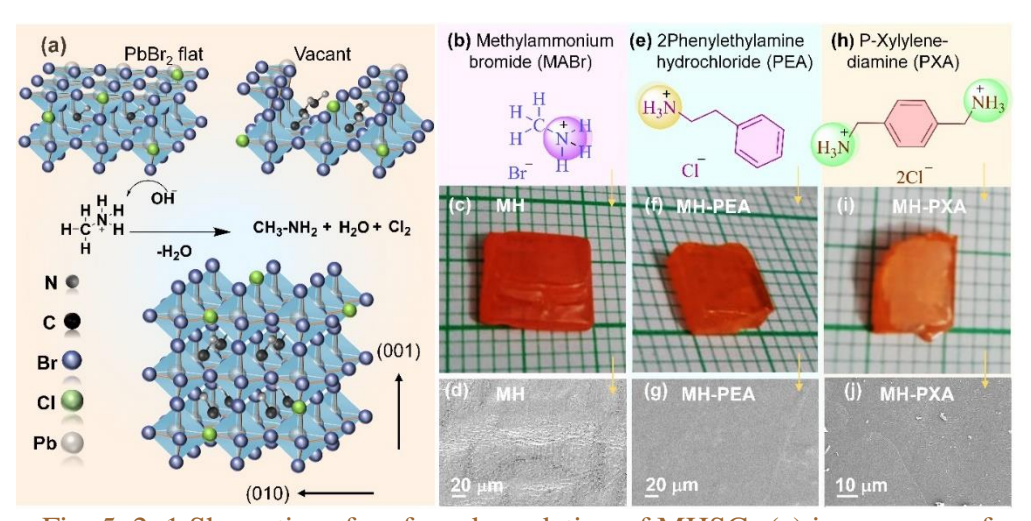


Fig. 5. 2. 1 Shematics of surface degradation of MHSCs (a) in presence of atmosphere moisture. Left Each column from (b-d), (e-g) and (h-j) represents the MABr, PEA, and PXA, chemical structure photographs and SEM images, respectively.

depend on crystal growth technique,<sup>32</sup> the stoichiometry of concentration/composition,<sup>33,34</sup> including solvent,<sup>35</sup> the precursor's annealing temperature,<sup>36</sup> and crystal growth period.<sup>37</sup> Cl-doping into perovskite precursor solutions has been widely reported to tune the optoelectronic properties of OIHPs.<sup>38,39</sup> Tyler Mix et al. investigated different Cl-doping concentrations and reported that increased LED performances in optimized MHSCs outperformed their counterpart in optoelectronic properties.<sup>38</sup> However, the challenges associated with MHSCs are phase segregation and compositional instability under ambient conditions, which are yet to explore more in MHSCs.<sup>38,39</sup> The phase segregation effect is well described in microcrystalline

thin films.<sup>40,41</sup> During this process, the perovskite demises into regions of differing halide content, adversely affecting the optoelectronic properties by acting as traps, limiting the prospects of MHSCs technology.<sup>42</sup> Hence, decreasing/increasing Cl concentration in MHSCs is anomalous and distinctly different from the monotonic growth trend reported in Br/Cl double-halide alloys, which depends on the nature of molecular bonds on the surface.<sup>42-44</sup> Nevertheless, limited reported techniques are available on the additives engineering for 3D MHSCs in the literature to mitigate phase segregation.<sup>42-44</sup> Herein, in this work, we have taken optimized 6.67% Cl-doped MHSCs to study the effect of aromatic additives on MHSCs' structural and optical properties. The aromatic additives used are phenylethylamine hydrochloride (PEA) and P- xylylene-diamine dihydrochloride (PXA).

#### **5.2.2. Results and Discussion**

### **5.2.2.1.** Morphology and Structural Properties

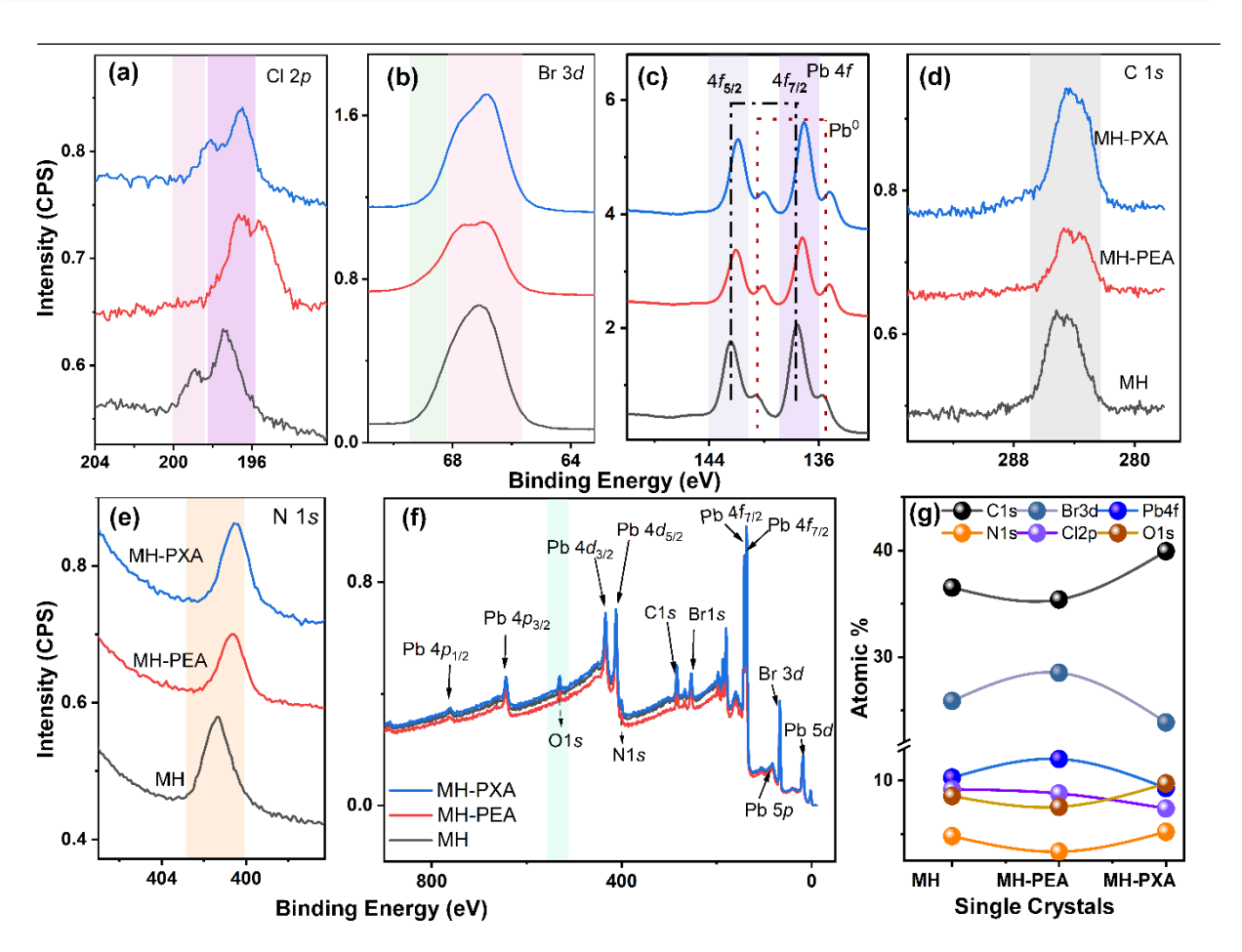


Fig. 5. 2. 2(a-e) XPS data of Cl 2p, Br 3d, Pb 4f, C 1s, and N1s core-level spectra with molecular level defect and chemical states behaviour in MHSCs with changing additives. (f)

Change in XPS survey of each SCs with different additive and (g) atomic % values

Methylammonium bromide (MABr) is hygroscopic salt: on the surface of the crystals, it absorbs moisture and converts to MA, resulting in the lead(II) halide (PbX<sub>2</sub>) and halogen gases (X<sub>2</sub>) forming a vacant surface on MHSCs, as illustrated in **Fig. 1a**. The N-based aromatic organic molecules with mono and diamine groups are prone to interact more with the inorganic octahedra and are more stable than their MABr counterparts. Each column in **Fig. 1** from (**b-d**), (**e-g**) and (**h-j**) represents the chemical structure of MABr, PEA and PXA, grown crystal images and changing crystal surface recorded using SEM, respectively. Interestingly,

we observed flat surfaces with more transparency and low surface roughness in modified MHSCs, suggesting the reduced surface trap states owing to effective bonding interaction with additives on the surface.<sup>46</sup> Weight % values of modified and pristine MHSCs (**Fig. S2**) and elemental ratios extracted from the EDX data (Appendix IV **Table 6**).

XPS studies have been conducted to predict the change in the chemical state behaviour of core-level orbitals with additives. A considerable shift in Cl 3d and Br 3d core-level spectrum toward the lower energies was observed in MH-PXA and MH-PEA SCs, indicating

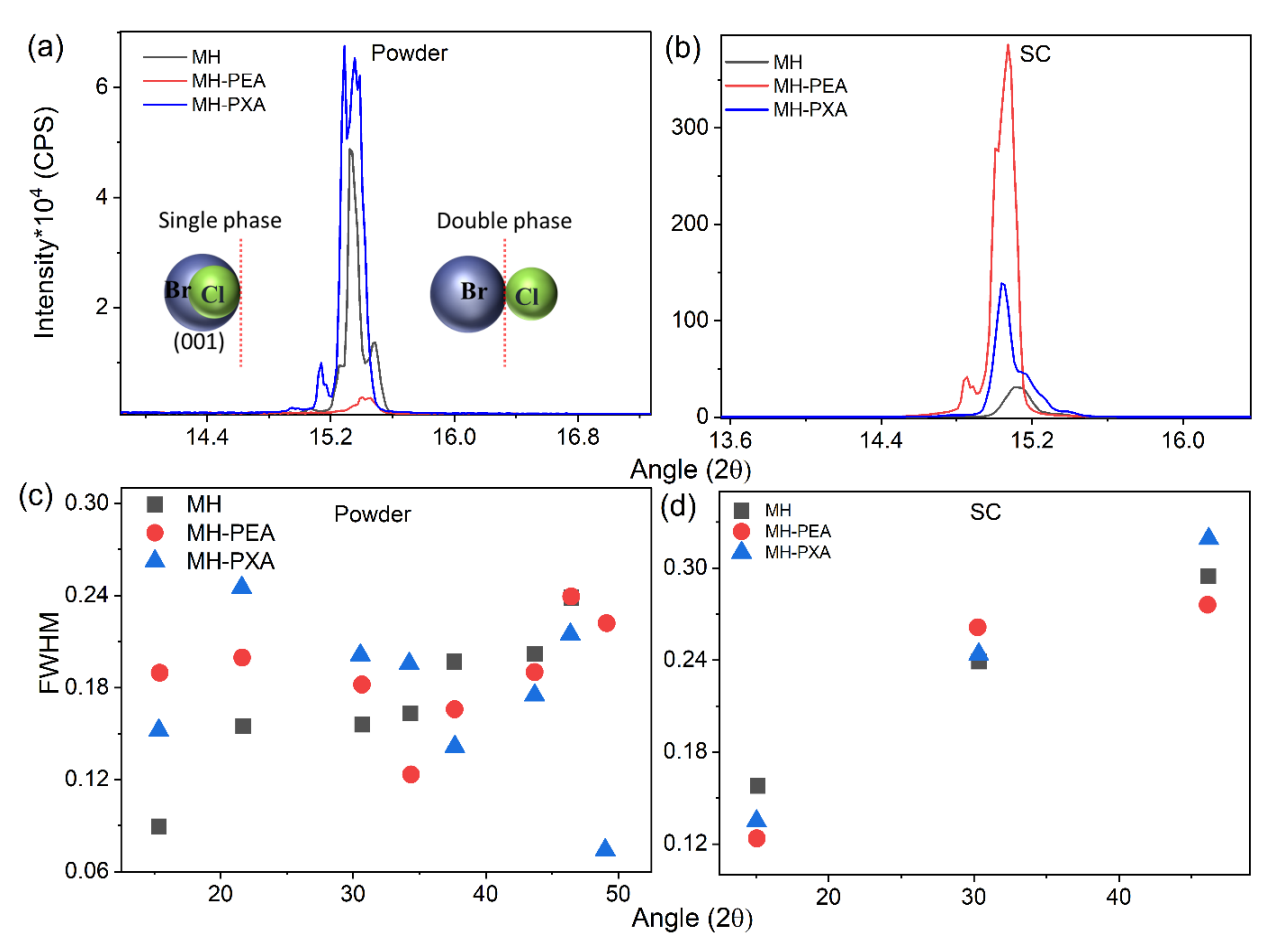


Fig. 5. 2. 3 The XRD pattern of the modified and pristine SCs, (a, b) Splitting and shifting of powder and single crystal (SC) p- XRD, (100) peaks shows the transition from single-phase MHSCs to double-phase segregation with different additives. (c, d) Change in FWHM

the decreased binding energy resulting from increased halide vacancies (**Fig. 2a, b**).<sup>47</sup> Interestingly, intensities of the additional peak in Pb 4*f*, C1*s* and N 1*s* core-level binding relating to a residual molecule Pb<sup>0</sup> and (CH<sub>3</sub>NH<sub>2</sub>) have decreased in modified crystal compared to pristine crystal (**Fig. 2c-e**). However, more intense molecular defects and Pb<sup>0</sup> peaks were seen in PXA-modified crystals. The XPS survey and changes in halides' atomic percentage (%) for MHSCs with additives are illustrated in **Fig. 2f,g**. The Cl-to-Pb ratio of the SC surface also increased when a higher fraction of Cl was injected into the precursor solution.

Further, p-XRD was conducted to verify the effect of additives on lattice parameters and diffraction angles ( $2\theta$  values) for powder and SC samples. The pristine Brawice latices MHSC corresponding to (100), (200) and (300) planes comply with the previously reported data (Fig. S3). 38,48 Generally, replacing Br with Cl in the perovskite lattice fosters the unit structure to expand due to the confinement effect caused by decreased Pb-X distances. Meanwhile, if the peak shift is towards higher angles, the host unit cell structure is contracting and vice-versa. From Fig. 3b, we could observe the diffraction peak of MHSCs toward the smaller diffraction angle after using the additives, indicating lattice expansion depending on the Cl concentration. As in MH-PEA, the bandgap evolution inflexion point (or the phase boundary between the single-phase double-halide alloy and phase segregation) consistently increased with increased N content. Fig. 3c,d indicates a more comprehensive single-phase range fullwidth half maxima (FWHM) and greater tolerance to phase segregation in the perovskite with higher Br content than that of MH-PXA with higher Cl content.<sup>49</sup> Subsequently, the microstrain values have been calculated from powder XRD data using Williamson-Hall (W-H) plots,  $8.436 \times 10^{-4}$ ,  $8.140 \times 10^{-4}$  and 0.950 for MH, MH-PEA, and MH-PXA, respectively (Fig. S4 (a-c)).<sup>50</sup> Higher lattice strain is observed in the case of MH-

PXA with more FWHM and peak splitting, which might be due to increased intrinsic defects due to halide segregation on the surface of PSCs. XPS data also strengthened the argument of increased intrinsic defects by decreasing the photoemission energy. However, structural evolution observed with XRD reveals the bandgap decrease at high Cl content was caused by phase segregation into two perovskite phases (**Fig. 3a insert**). Trends obtained in XRD peaks are consistent with the elemental ratios calculated using the XPS atomic % and suggest the segregation of a high-Br/Cl phase, which left behind a Br-rich surface.

Furthermore, Transmission Electron Microscopy (HR-TEM) measurements have been done to check the changes in the selected area electron diffraction (SEAD) pattern by changing

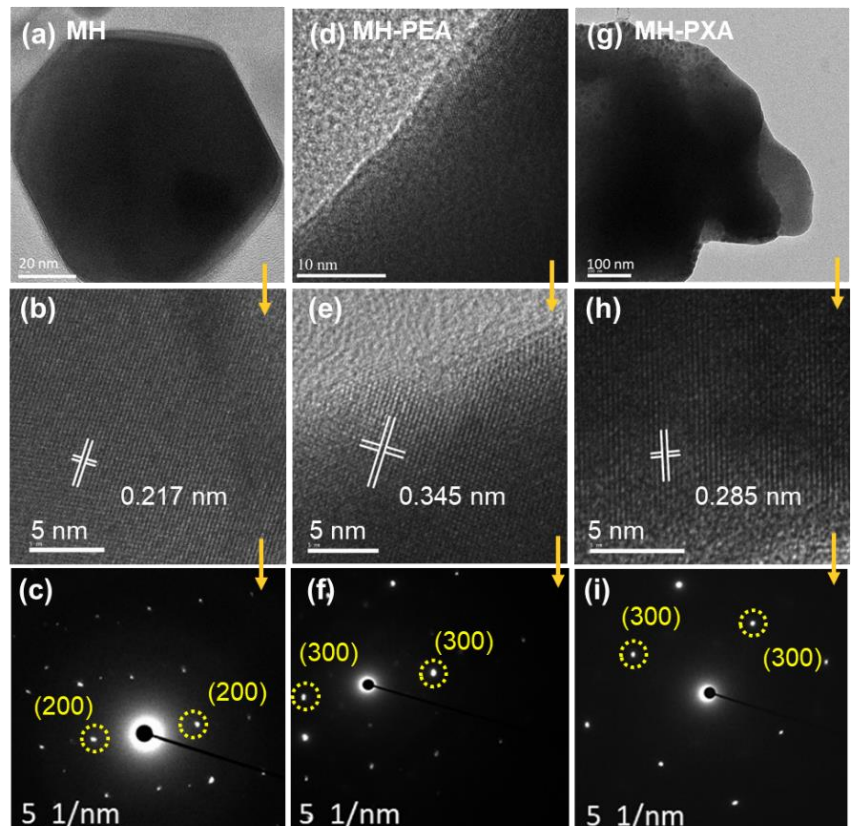


Fig. 5. 2. 4 From (a-c), (d-f) and (g-i) represnts TEM images, HRTEM images with lattice fringes and SAED of each MH, MH-PEA and MH-PXA SCs, respectivley.

additives.<sup>51,53</sup> Higher Resolution TEM images, lattice fringes and SAED have been recorded (**Fig. 4a-c, d-f** and **g-i**). The bright lattice fringes of modified MHSCs in HRTEM images depicted lattice plane distances (d space) 0.216, 0.345 and 0.250, corresponding to (220), (111), and (200) planes, respectively. SEAD patterns exhibit a well-defined crystalline nature of modified MHSCs. Consequently, for all MHSCs, the calculated lattice constant from TEM images (using GATAN software) is very close to the estimated value from p-XRD using the Bragg diffraction equation.

The collected TEM images were taken by selecting a spot from different locations on the grid because perovskite materials are volatile in high-energy electron beams. Hence, analyzing the element distribution for long-time electron beam exposure is challenging.

### **5.2.2.2 Optical properties**

In general, replacing Br<sup>-</sup> with Cl<sup>-</sup> in the perovskite lattice increases the band gap of materials, which is attributed to the downshift of the Valence band maximum (VBM) (increased electronegativity) and the upward shift of Conduction band minima (CBM) (increase in ionization energy). The decrease in Pb-X distances causes the confinement effect; both the electronegativity effect and the confinement effect of halides eventually increase the band gap. Hence, MH-PXA SC has more band gaps than other modified MHSCs. Band gap values of pristine MHSC are in congruence with previous reports.<sup>38,39</sup> As discussed in XPS measurements, a 0.112 eV increase in Pb<sup>+2</sup> orbitals binding energy was attributed to the reduced halide vacancies in MH-PEA SCs over the pristine. Considering both the contributions of surface defects towards photo-instability and optimized Cl ratio, this assumed that photo-induced phase segregation was reduced in the case of MH-PEA. Optical studies have been

carried out to further validate the generality of the defect-free surface on modified MHSCs and to investigate the impact of additives on bandgap. UV-VIS, spectroscopic measurements were performed in diffuse reflectance spectra (DRS) mode (**Fig. 5a**), and the bandgap was calculated based on the empirical Kubelka-Munk function (**Fig. 5b**). A slight decrement and increment of 0.002eV and 0.003 eV have been observed in MH-PEA and MH-PXA SCs.

To compare the light-induced phase segregation of modified MHSCs over the pristine PL measurements recorded under 800 nm laser (two-photon absorption) in ambient conditions (Fig. 5c). This two-photon absorption spectroscopy gives the details of the bulk materials. PL blue shift of modified MHSCs at a high Cl concentration level strongly suggests that incorporating Cl into the lattice employs the halide phase-segregation pathways, indicating the increase in nonradiative recombination (induced by deep traps Pb<sup>0</sup>, MA, etc.). <sup>55,56</sup> The order of PL emission intensity for SCs follows MH>MH-PEA>MH-PXA. The PL intensity shows quadratic dependence up to the 50 mW laser power; after that, it shows the saturation for all samples. R.A. Ganeev et al. showed a similar dependence of PL emission from MAPbBr3 thin films.<sup>57</sup> This order is more visible after crossing the 50 mW laser power. It represents the photostability of modified MHSCs at different laser power, forming the more halideconcentrated domains at high-intensity lasers. The XPS and PL data suggested a combination of mechanisms: suppress the nonradiative recombination, thereby increasing/decreasing the stability/defect states on the surface depending on the bonding interactions of additives, and an increase in intrinsic defect concentration concluded from structural and optical properties. The trends in the lattice constant and band gap were consistent; in all cases, the band gap-raising rate was ~0.002 eV, with each percentage of Cl alloyed. 38,39,58 The Fourier transform infrared (FT-IR) generally confirms the presence of additives using the functional group vibrational

modes strength in the spectrum and change in the vibrational modes.<sup>59</sup> The FT-IR spectrum of the pristine MHSC showed major shifts of the prominent peaks at 894 cm<sup>-1</sup>, 1245 cm<sup>-1</sup>, 1451 cm<sup>-1</sup>, and 3097 cm<sup>-1</sup>, which attribute to the C–N stretch (v5), sym-NH<sub>3</sub><sup>+</sup> bend (v3), asym-NH<sub>3</sub><sup>+</sup> bend (v9), and sym-NH<sub>3</sub><sup>+</sup>stretch (v1), respectively. This peak shifted by adding the additives owing to changes in the MA<sup>+</sup> interaction with the Pb–X inorganic octahedron. The N–H stretch trend should increase (band position increases) for Cl concentration as it is more

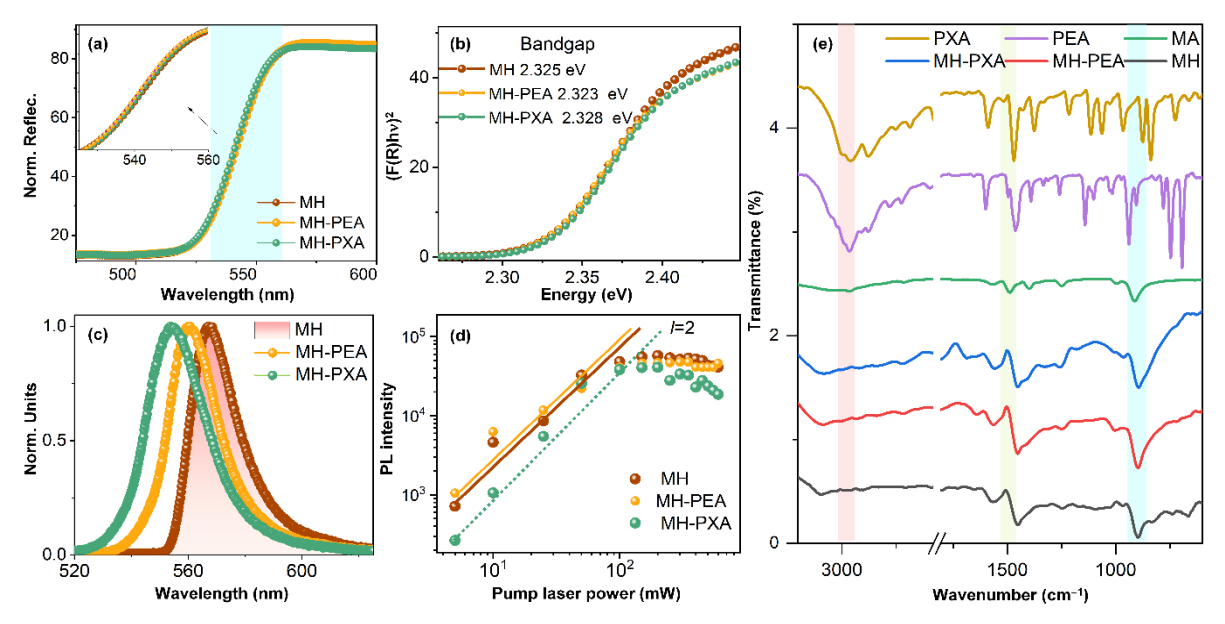


Fig. 5. 2. 5(a) UV-visible spectra, enlorged view in insert. (b) The energy vs F(R(hv))<sup>2</sup> plot.

The MH, MH-PEA and MH-PXA SCs are photoexcited with 800 nm, the corresponding (c)

PL spectra (d) PL intensity vs input laser power and (e) FT-IR spectra, vibrational modes

with respect to additives in the modified MHSCs.

electronegative than bromide. In the spectra of the modified MHSCs, the characteristic peaks of unsaturated benzene C-H vibrational mode in region 3005 cm<sup>-1</sup> are visible in the modified MHSCs spectrum, indicating the presence of aromatic additives on the surface, coordinated with the Pb<sup>+2</sup> ions. Change in vibrational modes with additives in the modified MHSCs from 1000 to 600 cm<sup>-1</sup> provided in SI, **Fig. S5.** 

#### 5.2.2.3. THz spectroscopy

THz studies were conducted in transmittance and reflection modes to justify surface artefacts and to study the crystal depth profile of MHSCs. THz radiation could be generated by focusing femtoseconds amplifier pulses of 800 nm and its second harmonic wavelengths (twocolour pump) into ambient air, which is one of the potential sources. 60-65 Several researchers explored the diversity of THz applications in optics, photonics, biomedical, and imaging. <sup>66–70</sup> Meanwhile, THz-TDS has developed a promising technique in sciences and medicines.<sup>71–74</sup> Earlier, research groups have studied a variety of organic-inorganic halide perovskites in the THz range. 75-83 Therefore, THz-TDS is one of the prominent techniques to ascertain a material's response in terms of transmission and reflection properties and can obtain the absorption coefficient raised due to the optical phonon vibrations. In the present study, we measured THz pulses' transmission and reflection from MH series PSCs. Fig. S1 depicts the experimental set-up used for THz time-domain spectroscopy. The corresponding transmission of the THz electric field (temporal profile) from MH, MH-PEA, MH-PXA; positioned at normal incidence to the reference THz pulse (transmission at 0°) (Fig. 6a), transmission/reflection 45° (**Fig. 6b/c**) for delay (ps). At the same time, transmission at 0° (**Fig.** 6d), transmittance/reflectance at 45° (Fig. 6e), absorption coefficients (Fig. 6f), and real conductivity at 0° and 45° (**Fig. 6g**), measured respective to frequency (THz).

The measured transmittance for PSCs at 0° (THz amplitude for PSCs/ THz amplitude reference pulse) (**Fig. S6a**). The reference THz pulse has a bandwidth of up to 3.0 THz having maximum peak intensity of around 1 THz. The transmitted/reflected THz pulses have less peak intensity and bandwidth due to the absorption of SCs. The SCs possess higher reflection than

transmission. Also, the reflectance (**Fig. S6**) (b, bottom panel); the additive SCs are much superior to transmittance (**Fig. S6**(b, upper panel)) compared to pristine. The transmission at 45° is lower than 0° due to extended path length because the orientation of MHSC at 45° increases the interacting length of THz pulses. It is familiar that based on the transmission data of THz pulses from SCs, one can obtain the absorption coefficient and conductivity by knowing the real/imaginary parts of the refractive index. The equations used for these measurements were reported elsewhere. Here, the thickness of PSCs plays a key role in these measurements. The measured thickness of MH, MH-PEA, and MH-PXA, using digital vernier callipers, is followed by 1.45, 1.44, and 1.47 mm, respectively. The measured absorption coefficients and real conductivity of SCs at T0° and T45° (**Fig. 6g,h**), respectively. The peak position absorption and conductivity for each SCs are almost identical except for the 1.5THz for MH.

Meanwhile. it observed that the modified **MHSCs** shift is their absorption/conductivity peaks compared to the pure MH crystal; this might be due to a change in the morphology and chemical composition of additive-based MHSCs. Earlier, three phonon modes (0.8,1.4, and 2.0 THz) associated with pure MAPbBr<sub>3</sub> SCs were determined by Inhee Maeng et al. 47 using first-principles simulations. The Pb-Br-Pb bonds show transverse and longitudinal optical vibrations at 0.8 and 1.4 THz, respectively. Whereas the 2.0 THz corresponds to optical Br vibration. However, other vibrational frequencies are present in the optical IR vibrational spectra reported by Inhee Maeng et al.<sup>47</sup> Those frequencies are labelled as solid red lines, and the corresponding values are shown on the top axis of Fig. 6g. Earlier, the vibrational modes of MAPbX<sub>3</sub> (X=Cl, Br, and I) using Raman spectroscopy and theoretical simulations were demonstrated by Brivio F. et al. 90 Chlorine-contained PSCs have higher vibrational frequencies than the bromide and iodine-based SCs.<sup>91</sup> In the present case, we have grown the MHSCs in different additives (PEA and PXA). Therefore, these additives

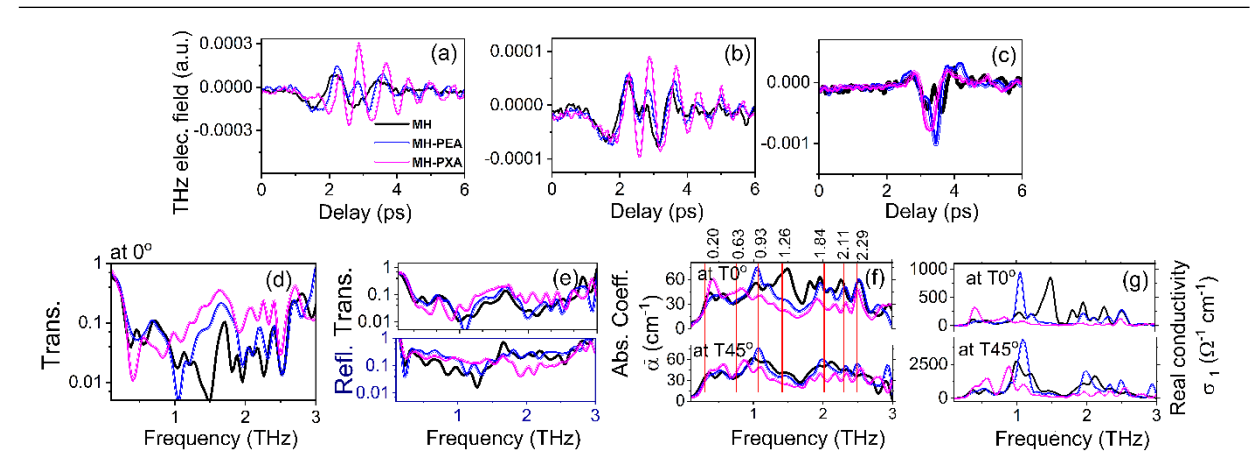


Fig. 5. 2. 6 The THz electric field of THz pulse. Transmission from MH, MH-PEA, MH-PXA SCs at (a) 0°, (b) 45° and (c) reflection at 45° with repective to delay (ps). Transmittance MH, MH-PEA, MH-PXA SCs (d) at 0°, (e) transmittance/reflectance at 45°, (f) absorption coefficients, and (g) real conductivity at 0° and 45°, measured with repective to frequency (THz).

contributed to the weight and atomic % changes in modified MHSCs than the pristine (C, N, Pb, Br and Cl) confirmed by XPS data. As a result, the vibrational frequencies depend on the chemical bonding between Pb-Br/Cl-Pb and individual Br and Cl optical vibrations. Hence, the frequencies of the resultant absorption /conduction spectra are shifted compared to pure MH SC. Moreover, the additive PEA has influenced crystal morphology and enhanced THz transmission and reflection. As a result, the absorption/conductivity becomes weaker, which implies the applicability of additive-based PSCs in the THz range.

#### 5.2.3. Conclusions.

In summary, we have successfully demonstrated an AE strategy for mitigating the mixed halide phase segregation effect of 6.67% Cl-doped MHSCs with the additives. Out of all the additives we have observed, a bluer shift in PL emission for MH-PXA SC when exited with a 2PA source laser indicates more nonradiative recombination. Interestingly, we observed increased crystallinity with mitigated phase segregation (concluded from p-XRD and XPS studies). The lattice constant of the PEA-MHSCs is more than other additives, suggesting increased Schottky order and transparency in the bulk perovskite. This explanation is consistent with the increased interaction between the formation of MHSCs, with PEA additives being more thermodynamically preferred than other additives. The present work will open the doors for getting more transparent flat surface crystals with low trap states for photodetection applications, particularly THz and higher energy radiation detection with excellent resolution.

#### ASSOCIATED CONTENT

Supporting Information: Experimental details of MHSCs, synthesis method, Instrumental details (**Fig.** S1), characterization details, EDX weight % values of modified and pristine MHSCs (**Fig.** S2). Elemental ratios extracted from the EDX data (Appendix IV **Table 6**), the p-XRD data, microstrain (**Fig.** S3 and **Fig.** S4), FT-IR spectra (**Fig.** S5) and the THz electric field of THz amplitude, phase and frequency spectra (**Fig.** S6) of modified and pristine MHSCs.

#### **Author Contributions**

Sarvani Jowhar Khanam: Conceptualization, Data curation, Investigation, Formal Analysis, Methodology Writing – original draft, Writing – review & editing. Srinivasa Rao Konda: Data curation, Investigation, Analysis, original draft, Writing – review & editing. Wei Li: Resources, Writing – review & editing. Murali Banavoth: Funding acquisition, Supervision, Project administration, Formal Analysis, Methodology Writing – original draft, Writing – review & editing.

#### **Conflicts of interest**

The authors declare there is no conflict of interest

#### Acknowledgements

This work is supported by the School of Chemistry, University of Hyderabad. MB acknowledges the Department of Science and Technology (DST), Indo-Korea grant (No. INT/Korea/P-40) and Institute of Eminence (UOH-IOE-RC2-21-008). The Innovation Grant of Changchun Institute of Optics, Fine Mechanics and Physics (CIOMP), Jilin Provincial Science and Technology Development Project (YDZJ202102CXJD002), Development Program of the Science and Technology of Jilin Province (20200802001GH), Chinese Academy of Sciences President's International Fellowship Initiative (2021PM0036). SRK thanks Rahul A. Rajan, GPL, for his assistance in collecting the 800 nm PL spectra.

# **References:**

- (1) Diyali, S.; Manna, M.; Mahato, S.; Kumar, V.; Roy Choudhury, A.; Biswas, B.; Bhandari, S. Hybrid Lead Bromide Perovskite Single Crystals Coupled with a Zinc(II) Complex for White Light Emission. *Journal of Physical Chemistry Letters* **2022**, 13, 10759–10766.
- (2) Xiao, Z.; Kerner, R. A.; Zhao, L.; Tran, N. L.; Lee, K. M.; Koh, T. W.; Scholes, G. D.; Rand, B. P. Efficient Perovskite Light-Emitting Diodes Featuring Nanometre-Sized Crystallites. *Nature Photonics*. **2017**, 11, 108–115.
- (3) Xiao, Z.; Kerner, R. A.; Tran, N.; Zhao, L.; Scholes, G. D.; Rand, B. P. Engineering Perovskite Nanocrystal Surface Termination for Light-Emitting Diodes with External Quantum Efficiency Exceeding 15%. *Advanced Functional Materials* **2019**, 29, 1807284.

- (4) Zhao, L.; Rolston, N.; Lee, K. M.; Zhao, X.; Reyes-Martinez, M. A.; Tran, N. L.; Yeh, Y.; Yao, N.; Scholes, G. D.; Loo, Y.; Selloni, A.; Dauskardt, R. H.; Rand, B. P. Influence of Bulky Organo-Ammonium Halide Additive Choice on the Flexibility and Efficiency of Perovskite Light-Emitting Devices. *Advanced Functional Materials* **2018**, 28, 1802060.
- Zhao, L.; Yeh, Y. W.; Tran, N. L.; Wu, F.; Xiao, Z.; Kerner, R. A.; Lin, Y. L.; Scholes,
  G. D.; Yao, N.; Rand, B. P. In Situ Preparation of Metal Halide Perovskite Nanocrystal Thin
  Films for Improved Light-Emitting Devices. *ACS Nano* 2017, 11, 3957–3964.
- (6) Xing, G.; Mathews, N.; Lim, S. S.; Yantara, N.; Liu, X.; Sabba, D.; Grätzel, M.; Mhaisalkar, S.; Sum, T. C. Low-Temperature Solution-Processed Wavelength-Tunable Perovskites for Lasing. *Nature Materials* **2014**, 13, 476–480.
- (7) Deschler, F.; Price, M.; Pathak, S.; Klintberg, L. E.; Jarausch, D. D.; Higler, R.; Hüttner, S.; Leijtens, T.; Stranks, S. D.; Snaith, H. J.; Atatüre, M.; Phillips, R. T.; Friend, R. H. High Photoluminescence Efficiency and Optically Pumped Lasing in Solution-Processed Mixed Halide Perovskite Semiconductors. *Journal of Physical Chemistry Letters* **2014**, 5, 1421–1426.
- (8) Xing, J.; Zhao, C.; Zou, Y.; Kong, W.; Yu, Z.; Shan, Y.; Dong, Q.; Zhou, D.; Yu, W.; Guo, C. Modulating the Optical and Electrical Properties of MAPbBr3 Single Crystals via Voltage Regulation Engineering and Application in Memristors. *Light: Science & Applications* **2020**, 9, 11.
- (9) Buriak, J. M.; Kamat, P. V.; Schanze, K. S.; Alivisatos, A. P.; Murphy, C. J.; Schatz, G. C.; Scholes, G. D.; Stang, P. J.; Weiss, P. S. Virtual Issue on Metal-Halide Perovskite Nanocrystals A Bright Future for Optoelectronics. *Chemistry of Materials* 2017, 29, 8915–8917.

- (10) Elkins, M. H.; Pensack, R.; Proppe, A. H.; Voznyy, O.; Quan, L. N.; Kelley, S. O.; Sargent, E. H.; Scholes, G. D. Biexciton Resonances Reveal Exciton Localization in Stacked Perovskite Quantum Wells. *Journal of Physical Chemistry Letters* **2017**, 8, 3895–3901.
- (11) Turren-Cruz, S. H.; Hagfeldt, A.; Saliba, M. Methylammonium-Free, High-Performance, and Stable Perovskite Solar Cells on a Planar Architecture. *Science* **2018**, 362, 449–453.
- (12) Jeong, J.; Kim, M.; Seo, J.; Lu, H.; Ahlawat, P.; Mishra, A.; Yang, Y.; Hope, M. A.; Eickemeyer, F. T.; Kim, M.; Yoon, Y. J.; Choi, I. W.; Darwich, B. P.; Choi, S. J.; Jo, Y.; Lee, J. H.; Walker, B.; Zakeeruddin, S. M.; Emsley, L.; Rothlisberger, U.; Hagfeldt, A.; Kim, D. S.; Grätzel, M.; Kim, J. Y. Pseudo-Halide Anion Engineering for α-FAPbI<sub>3</sub> Perovskite Solar Cells. *Nature* **2021**, 592, 381–385.
- (13) Jacobsson, T. J.; Hultqvist, A.; García-Fernández, A.; Anand, A.; Al-Ashouri, A.; Hagfeldt, A.; Crovetto, A.; Abate, A.; Ricciardulli, A. G.; Vijayan, A.; Kulkarni, A.; Anderson, A. Y.; Darwich, B. P.; Yang, B.; Coles, B. L.; Perini, C. A. R.; Rehermann, C.; Ramirez, D.; Fairen-Jimenez, D.; Di Girolamo, D.; Jia, D.; Avila, E.; Juarez-Perez, E. J.; Baumann, F.; Mathies, F.; González, G. S. A.; Boschloo, G.; Nasti, G.; Paramasivam, G.; Martínez-Denegri, G.; Näsström, H.; Michaels, H.; Köbler, H.; Wu, H.; Benesperi, I.; Dar, M. I.; Bayrak Pehlivan, I.; Gould, I. E.; Vagott, J. N.; Dagar, J.; Kettle, J.; Yang, J.; Li, J.; Smith, J. A.; Pascual, J.; Jerónimo-Rendón, J. J.; Montoya, J. F.; Correa-Baena, J. P.; Qiu, J.; Wang, J.; Sveinbjörnsson, K.; Hirselandt, K.; Dey, K.; Frohna, K.; Mathies, L.; Castriotta, L. A.; Aldamasy, M. H.; Vasquez-Montoya, M.; Ruiz-Preciado, M. A.; Flatken, M. A.; Khenkin, M. V.; Grischek, M.; Kedia, M.; Saliba, M.; Anaya, M.; Veldhoen, M.; Arora, N.; Shargaieva, O.; Maus, O.; Game, O. S.; Yudilevich, O.; Fassl, P.; Zhou, Q.; Betancur, R.; Munir, R.; Patidar, R.; Stranks, S. D.;

- Alam, S.; Kar, S.; Unold, T.; Abzieher, T.; Edvinsson, T.; David, T. W.; Paetzold, U. W.; Zia, W.; Fu, W.; Zuo, W.; Schröder, V. R. F.; Tress, W.; Zhang, X.; Chiang, Y. H.; Iqbal, Z.; Xie, Z.; Unger, E. An Open-Access Database and Analysis Tool for Perovskite Solar Cells Based on the FAIR Data Principles. *Nature Energy* **2022**, *7*, 107–115.
- (14) Kim, M.; Jeong, J.; Lu, H.; Lee, T. K.; Eickemeyer, F. T.; Liu, Y.; Choi, I. W.; Choi, S. J.; Jo, Y.; Kim, H. B.; Mo, S. I.; Kim, Y. K.; Lee, H.; An, N. G.; Cho, S.; Tress, W. R.; Zakeeruddin, S. M.; Hagfeldt, A.; Kim, J. Y.; Grätzel, M.; Kim, D. S. Conformal Quantum Dot-SnO<sub>2</sub> Layers as Electron Transporters for Efficient Perovskite Solar Cells. *Science* **2022**, 375, 302–306.
- (15) Yang, C.; Yin, J.; Li, H.; Almasabi, K.; Gutiérrez-Arzaluz, L.; Gereige, I.; Brédas, J.-L.; Bakr, O. M.; Mohammed, O. F. Engineering Surface Orientations for Efficient and Stable Hybrid Perovskite Single-Crystal Solar Cells. *ACS Energy Letters* **2022**, 7, 1544–1552.
- (16) Xiang, W.; Wang, Z.; Kubicki, D. J.; Tress, W.; Luo, J.; Prochowicz, D.; Akin, S.; Emsley, L.; Zhou, J.; Dietler, G.; Grätzel, M.; Hagfeldt, A. Europium-Doped CsPbI 2 Br for Stable and Highly Efficient Inorganic Perovskite Solar Cells. *Joule* **2019**, 3, 205–214.
- (17) Sheikh, T.; Anilkumar, G. M.; Das, T.; Rahman, A.; Chakraborty, S.; Nag, A. Combining π-Conjugation and Cation–π Interaction for Water-Stable and Photoconductive One-Dimensional Hybrid Lead Bromide. *Journal of Physical Chemistry Letters* **2023**, 1870–1876.
- (18) Bai, F.; Bian, K.; Huang, X.; Wang, Z.; Fan, H. Pressure Induced Nanoparticle Phase Behavior, Property, and Applications. *Chemical Reviews* **2019**, 119, 7673–7717.

- (19) Pan, Z.; Wu, L.; Jiang, J.; Shen, L.; Yao, K. Searching for High-Quality Halide Perovskite Single Crystals toward X-Ray Detection. *Journal of Physical Chemistry Letters* **2022**, 13, 2851–2861
- (20) Gui, P.; Chen, Z.; Li, B.; Yao, F.; Zheng, X.; Lin, Q.; Fang, G. High-Performance Photodetectors Based on Single All-Inorganic CsPbBr3 Perovskite Microwire. *ACS Photonics*. **2018**, 5, 2113–2119.
- (21) Zhang, H.; Nazeeruddin, M. K.; Choy, W. C. H. Perovskite Photovoltaics: The Significant Role of Ligands in Film Formation, Passivation, and Stability. *Advanced Materials*. **2019**, 3, e1805702.
- (22) Balis, N.; Zaky, A. A.; Athanasekou, C.; Silva, A. M.; Sakellis, E.; Vasilopoulou, M.; Stergiopoulos, T.; Kontos, A. G.; Falaras, P. Investigating the Role of Reduced Graphene Oxide as a Universal Additive in Planar Perovskite Solar Cells. *Journal of Photochemistry and Photobiology A: Chemistry* **2020**, 386, 112141.
- (23) Lin, Q.; Armin, A.; Burn, P. L.; Meredith, P. Filterless Narrowband Visible Photodetectors. *Nature Photonics*. **2015**, 9, 687–694.
- (24) Yao, F.; Gui, P.; Chen, C.; Li, B.; Li, R.; Tao, C.; Lin, Q.; Fang, G. High-Rubidium-Formamidinium-Ratio Perovskites for High-Performance Photodetection with Enhanced Stability. *ACS Applied Materials and Interfaces* **2019**, 11, 39875–39881.
- (25) Chao, L.; Xia, Y.; Li, B.; Xing, G.; Chen, Y.; Huang, W. Room-Temperature Molten Salt for Facile Fabrication of Efficient and Stable Perovskite Solar Cells in Ambient Air. *Chem* **2019**, 5, 995–1006.

- (26) Tran, N. L.; Elkins, M. H.; McMeekin, D. P.; Snaith, H. J.; Scholes, G. D. Observation of Charge Generation via Photo-induced Stark Effect in Mixed-Cation Lead Bromide Perovskite Thin Films. *Journal of Physical Chemistry Letters* **2020**, 11, 10081–10087.
- (27) Ding, J.; Gao, W.; Gao, L.; Lu, K.; Liu, Y.; Sun, J. L.; Yan, Q. Unraveling the Effect of Halogen Ion Substitution on the Noise of Perovskite Single-Crystal Photodetectors. *Journal of Physical Chemistry Letters* **2022**, 13, 7831–7837.
- (28) Shi, D.; Adinolfi, V.; Comin, R.; Yuan, M.; Alarousu, E.; Buin, A.; Chen, Y.; Hoogland, S.; Rothenberger, A.; Katsiev, K.; Losovyj, Y.; Zhang, X.; Dowben, P. A.; Mohammed, O. F.; Sargent, E. H.; Bakr, O. M. Low Trap-State Density and Long Carrier Diffusion in Organolead Trihalide Perovskite Single Crystals. *Science* **2015**, 347,
- (29) Efrati, A.; Aharon, S.; Wierzbowska, M.; Etgar, L. First Evidence of Macroscale Single Crystal Ion Exchange Found in Lead Halide Perovskites. *EcoMat.* **2020**, 2, e12016.
- (30) Liu, Y.; Yang, Z.; Cui, D.; Ren, X.; Sun, J.; Liu, X.; Zhang, J.; Wei, Q.; Fan, H.; Yu, F.; Zhang, X.; Zhao, C.; Liu, S. Two-Inch-Sized Perovskite CH<sub>3</sub>NH<sub>3</sub>PbX<sub>3</sub> (X = Cl, Br, I) Crystals: Growth and Characterization. *Advanced Materials* **2015**, 27, 5176–5183.
- (31) Yao, F.; Peng, J.; Li, R.; Li, W.; Gui, P.; Li, B.; Liu, C.; Tao, C.; Lin, Q.; Fang, G. Perovskite Single Crystals. *Nature Communications* **2019**, 31, 1–9.
- (32) Almora, O.; Matt, G. J.; These, A.; Kanak, A.; Levchuk, I.; Shrestha, S.; Osvet, A.; Brabec, C. J.; Garcia-Belmonte, G. Surface versus Bulk Currents and Ionic Space-Charge Effects in CsPbBr3Single Crystals. *Journal of Physical Chemistry Letters* **2022**, *13*, 3824–3830.
- (33) Schötz, K.; Askar, A. M.; Peng, W.; Seeberger, D.; Gujar, T. P.; Thelakkat, M.; Köhler, A.; Huettner, S.; Bakr, O. M.; Shankar, K.; Panzer, F. Double Peak Emission in Lead Halide Perovskites by Self-Absorption. *Journal of Material Chemistry C* **2020**, 8, 2289–2300.

- (34) Ng, M.; Halpert, J. E. Single Crystals of Mixed Br/Cl and Sn-Doped Formamidinium Lead Halide Perovskites: Via Inverse Temperature Crystallization. *RSC Advances* **2020**, 10, 3832–3836.
- (35) Saidaminov, M. I.; Abdelhady, A. L.; Murali, B.; Alarousu, E.; Burlakov, V. M.; Peng, W.; Dursun, I.; Wang, L.; He, Y.; Maculan, G.; Goriely, A.; Wu, T.; Mohammed, O. F.; Bakr, O. M. High-Quality Bulk Hybrid Perovskite Single Crystals within Minutes by Inverse Temperature Crystallization. *Nature Communications* **2015**, 6, 7586.
- (36) Liu, Y.; Zhang, Y.; Yang, Z.; Feng, J.; Xu, Z.; Li, Q.; Hu, M.; Ye, H.; Zhang, X.; Liu, M.; Zhao, K.; Liu, S. Low-Temperature-Gradient Crystallization for Multi-Inch High-Quality Perovskite Single Crystals for Record Performance Photodetectors. *Materials Today* **2019**, 22, 67–75.
- (37) Feng, Y.; Pan, L.; Wei, H.; Liu, Y.; Ni, Z.; Zhao, J.; Rudd, P. N.; Cao, L. R.; Huang, J. Low Defects Density CsPbBr<sub>3</sub> Single Crystals Grown by an Additive Assisted Method for Gamma-Ray Detection. *Journal of Material Chemistry C.* **2020**, 8, 11360–11368.
- (38) Mix, L. T.; Ghosh, D.; Tisdale, J.; Lee, M.-C.; O'Neal, K. R.; Sirica, N.; Neukirch, A. J.; Nie, W.; Taylor, A. J.; Prasankumar, R. P.; Tretiak, S.; Yarotski, D. A. Hot Carrier Cooling and Recombination Dynamics of Chlorine-Doped Hybrid Perovskite Single Crystals. *Journal of Physical Chemistry Letters* **2020**, 11, 8430–8436.
- (39) Qiu, L.; Wang, Z.; Luo, S.; Li, C.; Wang, L.; Ke, S.; Shu, L.; Mix, L. T.; Ghosh, D.; Tisdale, J.; Lee, M.-C.; O'Neal, K. R.; Sirica, N.; Neukirch, A. J.; Nie, W.; Taylor, A. J.; Prasankumar, R. P.; Tretiak, S.; Yarotski, D. A. Perovskite MAPb(Br<sub>1</sub>-xClx )<sub>3</sub> Single Crystals: Solution Growth and Electrical Properties. . *Journal of Crystal Growth* **2020**, 549, 125869.

- (40) Beal, R. E.; Hagström, N. Z.; Barrier, J.; Gold-Parker, A.; Prasanna, R.; Bush, K. A.; Passarello, D.; Schelhas, L. T.; Brüning, K.; Tassone, C. J.; Steinrück, H. G.; McGehee, M. D.; Toney, M. F.; Nogueira, A. F. Structural Origins of Light-Induced Phase Segregation in Organic-Inorganic Halide Perovskite Photovoltaic Materials. *Matter* **2020**, *2*, 207–219.
- (41) Mehdi, H.; Mhamdi, A.; Bouazizi, A. Effect of Perovskite Precursor Ratios and Solvents Volume on the Efficiency of MAPbI<sub>3-X</sub>Cl<sub>x</sub> Mixed Halide Perovskite Solar Cells. *Materials Science in Semiconductor Processing* **2020**, *109*, 104915.
- (42) Knight, A. J.; Herz, L. M. Preventing Phase Segregation in Mixed-Halide Perovskites: A Perspective. *Energy and Environmental Science* **2020**, 13, 2024–2046.
- (43) Ruan, S.; Surmiak, M.-A.; Ruan, Y.; McMeekin, D. P.; Ebendorff-Heidepriem, H.; Cheng, Y.-B.; Lu, J.; McNeill, C. R. Light Induced Degradation in Mixed-Halide Perovskites. *Journal of Materials Chemistry C* **2019**, *7*, 9326–9334.
- (44) Tang, S.; Chen, J.; Li, C.; Mao, Z.; Cheng, Z.; Zhang, J.; Zhu, M.; Xiang, S.; Zhang, Z. Mixing Halogens Improves the Passivation Effects of Amine Halide on Perovskite. *Electrochimica Acta* **2022**, *405*, 139782.
- (45) Wang, Z.; Zhang, Z.; Xie, L.; Wang, S.; Yang, C.; Fang, C.; Hao, F. Recent Advances and Perspectives of Photostability for Halide Perovskite Solar Cells. *Advanced Optical Materials* **2022**, *10* (3).
- (46) Billing, D. G.; Lemmerer, A. Synthesis and Crystal Structures of Inorganic-Organic Hybrids Incorporating an Aromatic Amine with a Chiral Functional Group. *CrystEngComm* **2006**, 8 (9), 686–695.
- (47) Maeng, I.; Lee, S.; Tanaka, H.; Yun, J.-H.; Wang, S.; Nakamura, M.; Kwon, Y.-K.; Jung, M.-C. Unique Phonon Modes of a CH<sub>3</sub>NH<sub>3</sub>PbBr<sub>3</sub> Hybrid Perovskite Film without the Influence

of Defect Structures: An Attempt toward a Novel THz-Based Application. *NPG Asia Materials* **2020**, 12, 53.

- (48) Xu, J.; Boyd, C. C.; Yu, Z. J.; Palmstrom, A. F.; Witter, D. J.; Larson, B. W.; France, R. M.; Werner, J.; Harvey, S. P.; Wolf, E. J.; Weigand, W.; Manzoor, S.; Van Hest, M. F. A. M.; Berry, J. J.; Luther, J. M.; Holman, Z. C.; McGehee, M. D. Triple-Halide Wide-Band Gap Perovskites with Suppressed Phase Segregation for Efficient Tandems. *Science* **2020**, *367*, 1097–1104.
- (49) Khanam, S. J.; Banerjee, D.; Soma, V. R.; Murali, B. Stability Enhancement and Pronounced Three-Photon Absorption in SrC12-Doped FAPbBr<sub>3</sub> Nano Crystals. *Journal of Materials Chemistry C* **2023**, *11*, 3275–3283.
- (50) Saidaminov, M. I.; Adinolfi, V.; Comin, R.; Abdelhady, A. L.; Peng, W.; Dursun, I.; Yuan, M.; Hoogland, S.; Sargent, E. H.; Bakr, O. M. Planar-Integrated Single-Crystalline Perovskite Photodetectors. *Nature Communications* **2015**, *6*, 8724.
- (51) Wang, X.; Li, Y.; Xu, Y.; Pan, Y.; Zhu, C.; Zhu, D.; Wu, Y.; Li, G.; Zhang, Q.; Li, Q.; Zhang, X.; Wu, J.; Chen, J.; Lei, W. Solution-Processed Halide Perovskite Single Crystals with Intrinsic Compositional Gradients for X-Ray Detection. *Chemistry of Materials* **2020**, *32*, 4973–4983.
- (52) Zou, Y.; Zou, T.; Zhao, C.; Wang, B.; Xing, J.; Yu, Z.; Cheng, J.; Xin, W.; Yang, J.; Yu, W.; Dong, H.; Guo, C. A Highly Sensitive Single Crystal Perovskite–Graphene Hybrid Vertical Photodetector. *Small* **2020**, *16*, 2000733.
- (53) Wang, Y.; Quintana, X.; Kim, J.; Guan, X.; Hu, L.; Lin, C.-H.; Jones, B. T.; Chen, W.; Wen, X.; Gao, H.; Wu, T. Phase Segregation in Inorganic Mixed-Halide Perovskites: From Phenomena to Mechanisms. *Photonics Research* **2020**, 8, A56-71.

- (54) Yamada, Y.; Hoyano, M.; Oto, K.; Kanemitsu, Y. Effects of Impurity Doping on Photoluminescence Properties of APbX<sub>3</sub> Lead Halide Perovskites. *Physica status B Basic Research* **2019**, 256, 1800545.
- (55) Zhang, F.; Zhu, K. Additive Engineering for Efficient and Stable Perovskite Solar Cells. *Advanced Energy Materials* **2020**, 10, 1902579.
- (56) Ganeev, R. A.; Rao, K. S.; Yu, Z.; Yu, W.; Yao, C.; Fu, Y.; Zhang, K.; Guo, C. Strong Nonlinear Absorption in Perovskite Films. *Optical Material Express.* **2018**, 8, 1472–1483.
- (57) Jiang, S.; Wang, X.; Wu, Y.; Li, Y. W.; Zhang, Q.; Li, G. W.; Wu, Y.; Zhang, W.; Zhang, X.; Wang, B.; Chen, J.; Lei, W. Balance Lead in Solution-Processed CH<sub>3</sub>NH<sub>3</sub>PbBr<sub>x</sub>Cl<sub>(3-x)</sub> Single Crystals for High Performance X-Ray Detection. Matter Letters **2019**, 236, 26–29.
- (58) Mahapatra, A.; Parikh, N.; Kumari, H.; Pandey, M. K.; Kumar, M.; Prochowicz, D.; Kalam, A.; Tavakoli, M. M.; Yadav, P. Reducing Ion Migration in Methylammonium Lead Tri-Bromide Single Crystal via Lead Sulfate Passivation. *Journal of Applied Physics* **2020**, 127, 185501.
- (59) Thomson, M. D.; Kreß, M.; Löffler, T.; Roskos, H. G. Broadband THz Emission from Gas Plasmas Induced by Femtosecond Optical Pulses: From Fundamentals to Applications. *Laser and Photonics Reviews* **2007**, 1, 349–368.
- (60) Fedorov, V. Y.; Tzortzakis, S. Powerful Terahertz Waves from Long-Wavelength Infrared Laser Filaments. *Light: Science & Applications* **2020**, 9, 186.
- (61) Xie, X.; Dai, J.; Zhang, X.-C. Coherent Control of THz Wave Generation in Ambient Air. *Physical Review Letters* **2006**, 96, 075005.
- (62) Cook, D. J.; Hochstrasser, R. M. Intense Terahertz Pulses by Four-Wave Rectification in Air. *Optics Letters* **2000**, 25, 1210–1212.

- (63) Chen, M.-K.; Kim, J. H.; Yang, C.-E.; Yin, S. S.; Hui, R.; Ruffin, P. Terahertz Generation in Multiple Laser-Induced Air Plasmas. *Optics letters* **2008**, 93, 231102.
- (64) Ma, D.; Dong, L.; Zhang, R.; Zhang, C.; Zhao, Y.; Zhang, L. Enhancement of Terahertz Wave Emission from Air Plasma Excited by Harmonic Three-Color Laser Fields. *Optics Communications* **2021**, 481, 126533.
- (65) Bera, A.; Bera, S.; Kalimuddin, S.; Gayen, S.; Kundu, M.; Das, B.; Mondal, M. Review of Recent Progress on THz Spectroscopy of Quantum Materials: Superconductors, Magnetic and Topological Materials. *European Physical Journal Special Topics* **2021**, 230, 4113–4139.
- (66) Heindl, M. B.; Kirkwood, N.; Lauster, T.; Lang, J. A.; Retsch, M.; Mulvaney, P.; Herink, G. Ultrafast Imaging of Terahertz Electric Waveforms Using Quantum Dots. *Light: Science & Applications* **2022**, 11, 31–33.
- (67) Roussel, E.; Szwaj, C.; Evain, C.; Steffen, B.; Gerth, C.; Jalali, B.; Bielawski, S. Phase Diversity Electro-Optic Sampling: A New Approach to Single-Shot Terahertz Waveform Recording. *Light: Science & Applications* **2022**, 11, 14.
- (68) Peng, Y.; Shi, C.; Zhu, Y.; Gu, M.; Zhuang, S. Terahertz Spectroscopy in Biomedical Field: A Review on Signal-to-Noise Ratio Improvement. *PhotoniX*. **2020**, 1, 12.
- (69) Chen, Z.; Segev, M. Highlighting Photonics: Looking into the next Decade. *eLight* **2021**, 1, 2.
- (70) Pyne, P.; Das Mahanta, D.; Gohil, H.; Prabhu, S. S.; Mitra, R. K. Correlating Solvation with Conformational Pathways of Proteins in Alcohol-Water Mixtures: A THz Spectroscopic Insight. *Physical Chemistry Chemical Physics* **2021**, 23, 17536–17544.
- (71) Sharma, P.; Kumar, M.; Awana, V. P. S.; Singh, A.; Gohil, H.; Prabhu, S. S. Comprehensive Analysis of Terahertz Frequency Response of Bi<sub>2</sub>Se<sub>3</sub> and Bi<sub>2</sub>Te<sub>3</sub> Single Crystals Using

Terahertz Time-Domain Spectroscopy. *Materials Science and Engineering B: Solid-State Materials for Advanced Technology* **2021**, 272, 115355.

- (72) Sindhu, P. S.; Mitra, N.; Ghindani, D.; Prabhu, S. S. Epoxy Resin (DGEBA/TETA) Exposed to Water: A Spectroscopic Investigation to Determine Water-Epoxy Interactions. *Journal of Infrared, Millimeter, and Terahertz Waves* **2021**, 42, 558–571.
- (73) Neu, J.; Schmuttenmaer, C. A. Tutorial: An Introduction to Terahertz Time Domain Spectroscopy (THz-TDS). *Journal of Applied Physics* **2018**, 124, 231101.
- (74) Chanana, A.; Liu, X.; Zhang, C.; Vardeny, Z. V.; Nahata, A. Ultrafast Frequency-Agile Terahertz Devices Using Methylammonium Lead Halide Perovskites. *Science Advances* **2018**, 4, eaar7353.
- (75) Sun, Q.; Yang, W.; Cheng, Y.; Dong, J.; Zhu, M.; Zhang, B. Bin; Dubois, A.; Zhu, M.; Jie, W.; Xu, Y. Anisotropic Dielectric Behavior of Layered Perovskite-like Cs<sub>3</sub>Bi<sub>2</sub>I<sub>9</sub>crystals in the Terahertz Region. *Physical Chemistry Chemical Physics* **2020**, 22, 24555–24560.
- (76) Zhao, D.; Chia, E. E. M. Free Carrier, Exciton, and Phonon Dynamics in Lead-Halide Perovskites Studied with Ultrafast Terahertz Spectroscopy. *Advanced Optical Materials* **2020**, 8, 1900783.
- (77) Bogue, R. Sensing with Terahertz Radiation: A Review of Recent Progress. *Sensor Review* **2018**, 38, 216–222.
- (78) Yettapu, G. R.; Talukdar, D.; Sarkar, S.; Swarnkar, A.; Nag, A.; Ghosh, P.; Mandal, P. Terahertz Conductivity within Colloidal CsPbBr<sub>3</sub> Perovskite Nanocrystals: Remarkably High Carrier Mobilities and Large Diffusion Lengths. *Nano Letters* **2016**, 16, 4838–4848.
- (79) Zhao, D.; Skelton, J. M.; Hu, H.; La-o-vorakiat, C.; Zhu, J.-X.; Marcus, R. A.; Michel-Beyerle, M.-E.; Lam, Y. M.; Walsh, A.; Chia, E. E. M. Low-Frequency Optical Phonon Modes

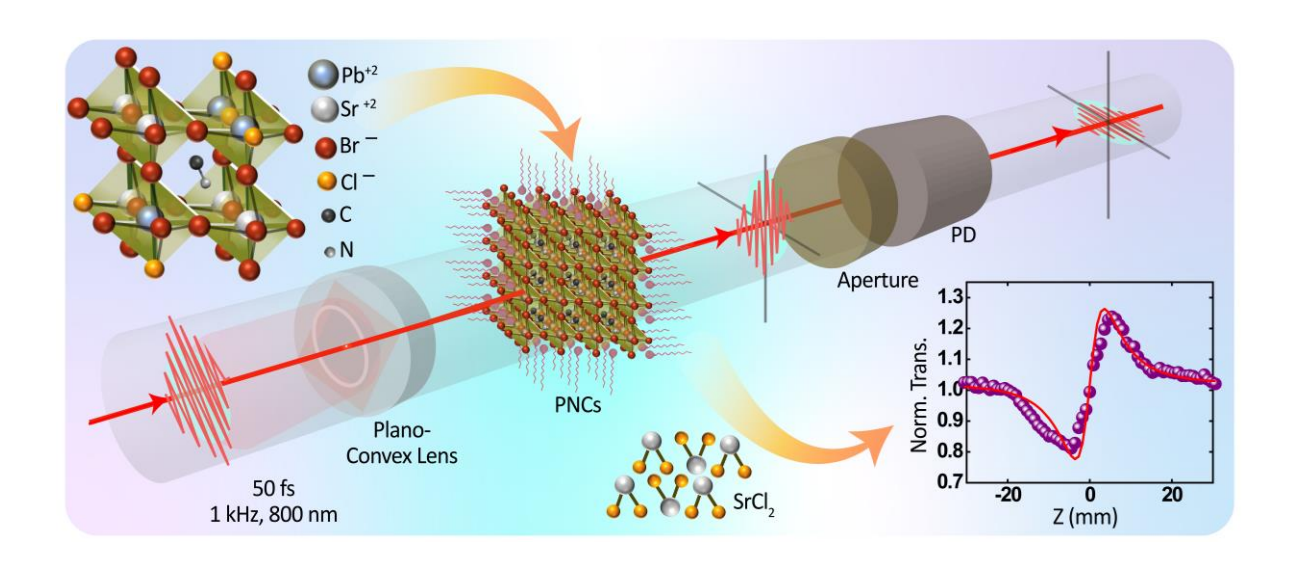
and Carrier Mobility in the Halide Perovskite CH<sub>3</sub>NH<sub>3</sub>PbBr<sub>3</sub> Using Terahertz Time-Domain Spectroscopy. *Applied Physics Letters* **2017**, 111, 201903.

- (80) Okochi, H.; Katsuki, H.; Tsubouchi, M.; Itakura, R.; Yanagi, H. Photon Energy-Dependent Ultrafast Photo-induced Terahertz Response in a Microcrystalline Film of CH<sub>3</sub>NH<sub>3</sub>PbBr<sub>3</sub>. *Journal of Physical Chemistry Letters* **2020**, 11, 6068–6076.
- (81) Ulatowski, A. M.; Herz, L. M.; Johnston, M. B. Terahertz Conductivity Analysis for Highly Doped Thin-Film Semiconductors. *Journal of Infrared, Millimeter, and Terahertz Waves* **2020**, 41, 1431–1449.
- (82) Xia, C. Q.; Peng, J.; Poncé, S.; Patel, J. B.; Wright, A. D.; Crothers, T. W.; Uller Rothmann, M.; Borchert, J.; Milot, R. L.; Kraus, H.; Lin, Q.; Giustino, F.; Herz, L. M.; Johnston, M. B. Limits to Electrical Mobility in Lead-Halide Perovskite Semiconductors. The *Journal of Physical Chemistry Letters* **2021**, 12, 3607–3617.
- (83) Duvillaret, L.; Garet, F.; Coutaz, J.-. A Reliable Method for Extraction of Material Parameters in Terahertz Time-Domain Spectroscopy. *IEEE Journal of Selected Topics in Quantum Electronics* **1996**, 2, 739–746.
- (84) Withayachumnankul, W.; Naftaly, M. Fundamentals of Measurement in Terahertz Time-Domain Spectroscopy. *Journal of Infrared, Millimeter, and Terahertz Waves* **2014**, 35, 610–637.
- (85) Yu, B. L.; Zeng, F.; Xing, Q.; Alfano, R. R. Probing Dielectric Relaxation Properties of Liquid CS<sub>2</sub> with Terahertz Time-Domain Spectroscopy. *Applied Physics Letters* **2003**, 82, 4633–4635.
- (86) Xia, C. Q.; Poncé, S.; Peng, J.; Ulatowski, A. M.; Patel, J. B.; Wright, A. D.; Milot, R. L.; Kraus, H.; Lin, Q.; Herz, L. M.; Giustino, F.; Johnston, M. B. Ultrafast Photo-Induced Phonon

Hardening Due to Pauli Blocking in MAPbI<sub>3</sub> single-Crystal and Polycrystalline Perovskites. *JPhys Materials* **2021**, 4, 044017.

- (87) Nienhuys, H.-K.; Sundström, V. Intrinsic Complications in the Analysis of Optical-Pump, Terahertz Probe Experiments. *Physical Review B* **2005**, 71, 235110.
- (88) Lloyd-Hughes, J.; Jeon, T.-I. A Review of the Terahertz Conductivity of Bulk and Nano-Materials. *Journal of Infrared, Millimeter, and Terahertz Waves* **2012**, 33, 871–925.
- (89) Brivio, F.; Frost, J. M.; Skelton, J. M.; Jackson, A. J.; Weber, O. J.; Weller, M. T.; Goñi, A. R.; Leguy, A. M. A.; Barnes, P. R. F.; Walsh, A. Lattice Dynamics and Vibrational Spectra of the Orthorhombic, Tetragonal, and Cubic Phases of Methylammonium Lead Iodide. *Physical Review B* **2015**, 92, 144308.
- (90) Sendner, M.; Nayak, P. K.; Egger, D. A.; Beck, S.; Mu, C.; Epding, B.; Kowalsky, W.; Kronik, L.; Snaith, H. J.; Pucci, A.; Lovrinc, R. Optical Phonons in Methylammonium Lead Halide Perovskites and Implications for Charge Transport†. *Materials Horizons* **2016**, 3, 613–620.

# CHAPTER-6 Stability Enhancement and Pronounced Three-photon Absorption in SrCl<sub>2</sub>-doped FAPbBr<sub>3</sub> Nano Crystals



Sarvani Jowhar Khanama, Dipanjan Banerjeeb, Venugopal Rao Somab,\* and Banavoth Muralia,\*

<sup>&</sup>lt;sup>a</sup>Solar Cells and Photonics Research Laboratory, School of Chemistry, University of Hyderabad, Hyderabad 500046, Telangana, India

<sup>&</sup>lt;sup>b</sup>Advanced Centre of Research in High Energy Materials (ACRHEM), DRDO Industry Academia – Centre of Excellence (DIA-COE), University of Hyderabad, Hyderabad 500046, Telangana, India

<sup>\*</sup>Corresponding Authors' e-mail: soma venu@uohyd.ac.in, murali.banavoth@uohyd.ac.in

Albeit, the size-dependent perovskite nanocrystals (PNCs) have manifested tremendous improvement in nonlinear optical (NLO) studies owing to their remarkable optical and electrical properties. However, the industrialization of these materials has been circumscribed by toxicity and instability. The quest for alluring candidates in the frontline for NLO properties explored to date includes both the organic-inorganic hybrid perovskites (OIHPs). Given the remarkable stability of formamidinium cation ( $HC(NH_2)^{2+} = FA+$ )) over methylammonium cation ( $MA^+$ ) in hybrid perovskites, the FAPbBr<sub>3</sub> is chosen as a prototype to investigate its interactions with  $Sr^{2+}$  ions. Intriguingly, SrCl2-doped FAPbBr<sub>3</sub> PNCs showed enhanced three-photon absorption (3PA) comparable/superior to some recently reported PNCs. This work paves the way for developing more stable, less toxic organic-inorganic hybrid (OIHPs) PNCs for optoelectronic applications.

### 6.1. Introduction

OIHPs materials are alluring candidates in almost all technology fields, such as photovoltaics,  $^{1-5}$  luminescent solar concentrators,  $^6$  light-emitting diodes (LEDs), leaser (or laser),  $^{7.8}$  memristors.  $^{9-13}$  Given the phenomenal performances of the OIHPS, the true potential of PNCs in the targeted optoelectronics needs to be ameliorated and is yet to plateau. Generally, perovskite materials rest in the ABX3 crystal structure, where A and B are monovalent, divalent cations, and X is a halide anion, respectively. The B cation coordinates with six halide anions forming the octahedra, and interconnecting these octahedra creates the voids in which A cations are located. In these materials, the upper edge of the valence band (VB) is dominated by the p

orbital of X, with minor antibonding contributions from Pb 6s. In contrast, B metal p orbitals contribute to the conduction band (CB) lower edge. Whereas A<sup>+</sup> ions indirectly contribute to the formation of the bandgap of these materials. 14 In literature, nine alternatives of B metal cations have been reported, Co, Cu, Fe, Mg, Ni, Sn and Zn, to check the tolerance impact on perovskite films towards photovoltaic application. <sup>15</sup> Interestingly, <3% of this metal replaced with Pb has higher tolerance without any loss in performance. <sup>16</sup> In 2015, Federico Bella used perovskites with polymer electrolytes for Solar Cells (SC) application.<sup>17</sup> Sansoni et al. synthesized CsPbBr<sub>3</sub> NCs in ambient conditions via a top-down approach. <sup>18</sup> OIHPs PSCs were used in a highly integrated flexible photo-rechargeable system based on quasi-solid-state zincion micro-batteries. 19 Interestingly, OIHPs-based SCs achieved a power conversion efficiency (PCE) of 25.8%. <sup>20</sup> Herein, higher performance has been achieved by tuning the optoelectronic properties of OIHPs. Notably, bandgap engineering was achieved using different halides,<sup>21</sup> metals<sup>15</sup> and organic cations<sup>14</sup> as the dopants. <sup>22,23,24</sup> Cumulative study on OIHPs devices as a renewable energy source to split water into H<sub>2</sub> and O<sub>2</sub> was done by Pirrone et al.<sup>25</sup> Cheaper and large-scale processable technique for stable large-area perovskite SCs (PSC) using carbonbased materials was demonstrated by Fagiolari et al.<sup>26</sup> However, considering the lead toxicity, more recent advances in lead-free PSCs for sustainable and clean energy production have been reviewed in literature and achieved High Open-Circuit Voltage Cs2AgBiBr6 Carbon-Based PSC.<sup>27,28</sup>

In the past few decades, scientists have been fascinated by the optical nonlinearity of numerous interesting optical materials for their momentous applicability.<sup>29,30</sup> The diverse applicability of novel entities in the nonlinear domain establishes them as potential candidates in significant photonic applications such as optical switching, optical limiting,

Chapter-6

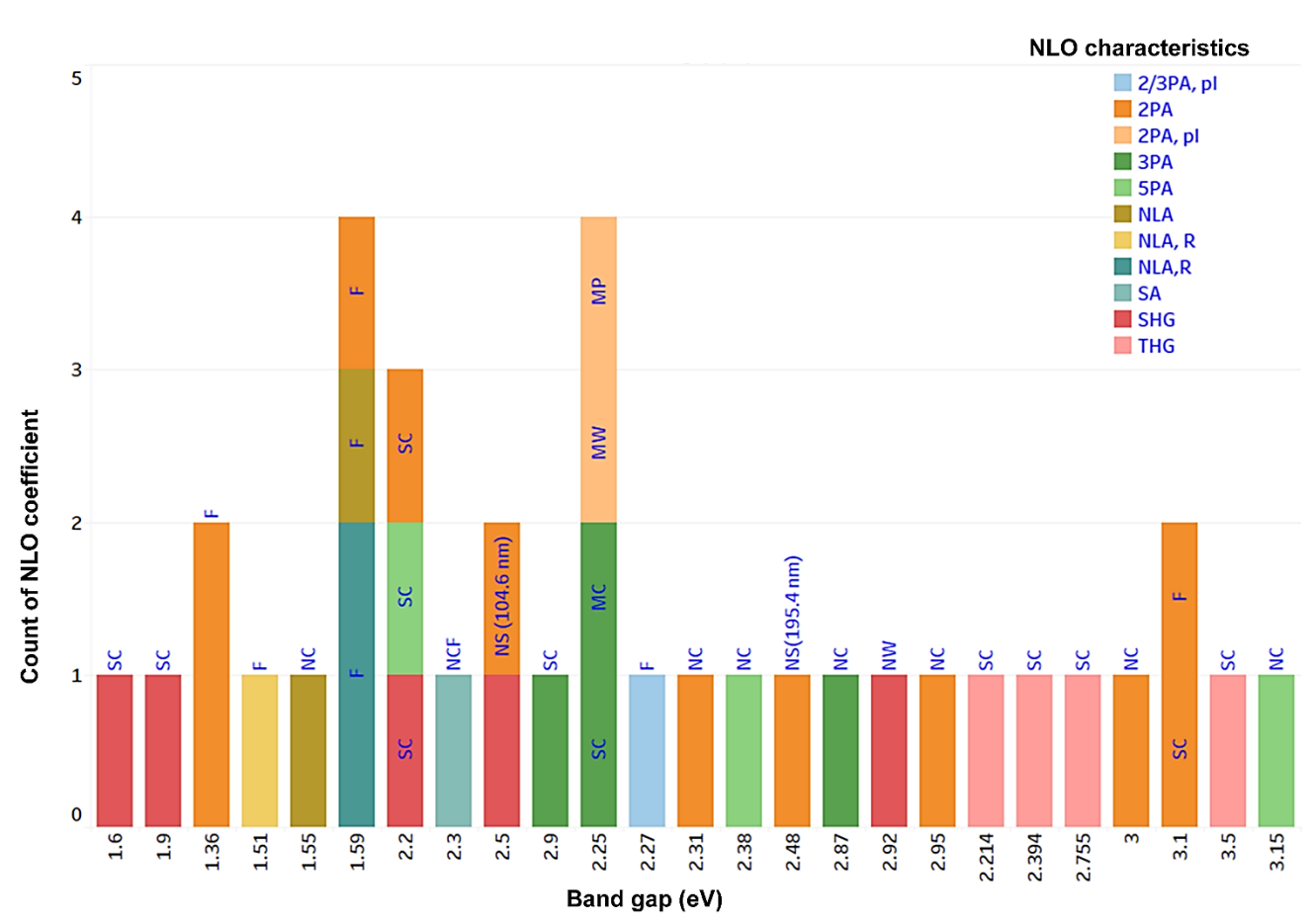


Fig. 6. 1 Distinct count of NLO coefficients for each bandgap broken down by morphology. Colour shows details about NLO characteristics. SC–Single crystal, F–Film, NC–Nanocrystal, NS-Nanostructure.

optical communications, biomedical imaging etc. In recent years significant reports and reviews in PNCs have emerged as remarkable optical materials in NLO and electronic responses interacting with an ultrafast laser pulse, giant 2/multi-photon absorption (PA).<sup>31-35</sup> Generally, over a broad range of excitation wavelengths, PCNs have shown <sup>3</sup>/<sub>4</sub> PA.<sup>36</sup> Some of the research groups have established their candidature as strong saturable absorbers.<sup>37</sup> Rhodamine B (Rh B), an organic laser dye, was recently doped in layered hybrid halide perovskite (LHHP) bis(4-methoxybenzylammonium) tetra-chlorido cadmate (4MBA<sub>2</sub>CdCl<sub>4</sub>) using simple and cost-effective slow solvent evaporation technique. The NLO properties of this perovskite have been studied using the Z-scan method with a 785 nm CW laser, where the RSA

with a low optical limiting threshold of 0.8 MW/cm² was reported by Ranjhani *et al.*<sup>38</sup> Zhang *et al.*<sup>39</sup> also reported the NLA coefficient of Cs<sub>4</sub>Cu<sub>x</sub>Ag<sub>2-2x</sub>Sb<sub>2</sub>Cl<sub>12</sub> double PNCs using 800 nm, 250 nJ, 500 Hz fs laser to be ~10<sup>-8</sup> cm/W. The NLO properties of Cs<sub>2</sub>AgBiBr<sub>6</sub> double PNCs, exhibiting TPA cross sections of ~1906 GM and TPA coefficient of ~10<sup>-11</sup> cm/W, were investigated.<sup>40</sup> Our group has carried out extensively broadband ultrafast laser-interaction triggered spectroscopic studies engaging novel systems such as nano entities,<sup>41-43</sup> PNCs,<sup>29,30</sup> organic, inorganic compounds etc.,<sup>44-46</sup> unveiling their exotic photonic responses in the NLO domain. In the present work, FAPbBr<sub>3</sub> is chosen as a prototype to investigate its interactions with Sr<sup>2+</sup>, Cl<sup>-</sup> ions and its advancement toward NLO studies. A summarized presentation regarding the NLO responses of the recently reported perovskites has been included in **Fig. 1**.

### **6.2.** Materials and methods

### Synthesis of FAPbBr3 PNCs

FAPbBr<sub>3</sub> NCs were doped using the strontium chloride (SrCl<sub>2</sub>) at 2%, 4% and 6% concentrations to investigate the SrCl<sub>2</sub>-doped FAPbBr<sub>3</sub> NCs in the NLO studies and labelled as FB-2, FB-2 and FB-4, respectively. The FAPbBr<sub>3</sub> PNCs synthesis was carried out under the glovebox using the room-temperature synthetic (RTS) method.<sup>47,48</sup> For the preparation of doped FAPbBr<sub>3</sub> PNCs (FB-2 to FB-4) followed the same procedure as mentioned in Chapter 2.

### **6.3. Experimental Details**

The absorption spectra were obtained using a UV-Vis spectrophotometer (UV-2600 of SHIMADZU). PL spectra were recorded with an FP-8500 spectrometer. UV and PL data were recorded using toluene. The structural studies have been done by using a Bruker D8 Advance powder diffractometer (powder X-ray diffraction (p-XRD) with Cu Kα radiation and 5 to 85° for 15 min in ambient conditions. High-resolution transmission electron microscopy (HR-TEM) of JEM-F200 kV was used to record selected area electron diffraction (SAED). ImageJ and Gatan Digital Micrograph (GDM) software were used to analyze the TEM images.

To perform the NLO studies, a femtosecond (fs) laser (M/s Coherent, Libra), 50 fs, 1 kHz, 800 nm, has been utilized. Complete details of the experiments have been reported in our earlier work. A LabVIEW-based lock-in amplifier and a photo-diode for the signal collection were engaged. We have utilized a linear translational stage to scan the sample within the Rayleigh range to obtain the NLA and intensity-dependent refraction data.

### 6.4. Results and Discussion

#### **6.4.1.** Morphology and structural properties

The electronic properties of PNCs strongly depend on the morphology, particle size, crystallinity and crystal orientation.<sup>54</sup> A few well-established techniques for efficient PNCs synthesis involve hot-injection (HI) methods and ligand-assisted reprecipitation (LARP) methods. Nevertheless, small fluctuations in the temperature may result in poor quality control. Hence, most of the efforts have been devoted to the RTS method. <sup>47,48</sup> Herein, PNCs

Chapter-6

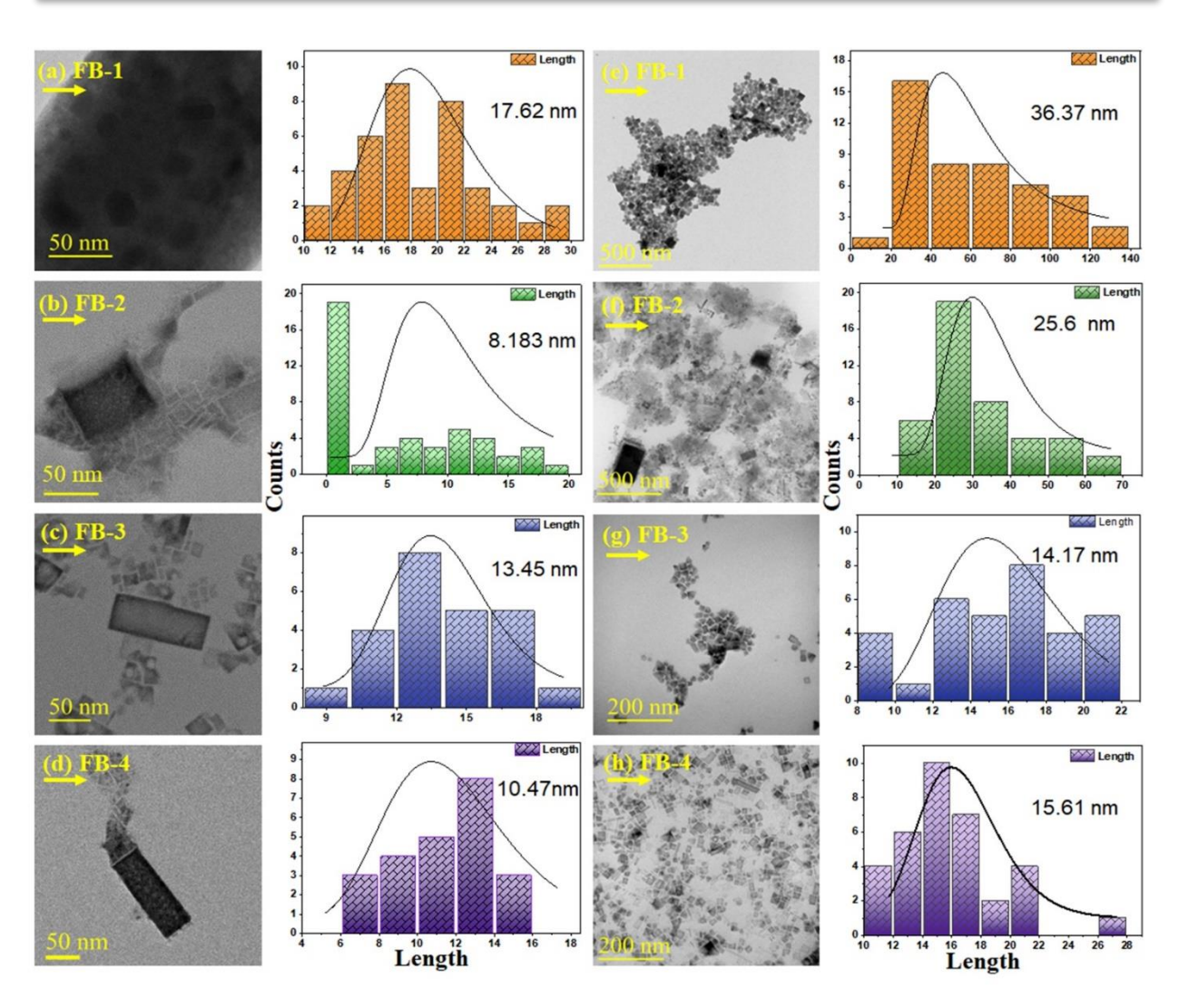


Fig. 6. 2 TEM micrographs and calculated particle sizes for each sample at right to it for (a-d) powder and (e-h) solutions respectively.

were synthesized using the RTSM to achieve higher quality. Further, the optical spectroscopic measurements (UV-Visible and PL) were carried out periodically (>10 times) to check the reproducibility employing the RTS method. The noticeable difference in the band gap that was observed as time increased for data collection (Fig S4) was in the tolerable limit in the case of doped samples compared to undoped samples. The spectroscopic characterization techniques such as Fourier transform infrared (FTIR), energy-dispersive X-ray (EDX) and UV-Visible spectroscopy were used to characterize the reported compounds. EDX and mapping on

individual grains confirmed the homogeneous distribution of Sr<sup>2+</sup> and Cl<sup>-</sup> ions on the film surface (Fig. S1(a-c)). Additional characterization techniques, p-XRD and TEM, facilitated to draw off a more detailed picture of the chemical composition of doped FAPbBr<sub>3</sub> (FA-2 to FA-4). Diffraction peaks were indexed to Pm-3m cubic structure, which was in good agreement with previously reported values for pristine PNCs (FA-1) (Fig. 4(a,d)).<sup>49,50</sup> The lower angle shift of the (001) Bragg plane for the excess doping of SrCl<sub>2</sub> was attributed to lattice expansion and negative surface tension by incorporating Cl<sup>-</sup> and Sr<sup>2+</sup> ions (Fig. 4d).<sup>51</sup> Importantly, no additional peaks were seen in the doped samples, which could be due to the not affected crystal unit cell structure with the replacement of Br<sup>-</sup> with Cl<sup>-</sup>. The corresponding interplanar distance with complementary diffraction angles and micro-strain associated with the crystal in the lattice was calculated using the Williamson-Hall plot (W-H) plots. However, an increase in lattice strain in the case of 6% doping (FB-4 sample) is attributed to an increasing concentration of Sr<sup>2+</sup> and Cl<sup>-</sup> ions in the FB-4 sample compared to others (Fig. S2(a-d)). Furthermore, to predict the tendency of particle agglomeration in doped PNCs, we have calculated particle sizes using TEM micrographs in colloidal and dry samples, illustrated in Fig. 3. Interestingly, in the FB-3 sample, we have not observed much difference in particle size between the two forms, representing the lower agglomeration in the samples. An interplanar distance of 0.28 nm was observed in a pristine (FB-1) sample, corresponding to the (022) Bragg plane of the cubic structure, very close to the values obtained from the P-XRD data using the Bragg diffraction equation, which agrees well with the reported FAPbBr<sub>3</sub> PNCs (Fig. S3(a-d)). 49,50,52-54

### **6.4.2. Optical properties**

The optical properties of materials are of prime importance for any optoelectronic application.<sup>55</sup> Optical characterizations have been recorded using UV-Vis spectra and PL emission for 4 PNCs in toluene, a solvent. Absorption spectra and band gap values for pristine PCNs (**Fig. 4(e)**) are similar to those reported in the literature.<sup>47,48</sup> Notable differences in absorption values for doped PNCs indicate particle size changes with increasing doping concentration. Whereas blue-shift in PL of the FB-3 sample with 3% of the SrCl<sub>2</sub> concentration (**Fig. 4(f)**), attributed to quantum confinement effects (lower average size distribution), was consistent with the sizes calculated from the powder sample HR-TEM micrographs.<sup>55,56</sup> Significant enhancement in photoluminescence quantum yield (PLQY) was observed from 40% to 72% upon increasing SrCl<sub>2</sub> doping to pristine PNCs in colloidal form.<sup>47,48</sup> We used two organic surfactants during the synthesis: OAm enhances the solubility of lead salts, while OA acts as a hydrophobic ligand. The presence of surface ligands was analyzed using FTIR, as shown in **Fig. 4(b,c)**. From previous reports, it has been noticed that purification may etch the surface of the QDs with the removal of the ligand.<sup>57</sup> Intriguingly, no

significant change was observed between the four samples in the FTIR spectrum, indicating that all surfactants (OA and OAm) were retained after purification. Hence, it can be fairly established from the data obtained from the UV, PL, p-XRD and FTIR +that toluene did not induce a measurable change in the state of the surface of the PNCs, and it represents the stable 4% doped (FB-3) sample compared to the pristine (FA-1).

### 6.4.3. Applications of SrCl<sub>2</sub> doped FAPbBr<sub>3</sub> PNCs towards NLO

Femtosecond (fs) Z-scan studies have been performed using the Z-scan technique initiated by Sheik-Bahae and co-researchers.<sup>42</sup> We aimed to divulge the electronic nonlinearity of these novel perovskite entities using fs excitation. A schematic NLO

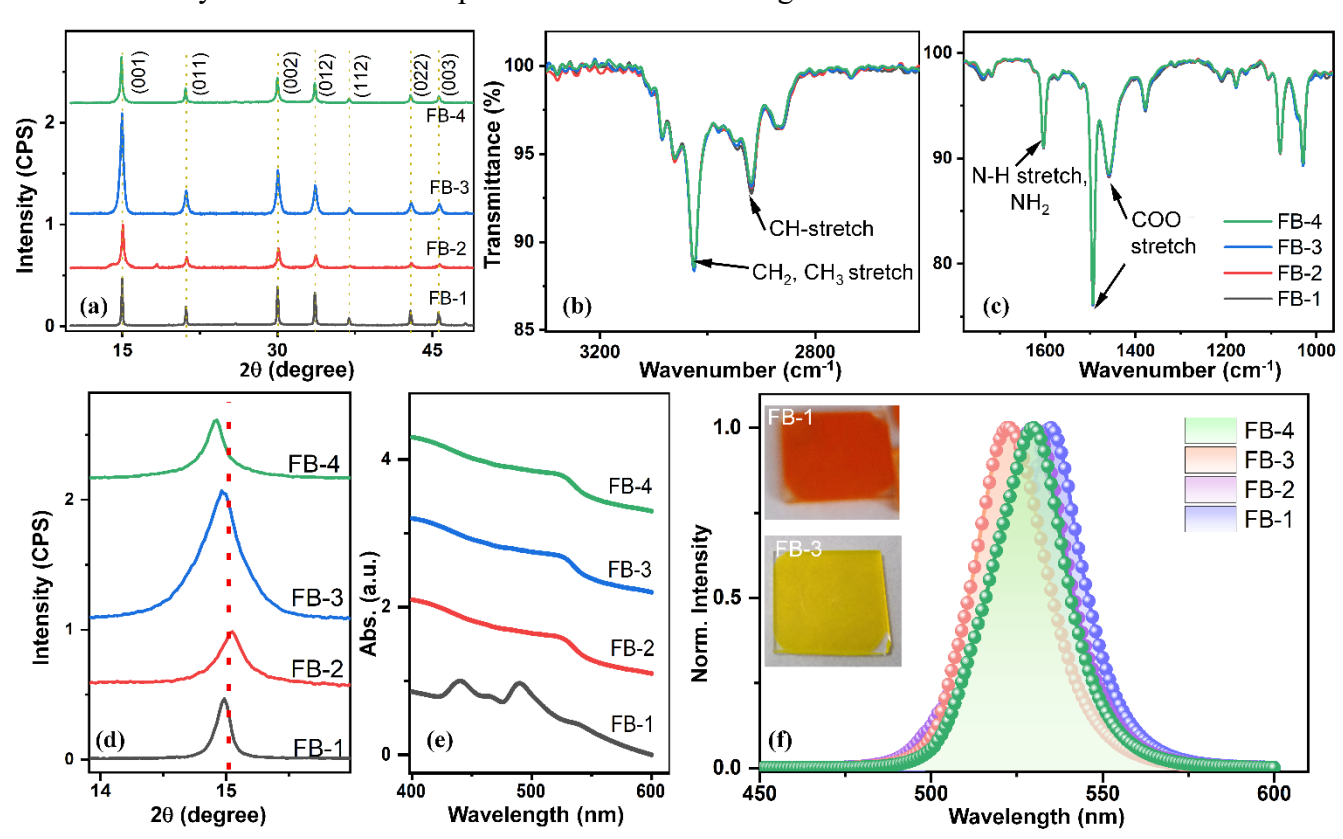


Fig. 6. 3 (a) p-XRD diffraction pattern. (b, c) FT-IR spectra. (d) p-XRD peak at 15 degrees showing the lower angle shift (e) UV-visible absorption spectra and (f) PL spectra of FAPbBr3 NCs (FB-1) along with doped samples as labelled from FB-2 to FB-4

experimental setup has been presented in Chapter 2 (**Fig. 2.13**). Our previous reports have detailed elaborations on the Z-scan calculations using fs pulses.<sup>42,43</sup>

We engaged 50 fs, 1 kHz and 800 nm amplifier pulses to systematically experiment with a ~230 GM/cm<sup>2</sup> peak intensity. In interaction with the fs amplifier pulses, all four different concentrations of SrCl<sub>2</sub> doped FAPbBr<sub>3</sub> were observed to depict a strong 3PA. The inherent NLA phenomena can be attributed to the reverse saturable absorption (RSA) nature observed

Table. 6.3. Detailed NLO parameters corresponding to four SrCl<sub>2</sub> doped FAPbBr<sub>3</sub> PNCs.

NCs	$\beta \times 10^{-11}$ (cm W <sup>-1</sup> )	$\gamma \times 10^{-22}$ $(cm^3/W^2)$	σ <sub>3</sub> (cm <sup>6</sup> s <sup>2</sup> )	n <sub>2</sub> × 10 <sup>-16</sup> (cm <sup>2</sup> /W)	Re [χ <sup>(3)</sup> ] × 10 <sup>-14</sup> (e.s.u.)
FB-1	-	1.3	2.6	7.1	6
FB-2	-	2.3	4.7	7.7	6.5
FB-3	-	1.4	2.9	7.8	6.6
FB-4	-	1.6	3.3	8.8	7.4
Toluene	0.29	-	-	0.2	-

3pa

in the open aperture transmittance curves. Particularly from our detailed NLO studies involving the doped FAPbBr<sub>3</sub> NCs, we retrieved the NLO parameters such as 3PA cross-section  $\sigma_{3PA}$  (cm<sup>6</sup>s<sup>2</sup>), 3PA coefficient  $\gamma$  (cm<sup>3</sup>W<sup>-2</sup>), nonlinear refractive index n<sub>2</sub> (cm<sup>2</sup>/W) and third-order NLO susceptibility index [ $\chi^{(3)}$ ], corresponding to each colloidal nanocrystal system. Among all the four samples, FB-1, FB-2, FB-3 and FB-4, depicting prominent RSA nature, FB-2 NLA was inherently RSA, but with comparatively a higher 3PA coefficient. We believe that the

percentage of SrCl<sub>2</sub> dopant and the average size of the NCs can be attributed as determining factors for generating more defect states suitable for resonant multi-photon transitions and tuning the optical nonlinearity. The theoretically fitted data unveiled the 3PA coefficients ( $\gamma$ ) to be  $1.3 \times 10^{-22}$  cm<sup>3</sup>/W<sup>2</sup>,  $2.3 \times 10^{-22}$  cm<sup>3</sup>/W<sup>2</sup>,  $1.4 \times 10^{-22}$  cm<sup>3</sup>/W<sup>2</sup>,  $1.6 \times 10^{-22}$  cm<sup>3</sup>/W<sup>2</sup>, respectively, for FB-1, FB-2, FB-3 and FB-4, respectively. The corresponding 3PA cross-sections were estimated to be  $2.6 \times 10^{-77}$  cm<sup>6</sup> s<sup>2</sup>,  $4.7 \times 10^{-77}$  cm<sup>6</sup> s<sup>2</sup>,  $2.9 \times 10^{-77}$  cm<sup>6</sup> s<sup>2</sup>, and  $3.3 \times 10^{-77}$  cm<sup>6</sup> s<sup>2</sup>. The correlation of the observed change in NLO absorption coefficients with different amounts of SrCl<sub>2</sub> doping can be established partly by understanding the variation in energy levels. The linear transmittance for FB-1, FB-2, FB-3 and FB-4 were 0.78, 0.80, 0.76 and 0.81, respectively. The experiments were performed with similar concentrations for all the samples. The nonlinear absorption also depends strongly on the structural deviation (in terms of size), which is also related to the linear optical absorption (revealing the change in electronic energy levels). The nonlinear absorption also depends on the excitation strength of high-intensity laser pulses and the concentration of the nanoparticles. In the UV-visible absorption signature of FB-1 [Fig. 4(e)], two possible inter-band transitions, i.e., 430 nm and 488 nm, were observed in the perovskite system, which supports resonances for effective 3PA (2PA + excited state absorption). The disappearance of the ~430 nm peak in all the FB-2, Fb-3 and FB-4 spectra of Fig 4(e) significantly conveys a rearrangement of the energy levels and changes in the corresponding charge transitions due to SrCl<sub>2</sub> doping. On the other hand, in the FB-2 absorption spectrum, the noticeable maximum redshift in the ~488 nm peak towards ~518 nm compared to FB-3 and FB-4. The enhanced 3PA can be attributed to the relatively larger sizes and distribution of the NCs (Fig. 3) achieved for FB-2 (25 nm; 10 nm-70 nm) in comparison with FB-3 (14 nm; 8 nm – 22 nm) and FB-4 (16 nm; 10 nm -26 nm). The variation in the SrCl<sub>2</sub>

doping has led to the size alteration of the NCs and optical responses of the same, subsequently. The size alternation has been significantly interrelated with the lattice expansion and negative surface tension by incorporating Cl<sup>-</sup> and Sr<sup>2+</sup> ions on the NCs surfaces. This variation in size distribution has decisively controlled the tunability of the optical absorption, leading to the alteration in the inherent electronic states and the band gap. A combination of energy level restructuring (with doping) and the size effects could have resulted in an enhanced 3PA for FB-2. In the case of the closed aperture mode, the intensity-dependent valley-peak type refractive index phenomenon was observed. The n<sub>2</sub> measured here is ultrafast and depends on the electron distribution, which again has been altered due to doping; this could be a reason for the strong n<sub>2</sub> observed in the case of FB-4. The overall third-order nonlinearity depends on the sizes of the NCs owing to quantum confinement effects. 55,56 A reasonable structure-property relationship can only be achieved with equal-sized pure and doped PNCs and experiments performed with similar conditions such as concentrations, peak intensity, etc. The PNCs closed aperture data conspicuously revealed a positive refractive index based on the Kerr-lens effect. The valley-peak curves confirmed the focusing nature of the NC systems. The inherent n<sub>2</sub> values were retrieved from theoretical fittings of the closed aperture transmittance data. The calculated n<sub>2</sub> values were  $6 \times 10^{-16}$  cm<sup>2</sup>/W,  $6.5 \times 10^{-16}$  cm<sup>2</sup>/W,  $6.6 \times 10^{-16}$  cm<sup>2</sup>/W and  $7.4 \times 10^{-16}$  cm<sup>2</sup>/W 10<sup>-16</sup> cm<sup>2</sup>/W for FB-1, FB-2, FB-3 and FB-4, respectively. Interestingly, the FB-4 exhibited superior nonlinearity in intensity-dependent focusing Kerr lens response. Subsequently, the real part of the third-order optical susceptibility  $[\chi^{(3)}]$  was also methodically assessed for each corresponding n<sub>2</sub>. The order of magnitude of the real part of  $\chi^{(3)}$  was found to be  $\sim 10^{-14}$  e.s.u.

Having the complete picture established, it is evident that the SrCl<sub>2</sub> doping has decisively increased the NLO response of the NCs, making them superior candidates for all-optical switching and photonic applications. The nonlinear absorption coefficients are some of the strongest reported for such molecules in recent literature. The complete summary of the obtained NLO coefficients has been presented in **Table** 6.1. Thorough theoretical fitting aspects and mathematical relations utilized to calculate various NLO parameters have already been reported in our previous works. The solvent (toluene in this case) contribution to overall optical nonlinearity was also measured under identical experimental parameters. It was negligible (Appendix V **Fig. 5**). Perovskites have been explored in photovoltaics, light-emitting diodes

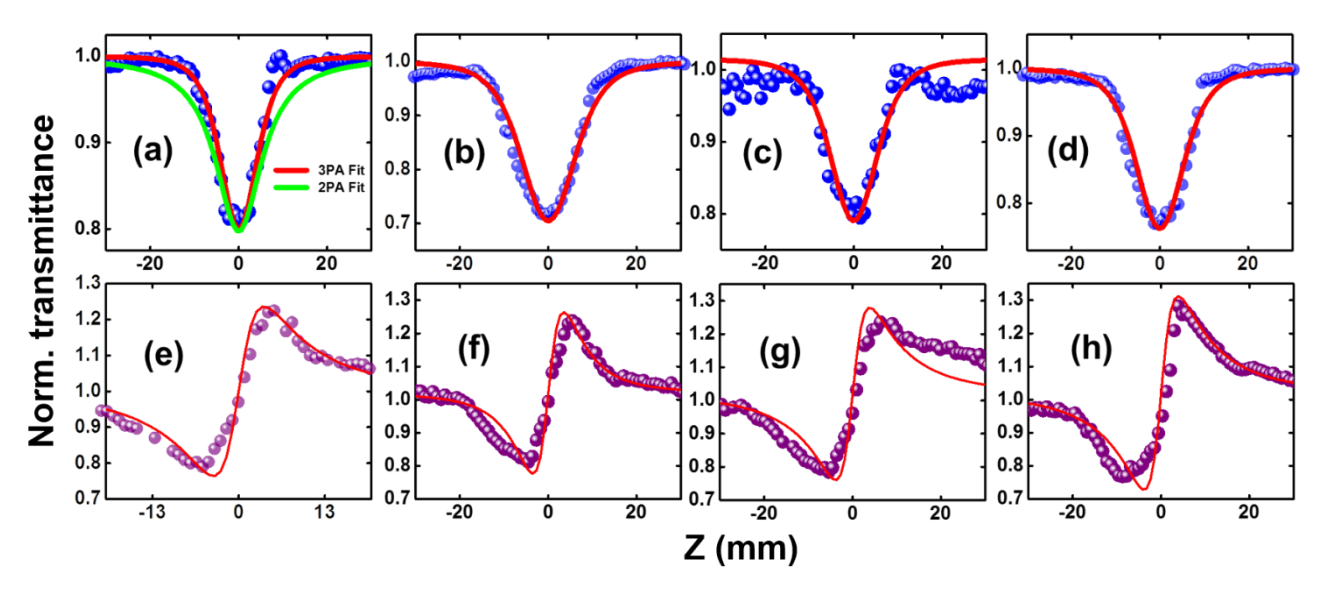


Fig. 6. 4 Open aperture NLO data of (a) FB-1, (b) FB-2, (c) FB-3, (d) FB-4, respectively, under the excitation of 1 kHz, 70 fs, 800 nm fs pulses. Experimental data have been presented in 3-d (blue) spheres and theoretically fitted 3PA Z-scan data is represented by the solid red lines (top). The solid green line (bottom) in (a) represents the two-photon absorption fitting curve. Closed aperture Z-scan data can be observed in olive-colored spheres in (e) FB-1, (f) FB-2, (g) FB-3, (h) FB-4, along with the corresponding theoretical fits (red solid lines).

Chapter-6

and lasers due to NLO properties with high chemical stability. Mushtaq et al.58 reported the femtosecond Z-scan method's NLO properties of lead-free double perovskite Cs<sub>2</sub>AgIn<sub>0.9</sub>Bi<sub>0.1</sub>Cl<sub>6</sub> nanocrystals. The study demonstrates the presence of a strong 3PA, suitable for Kerr nonlinearity-based nonlinear applications such as optical shutters for picosecond lasers. Ban et al.<sup>59</sup> experimented with NLO properties such as 2PA for individual CsPbBr<sub>3</sub> superlattices. TPA has been observed to be enhanced 16 times compared with randomly oriented nanocrystals. The polarization-dependent PL revealed a 4-fold symmetry similar to the single crystal film. The intensity-dependent absorption revealed that the TPA coefficient could be more prominent than WS<sub>2</sub> and ZnO. Due to these strong NLO signatures, CsPbBr<sub>3</sub> is used for NLO devices like optical power limiting and switching. **6.5. Conclusions** We have successfully optimized and demonstrated the more stable SrCl<sub>2</sub>-doped FAPbBr<sub>3</sub> NCs for ultrafast NLO studies. Enhanced stability and lowered agglomeration tendency were confirmed from the spectroscopy and TEM micrographs in the FB-3 sample, with enhanced 3PA. Interestingly, we observed an increase in PLQY with increasing dopant concentration from 40% to 72%. This work paves the way for achieving more stable, less toxic organic-inorganic hybrid PNCs. The PNCs studied herein can be potential candidates for photonic applications, and further scope for improvement in the NLO parameters is possible by tuning their sizes. Further, wavelength-dependent studies in the NIR region can provide more possibilities for other optoelectronic applications of these materials.

### **References:**

(1) Liu, Z.; Qiu, L.; Juarez-Perez, E. J.; Hawash, Z.; Kim, T.; Jiang, Y.; Wu, Z.; Raga, S. R.; Ono, L. K.; Liu, S. (Frank); Qi, Y. Gas-Solid Reaction Based over One-Micrometer Thick

Stable Perovskite Films for Efficient Solar Cells and Modules. *Nature Communications* **2018**, *9*, 1–11.

- (2) Kim, M.; Kim, G. H.; Lee, T. K.; Choi, I. W.; Choi, H. W.; Jo, Y.; Yoon, Y. J.; Kim, J. W.; Lee, J.; Huh, D.; Lee, H.; Kwak, S. K.; Kim, J. Y.; Kim, D. S. Methylammonium Chloride Induces Intermediate Phase Stabilization for Efficient Perovskite Solar Cells. *Joule* 2019, 3, 2179–2192.
- (3) Huan, T. N.; Dalla Corte, D. A.; Lamaison, S.; Karapinar, D.; Lutz, L.; Menguy, N.; Foldyna, M.; Turren-Cruz, S. H.; Hagfeldt, A.; Bella, F.; Fontecave, M; and Mougel, V. Low-cost high-efficiency system for solar-driven conversion of CO<sub>2</sub> to hydrocarbons, *Proceedings of the National Academy of Sciences of the United States of America* 2019, 116, 9735–9740.
- (4) Wang, Z.; Lin, Q.; Wenger, B.; Christoforo, M. G.; Lin, Y. H.; Klug, M. T.; Johnston, M. B.; Herz, L. M.; Snaith, H. J. High Irradiance Performance of Metal Halide Perovskites for Concentrator Photovoltaics. *Nature Energy* 2018, 3, 855–861.
- (5) Abate, A.; J.-P. Correa-Baena, Saliba, M.; Su'ait, M. S.; and Bella, F. Perovskite Solar Cells: From the Laboratory to the Assembly Line, *Chemistry A European Journal* **2018**, *24*, 3100.
- (6) Xia, P.; Xu, S.; Wang, C.; Ban, D. Perovskite Luminescent Solar Concentrators for Photovoltaics Perovskite Luminescent Solar Concentrators for Photovoltaics. APL Photonics 2021, 6, 120901.
- (7) Xing, G.; Mathews, N.; Lim, S. S.; Yantara, N.; Liu, X.; Sabba, D.; Grätzel, M.; Mhaisalkar, S.; Sum, T. C. Low-Temperature Solution-Processed Wavelength-Tunable Perovskites for Lasing. *Nature Materials* **2014**, *13*, 476–480.
- (8) Deschler, F.; Price, M.; Pathak, S.; Klintberg, L. E.; Jarausch, D. D.; Higler, R.; Hüttner, S.; Leijtens, T.; Stranks, S. D.; Snaith, H. J.; Atatüre, M.; Phillips, R. T.; Friend, R. H. High Photoluminescence Efficiency and Optically Pumped Lasing in Solution-Processed Mixed

Halide Perovskite Semiconductors. *Journal of Physical Chemistry Letters* **2014**, *5*, 1421–1426.

- (9) Xing, J.; Zhao, C.; Zou, Y.; Kong, W.; Yu, Z.; Shan, Y.; Dong, Q.; Zhou, D.; Yu, W.; and Guo, C. Modulating the optical and electrical properties of MAPbBr<sub>3</sub> single crystals via voltage regulation engineering and application in memristors, *Light: Science and Applications* **2020**, 9, 11.
- (10) Balis, N.; Zaky, A. A.; Athanasekou, C.; Silva, A. M.; Sakellis, E.; Vasilopoulou, M.; Stergiopoulos, T.; Kontos, A. G.; Falaras, P. Investigating the Role of Reduced Graphene Oxide as a Universal Additive in Planar Perovskite Solar Cells. *Journal of Photochemistry and Photobiology A: Chemistry* **2020**, *386*, 112141.
- (11) Chao, L.; Xia, Y.; Li, B.; Xing, G.; Chen, Y.; Huang, W. Room-Temperature Molten Salt for Facile Fabrication of Efficient and Stable Perovskite Solar Cells in Ambient Air. *Chem Open Journal* **2019**, *5*, 995–1006.
- (12) Lin, Q.; Armin, A.; Burn, P. L.; Meredith, P. Filter less Narrowband Visible Photodetectors. *Nature Photonics* **2015**, *9*, 687–694.
- (13) Yao, F.; Gui, P.; Chen, C.; Li, B.; Li, R.; Tao, C.; Lin, Q.; Fang, G. High-Rubidium-Formamidinium-Ratio Perovskites for High-Performance Photodetection with Enhanced Stability. *ACS Applied Materials and Interfaces* **2019**, *11*, 39875–39881.
- (14) Zhang, F.; and Zhu, K. Advanced Energy Materials, Additive Engineering for Efficient and Stable Perovskite Solar Cells, *Advanced Energy Materials* **2020**, 10, 1–26.
- (15) Levchuk, I.; Herre, P.; Brandl, M.; Osvet, A.; Hock, R.; Peukert, W.; Schweizer, P.; Spiecker, E.; Batentschuk, M.; Brabec, C. J. Ligand-Assisted Thickness Tailoring of Highly Luminescent Colloidal CH<sub>3</sub>NH<sub>3</sub>PbX<sub>3</sub> (X = Br and I) Perovskite Nanoplatelets. *Chemical Communications* **2017**, *53*, 244–247.
- (16) Ketavath, R.; Katturi, N. K.; Ghugal, S. G.; Kolli, H. K.; Swetha, T.; Soma, V. R.; Murali, B. Deciphering the Ultrafast Nonlinear Optical Properties and Dynamics of Pristine and Ni-Doped CsPbBr<sub>3</sub> Colloidal Two-Dimensional Nanocrystals. *Journal of Physical Chemistry Letters* 2019, *10*, 5577–5584.

(17) Bella, F. Polymer electrolytes and perovskites: lights and shadows in photovoltaic devices, *Electrochimica Acta*, **2015**, *175*, 151–161.

- (18) Sansoni, S.; Anoè F. M.; and Meneghetti, M.; Simple and sustainable synthesis of perovskite-based optoelectronic material: CsPbBr<sub>3</sub> nanocrystals via laser ablation in alcohol, *Nanoscale Advances*, **2022**, *4*, 5009–5014.
- (19) Bi, J.; Zhang, J.; Giannakou, P.; Wickramanayake, Yao, T. X.; Wang, M.; Liu, X.; Shkunov, M.; Zhang, W.; and Zhao, Y. A Highly integrated flexible photo-rechargeable system based on stable ultrahigh-rate quasi-solid-state zinc-ion micro-batteries and perovskite solar cells, *Energy Storage Materials* 2022, 51, 239–248.
- (20) Min, H.; Y. Lee, D.; Kim, J.; Kim, G.; Lee, K. S.; Kim, J.; Paik, M. J.; Kim, Y. K.; Kim K. S.; Kim, M; Shin G, T. J.; and Il Seok, S. Perovskite solar cells with atomically coherent interlayers on SnO<sub>2</sub> electrodes, *Nature* **2021**, *598*, 444–450.
- (21) Navas, J.; Sánchez-Coronilla, A.; Gallardo, J. J.; Cruz Hernández, N.; Piñero, J. C.; Alcántara, R.; Fernández-Lorenzo, C.; De Los Santos, D. M.; Aguilar, T.; Martín-Calleja, J. New Insights into Organic-Inorganic Hybrid Perovskite CH<sub>3</sub>NH<sub>3</sub>PbI<sub>3</sub> Nanoparticles. An Experimental and Theoretical Study of Doping in Pb<sup>2+</sup> Sites with Sn<sup>2+</sup>, Sr<sup>2+</sup>, Cd<sup>2+</sup> and Ca<sup>2+</sup>. *Nanoscale* **2015**, *7*, 6216–6229.
- (22) Lau, C. F. J.; Zhang, M.; Deng, X.; Zheng, J.; Bing, J.; Ma, Q.; Kim, J.; Hu, L.; Green, M. A.; Huang, S.; Ho-Baillie, A. Strontium-Doped Low-Temperature-Processed CsPbI<sub>2</sub>Br Perovskite Solar Cells. *ACS Energy Letters* **2017**, *2*, 2319–2325.
- (23) Liang, J.; Zhao, P.; Wang, C.; Wang, Y.; Hu, Y.; Zhu, G.; Ma, L.; Liu, J.; and Jin, Z.; CsPb<sub>0.9</sub>Sn<sub>0.1</sub>IBr<sub>2</sub> Based All-Inorganic Perovskite Solar Cells with Exceptional Efficiency and Stability, *Journal of the American Chemical Society*, **2017**, *139*, 14009–14012.
- (24) Bella, F.; Griffini, G.; Correa-Baena, J. P.; Saracco, G.; Grätzel, M.; Hagfeldt, A.; Turri S. and Gerbaldi, C. Improving efficiency and stability of perovskite solar cells with photocurable fluoropolymers, *Science*, **2016**, *354*, 203–206.
- (25) Pirrone, N.; Bella F.; and Hernández, S. Solar H<sub>2</sub> production systems: current status and prospective applications, Green Chemistry, **2022**, *24*, 5379–5402.

(26) Fagiolari L.; and Bella, F.; Carbon-based materials for stable, cheaper and large-scale processable perovskite solar cells, *Energy and Environmental Science* **2019**, *12*, 3437–3472.

- (27) Ikram, M.; Malik.; Raees, R. R.; Imran, M. F. Wang, Ali, S.; Khan M.; Khan, Q.; Maqbool, M. Recent advancements and future insight of lead-free non-toxic perovskite solar cells for sustainable and clean energy production: A review, *Sustainable Energy Technologies and Assessments*, 2022, 53, 102433.
- (28) Schmitz, F.; Lago, L.; Fagiolari, J.; Burkhart, A.; Cester, A.; Polo, M.; Prato Meneghesso, G.; Gross, S. N.; Bella, F.; Lamberti, F.; and Gatti, T. High Open-Circuit Voltage Cs<sub>2</sub>AgBiBr<sub>6</sub> Carbon-Based Perovskite Solar Cells via Green Processing of Ultrasonic Spray-Coated Carbon Electrodes from Waste Tire Sources, *ChemSusChem*, **2022**, 15, e202201590.
- (29) Ketavath, R.; Katturi, N. K.; Ghugal, S. G.; Kolli, H. K.; Swetha, T.; Soma, V. R.; Murali, B. Deciphering the Ultrafast Nonlinear Optical Properties and Dynamics of Pristine and Ni-Doped CsPbBr<sub>3</sub> Colloidal Two-Dimensional Nanocrystals. *Journal of Physical Chemistry Letters* 2019, 10, 5577–5584.
- (30) Konda, S. R.; Soma, V. R.; Ganeev, R. A.; Banavoth, M.; Ketavath, R.; Li, W. Third-Order Optical Nonlinearities and High-Order Harmonics Generation in Ni-Doped CsPbBr3 Nanocrystals Using Single- and Two-Color Chirped Pulses. *Journal of Material Science* 2022, 57, 3468–3485.
- (31) Shen, W.; Chen, J.; Wu, J.; Li, X.; Zeng, H. Nonlinear Optics in Lead Halide Perovskites: Mechanisms and Applications. *ACS Photonics***2021**, *8*, 113–124.
- (32) Wang, G.; Mei, S.; Liao, J.; Wang, W.; Tang, Y.; Zhang, Q.; Tang, Z.; Wu, B.; Xing, G. Advances of Nonlinear Photonics in Low-Dimensional Halide Perovskites. *Small* **2021**, *17*, 1–21.
- (33) Chen, W.; Zhang, F.; Wang, C.; Jia, M.; Zhao, X.; Liu, Z.; Ge, Y.; Zhang, Y.; Zhang, H. Nonlinear Photonics Using Low-Dimensional Metal-Halide Perovskites: Recent Advances and Future Challenges. *Advanced Materials* **2021**, *33*, 1–46.

(34) Shen, W.; Chen, J.; Wu, J.; Li, X.; Zeng, H. Nonlinear Optics in Lead Halide Perovskites: Mechanisms and Applications. *ACS Photonics* **2021**, *8*, 113–124.

- (35) Li, M.; Wang, C.; Wang, L.; Zhang, H. Colloidal Semiconductor Nanocrystals: Synthesis, Optical Nonlinearity, and Related Device Applications. *Journal of Physical Chemistry C* **2021**, *9*, 6686–6721.
- (36) Krishnakanth, K. N.; Seth, S.; Samanta, A.; Rao, S. V. Broadband Femtosecond Nonlinear Optical Properties of CsPbBr<sub>3</sub> Perovskite Nanocrystals. *Optics Letters* **2018**, *43*, 603-606.
- (37) Krishnakanth, K. N.; Seth, S.; Samanta, A.; Venugopal Rao, S. Broadband Ultrafast Nonlinear Optical Studies Revealing Exciting Multi-Photon Absorption Coefficients in Phase Pure Zero-Dimensional Cs<sub>4</sub> PbBr<sub>6</sub> Perovskite Films. *Nanoscale* **2019**, *11*, 945–954.
- (38) Ranjani, E.A.; Sangeetha, K.; Sabari Girisun, T. C. Effect of Dye on Luminescent and Nonlinear Optical Properties of Bis(4-Methoxybenzylammonium) Tetra-Chlorido Cadmate (4MBA<sub>2</sub>CdCl<sub>4</sub>) Perovskite. *Optical Materials* **2022**, *125*, 112096.
- (39) Zhang, Y.; Sui, N.; Kang, Z.; Meng, X.; Yuan, L.; Li, X.; Zhang, H. Z.; Zhang, J.; Wang, Y. Scanning the Optoelectronic Properties of Cs<sub>4</sub>Cu<sub>x</sub>Ag<sub>2-2x</sub>Sb<sub>2</sub>Cl<sub>12</sub> Double Perovskite Nanocrystals: The Role of Cu<sup>2+</sup> Content. *Journal of Physical Chemistry C* **2022**, *10* (14), 5526–5533.
- (40) Zhang, Y.; Wang, Q.; Sui, N.; Kang, Z.; Li, X.; Zhang, H. Z.; Zhang, J.; Wang, Y. Temperature-Dependent and Nonlinear Optical Response of Double Perovskite Cs<sub>2</sub>AgBiBr<sub>6</sub> Nanocrystals. *Applied Physics Letters* **2021**, *119* (16), 161904.
- (41) Sheik-Bahae, M.; Said, A. A.; Wei, T. H.; Hagan, D. J.; Van Stryland, E. W. Sensitive Measurement of Optical Nonlinearities Using a Single Beam. *IEEE Journal of Quantum Electronics*. **1990**, *26*, 760–769.
- (42) Banerjee, D.; Moram, S. S. B.; Byram, C.; Rathod, J.; Jena, T.; Podagatlapalli, G. K.; Soma, V. R. Plasmon-Enhanced Ultrafast and Tunable Thermo-Optic Nonlinear Optical Properties

of Femtosecond Laser Ablated TiO2 and Silver-Doped TiO2 Nanoparticles. *Applied Surface Science* **2021**, *569* (July), 151070.

- (43) Kumar, S.; Acharyya, J. N.; Banerjee, D.; Soma, V. R.; Vijaya Prakash, G.; Sankar, M. Strong Two-Photon Absorption and Ultrafast Dynamics of: Meso -Functionalized "Push-Pull" Trans -A2BC Porphyrins. *Dalton Transactions* **2021**, *50* (18), 6256–6272.
- (44) Biswas, C.; Palivela, S. G.; Giribabu, L.; Soma, V. R.; Raavi, S. S. K. Femtosecond Excited-State Dynamics and Ultrafast Nonlinear Optical Investigations of Ethynylthiophene Functionalized Porphyrin. *Optical Materials* **2022**, *127*, 112232.
- (45) Srivishnu, K. S.; Banerjee, D.; Ramnagar, R. A.; Rathod, J.; Giribabu, L.; Soma, V. R. Optical, Electrochemical, Third-Order Nonlinear Optical Investigations of 3,4,5-Trimethoxy Phenyl Substituted Non-Aqueous Phthalocyanines. *Frontiers in Chemistry* **2021**, *9*, 1–14.
- (46) Rathi, P.; Ekta; Kumar, S.; Banerjee, D.; Soma, V. R.; Sankar, M. Unsymmetrical β-Functionalized "push-Pull" Porphyrins: Synthesis and Photophysical, Electrochemical and Nonlinear Optical Properties. *Dalton Transactions* **2020**, *49*, 3198–3208.
- (47) Levchuk, I.; Osvet, A.; Tang, X.; Brandl, M.; Perea, J. D.; Hoegl, F.; Matt, G. J.; Hock, R.; Batentschuk, M.; Brabec, C. J. Brightly Luminescent and Color-Tunable Formamidinium Lead Halide Perovskite FAPbX<sub>3</sub> (X = Cl, Br, I) Colloidal Nanocrystals. *Nano Letters* **2017**, *17*, 2765–2770.
- (48) Dey, A.; Ye, J.; De, A.; Debroye, E.; Ha, S. K.; et al. State of the Art and Prospects for Halide Perovskite Nanocrystals. *ACS Nano* **2021**, *15* (7), 10775–10981.
- (49) Mannino, G.; Deretzis, I.; Smecca, E.; La Magna, A.; Alberti, A.; Ceratti, D.; Cahen, D. Temperature-Dependent Optical Band Gap in CsPbBr3, MAPbBr3, and FAPbBr3 Single Crystals. *Journal of Physical Chemistry Letters* 2020, 11, 2490–2496.
- (50) Tong, Y. L.; Zhang, Y. W.; Ma, K.; Cheng, R.; Wang, F.; Chen, S. One-Step Synthesis of FA-Directing FAPbBr3 Perovskite Nanocrystals toward High-Performance Display. *ACS Applied Materials and Interfaces* **2018**, *10*, 31603–31609.

Chapter-6

(51) An, Y.; Hidalgo, J.; Perini, C. A. R.; Castro-Méndez, A.-F. J.; Vagott, N.; Bairley, K.; Wang, S.; Li, X.; and J.-P. Correa-Baena, Structural Stability of Formamidinium- and Cesium-Based Halide Perovskites, ACS Energy Letters 2021, 6, 1942–1969.

- (52) Wang, X.; Li, Y.; Xu, Y.; Pan, Y.; Zhu, C.; Zhu, D.; Wu, Y.; Li, G.; Zhang, Q.; Li, Q.; Zhang, X.; Wu, J.; Chen, J.; Lei, W. Solution-Processed Halide Perovskite Single Crystals with Intrinsic Compositional Gradients for X-Ray Detection. *Chemistry of Materials* 2020 32, 4973–4983.
- (53) Zou, Y.; Zou, T.; Zhao, C.; Wang, B.; Xing, J.; Yu, Z.; Cheng, J.; Xin, W.; Yang, J.; Yu, W.; Dong, H.; Guo, C. A Highly Sensitive Single Crystal Perovskite–Graphene Hybrid Vertical Photodetector. Small 2020 16, 2000733.
- (54) Saidaminov, M. I.; Adinolfi, V.; Comin, R.; Abdelhady, A. L.; Peng, W.; Dursun, I.; Yuan,
   M.; Hoogland, S.; Sargent, E. H.; Bakr, O. M. Planar-Integrated Single-Crystalline
   Perovskite Photodetectors. *Nature Communications* 2015, 6, 1–7.
- (55) Dias, S.; Murali, B.; and Krupanidhi, S. B.; Solution processible Cu<sub>2</sub>SnS<sub>3</sub> thin films for cost-effective photovoltaics: Characterization, Materials Chemistry and Physics **2015**, 167, 309–314.
- (56) Butkus, J.; Vashishtha, P.; Chen, K.; Gallaher, J. K.; Prasad, S. K. K.; Metin, D. Z.; Laufersky, G.; Gaston, N.; Halpert, J. E.; and Hodgkiss, J. M. The Evolution of Quantum Confinement in CsPbBr<sub>3</sub> Perovskite Nanocrystals, *Chemistry of Materials* **2017**, 29, 3644–3652.
- (57) Yuan, L.; Patterson, R.; Wen, X.; Zhang, Z.; Conibeer, G.; Huang, S. Investigation of Anti-Solvent Induced Optical Properties Change of Cesium Lead Bromide Iodide Mixed Perovskite (CsPbBr<sub>3-x</sub>I<sub>x</sub>) Quantum Dots. *Journal of Colloid and Interface Science* **2017**, 504, 586–592.

(58) Mushtaq, A.; Pradhan, B.; Kushavah, D.; Zhang, Y.; Wolf, M.; Schrenker, N.; Fron, E.; Bals, S.; Hofkens, J.; Debroye, E.; Pal, S. K. Third-Order Nonlinear Optical Properties and Saturation of Two-Photon Absorption in Lead-Free Double Perovskite Nanocrystals under Femtosecond Excitation. ACS Photonics 2021, 8, 3365–3374.

(59) Ban, J.; Yu, Y.; Yue, P.; Lian, L.; Xu, C.; Guo, L.; Liu, S. D. Two-Photon Absorption and Photoluminescence of Individual CsPbBr<sub>3</sub> Nanocrystal Superlattices. *Journal of Physical Chemistry C* **2022**, 126, 8400–8407.

### **CHAPTER-7**

## Challenges and

### **Future Directions**

### 7.1. Challenges and Future Directions

The major challenge is retaining fundamental properties such as absorption coefficient, bandgap, charge transport, higher resistivity & ease of fabrication. Getting a spectrum of  $\gamma$ -rays with high photopeak energy resolution at room temperature is one of the significant challenges. Major challenges in perovskite photodetectors are mentioned below.

### 7.2. Performance enhancement

An ideal photodetector should possess excellent spectral selectivity, high responsivity, large detectivity, fast speed, and excellent stability. Getting a high-energy  $\gamma$ -ray spectrum is challenging precisely because high resistivity and high  $\mu\tau E$  are required, where E is the applied electric field. Moreover, a large bias can result in ion migration and thus lead to severe hysteresis phenomena in devices.

Doping makes perovskite attractive for radiation detection due to excellent optoelectronic properties; unfortunately, it is challenging to dope them intentionally—only part of photodetection characteristic enhancement achieved due to substantial technological issues in designing high-performance photodetectors. Novel perovskite structures and device configurations must develop for further performance improvement.

### 7.3. Operational stability

At room temperature, the long-term continuous operation of halide perovskite devices under a large field to detect  $\gamma$ -rays is still a concern due to the polarisation effect. The environmental stability and durability determine the device's lifespan, so it is a crucial

parameter for photodetector. Unluckily, perovskites easily degrade in the air with oxygen and moisture. Postprocessing method, encapsulation has been demonstrated to enhance perovskite photodetector stability. However, it is a Degradation that still occurs before the encapsulation. More novel strategies are required to develop more stable perovskite at the beginning of the growth.<sup>2</sup>

### 7.4. Environment-friendly perovskite materials

Most of the widely studied perovskite materials, such as MAPbI<sub>3</sub> and MAPbCl<sub>3</sub>, consists of toxic Pb element, and their toxicities have cast a gloomy shadow over their application progress. Thus, more effort is needed to develop environment-friendly perovskite materials with nontoxic elements instead of Pb. Recently, *Wu et al.* reported lead-free Cs<sub>4</sub>EuX<sub>6</sub> (X=Br<sup>-</sup>, I<sup>-</sup>) perovskite single crystals as self-activated scintillators with superior performance for γ-ray spectroscopy.<sup>3</sup>

### 7.5. Nanosystem with multifunction

Smart circuits, optoelectronic devices, and integrated nanosystems have aroused intensive research attention due to their wide application in the future. The multifunctional device can be attained in one nanosystem by coupling the perovskite photodetectors with other functional nanodevices, such as light-emitting diodes, solar cells, and nanolasers. The charge collection & charge recombination mechanism in these perovskite crystals is yet to be understood in a Broadway. Using various doping strategies with more electronegative anions  $(Cl^-, Br^-)$ . So a using high work function contacts to block out the dark noise and optimizing the bandgap, we can get more photopeak energy-resolved  $\gamma$ -ray spectrum.

### 7.6. Future Outlook

Perovskite PDs are emerging tremendously compared to traditional semiconductors because of their simple preparation method, low cost of materials, and the application potential for flexible devices. Considering the merits and demerits PDs, some new concepts and strategies should be discussed. The toxicity caused by Pb cannot be ignored, threatening human health and polluting the environment. Many researchers have been focusing on lead-free perovskites, but the performance of the devices is not as good as lead-based photodetectors because after replacing Pb with Sn or Bi. The carrier's transfer resulted in poor performance and lower stability. Unfortunately, lead-free detectors are not so competitive with lead perovskite because lead plays the leading role in generating and transporting charges among the components. Lots of research have proved that the role of Pb is irreplaceable. Recently many research papers were published demonstrating the success of recycling lead from wasted batteries and electric devices by the following step-to-step chemical reactions. In the future, the development of photodetectors will focus on low-cost, highly efficient, more stable, room temperature based and lightweight. There is a demand for thermostability, long life, higher durability towards HEIRs, and high-performance self-driven photodetectors working under zero bias. Generally, the perovskite photodiodes with p-n, n-i-p, p-i-n or Schottky junction, similar to the structure of the solar cell, are easy to realize self-power without depending on load voltage. These perovskite photodetectors use the photovoltaic and triboelectric effects to convert incident light into electrical signals. The metal electrode periodically contacts the perovskite layer in the triboelectric effect device to generate an electromotive force.<sup>3</sup> Besides

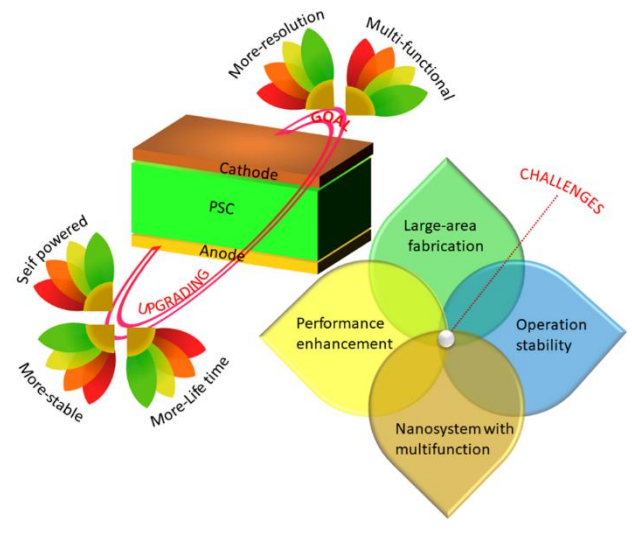


Fig. 7. 1

the innovation of the photodetector structure self-powered electro-optic system was developed by using planar Perovskite solar as a power source to operate the photodetector. Flexible perovskite photodetectors are carriable and lightweight for applications in wearable or portable devices. The flexible perovskite photodetectors need to improve flexibility and repeatability in the future, better than rigid material like Si. These flexible and stretchable photodetectors have many applications in imaging and optical telecommunication. Another significant challenge towards the commercialization of perovskite-based photodetectors is the fabrication of large-area photodetectors and their stability, so most current studies focus on the discrete, small-area, carriable PDs.

Despite the limitation of PSCs towards large applications, these materials have many potentials compared to conventional detectors that cannot be underestimated. The stability of a device can be increased by selecting different optimized inorganic perovskite materials (with mixed cat ion or halides), optimized material composites, selecting appropriate fabrication methods with different electrodes and engineering thickness of each layer. However, more

scientific and technological research is ongoing on material stability and large-scale multifunctional device fabrication. Presciently inevitable success has been accelerated over the past decades in single perovskite crystals for gamma photon detection. Less leakage current was recorded in MAPbl<sub>3</sub> and CsPbBr<sub>3</sub> Schottky type device design and demonstrated successfully for gamma-ray Detection.

Further development of centimetre-sized PSC can be done by preparing SC with a low density of trap states, which remains challenging. Hybrid MA and FA-based perovskite are unstable compared to inorganic Perovskite-based detectors. FA-based perovskite undergoes phase transitions; this issue is solved by allowing A site cation with Cs to form. Another critical challenge is long-term device operation stability (LTDOS). The halide ion migration in hybrid perovskite is a barrier to commercialization; it degrades device performance by creating an internal electrical counter field. Still, we need to develop high-performance perovskite materials, invent advanced device structures, improve device performance and try more innovations.

#### **References:**

- Zhuang, R.; Wang, X.; Ma, W.; Wu, Y.; Chen, X.; Tang, L.; Zhu, H.; Liu, J.; Wu, L.; Zhou, W.; Liu, X.; Yang, Y. M. Highly Sensitive X-Ray Detector Made of Layered Perovskite-like (NH<sub>4</sub>)<sub>3</sub>Bi<sub>2</sub>I<sub>9</sub> Single Crystal with Anisotropic Response. *Nature Photonics* 2019, 13, 602–608.
- 2. Loferski, J. J.; Rappaport, P. Radiation Damage in Ge and Si Detected by Carrier Lifetime Changes: Damage Thresholds. *Physical Review* **1958**, *111*, 432–439.
- 3. Li, C.; Ma, Y.; Xiao, Y.; Shen, L; Ding, L. Advances in perovskite photodetectors. *InfoMat* **2020**, *2*, 1247-1256.
- 4. Wang, X.; Zhao, D.; Qiu, Y.; Huang, Y.; Wu, Y.; Li, G.; Huang, Q.; Khan, Q.; Nathan, A.; Lei, W.; Chen, J. PIN Diodes Array Made of Perovskite Single Crystal for X-Ray Imaging. Physica status solidi Rapid Research Letters **2018**, *12*, 1800380.
- 5. Wei, H.; Desantis, D.; Wei, W.; Deng, Y.; Guo, D.; Savenije, T. J.; Cao, L.; Huang, J. Dopant Compensation in Alloyed CH<sub>3</sub>NH<sub>3</sub>PbBr<sub>3-x</sub>Cl<sub>x</sub> Perovskite Single Crystals for Gamma-Ray Spectroscopy. *Nature Materials* **2017**, *16*, 826–833.
- Yakunin, S.; Dirin, D. N.; Shynkarenko, Y.; Morad, V.; Cherniukh, I.; Nazarenko, O.; Kreil, D.; Nauser, T.; Kovalenko, M. V. Detection of Gamma Photons Using Solution-Grown Single Crystals of Hybrid Lead Halide Perovskites. *Nature Photonics* 2016, 10, 585–589.
- 7. Johns, P. M.; Nino, J. C. Room Temperature Semiconductor Detectors for Nuclear Security. *Journal of Applied Physics* **2019**, *126*, 040902.
- 8. Gao, L.; Yan, Q. Recent Advances in Lead Halide Perovskites for Radiation Detectors. *Solar RRL***2020**, *4*, 2.
- Feng, A.; Jiang, X.; Zhang, X.; Zheng, X.; Zheng, W.; Mohammed, O.F.; Chen, Z.; Bakr,
   O. M. Control of Metal Halide Perovskite Single Crystals: From Bulk to Nanoscale.
   Chemistry of Materials 2020, 32, 7602–7617.

# **Appendix I**

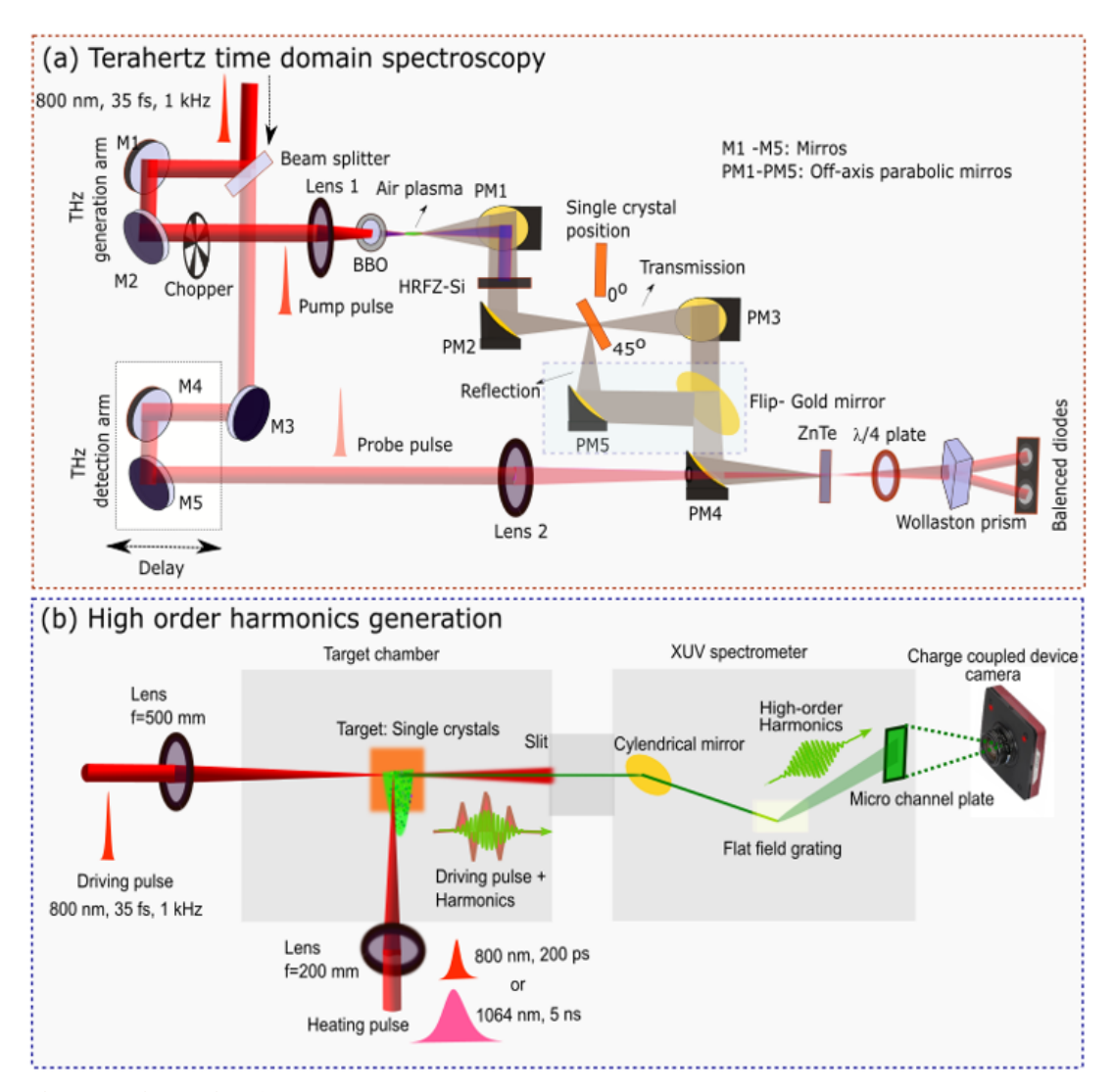
#### 1. Materials and Methods:

#### 1.1. Synthesis of MAPbBr<sub>3</sub> Crystals Growth with additives:

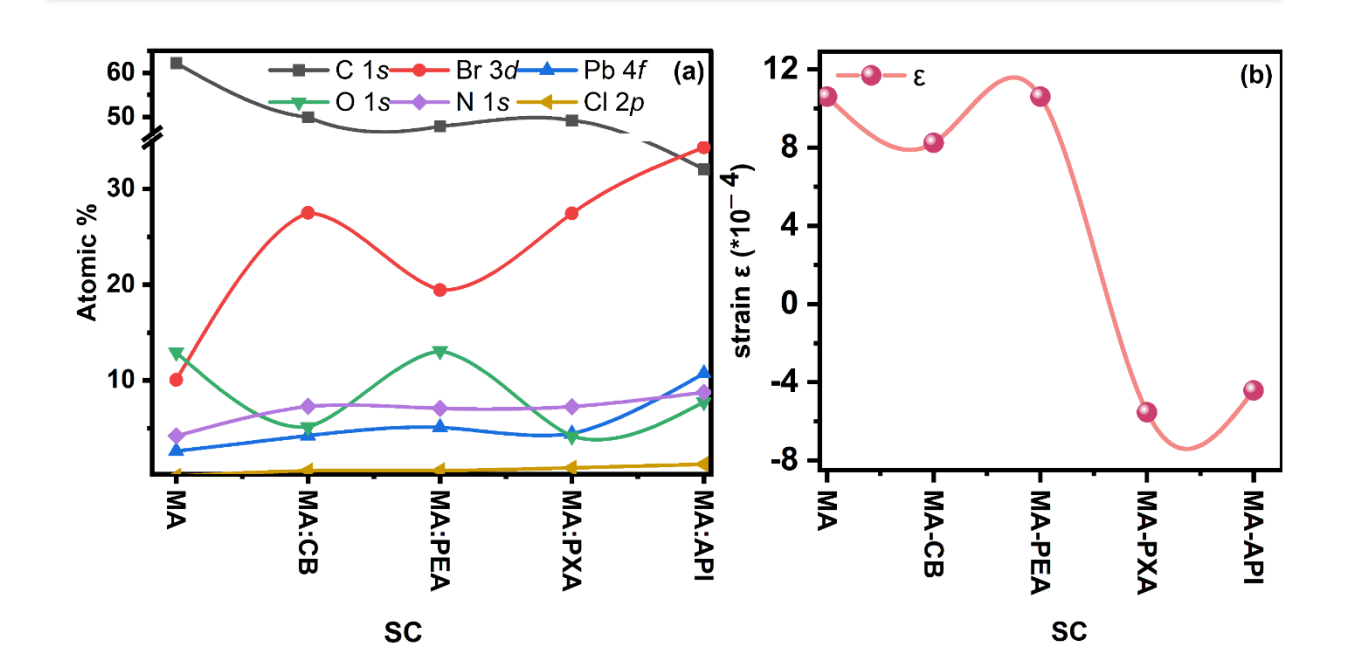
**Appendix I Table 1.** Literature review

Year	Growth	Additives	Perovskite material	Application	Ref
	Method	used	used		
2016	ITC	_	CH <sub>3</sub> NH <sub>3</sub> PbI <sub>3</sub> (Cl)	Optoelectronic Devices	5
2016	_	_	CH <sub>3</sub> NH <sub>3</sub> PbI <sub>3</sub> single	_	6
			crystals.		
2017	ITC	_	$(FAPbI_3; FA^+ =$	_	7
			HC(NH <sub>2</sub> ) <sub>2</sub> <sup>+</sup> ) single		
			crystals		
2018	AVC	_	$MAPbX_3$	Alpha Source	8
2019	AVC		CsPbBr3 microrod	High Detectivity	9
			Single Crystals	Photodetectors	
2019	ITC		MAPbBr <sub>3-X</sub> Cl <sub>X</sub> (MH)	Scintillation	10
2020	ITC	_	$MAPbBr_{3-X}Cl_{X}$ (MH)	_	11

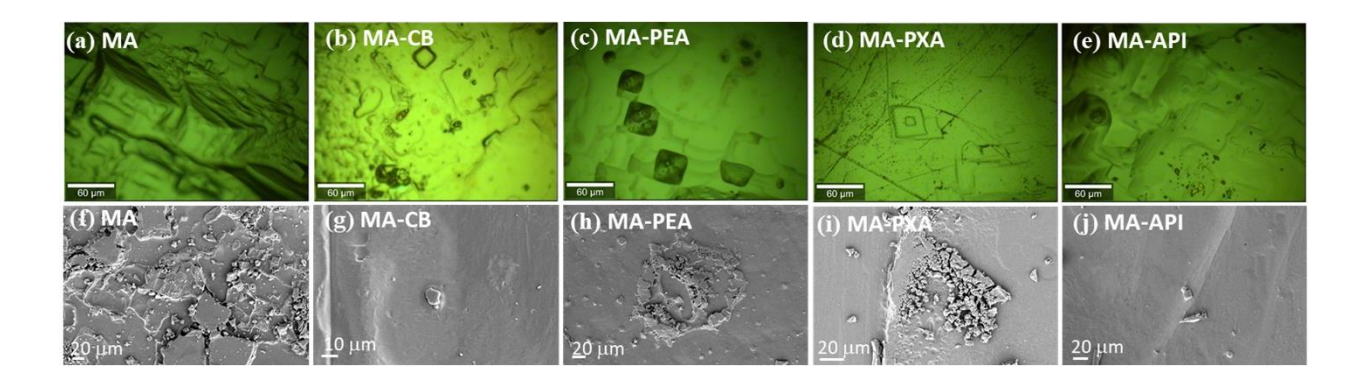
2020	ITC	_	$MAPb(Br_{1-X}Cl_X)_3$	Electrical	12
				<b>.</b>	
				Properties	
2020	ITC	Choline	CsPbBr <sub>3</sub> Single Crystals	γ-Ray Response	13
		Bromide			
		(CB)			
2020	ITC	_	MH-3D-Single Crystals	Cr/MAPbBr <sub>3-X</sub> Cl <sub>X</sub> /Cr	14
				Γ-Ray Responses.	
2021	ITC	Polymer	FAPbI <sub>3</sub> , MAPbI <sub>3</sub> ,	_	15
			MAPbBr <sub>3</sub> , and FAPbBr <sub>3</sub>		
2021	Spin-	2-(2-(2-	FAPbI <sub>3</sub> -Film	Perovskite LEDs	16
	Coated				
		Aminoethoxy			
		)ethoxy)acetic			
		acid,			
2021	Bridgman	_	CsPbBr <sub>3</sub> Single Crystals	Γ-Ray Response	17
	crystal				
	growth				
	method				
2022	ITC	Polymer	$MAPbI_3$	Photodetection	18
2022	ITC	Chiral and	MAPbBr <sub>3</sub>	THz and HHG	This work
		non-Chiral			
		additives			



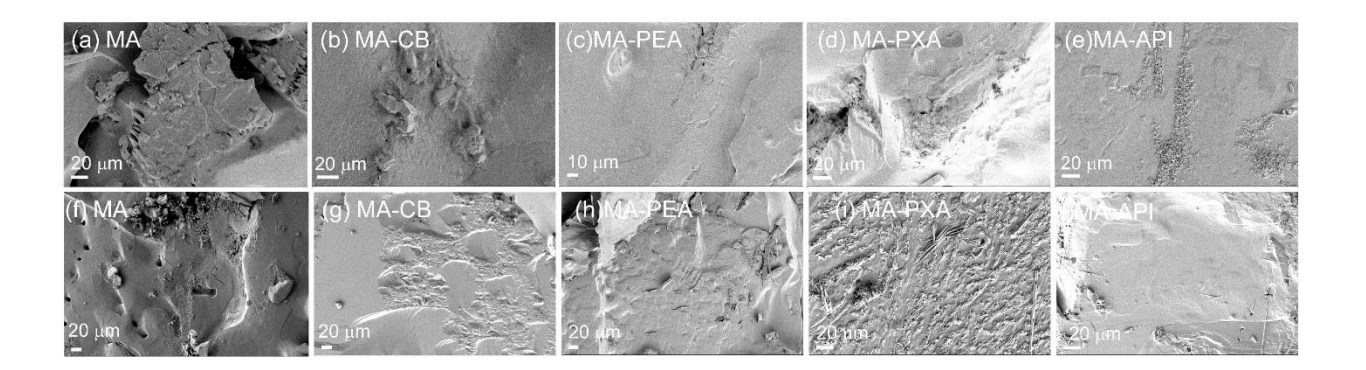
**Appendix I Fig. 1.** Experimental layout for (a) terahertz time-domain spectroscopy and (b) high-order harmonics from laser-induced plasma plumes of single perovskite crystals.



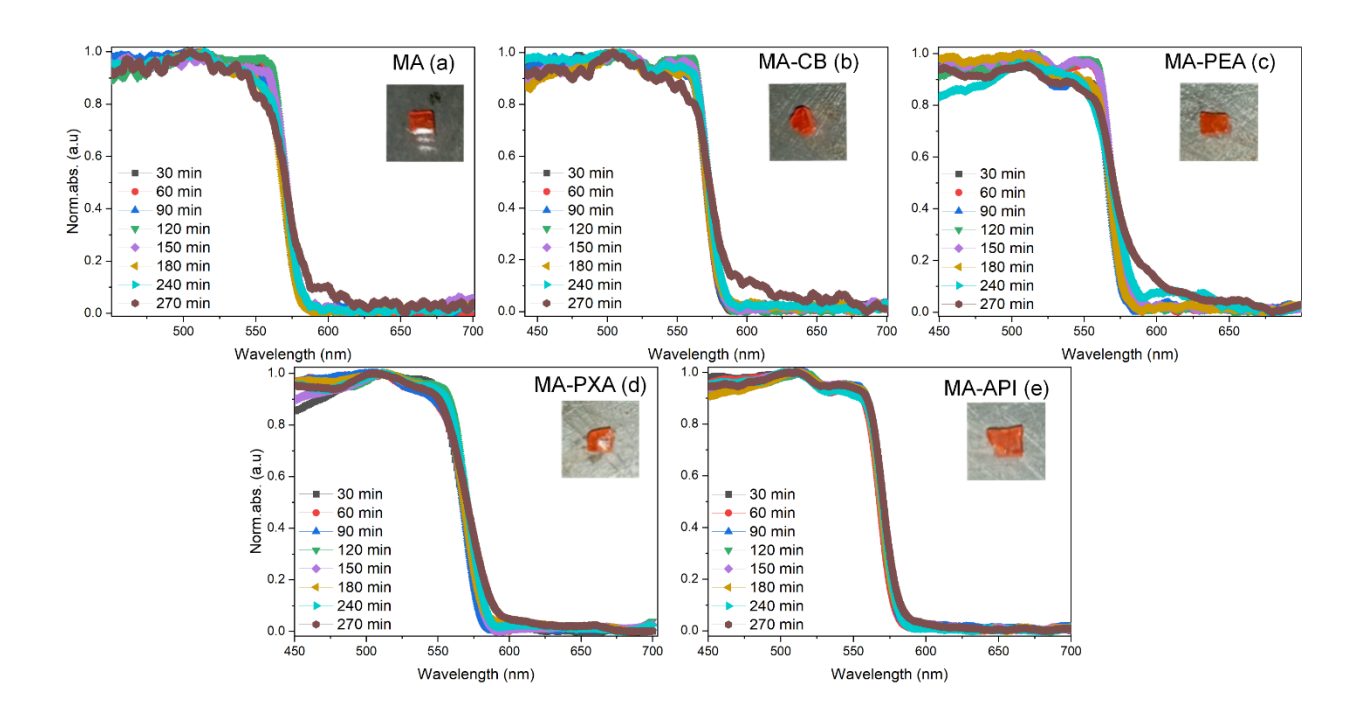
**Appendix I Fig. 2.** (a) Atomic Ratio of MAPbBr<sub>3</sub> perovskite single crystal with changing additives. (b) Lattice strain values of each reported crystal were calculated from the W-H plot using the XRD data.



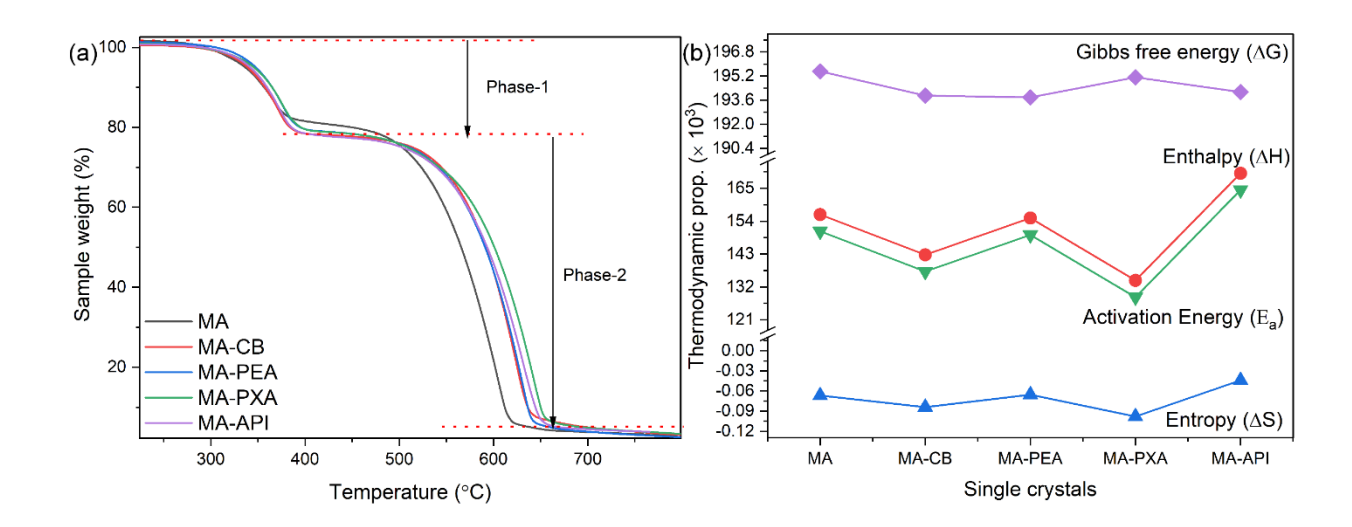
**Appendix I Fig. 3.** (a-e) Confocal and (f-j) scanning electron microscopy (SEM) images of MA crystals grown using the additives corresponding to CB, PEA, PXA, and API samples, respectively.



**Appendix I Fig.** 4. SEM images taken after keeping PSCs in ambient conditions for three and (f-j) seven days, respectively.



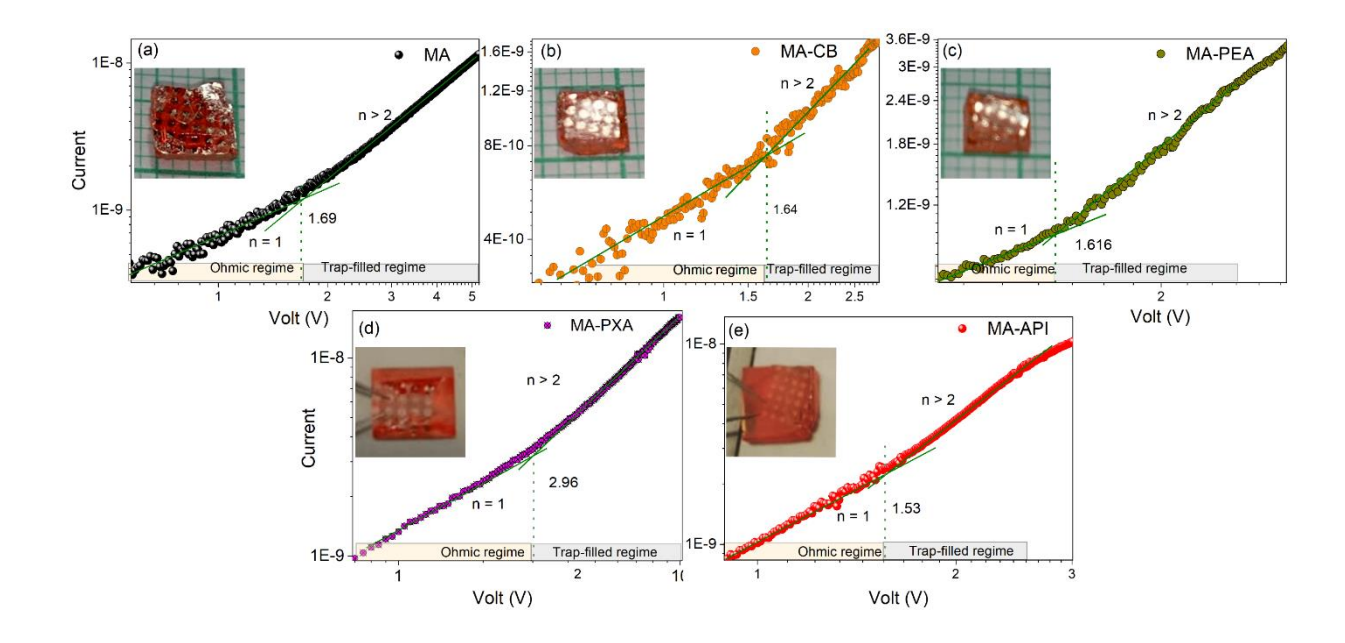
**Appendix I Fig. 5.** (a)-(e) Surface degradation of SCs in the outer atmosphere at a constant temperature at different time intervals was studied using UV spectroscopy.



**Appendix I Fig. 6.** (a)-(b) Comparative Study of MHPSCs Thermogravimetric Analysis (TGA), and thermodynamic properties of phase one (P1- Organic part decomposition) for all the crystals.

**Appendix I Table 2.** Crystal data and structure refinement for MA and modified PSCs.

Single crystals	Initial temperature	Activation energy	Entropy change	Enthalpy change	Gibbs free energy
	(K)	Ea	$\Delta S$	ΔН	$\Delta G$
	(K)	(kJ mol <sup>-1</sup> )	(J/g K)	(kJ/g)	(kJ mol <sup>-1</sup> )
MA	225	156.22	-66.69	150.63	195.52
MA-CB	231	142.77	-84.063	137.16	193.91
MA-PEA	230	155.05	-65.44	149.41	193.79
MA-PXA	224	134.20	-98.16	128.57	195.12
MA-API	232	170.03	-44.032	164.42	194.14



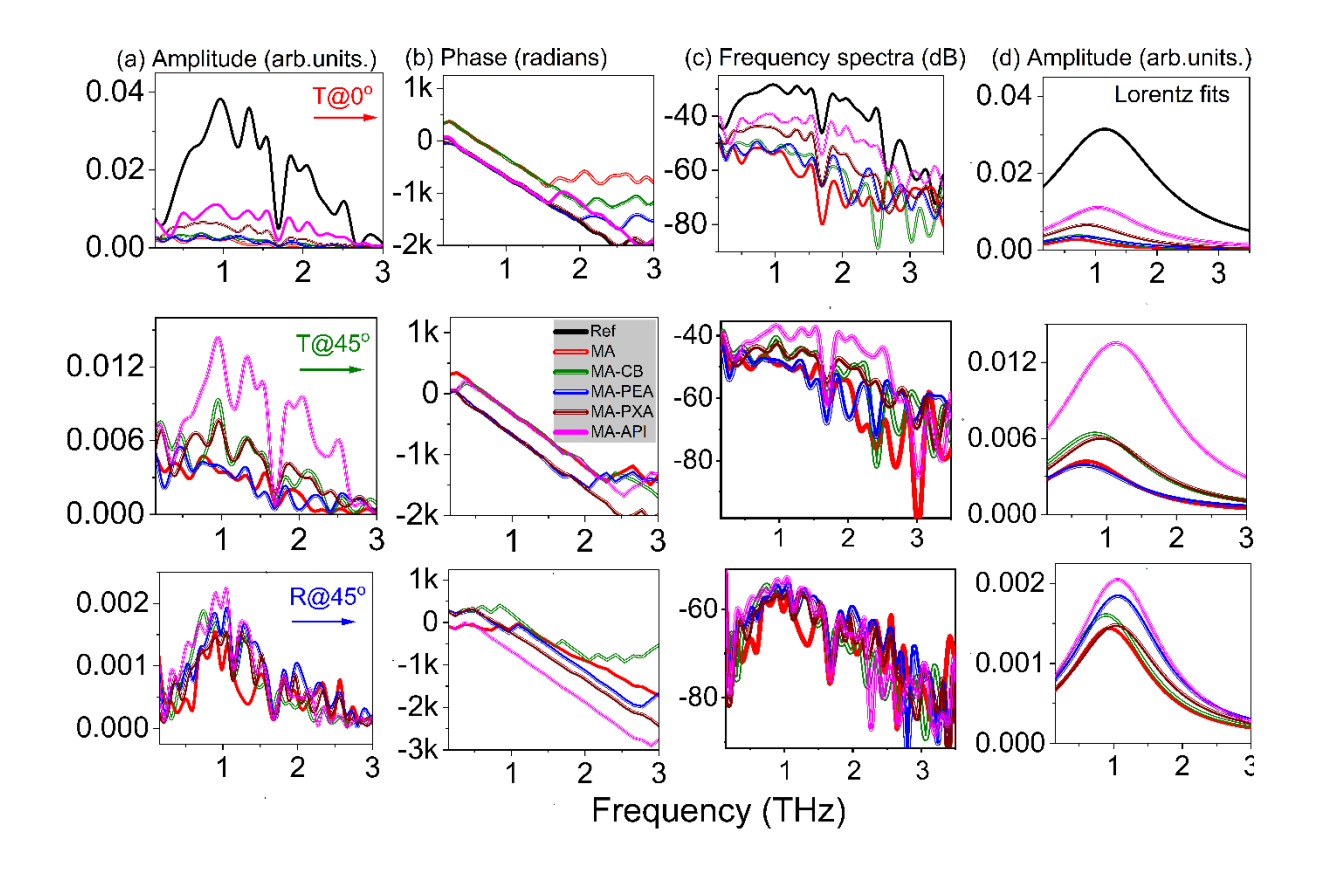
Appendix I Fig. 7. (a)-(e) Current-voltage traces with insert showing SCs deposited with Au.

The linear fitting is denoted with the green markers showing different regimes (at 300 K).

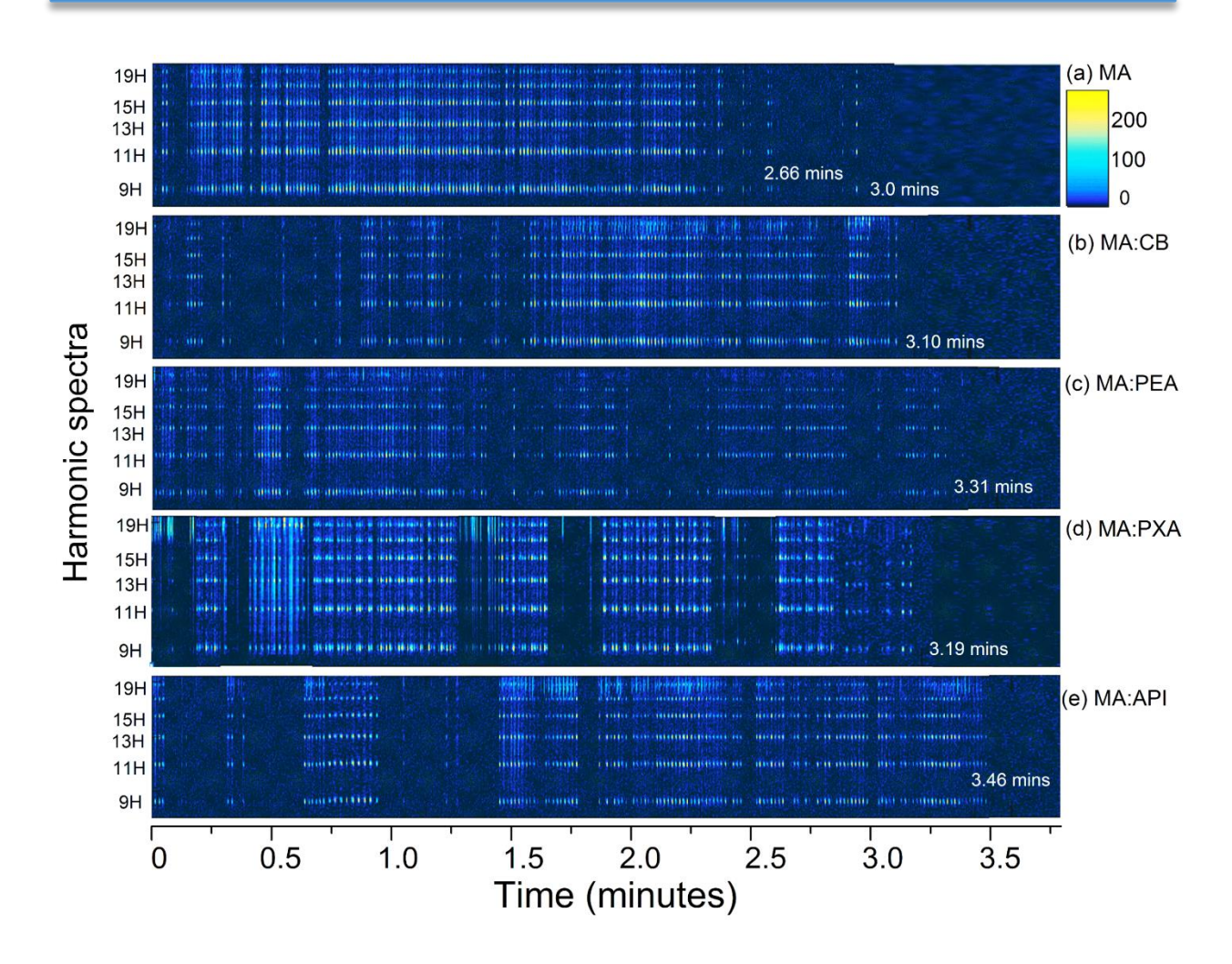
Appendix I Table 3 Crystal data and structure refinement for MA and modified PSCs.

Parameters	MA	MA-CB	MA-PEA	MA-PXA	MA-API
Temperature	296(2) K	293(2) K	293(2) K	295(2) K	299(2) K
Wavelength	71.073 pm	71.073 pm	71.073 pm	71.073 pm	71.073 pm
Crystal	Cubic	Cubic	Cubic	Cubic	Cubic
system					
Space group	P m -3 m	P -4 3 m	P m -3 m	P m -3 m	P m -3 m
Unit cell	a = b = c	a = b = c	a = b = c	a = b = c	a = b = c
dimensions	= 5.9  Å	$= 5.8 \mathrm{\AA}$	$= 5.9 \mathrm{\AA}$	$= 5.9 \mathrm{\AA}$	$= 5.9 \mathrm{\AA}$
	$\alpha = \beta = \gamma = 90^{\circ}$	$\alpha = \beta = \gamma = 90^{\circ}$	$\alpha = \beta = \gamma =$ 90°	$\alpha = \beta = \gamma = 90^{\circ}$	$\alpha = \beta = \gamma =$ 90°
			70	70	

Volume	$0.207885 \text{ nm}^3$	$0.20413 \text{ nm}^3$	$0.2073 \text{ nm}^3$	$0.20783 \text{ nm}^3$	$0.20712 \text{ nm}^3$
Z	1	3	1	1	1
Density	5.984 mg/m <sup>3</sup>	$4.319 \text{ mg/ m}^3$	3.789 mg/	4.346 mg/ m <sup>3</sup>	4.257 mg/ m <sup>3</sup>
(calculated)			$m^3$		
Absorption	34.73 mm <sup>-1</sup>	35.28 mm <sup>-1</sup>	34.70 mm <sup>-1</sup>	34.66 mm <sup>-1</sup>	34.77 mm <sup>-1</sup>
coefficient					
F(000)	338	229	200	236	229
Crystal size	0.240 x 0.200	0.24 x 0.14 x	0.250 x	0.210 x 0.200	0.200 x 0.190
	$x \ 0.190 \ mm^3$	$0.21 \text{ mm}^3$	0.230 x	$x \ 0.170 \ mm^3$	$x \ 0.140 \ mm^3$
			$0.170 \text{ mm}^3$		
Theta range	3.439 to	3.457 to	3.439 to	3.439 to	3.443 to
for data	26.930°	26.858°	27.508°	26.676°	26.966°
collection					
Index ranges	-7<=h<=7, -	-6<=h<=7, -	-7<=h<=7, -	-7<=h<=7, -	-7<=h<=7, -
	7<=k<=7, -	7<=k<=6, -	7<=k<=7, -	4<=k<=4, -	7<=k<=6, -
	7<=1<=7	7<=1<=5	7<=1<=7	7<=1<=4	7<=1<=7
Reflections	4933	787	1794	507	1500
collected					
Independent	70 [R(int) =	107 [R(int) =	74 [R(int) =	69 [R(int) =	70 [R(int) =
reflections	0.4355]	0.9681]	0.5778]	0.4153]	0.5472]
Completeness	100.0 %	98.2 %	100.0 %	100.0 %	100.0 %
to $\theta = 25.242^{\circ}$					
Refinement	Full-matrix	Full-matrix	Full-matrix	Full-matrix	Full-matrix
method	least-squares	least-squares	least-	least-squares	least-squares
	on F2	on F2	squares on	on F2	on F2
			F2		
Data/restraint	70 / 0 / 9	107 / 0 / 8	74 / 0 / 8	69 / 0 / 5	70 / 0 / 5
s/parameters					



Appendix I Fig. 8. After the conversion of the THz electric field to FFT spectra, the obtained (a) THz amplitude, (b) phase, (c) frequency spectra in dB, (d) Lorents fits of data points from THz amplitude shown in (a), for transmittance (T) @ 0°,(upper row), T@ 45° (middle row), reflection @ 45° from reference and perovskite single crystals, respectively. The legend is shown in (b, middle panel), applicable to all panels; Black: solid line, red: solid line, green: double line, blue: thick-thin line, wine: thin-thick line, and magenta: triple lines corresponding to reference pulse, for Singles crystals MA, MA-CB, MA-PEA, MA-PXA and MA-API. The Y-axis labels are shown on top of each column after the Fig. labels (a),(b),(c) and (d).



**Appendix I Fig. 9.** (a)-(e)The vertical representation of harmonic spectra of SCs. The spectra were recorded for time duration. The plasma plumes are produced by nanoseconds heating pulses at a fixed position on the surface of SCs.

**Appendix I Table 4** First and second ionization potentials for chemical elements present in single crystals.

Single crystal	Molecular formula	Elements	Ionization	potential
			(eV)	
			I	II
MA	CH <sub>3</sub> NH <sub>3</sub> PbBr <sub>3</sub>	С	11.26	24.38
		Н	13.59	-
		N	14.53	29.60
		Pb	7.41	15.03
		Br	11.81	21.80
MA-CB	CH <sub>3</sub> NH <sub>3</sub> PbBr <sub>3</sub> :C <sub>5</sub> H <sub>14</sub> BrNO	0	13.61	35.11
MA-PEA	CH <sub>3</sub> NH <sub>3</sub> PbBr <sub>3</sub> :C <sub>8</sub> H <sub>12</sub> ClN	Cl	12.96	23.81
MA-PXA	CH <sub>3</sub> NH <sub>3</sub> PbBr <sub>3</sub> :C <sub>8</sub> H <sub>14</sub> Cl <sub>2</sub> N <sub>2</sub>	*		
MA-API	CH <sub>3</sub> NH <sub>3</sub> PbBr <sub>3</sub> :C <sub>5</sub> H <sub>14</sub> Cl <sub>2</sub> N <sub>2</sub>	*		

#### **References:**

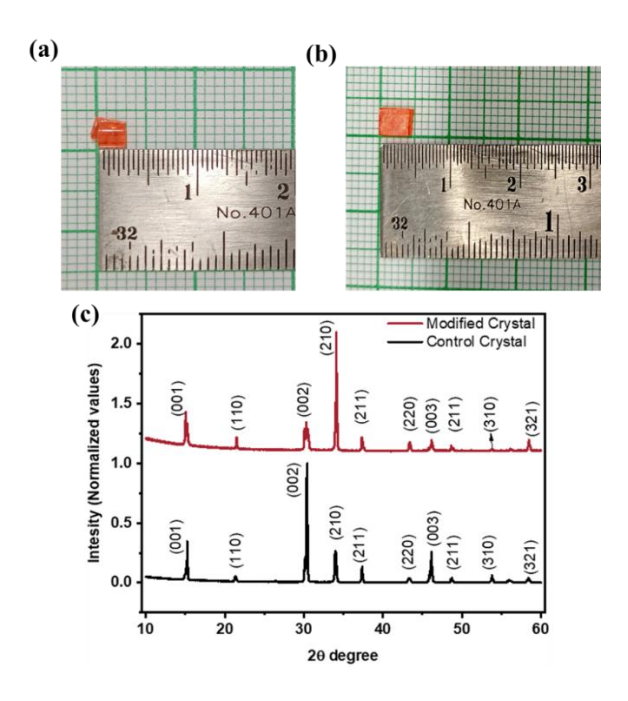
(1) Lian Z.; Yan, Q.; Gao, T.; Ding, J.; Lv, Q.; Ning, C.; Li, Q.; Sun, J.L. Perovskite CH<sub>3</sub>NH<sub>3</sub>PbI<sub>3</sub>(Cl) Single Crystals: Rapid Solution Growth, Unparalleled Crystalline Quality, and Low Trap Density toward 10(8) cm(-3). *Journal of the American Chemical* 

- Society 2016, 138, 9409-9412.
- (2) Ketavath, R.; Katturi, N. K.; Ghugal, S. G.; Kolli, H. K.; Swetha, T.; Soma, V. R.; Murali, B. Deciphering the Ultrafast Nonlinear Optical Properties and Dynamics of Pristine and Ni-Doped CsPbBr<sub>3</sub> Colloidal Two-Dimensional Nanocrystals. *Journal of Physical Chemistry Letters* **2019**, *10*, 5577–5584.
- (3) Sekimoto, T.; Suzuka, M.; Yokoyama, T.; Uchida, R.; Machida, S.; Sekiguchi, T.; Kawano, K. Energy Level Diagram of HC(NH<sub>2</sub>)<sub>2</sub>PbI<sub>3</sub> Single Crystal Evaluated by Electrical and Optical Analyses. *Physical Chemistry Chemical Physics* **2018**, *20*, 1373–1380.
- (4) Shen, H.; Nan, R.; Jian, Z. J; Li, X. Materials Defect Step Controlled Growth of Perovskite MAPbBr<sub>3</sub> Single Crystal. *Journal of Materials Science* **2019**, *54*, 11596–11603.
- (5) Cheng, X.; Yuan, Y.; Jing, L.; Zhou, T.; Li, Z.; Peng, Z.; Yao, Q.; Zhang, J.; Ding, J. Nucleation-controlled growth of superior long-oriented CsPbBr<sub>3</sub> microrod single crystals for high detectivity photodetectors. *Journal of Materials Chemistry C*, 2019, 7, 14188–14197.
- (6) Li, Y.; Shao, W.; Ouyang, X.; Ouyang, X.; Zhu, Z.; Zhang, H.; Liu, B.; Xu, Q.; Scintillation Properties of Perovskite Single Crystals. *Journal of Physical Chemistry C* 2019, 123, 17449–17453.
- (7) Mix, L. T.; Ghosh, D.; Tisdale, J.; Lee, M.-C.; O'Neal, K. R.; Sirica, N.; Neukirch, A. J.; Nie, W.; Taylor, A. J.; Prasankumar, R. P.; Tretiak, S.; Yarotski, D. A. Hot Carrier Cooling and Recombination Dynamics of Chlorine-Doped Hybrid Perovskite Single Crystals. *The Journal of Physical Chemistry Letters* 2020, 11, 8430–8436.
- (8) Qiu, L.; Wang, Z.; Luo, S.; Li, C.; Wang, L.; Ke, S.; Shu, L.; Mix, L. T.; Ghosh, D.;

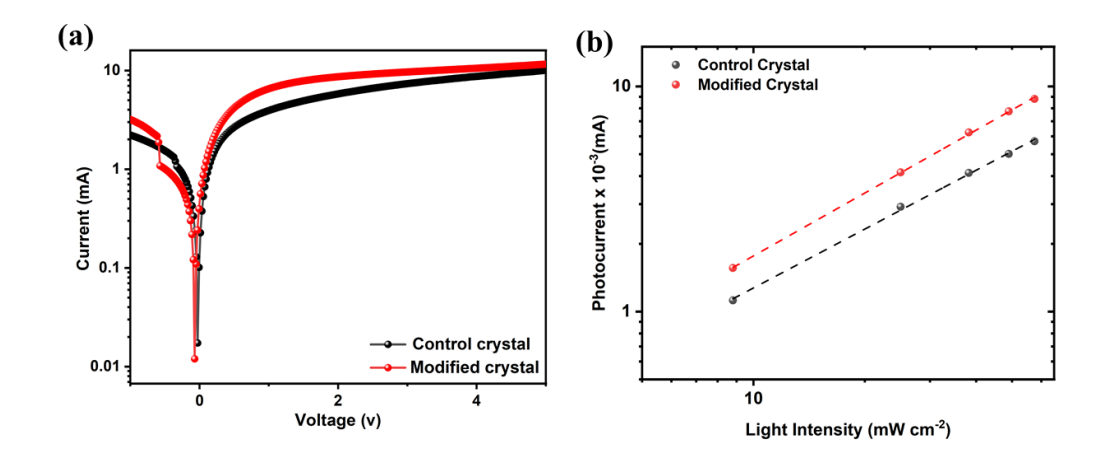
- Tisdale, J.; Lee, M.-C.; O'Neal, K. R.; Sirica, N.; Neukirch, A. J.; Nie, W.; Taylor, A. J.; Prasankumar, R. P.; Tretiak, S.; Yarotski, D. A. Perovskite MAPb(Br<sub>1</sub>-xClx)<sub>3</sub> Single Crystals: Solution Growth and Electrical Properties. *Journal of Crystal Growth* **2020**, *549*, 125869.
- (9) Feng, Y.; Pan, L.; Wei, H.; Liu, Y.; Ni, Z.; Zhao, J.; Rudd, P. N.; Cao, L. R.; Huang, J. Low Defects Density CsPbBr<sub>3</sub> Single Crystals Grown by an Additive Assisted Method for Gamma-Ray Detection. *Journal of Materials Chemistry C* **2020**, *8*, 11360–11368.
- (10) Rybin, N.; Ghosh, D.; Tisdale, J.; Shrestha, S.; Yoho, M.; Vo, D.; Even, J.; Katan, C.; Nie, W.; Neukirch, A. J.; Tretiak, S. Effects of Chlorine Mixing on Optoelectronics, Ion Migration, and Gamma-Ray Detection in Bromide Perovskites. *Chemistry of Materials* 2020, 32, 1854–1863.
- (11) Ma, L.; Yan, Z.; Zhou, X.; Pi, Y.; Du, Y.; Huang, J.; Wang, K.; Wu, K.; Zhuang C.; Han, X. *Nature Communications* **2021**, *12*, 2023.
- (12) L. Zhu, H. Cao, C. Xue, H. Zhang, M. Qin, J. Wang, K. Wen, Z. Fu, T. Jiang, L. Xu, Y. Zhang, Y. Cao, C. Tu, J. Zhang, D. Liu, G. Zhang, D. Kong, N. Fan, G. Li, C. Yi, Q. Peng, J. Chang, X. Lu, N. Wang, W. Huang and J. Wang, *Nature Communications*, 2021, 12, 5081.
- (13) He, Y.; Petryk, M.; Liu, Z.; Chica, D. G.; Hadar, I.; Leak, C.; Ke, W.; Spanopoulos, I.; Lin, W.; Chung, D. Y.; Wessels, B. W.; He Z.; Kanatzidis, M. G. *Nature Photonics* **2021**, 15, 36–42.
- (14) Parikh, N.; Sevak, P.; Khanam, S. J.; Prochowicz, D.; Akin, S.; Satapathi, S.; Tavakoli,
   M. M.; Banavoth, M.; Kalam A.; Yadav, P. Rationalizing the Effect of Polymer-Controlled Growth of Perovskite Single Crystals on Optoelectronic Properties. ACS

Omega **2022**, 7, 36535–36542.

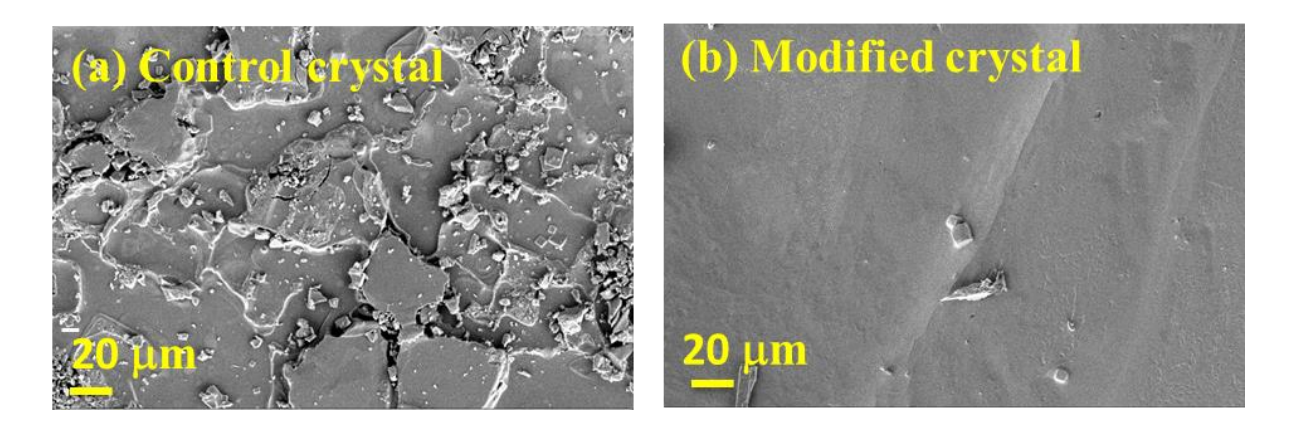
### **Appendix II**



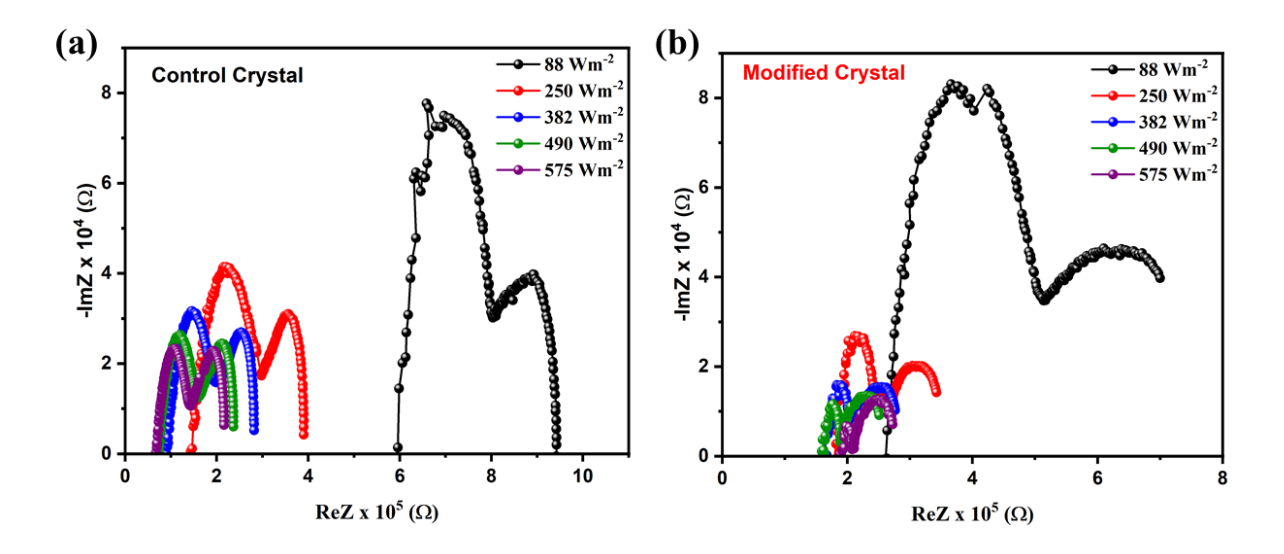
**Appendix II Fig. 1.** Optical images of (a) control and (b) modified SC (c) Powder X-ray diffraction (PXRD) pattern SC of both the.



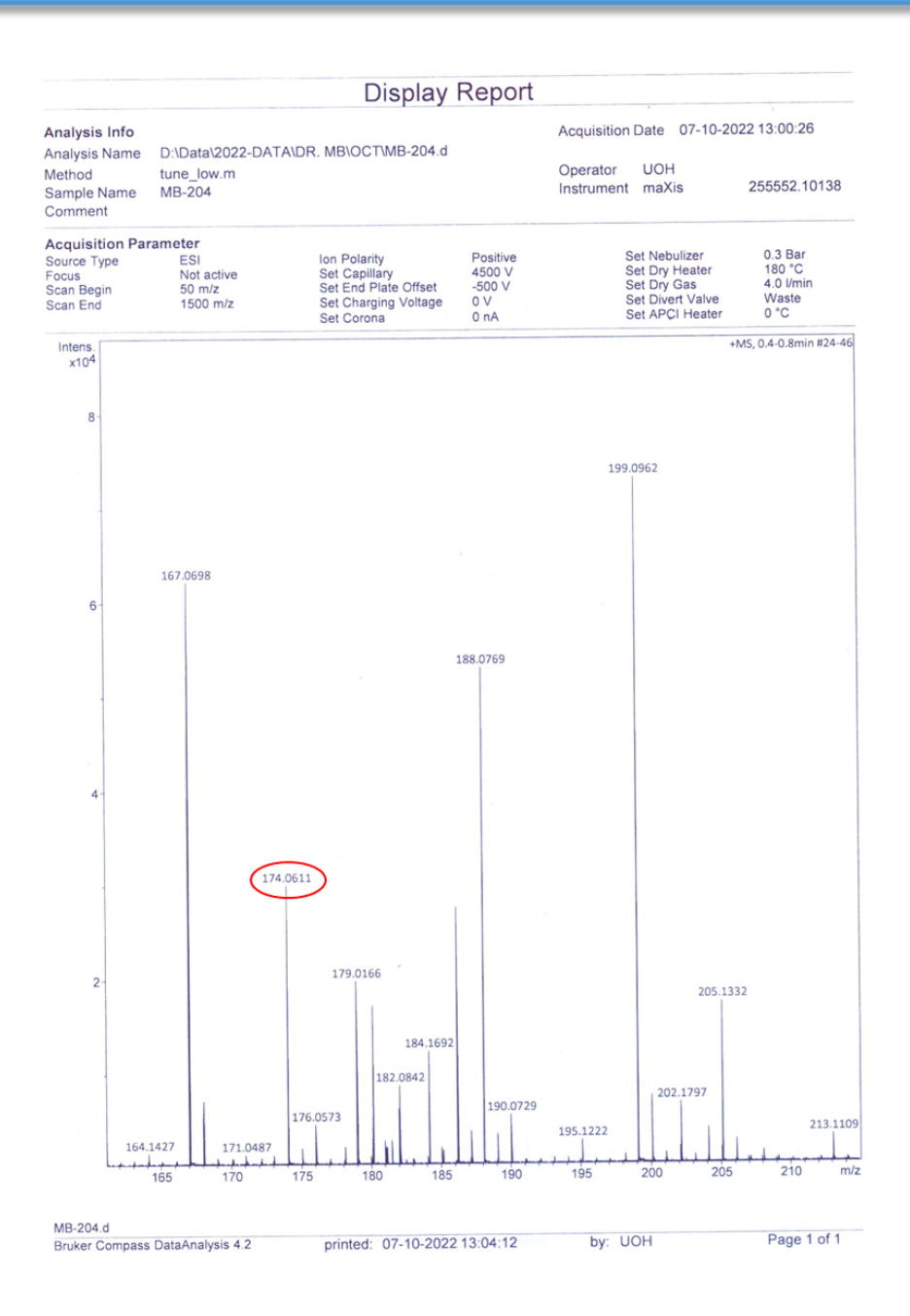
**Appendix II Fig. 2.** (a) Current-Voltage characteristics of both the crystals at 575 Wm<sup>-2</sup> illumination (b) Photocurrents of both the crystals as a function of illumination intensity



**Appendix II Fig. 3.** SEM images of (a) Control and (b) modified SCs. Scale bar 20μm.



**Appendix II Fig. 4.** Nyquist spectra as a function of illumination for (a) Control and (b) Modified crystals recorded in the frequency range of 1 MHz to 1Hz.



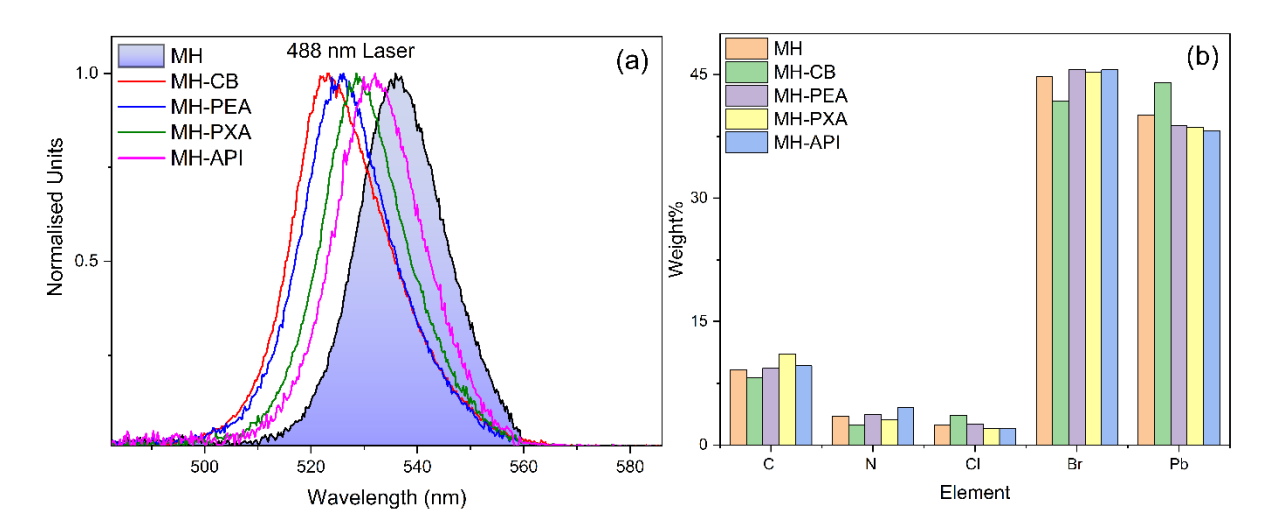
**Appendix II Fig. 5** HRMS data of modified crystal High-resolution mass spectrometry (HRMS) data. Molecular ion peak [M+H<sup>+</sup>] at 174.0611 related to API (3-Aminopiperidine dihydrochloride).

# **Appendix III**

#### Appendix III Table 1 Literature Review

C N	<b>X</b> 7	Growth	Additives	Perovskite material	A 1' 4'	D. C
S.No	Year	Method	used	used	Application	Ref
1.	2015	ITC		MAPbBr <sub>3-X</sub> Cl <sub>X</sub>	PD	(1)
	2016	ITC		CH <sub>3</sub> NH <sub>3</sub> PbI <sub>3</sub> (Cl)	Optoelectronic	(2)
2.	2010	110	_	C1131 V1131 V13(C1)	Devices	
3.	2018	ITC		CH3NH3PbI <sub>3-x</sub> Br <sub>x</sub>	_	(3)
4.	2019	ITC		MAPbBr <sub>3-X</sub> Cl <sub>X</sub>	Scintillation	(4)
5.	2020	ITC	_	$MAPbBr_{3-X}Cl_{X}$	_	(5)
6.	2020	ITC	_	$MAPb(Br_{1-X}Cl_X)_3$	Electrical	(6)
					Properties	
7.	2020	ITC	_	$MAPbBr_{3-X}Cl_{X}$	Γ-Ray Responses.	(7)
8.	2021	Bridgma n		CsPbBr <sub>3-3n</sub> $X_{3n}$ ( $X = Cl$ , $I$ )	X-ray	(8)
9.	2021	ITC	_	$(FA_XMA_yCs_{1-x-}$ $_y)Pb(I_zBr_{1-z})_3$	Solar cell	(9)
10.	2022	ITC	-	CH <sub>3</sub> NH <sub>3</sub> Pb(Br <sub>x</sub> I <sub>1-x</sub> ) <sub>3</sub>	PD	(10)
11.	2023	ITC	-	$CH_3NH_3(Br_{1-X}Cl_X)_3$	-	(11)

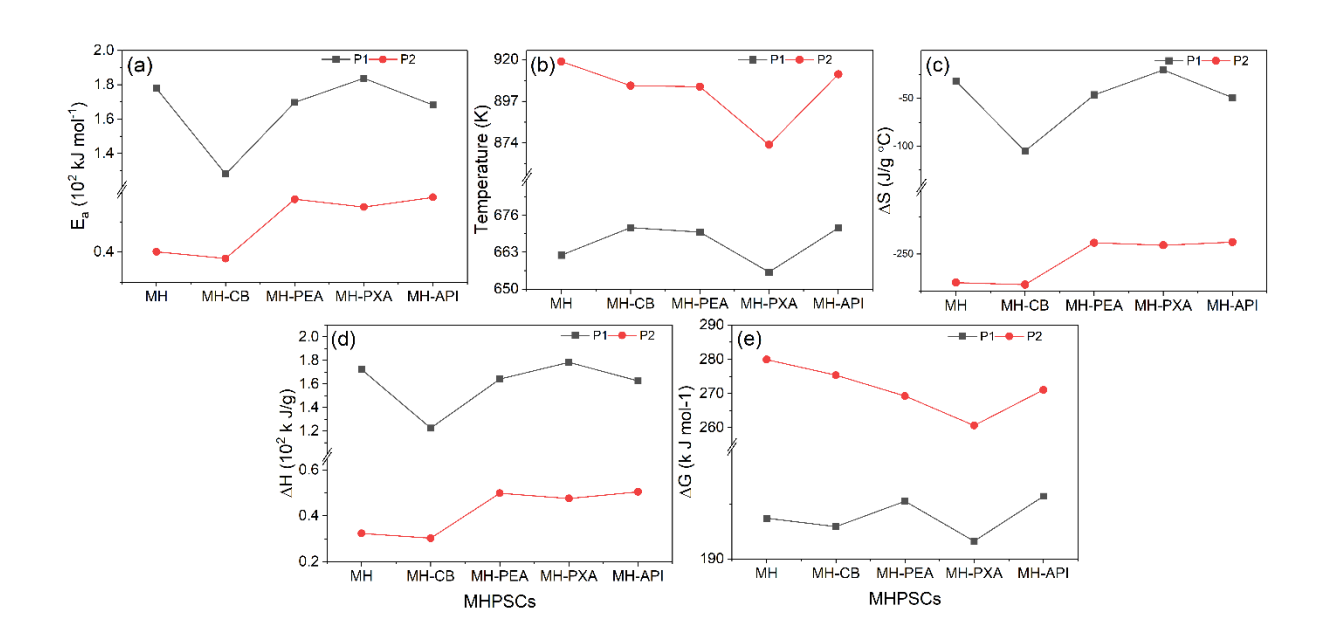
12.	2023	ITC	CB, PEA, PXA, API	MAPb(Br <sub>1-x</sub> Cl <sub>x</sub> ) <sub>3</sub>	HHG study	This work
-----	------	-----	----------------------	---	-----------	-----------



**Appendix III Fig. 1.** (a) PL spectra recorded with 488 nm laser and (b) EDX data representing elemental weight % correspond to MH, MH-CB, MH-PEA, MH-PXA, and MH-API, respectively.

Appendix III Table 2 Comparative study of MHPSCs TRPL decay profiles.

MHPSCS	τ (ns)
MH	0.37
МН-СВ	1.51
MH-PEA	0.84
MH-PXA	0.63
MH-API	0.56



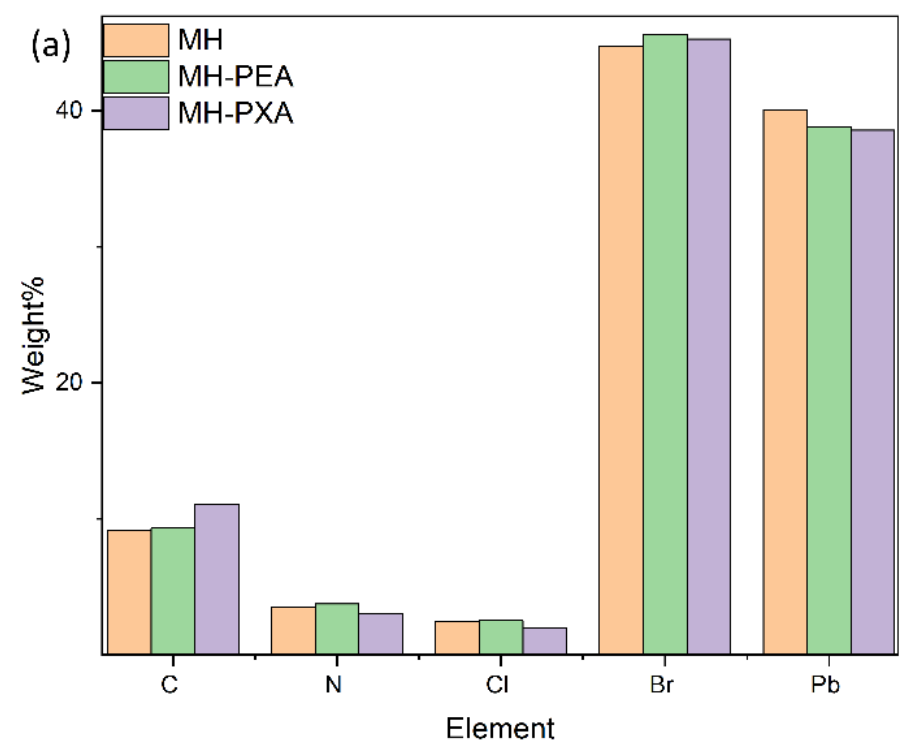
**Appendix III Fig. 2 (a-e)**. Comparative study of MHPSCs thermodynamic properties of phase one (P1) and two (P2) transformations.

#### **References:**

- (1) Fang, Y.; Dong, Q.; Shao, Y.; Yuan, Y.; Huang, J. Highly Narrowband Perovskite Single-Crystal Photodetectors Enabled by Surface-Charge Recombination. *Nature Photonics* **2015**, *9* (10), 679–686.
- (2) Lian Z.; Yan, Q.; Gao, T.; Ding, J.; Lv, Q.; Ning, C.; Li, Q.; Sun, J.L. Perovskite CH<sub>3</sub>NH<sub>3</sub>PbI<sub>3</sub>(Cl) Single Crystals: Rapid Solution Growth, Unparalleled Crystalline Quality, and Low Trap Density toward 10(8) cm(-3). *Journal of the American Chemical Society* **2016**, *138*, 9409-9412.
- (3) Wang, W.; Su, J.; Zhang, L.; Lei, Y.; Wang, D.; Lu, D.; Bai, Y. Growth of mixed-halide perovskite single crystals. *CrystEngComm* **2018**, *20*, 1635-1643.
- (4) Li, Y.; Shao, W.; Ouyang, X.; Ouyang, X.; Zhu, Z.; Zhang, H.; Liu, B.; Xu, Q.; Scintillation Properties of Perovskite Single Crystals. *Journal of Physical Chemistry C* **2019**, *123*, 17449–17453.
- (5) Qiu, L.; Wang, Z.; Luo, S.; Li, C.; Wang, L.; Ke, S.; Shu, L.; Perovskite MAPb(Br1-xClx)<sub>3</sub> single crystals: Solution growth and electrical properties. *Journal of Crystal Growth* **2020**, *549*, 125869.
- (6) N. Rybin, D. Ghosh, J. Tisdale, S. Shrestha, M. Yoho, D. Vo, J. Even, C. Katan, W. Nie, A.J. Neukirch, S. Tretiak, Effects of Chlorine Mixing on Optoelectronics, Ion Migration, and Gamma-Ray Detection in Bromide Perovskites. *Chemistry of Materials* 2020, 32, 1854-1863.
- (7) Zhang, P.; Hua, Y.; Li, X.; Zhang, L.; Liu, L.; Li, R.; Zhang, G.; Tao, X. Filter-free color image sensor based on CsPbBr<sub>3-3n</sub>X<sub>3n</sub> (X = Cl, I) single crystals. *Journal of Materials Chemistry C* **2021**, *9*, 2840-2847.

- (8) Liu, Y.; Zhang, Y.; Zhu, X.; Yang, Z.; Ke, W.; Feng, J.; Ren, X.; Zhao, K.; Liu, M.; Kanatzidis, M.;. Liu, G.S. Inch-sized high-quality perovskite single crystals by suppressing phase segregation for light-powered integrated circuits. *Science Advances* **2021**, *7*, 112.
- (9) Ding, J.; Gao, W.; Gao, L.; Lu, K.; Liu, Y.; Sun, J.L.; Yan, Q.; Unraveling the Effect of Halogen Ion Substitution on the Noise of Perovskite Single-Crystal Photodetectors *Journal of Physical Chemistry Letters* **2022**, *13*, 7831-7837.
- (10) Z. Xiao, T. Tao, J. Shu, R. Pan, W. Dang, N. Zhao, S. Pan, W. Zhang, Charge Carrier Recombination Dynamics in MAPb(Br<sub>x</sub>Cl<sub>1-x</sub>)<sub>3</sub> Single Crystals. *The Journal of Physical Chemistry Letters* **2023**, *14*, 245.

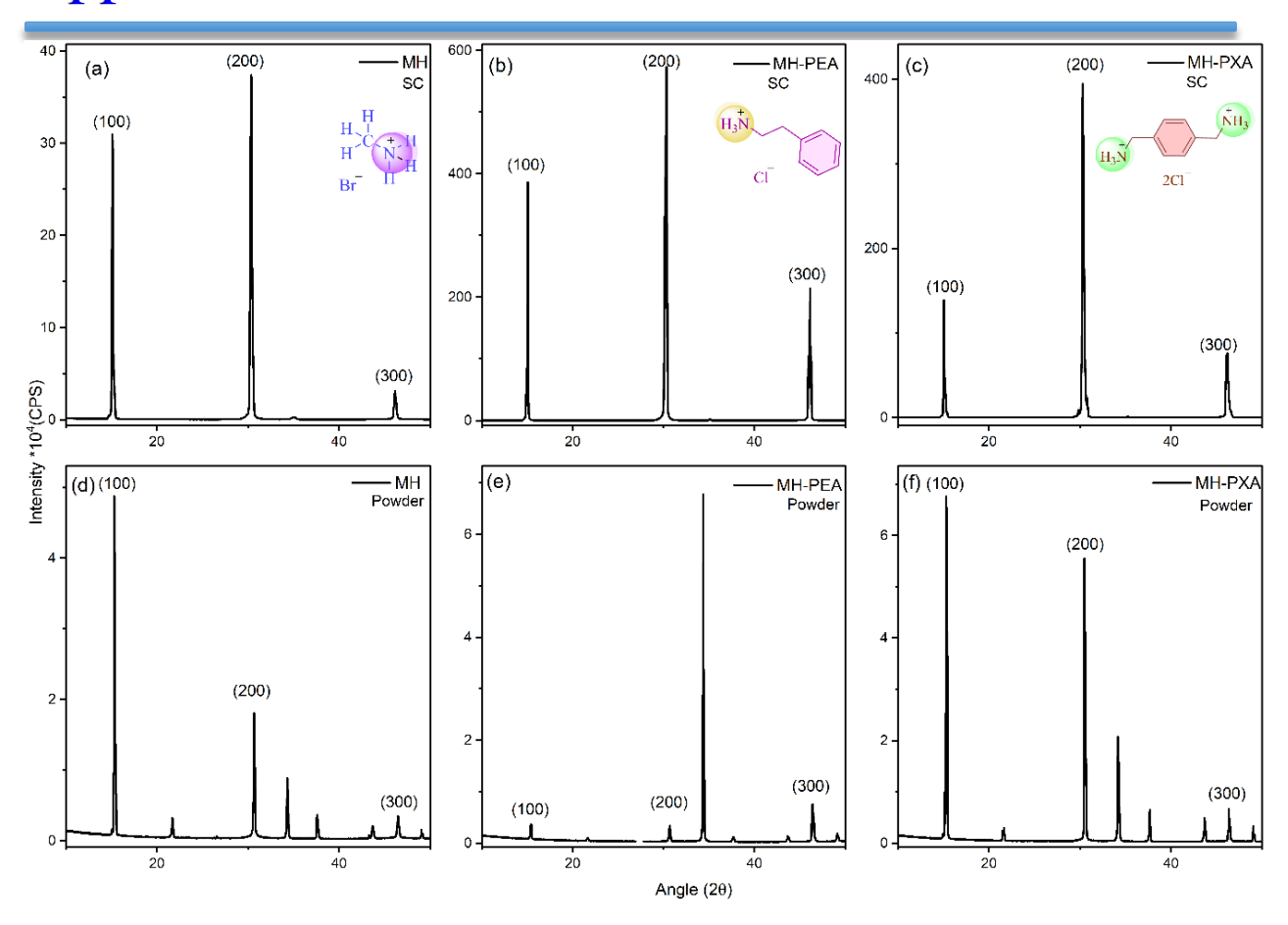
# **Appendix IV**



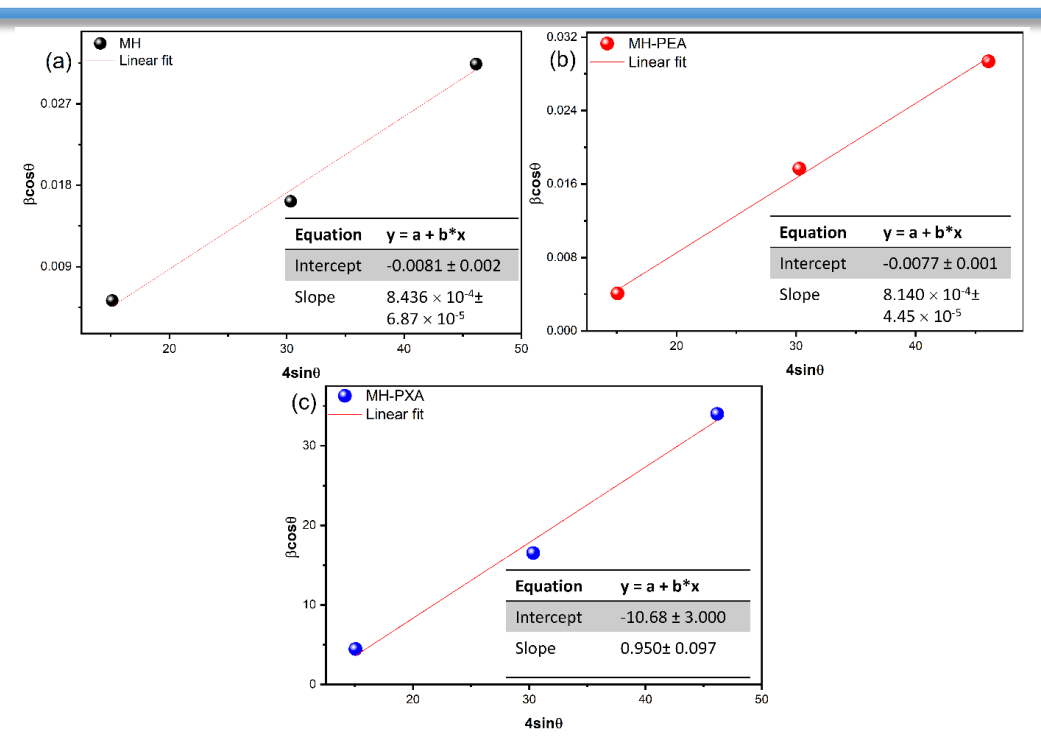
Appendix IV Fig 1. The EDX weight % values of the modified and pristine MHSCs.

**Appendix IV Table 1** The following table represents the elemental ratios extracted from the EDX data.

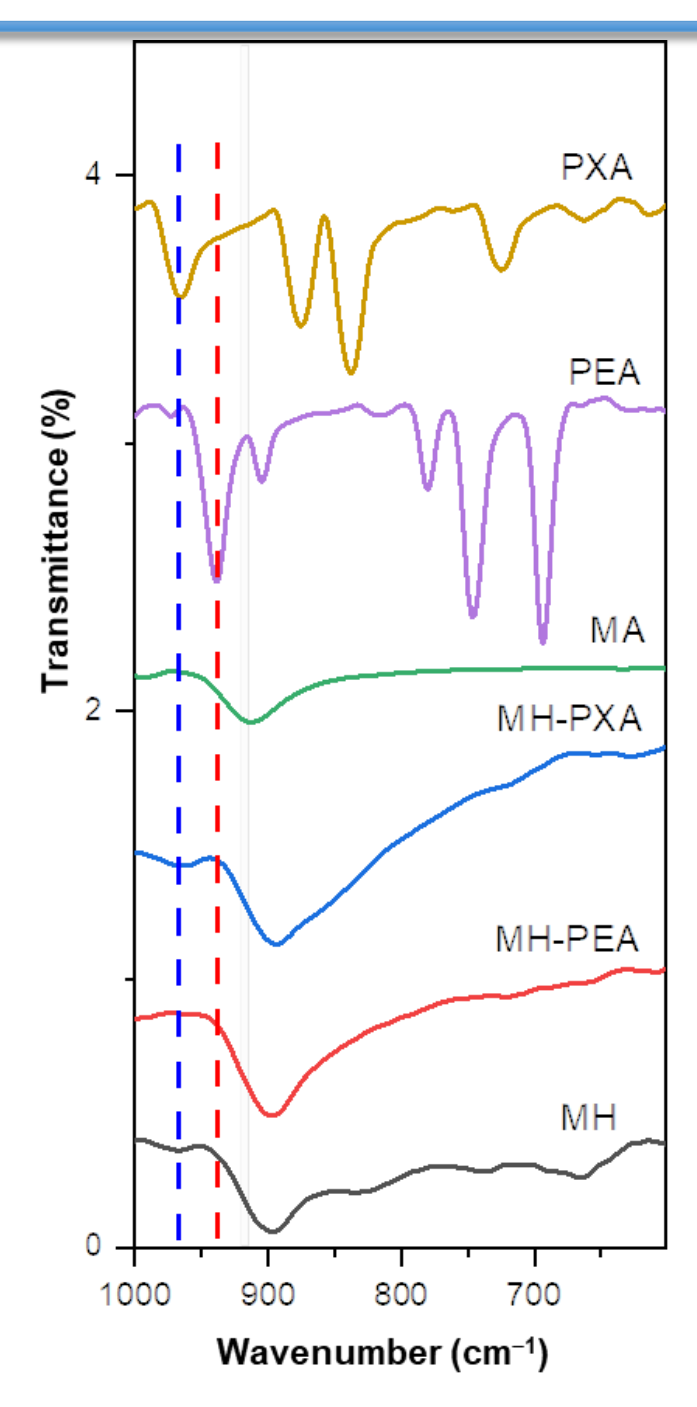
N : Pb : Br : Cl	N : Pb : Br : Cl	
(Calculated)	(Observed)	
1:1:2.8:0.2	1.3:1:2.8:0.3	
1.02 : 1 : 2.8 : 0.21	1.4:1:3.1:0.4	
1.03 : 1 : 2.8 : 0.22	1.2:1:3:0.3	
	(Calculated) 1:1:2.8:0.2 1.02:1:2.8:0.21	



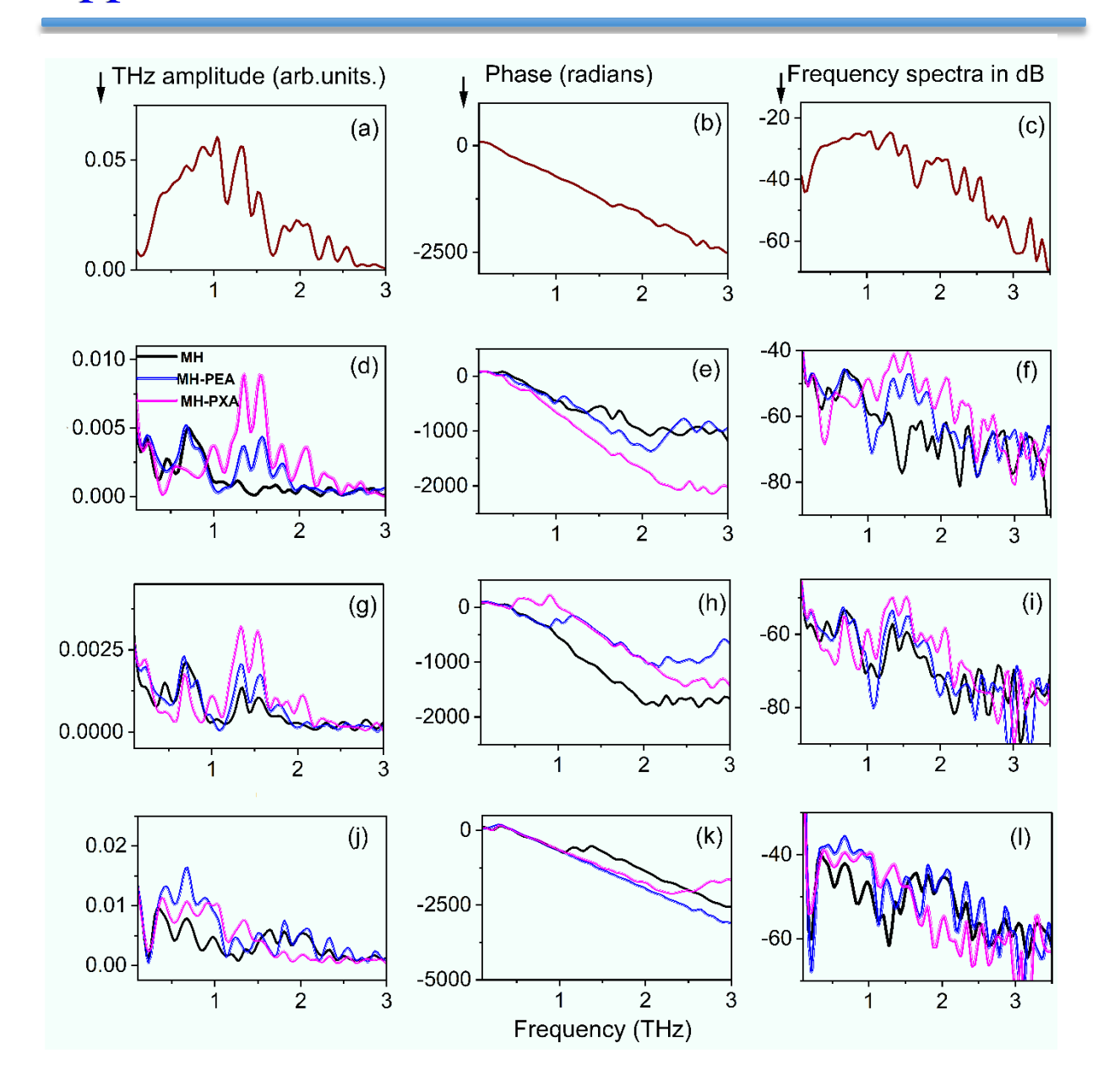
**Appendix IV Fig 2.** The p-XRD pattern of the modified and pristine MHSCs, (a-c) single crystal (SC) and (d-f) powder samples.



**Appendix IV Fig 3.** (a-c) The calculated microstrain parameters from powder XRD data of each MH, MH-PEA, and MH-PXA SCs.



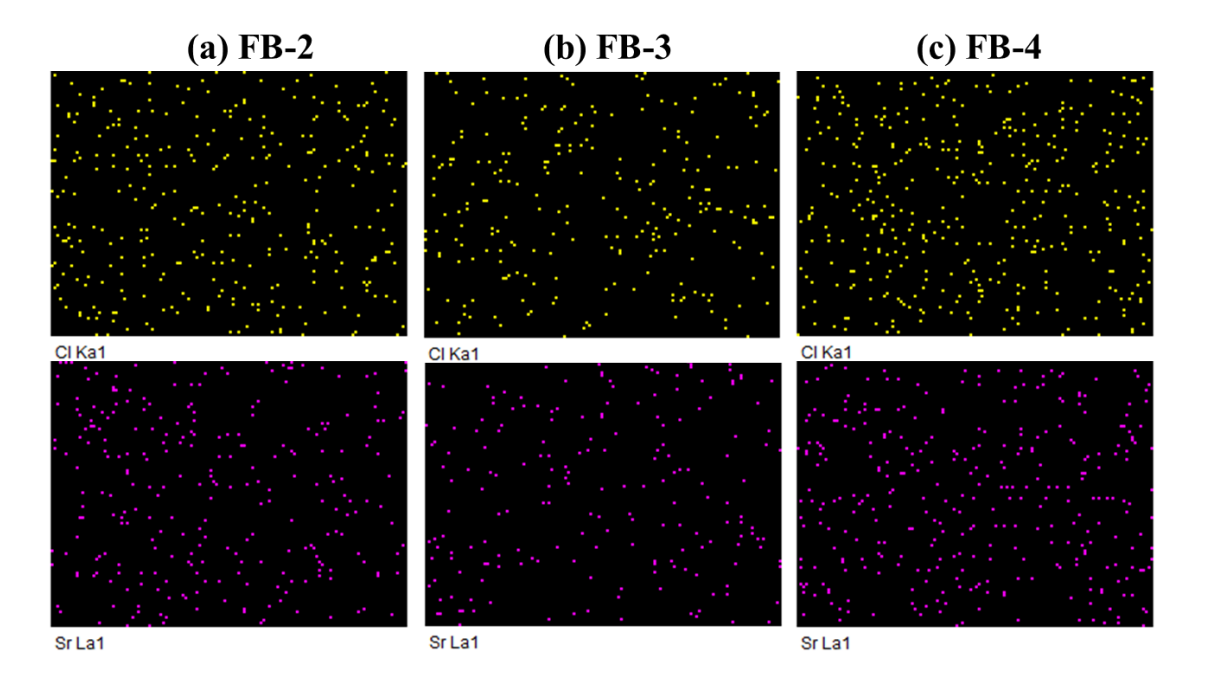
**Appendix IV Fig 4.** FT-IR spectra, changing vibrational modes with respect to additives in the modified MHSCs from 1000 to 600 cm<sup>-1</sup>.



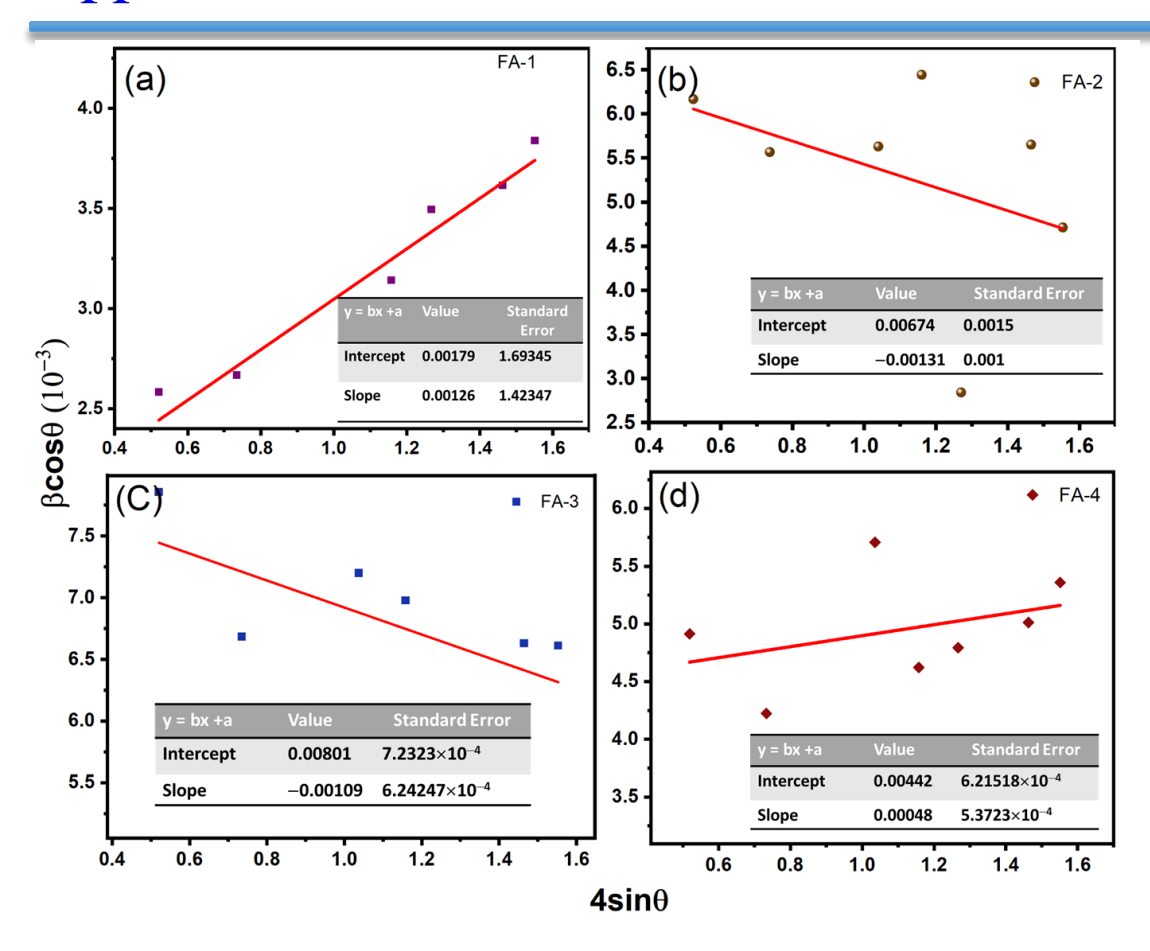
**Appendix IV Fig 5.** The THz electric field of THz amplitude, phase and frequency spectra in dB (a-c) for reference pulse, (d-f) for single crystals transmission at 0°, (g-i) transmission at 45°, and (j-l) reflection at 45°, respectively. The legends used for all the subgraphs in this Fig. are the same (Solid Wine: Reference THz pulse, Simple Black: MH, Double Red: MH-CB, Thick-Thin Blue: MH-PEA, Thin-Thick Magenta: MH-PXA, Triple Olive: MH-API).

## **Appendix V**

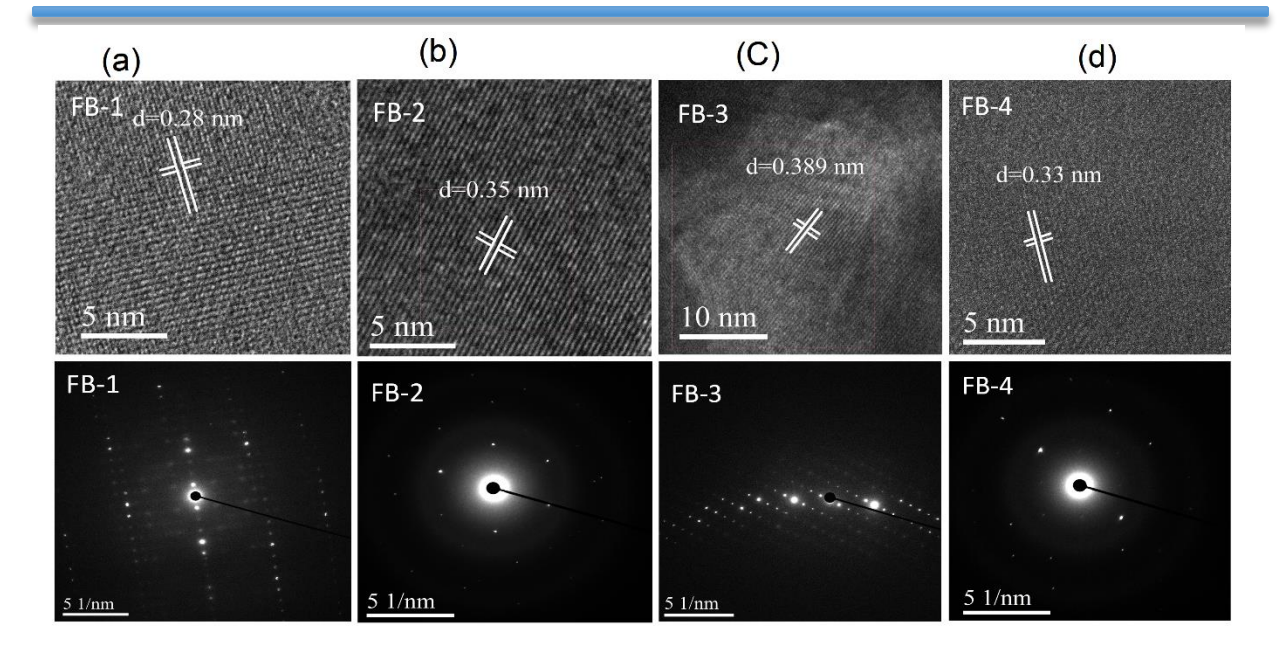
# Stability Enhancement and Pronounced Three-photon Absorption in SrCl<sub>2</sub>-doped FAPbBr<sub>3</sub> Nano Crystals



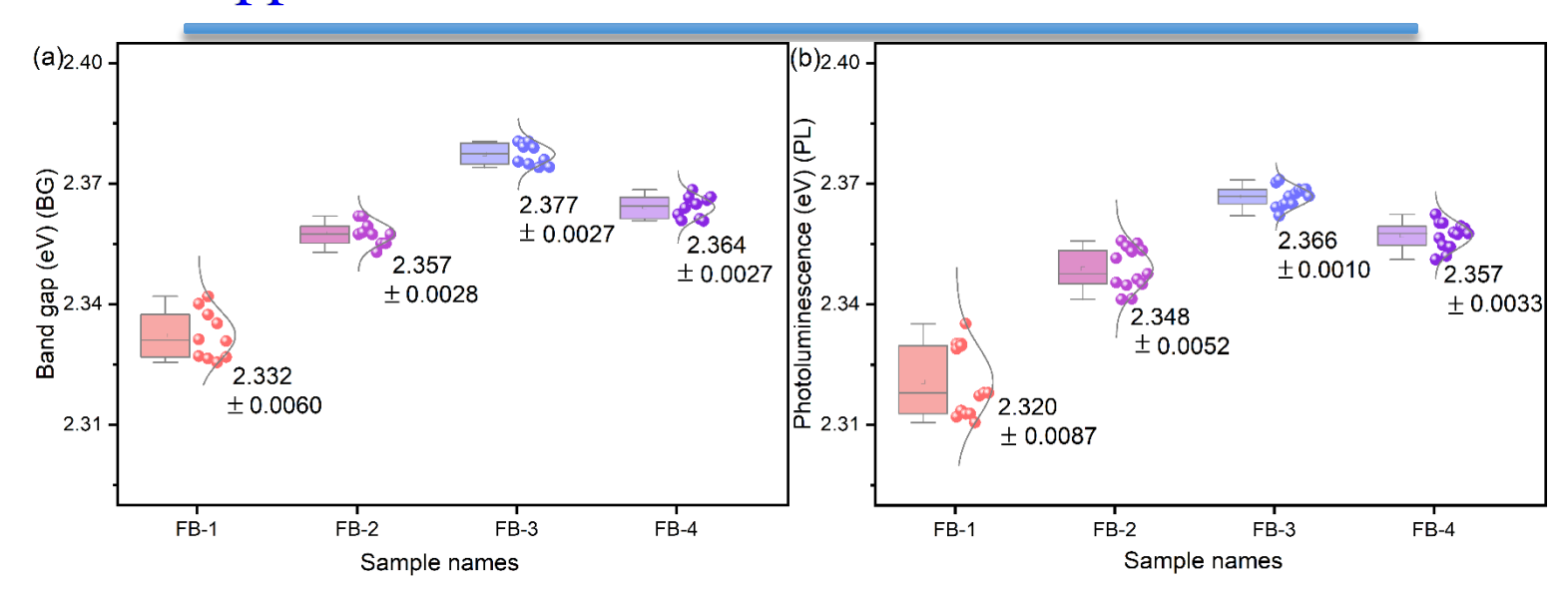
**Appendix V Fig. 1.** (a-c) Elemental mapping of Cl (top panel) and Sr (bottom panel) ions for doped sample from left to right and accordingly labels at the top of each image.



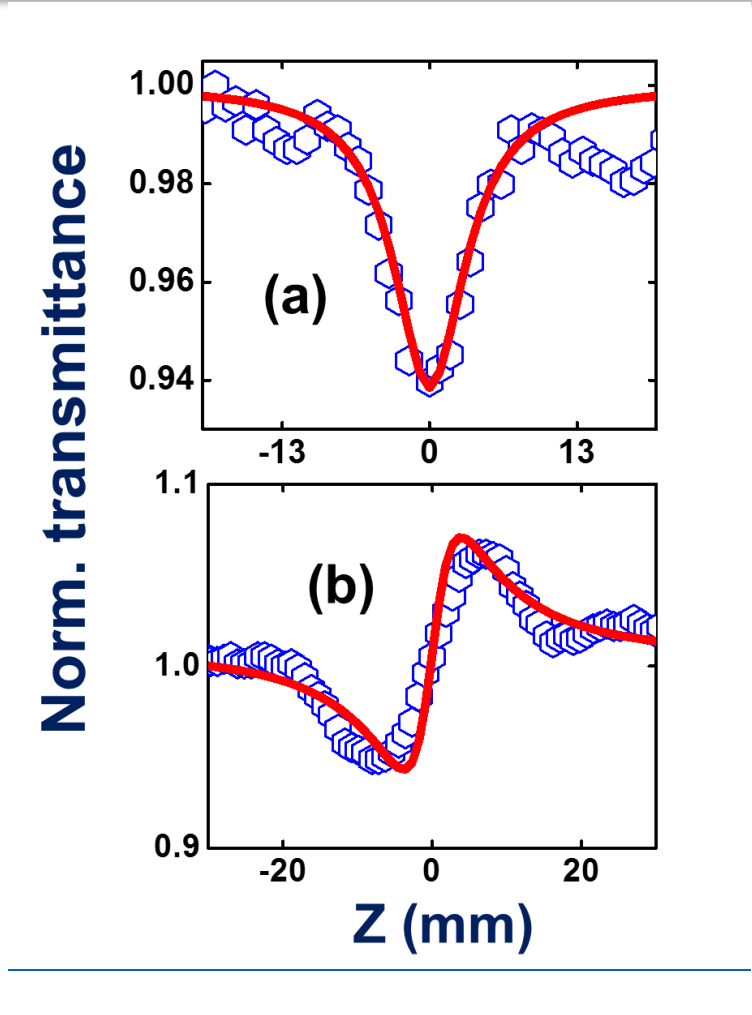
**Appendix V Fig. 2.** The calculated microstrain parameters from powder XRD data of each sample; labels are at the top of each sample image, respectively.



**Appendix V Fig. 3.** (a-d) HR-TEM images and SAED pattern (below) patterns for each sample are illustrated from left to right, and labels are at the top of each sample image.



**Appendix V Fig. 4.** Distribution box plot represents the four samples repeated experimental values of (a) bandgap and (b) PL.



**Appendix V Fig. 5.** (a) OA data for toluene (solvent) (b) CA data for toluene. Red lines in both OA and CA data represent the fitted curves, while the open hexagons represent the experimental data.

# Unveiling the Perovskite Single Crystals for Photonics Applications via Facile Molecular Engineering

by Sarvani Jowhar Khanam

Submission date: 27-Jun-2023 12:40PM (UTC+0530)

**Submission ID:** 2123365742

File name: Sarvani Jowhar Khanam.pdf (834.85K)

Word count: 27147

Character count: 147115

# Unveiling the Perovskite Single Crystals for Photonics Applications via Facile Molecular Engineering

ORIGINALITY REPORT

SIMILARITY INDEX

INTERNET SOURCES

**PUBLICATIONS** 

STUDENT PAPERS

**PRIMARY SOURCES** 

Sarvani Jowhar Khanam, Srinivasa Rao Konda, Azmeera Premalatha, Ravi Ketavath, Wufeng Fu, Wei Li, Murali Banavoth. ""Additive Engineering in CH3NH3PbBr3 Single Crystalsfor Terahertz Devices and Tunable High Order Harmonics"", Journal of Materials Chemistry

Publication

Sarvani Jowhar Khanam, Dipanjan Banerjee, Venugopal Rao Soma, Banavoth Murali. " Stability enhancement and pronounced threephoton absorption in SrCl -doped FAPbBr nano crystals", Journal of Materials Chemistry C, 2023

Publication

Sarvani Jowhar Khanam, Srinivasa Rao Konda, Wei Li, Banavoth Murali. "Aromatic Additives Boost the Terahertz Properties of Mixed Halide Perovskite Single Crystals", The Journal of Physical Chemistry Letters, 2023 Publication

University of Hyderabad

Hyderabad - 500 046

Associate Professor School of Chemistry. University of Fryderabad

Hyderabad 500 046

4	Sarvani Jowhar Khanam, Nishi Parikh, Soumitra Satapathi, Abul Kalam, Murali Banavoth, Pankaj Yadav. "Role of Heterocyclic Organic Compounds on the Optoelectronic Properties of Halide Perovskite Single Crystals", ACS Applied Energy Materials, 2022  School Publication	Blevery Blevery Blevery of Hyders of Chemistry of Hyders
5	Submitted to University of Hyderabad, Hyderabad Student Paper	4%
6	www.ncbi.nlm.nih.gov Internet Source	1 %
7	Chenglong Li, Yao Ma, Yifan Xiao, Liang Shen, Liming Ding. "Advances in perovskite photodetectors", InfoMat, 2020	1 %
8	Lei Gao, Qingfeng Yan. "Recent Advances in Lead Halide Perovskites for Radiation Detectors", Solar RRL, 2019	1 %
9	Tiebin Yang, Feng Li, Rongkun Zheng. "Recent Progress on Cesium Lead Halide Perovskites for Photodetection Applications", ACS Applied Electronic Materials, 2019	<1%
10	Wei Tian, Huanping Zhou, Liang Li. "Hybrid Organic-Inorganic Perovskite Photodetectors",	<1%

	Publication	
11	www.researchgate.net Internet Source	<1%
12	Apurba Mahapatra, Vishnu Anilkumar, Rohit D. Chavan, Pankaj Yadav, Daniel Prochowicz. " Understanding the Origin of Light Intensity and Temperature Dependence of Photodetection Properties in a MAPbBr Single-Crystal-Based Photoconductor ", ACS Photonics, 2023 Publication	<1%
13	onlinelibrary.wiley.com Internet Source	<1%
14	www.unboundmedicine.com Internet Source	<1%
15	researchmgt.monash.edu Internet Source	<1%
16	www.lu.lv Internet Source	<1%
17	Yihui He, Liviu Matei, Hee Joon Jung, Kyle M. McCall et al. "High spectral resolution of gamma-rays at room temperature by perovskite CsPbBr3 single crystals", Nature	<1%

Publication

Communications, 2018

18	onceuponaman.blogspot.com Internet Source	<1%
19	cdr.lib.unc.edu Internet Source	<1%
20	pubs.acs.org Internet Source	<1%
21	Muhammad Akhyar Farrukh, Komal Mehmood Butt, Kok-Keong Chong, Wei Sea Chang. "Photoluminescence emission behaviour on the reduced band gap of Fe doping in CeO2-SiO2 nanocomposite and photophysical properties", Journal of Saudi Chemical Society, 2018 Publication	<1%
22	aip.scitation.org Internet Source	<1%
23	patents.google.com Internet Source	<1%
24	en.wikipedia.org Internet Source	<1%
25	Nikita Rybin, Dibyajyoti Ghosh, Jeremy Tisdale, Shreetu Shrestha et al. "Effects of Chlorine Mixing on Optoelectronics, Ion Migration, and Gamma-Ray Detection in Bromide Perovskites", Chemistry of Materials, 2020 Publication	<1%

26	Submitted to University of Asia Pacific Student Paper	<1%
27	Fangze Liu, Rong Wu, Jing Wei, Wanyi Nie, Aditya D. Mohite, Sergio Brovelli, Liberato Manna, Hongbo Li. "Recent Progress in Halide Perovskite Radiation Detectors for Gamma- Ray Spectroscopy", ACS Energy Letters, 2022	<1%
28	Submitted to Indian Institute of Technology, Kanpur Student Paper	<1%
29	www.rsc.org Internet Source	<1%
30	pubs.rsc.org Internet Source	<1%
31	Submitted to King Abdullah University of Science and Technology (KAUST) Student Paper	<1%
32	wrap.warwick.ac.uk Internet Source	<1%
33	Submitted to South Asian University Student Paper	<1%
34	Fangze Liu, Michael Yoho, Hsinhan Tsai, Kasun Fernando et al. "The working principle of hybrid perovskite gamma-ray photon counter", Materials Today, 2020	<1%

35	www.science.org Internet Source	<1%
36	Danilo Dini, Mário J. F. Calvete, Michael Hanack. "Nonlinear Optical Materials for the Smart Filtering of Optical Radiation", Chemical Reviews, 2016 Publication	<1%
37	Makhsud I. Saidaminov, Md Azimul Haque, Jawaher Almutlaq, Smritakshi Sarmah et al. "Inorganic Lead Halide Perovskite Single Crystals: Phase-Selective Low-Temperature Growth, Carrier Transport Properties, and Self-Powered Photodetection", Advanced Optical Materials, 2017 Publication	<1%
38	Naveen Kumar Tailor, Nishi Parikh, Pankaj Yadav, Soumitra Satapathi. "Dielectric Relaxation and Polaron Hopping in Cs AgBiBr Halide Double Perovskites ", The Journal of Physical Chemistry C, 2022	<1%
39	www.erachair.lu.lv Internet Source	<1%
40	Submitted to National Institute of Technology, Rourkela Student Paper	<1%

41	Submitted to SASTRA University Student Paper	<1%
42	Zheng Zhang, Ge Yang. "Recent advancements in using perovskite single crystals for gamma-ray detection", Journal of Materials Science: Materials in Electronics, 2020 Publication	<1%
43	infoscience.epfl.ch Internet Source	<1%
44	Srinivasa Rao Konda, Yucai Lin, Rahul A. Rajan, Weili Yu, Wei Li. "Measurement of Optical Properties of CH3NH3PbX3 (X = Br, I) Single Crystals Using Terahertz Time-Domain Spectroscopy", Materials, 2023 Publication	<1%
45	link.springer.com Internet Source	<1%
46	www.semiconductor-today.com Internet Source	<1%
47	Mehri Ghasemi, Songyang Yuan, Jiandong Fan, Baohua Jia, Xiaoming Wen. "The Challenges Toward the Development of Metal-Halide Perovskite Single Crystal Solar Cells", Journal of Materials Chemistry A, 2023 Publication	<1%

Exclude quotes On Exclude matches < 14 words

Exclude bibliography On